ISSN 0469-4732

INSTITUTE OF PLASMA PHYSICS

NAGOYA UNIVERSITY

Proceedings of Symposium
on
Physics of Target Implosion
and
Pulsed Power Techniques

Edited by Keishiro Niu

(Received — Feb. 5, 1988)

IPPJ- 859 Feb. 1988

RESEARCH REPORT

NAGOYA, JAPAN

(1)

Proceedings of Symposium
on
Physics of Target Implosion
and
Pulsed Power Techniques

Edited by Keishiro Niu

(Received — Feb. 5, 1988)

IPPJ- 859 Feb. 1988

Further communication about this report to be sent to the Research Information Center, Institute of Plasma Physics, Nagoya University, Nagoya 464, Japan.

PREFACE

It is reported that by using the Nd glass laser, experiments of beam-target interaction are carried out and neutrons are observed, released from targets. The maximum number of observed neutrons, however, is of the order of 10^{13}, which is much less than that for the real goal, i.e., 10^{21}. The physics nowadays occuring in a tiny test-target will differ from that in a practical target in a reactor. It is very important at present to reveal the phenomena occuring in a practical target and to make clear the physics of target implosion. At the end of 1985, construction of PBFA-II in Sandia National Laboratories was finished. PBFA-II can extract the lithium beams of 2MJ. By this value, are expected achievement of breakeven and release of nearly practical amount of fusion energy from a target. Unfortunately, experiments regarding beam-target interaction are not realized yet. Thus the theoretical and numerical approaches will play an important role in ICF research at present. And developement of pulsed power techniques in Japan seems urgent for fusion research.

On September 30 and October 1, symposium on "Physics of Target Implosion and Pulsed Power Techniques" was held in Yokohama, being participated by three professors from Spain, where the theoretical and numerical studies are being performed most earnestly for the ICF research. Prof. L. Drska, one of the organizer of the 18th ECLIM, of Tech. Univ. of Prague, could not attend the symposium due to delay of the arrival at Japan, but kindly has submitted the manuscript for the proceedings. The proceedings will be useful for ICF researchers, I believe, and many requests from abroad to receive them have been accepted.

In summary, describing the program of symposium here, I would like to express my cordial thanks to the Institute of Plasma Physics, Nagoya University, for the fact that almost all works by Japanese reported here, have been carried out by using the facilities in IPP Nagoya, according to the cooperative program of the Institute.

Keishiro Niu
Tokyo Inst. of Tech.

PROGRAM OF SYMPOSIUM
ON
Physics of Target Implosion and Pulsed Power Techniques

September 30 (Wed)

Chairman Tomokazu Kato

1. 9.30-10.00 K. Niu (Tokyo Inst. Tech.)
   Fuel Implosion in ICF Target and Pellet Gain
2. 10.00-10.30 H. Takeda (Tokyo Inst. Tech.)
   Numerical Analysis for Influence of Nonuniformities on Target Implosion
3. 10.30-11.00 K. Furuta (Tokyo Inst. Tech.)
   Stability Analysis for Burn Wave in LIB-ICF Target
4. 11.00-11.30 S. Yanashima (Tokyo Inst. Tech)
   Analysis for Imploding Shock Wave in LIB-ICF Target
5. 11.30-12.00 K. Ozaki (Tokyo Inst. Tech.)
   Development of Electromagnetic PIC Code for LIB Diode

Lunch Break 12.00-13.00

Chairman Takashi Yabe

6. 13.00-13.30 T. Kaneda (Tokyo Inst. Tech.)
   Kinetic Theoretical Analysis for Propagation of Rotating Ion Beam in ICF
7. 13.30-14.00 T. Aoki (Tokyo Inst. of Tech.)
   Hybrid Particle Simulation for Focusing of Rotating and Propagating Ion Beam
8. 14.00-14.30 T. Ishimoto and T. Kato (Waseda Univ.)
   Electron Current Effect on Stability of Plasma Channel
9. 14.30-15.00 S. Kawata, M. Matsumoto and Y. Masubuchi (Tech. Univ. Nagaoka)
   Numerical Simulation in LIB ICF
10. 15.00-15.30 J. M. Perlado (Univ. Politec. Madrid)
    Simulation Code for ICF including Radiative Energy Transfer

Coffee Break 15.30-15.50

Chairman Masatada Ogasawara

11. 15.50-16.20 Y. Masubuchi and S. Kawata (Tech. Univ. Nagaoka)
    Numerical Analysis of Target Implosion in LIB ICF
12. 16.20-16.50 K. Mima (Osaka Univ.)
    Scaling Law for Critical Implosion Plasma Irradiated by Laser (temporal)
13. 16.50-17.20 M. Murakami and K. Nishihara (Osaka Univ.)
    Efficient Shell Implosion and Target Design
14. 17.20-17.50 T. Okada (Tokyo Univ. Agri. Tech.)
    Microinstabilities in Ion Beam Propagation
15. 17.50-18.20 R. Kawasaki and T. Kato (Waseda Univ.)
    Effect of Surrounding Gas on Propagation of Light Ion Beam through the Z-Discharge Channel

Get Together Party 19.00-20.00

October 1 (Thu)

Chairman Kiyoshi Yatsui

16. 9.30-10.00 H. Takabe (Osaka Univ.)
    Stability Requirement for Ignition and High Gain Implosion
17. 10.00-10.30 J. R. Sanmartín (Univ. Politec. Madrid)
    Non-Uniform Irradiation of Laser Targets
18. 10.30-11.00 A. Barrero (Univ. Sevillia)
    Non-Uniform Illumination Effects in Laser Irradiated Spherical Pellets
19. 11.00-11.30 T. Yabe (Osaka Univ.)
    Feasibility of Soft X-Ray Driver in ICF

Lunch Break 11.30-13.00

Chairman Koichi Kasuya

20. 13.00-13.30 Y. Matsukawa (Osaka City Univ.)
    Generation of High Brightness Ion Beam from Insulated Anode PED
21. 13.30-14.00 N. Sasaki, N. Takagi and S. Yano (Kobe Univ. Mercantile Marine)
    The Application of Rutherford Backscattering for Analyzing Multi-layer Structure Change Induced by Pulsed Ion Beam Bombardment
22. 14.00-14.30 K. Yatsui, K. Masugata, K. Aga, H. Isobe and Y. Araki (Tech. Univ. Nagaoka)
    *Production of Highly Focused, Intense Pulsed Ion Beam and Its Interaction with Targets*20. 11.30-12.00 T. Yabe (Osaka Univ.)
23. 14.30-15.00 T. Yabe (Osaka Univ.)
    Critical Physics in Laser-Driven Implosion Dynamics

Coffee Break 15.00-15.20

Chairman Keishiro Niu

24. 15.20-15.50 H. Yoneda, H. Tomita, K. Horioka and K. Kasuya (Tokyo Inst. Tech.)
    Research on Anode Plasma Behavior of Flashover Pulsed Ion Sources
25. 15.50-16.20 K. Masugata, H. Isobe, H. Uenaga, Y. Kawano, Y. Araki and K. Yatsui (Tech. Univ. Nagaoka)
    Time-Resolvable Measurement of Anode Plasma and Ion Beam Extraction
26. 16.20-16.50 K. Horioka, Y. Kim, T. Saito, H. Sumitani, H. Yoneda and K. Kasuya (Tokyo Inst. Tech.)
    Study on the Flashover Ion Diode with a Cryogenic
27. 16.50-17.20 *H. Matsuzawa (Yamanashi Univ.)*
    High Pressure Operation of Beam Diodes for REB's

CONTENT

ANALYSIS FOR FUEL IMPLOSION IN ICF TARGET AND PELLET GAIN

Keishiro Niu, Takayuki Aoki and Hiroshi Takeda
Department of Energy Sciences, The Graduate School at Nagatsuta
Tokyo Institute of Technology
Nagatsuta, Midori-ku, Yokohama 227, Japan

A power plant to extract 1GW electric output power is proposed. After the properties of the DT fuel is examined, the compression and the heating of the fuel in the target due to the implosion motion is analyzed. The optimized parameters of the target is investigated for extracting the maximum fusion energy.

§1. Introduction

Pulsed power of 36MW by using proton beams for inertial confinement is proposed here to obtain 1GW electric output power from a fusion power plant. One shell, three layers, cryogenic target with the optimized parameters is shown for proton beams as the energy driver, and the deuterium-tritium (DT) fuel in the target is analyzed related with its implosion motion.

1 = Type 1 and 2 power supply systems
2 = Type 3 power supply system for biasing target
3 = Reactor cavity
4 = Motor to rotate the reactor vessel
5 = Deuterium separator from the argon gas
6 = Tritium separator from the argon gas and the Flibe
7 = Heat exchanger from the Flibe to $NaF \cdot BF_3$
8 = Heat exchanger from $NaF \cdot BF_3$ to the water
9 = Steam turbine
10 = Electric power generator

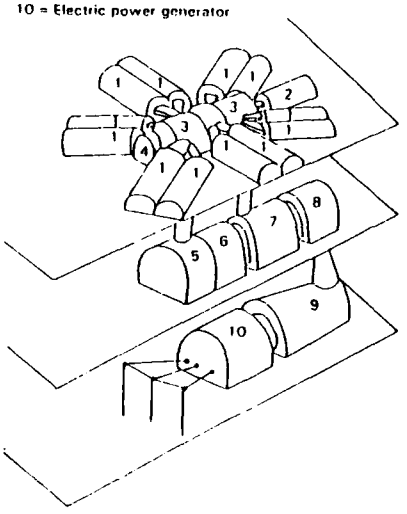

Fig. 1. Power plant.

§2. Pulsed Power

A typical inertial confinement fusion (ICF) power plant is schematically illustrated in Fig.1. In the rotating reactor vessel made of a nickel compound, the molten salt flibe flows as the coolant and the T breeder. Six proton beams are irradiated in a spherically symmetric way on the target at the reactor centre through the beam port on the vessel wall. Figure 2 gives an idea of rotating reactor vessel. The power

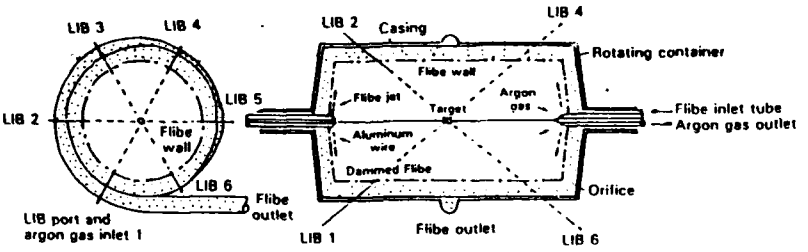

Fig. 2. Fusion reactor.

GS = Gap switch
ICL = Impedance conversion line
ISC = Intermediate storage capacitor
Marx = Marx generator
MGS = Magnetic gap switch
MITL = Magnetically insulated transmission line
PEOS = Plasma erosion opening switch
PFL = Pulse forming line

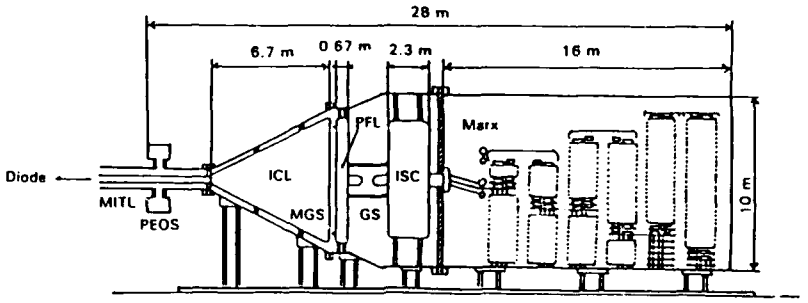

Fig. 3. Type I power supply system.

supply system shown in Fig.3 consists of the Marx generator, the intermediate strage capacitor, pulse forming line, the impedance changing line and the magnetically insulated transmition line. To extract proton beams, the plasma erosion opening switch can be skipped because of its instability of the operation. The optimum particle energy of proton beams for ICF is 4MeV, which will be shown later, 10MV output voltage from the power supply system is desirable, because the rotating beams is used for propagation in the reactor vessel. The beam protons have the energy of 4MeV for propagation, 3MeV for rotation and 1MeV for thermal motion in the radial direction. Thus one example of the power supply system is as follows;

1. Marx generator

   capacitance of a condenser C=52μF, charging voltage V_c=200kV, number of stage N_c=32, output voltage V_m=6.4MV, total storage energy E_m =2.7MJ.

2. Pulse forming line

   pulse width t_p=30ns, output voltage V_p=3.2MV.

3. Impedance conversion line

   entrance impedance Z_{en}=0.3Ω, exit impedance Z_{ex}=2.7Ω, output voltage V_i=9.6MV.

Twelve modules of this power supply system, two of which is combined to extract one proton beam, can supply us the beam energy of 10MJ, the

particle energy of 10MeV, with the pulse width of 30ns.

§3. Extraction and Propagation of Rotating Beam

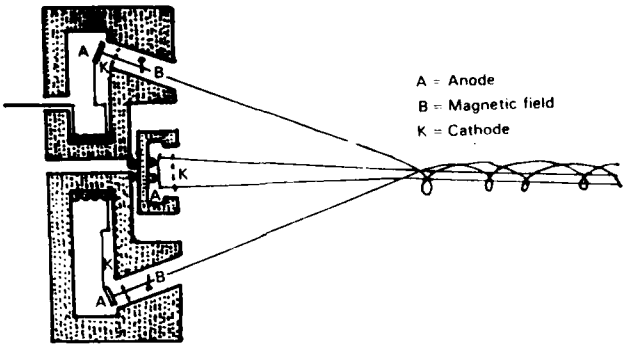

Fig. 4. Combination of two diodes

The magnetically insulated diode, schematically illustrated in Fig.4, extracts a rotaing proton beam with the beam current of 10MA. In the argon gas with a low pressure of 0.1 torr in the reactor vessel the rotation of the proton beam induce a magnetic field in the axial direction, which stabilizes the propagation of the beam in the reactor.[4]

§4. Fuel in Target

If we want to have a fusion power plant, from which the net electric power of 1GW is delivered, then the thermal fusion output energy of 3GJ must be derived from a target, provided that the repetition rate is f=1Hz. The number N of DT reactions in a target is given by

$$N=3GJ/17.6MeV=1.06\times10^{21}, \quad (1)$$

where E_f=17.6MeV is the released fusion energy per DT reaction. The fusion reaction rate is expressed by

$$dn/dt=-1/2.\langle\sigma v\rangle, \quad (2)$$

where n is the number density of the DT fuel, σ is the fusion cross-sectional area and $\langle\sigma v\rangle$ is the average reaction frequency. The burning fraction F of the fuel is related by the number density n and expressed as

$$F=(n_0-n)/n_0=\langle\rho R\rangle/(8mC/\langle\sigma v\rangle+\langle\rho R\rangle), \quad (3)$$

where ρ is the fuel density, R is the fuel radius and m is the mean DT ion mass ($m=4.19\times10^{-27}$kg). The suffix 0 refers to the initial value and

<> refers to the average value. If the initial fuel temperature is assumed to be T_0=4keV, then the self-heating of the fuel by α-particles as a fusion product increases the fuel temperature to 80keV at the final stage of burning. Thus it is expected that the average fuel temperature is T=20keV. Thus we have $8mC/\langle\sigma v\rangle = 63kg/m^2$. In order to achieve F=35%, eq.(3) leads the fusion parameter <ρR> to

$$\langle\rho R\rangle = 35kg/m^2. \tag{4}$$

The fuel mass M_{DT} in a target is given by

$$M_{DT} = mN/f = 2.0\times10^{5}kg = 4\pi R^3/3. \tag{5}$$

In summary, the fuel in the target must satisfy

$$T > 4keV, \quad \langle\rho R\rangle > 40kg/m^2, \tag{6}$$

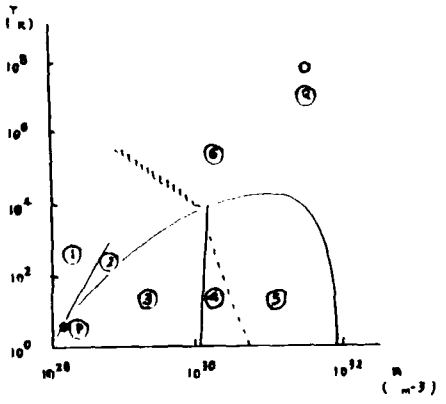

Fig.4 The phase diagram of the DT fuel. 1 Gas. 2 Liquid. 3 Hydrogen crystal (Solid). 4 Superconductor (Solid). 5 Metal hydrogen (Solid). 6 Plasma. P Before the implosion. Q After the implosion.

in order to extract the practical amount of fusion energy from the target. From eqs.(4) and (5), the relations

$$\rho = 4.16\times10^{4}kg/m^3,$$
$$R = 8.42\times10^{-4}m, \tag{7}$$

are derived. Equation (7) shows that the DT fuel must be compressed on the average to 220 times the solid density of n_s =190kg/m^3 (more than 2000 times at the central part and about 20 times at the circumference).

The phase diagram of the fuel is drawn in Fig.5[3]. The Dt

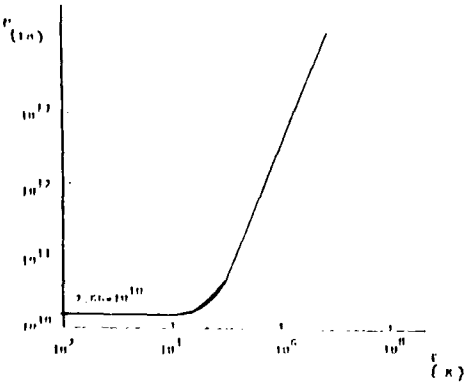

Fig.5 The pressure p versus the temperature T of the DT fuel for n=4.5x10^{28}/m^3.

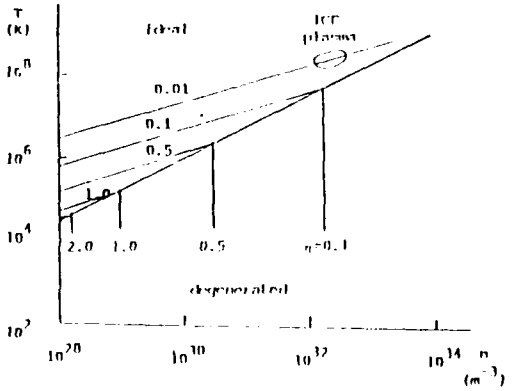

Fig.6 Coulomb coupling coefficient of the fuel plasma as functions of n and T.

fuel makes one solid layer ($n_s=4.5\times10^{28}m^{-3}$, T=8K) in a spherical target around the void which is filled with the gas of the saturation presuure of 7×10^{7}Pa. After Implosion and before burning, the fuel is in the plasma state ($n=10^{32}m^{-3}$, $T=5\times10^{7}K$). It is not clear that the path of the fuel which connects the initial state with the final state of the implosion in the phase diagram. The equation of the state for the plasma with a high temperature and a low density is, of course, that of the ideal gas. When the density of the plasma is high and its temperature is low, the electron in the plasma is weakly degenerated. If the density becomes higher and the temperature becomes lower, the electron degenerates strongly and at last reaches the perfectly degenerate state. Figure 6 shows the pressure p of the plasma versus the temperature T for the solid number density $n_s=4.5\times10^{28}m^{-3}$ of the DT fuel. Under the temperature of $T=10^{4}K$, the electron is perfectly degenerated and the pressure is constant of $p=2.66\times10^{10}$Pa regardless of the temperature. The Coulomb coupling coefficient η of the plasma is defined by

η=(Coulomb potential energy)/(particle kinetic energy)

$$=(e^2/4\pi\varepsilon a)/[1/2.mv^2]=7.2\times10^{-6}n^{1/3}/T, \qquad (8)$$

where ε is the dielectric constant in the vacuum and a is the mean distance between ions. In Fig.7, the Coulomb coupling constant of the plasma is shown as functions of n and T. If $n=10^{32}m^{-3}$ and $T=10^{8}K$ are substituted into eq.(7), η becomes 0.03. Thus the ICF plasma is weekly coupled. The Debye radius r_D is given by

$$r_D=(2kT_e/ne^2)^{1/2}=6.90\times10^{3}(T_e/n)^{1/2}=6.9\times10^{-9}m,$$

for $n=10^{32}m^{-3}$ and $T=10^{8}K$, while the mean distance a between ions is

$$a=(3/4.n)^{1/2}=0.62\times(1/n)^{1/3}=1.3\times10^{-11}m,$$

for $n=10^{32}m^{-3}$. When $r_D>a$, $\langle\sigma v\rangle$ increases from the classical value by decresing the screening potential around the ion. But for ICF plasma, $\langle\sigma v\rangle$ will increase from the classical value by the order of 10%. After the compression to $\rho=2000\rho_s$ and the heating to T=4keV of the fuel by the implosion, the central fuel will have a very high pressure of $p=\frac{\rho}{A}RT=5.72\times10^{16}$Pa.

The work done on the fuel to compress the density to 220 times the solid density is minimum when the plasma is initially perfectly degenerated, and is given by

$$W=\int_{V_1}^{V_2}pdV=\int_{V_1}^{V_2}1/20.(3/\pi)^{2/3}h^2n_e^{5/3}/(5m_e).dV=4.18\times10^{3}J, \qquad (9)$$

where V is the volume of the fuel. The suffix 1 refers to the value before the compression and 2 refers to those after the compression. Figure 6 indicates that the fuel becomes plasma at $T_1=10^5$K. If we take $T_1=10^5$K, the initial pressure becomes higher about 5 times and the work W' is changed to $W'=2\times10^4$J. This value gives the minimum work (without shock waves in the fuel) to compress the fuel to 220 times the solid density.

As the fuel temperature does not reach $T_2'=3.6\times10^6$K due to the adiabatic compression only, the energy

$$W''=Nk(T_2-T_2')=3.55\times10^6 J \tag{10}$$

must be added to the fuel to increase the temperature by one order of magnitude more. This value W" is too large, because it is the amount of energy to heat the whole fuel to 4keV. The stopping range of α-particles in the DT fuel with T=4keV is $X=31\text{kg/m}^2$. The range of α-particles in the compressed fuel, whose density is $=4.16\times10^4\text{kg/m}^3$, is $X=7.21\times10^{-6}$m. The number N" of the fuel particles in the radius of X is $N''=N(X/R)=3.80\times10^{18}$. If the fuel of N" particles at the central part of the fuel is heated to 4keV, the whole part of the fuel will be burnt by the self-heating of α-particles. The energy W" to heat N" particles to 4keV is $W''=2.23\times10^3$J. Thus the minimum energy which must be given to the fuel to compress and heat the fuel is

$$W'+W''=2.22\times10^4 J. \tag{11}$$

It is impossible to heat the small amount of the fuel near the centre only, in reality. As W", an intermediate value between 3.35×10^6J and 2.23×10^3J is necessary for realizing the particle fusion reactions.

§5. Spherically symmetric Implosion of Fluid

To extract the practical amount of nuclear fusion energy from the deuterium-tritium (DT) fuel by the method of inertial confinement fusion (ICF), the DT fuel is required to be compressed to more than 1000 times the solid density ($\rho_s=4.5\times10^{28}/\text{m}^3$) and to be heated to higher than 4keV.[1] The pressure p_f of the fuel then reaches an extremely high value of $p_f=2nkT=5.72\times10^{16}$Pa, even if in the state of the number density of $n=4.5\times10^{31}/\text{m}^3$ and of the temperature of T=4keV. When a cryogenic one-shell hollow target, which consists of three layers of lead, aluminium and solid DT fuel, is irradiated by the proton beams of 200TW, the pressure p_p of the aluminium pusher layer increases with time and

arrives at the order of $p_p=10^{12}$Pa after the several nano second from the start of beam irradiation, and the value of pressure remains constant since then because the beam energy deposition in the pusher layer balances with the work done on the fuel layer.[1] It seems impossible that the pressure p_p of the pusher layer approaches or exceeds the required fuel pressure $p_f=10^{17}$Pa even with the highest intensity of the driver beam under the present technological stage. The aim of this article is to reveal the fact in a hydrodynamical way that the momentum of the fuel implosion can be changed to the fuel pressure beyond the required value.

The adiabatic compression[5,6] and the similar solusion[7] have been proposed to analyze the fuel implosion. According to their methods, however, the required fuel compression can be achieved only on the condition that the final pusher pressure p_p exceeds the required fuel pressure p_f. This condition cannot be satisfied in the real situations as it is described above. Another beautiful similar solution for the implosion[8] does not lead to a high compression of the fuel.

It will become clear in this article that the fuel near the inner boundary is accelerated strongly because the cross-sectional area of the fuel path in the spherical target becomes smaller when the inner boundary of the fuel approaches the target centre. The acceleration of the fuel near the inner boundary is fed by the deceleration of the implosion velocity of the main part of the fuel in the final stage of the implosion. In other words, the high compression of the fuel during the implosion is performed by the high pressure which is carried by the impulse during the short period as a result of decreasing cross-sectional area of the fuel path. It is reasonably understood that spherical geometry of the implosion motion substantially causes the high adiabatic compression of the fuel.

§6. Governing Equation for Implosion

One of the govering equations for the fuel implosion in the spheical target is the equation of continuity,

$$\partial\rho/\partial t+1/r^2\cdot\partial/\partial r(r^2\rho u)=0, \tag{12}$$

where t is time, r is the radial coordinate, ρ is the denisty of the fuel and u is its radial velocity. Another one is the equation of motion,

$$\partial u/\partial t+u\partial u/\partial r=-\partial p/\partial r, \tag{13}$$

where p is pressure, which is related with the density ρ through the

adiabatic relation,

$$p=\Gamma\rho^{\gamma}. \tag{14}$$

In the above equation, the adiabatic exponent γ is $\gamma=5/3$ for the fully ionized fuel (in the case of the ideal gas or of the completely degenerated electrons) and Γ is constant provided that the fuel is isentropic throughout the process of implosion. In this article, the analysis is limited to the fuel implosion only. The energy dissipations due to the viscosity, thermal conductivity and the radiative energy transfer are completely neglected to simplify the analysis and to find the substantial mechanism of the fuel compression.

§7. Acceleration of Fuel

Under the temperature of 10K, the DT fuel is in the solid state, and coexists with the saturated vapour pressure $p_s=7\times10^7$pa for the temperature of T=8K.[9] Although the saturated vapour pressure is of course of the function of the fuel temperature, the vapour pressure P_s in the central hole surrounded by the solid fuel may be approximated by a constant value, since the implosion velocity U (of the order of 10^5m/s) of the fuel is high enough in comparsion with the thermal velocity of the vapour and the surface of the solid fuel absorbs the hitting vapour partices. The short time interval τ (of the order of 10 ns) of the implosion is also one of the cause to discard the change in the vapour pressure in the hole. At any rate, the vapour pressure does not affect much the implosion velocity, being neglected compared with the pusher pressure. The fact that the vapour pressure seems to be constant during the implosion means the constant pressure ($p_i=p_s=7\times10^7$Pa) on the inner surface of the fuel layer.

The pusher pressure P_p increases rapidly with time after the beam-energy deposition in the layer. If the proton beam intensity of 200TW impinges in the spherically symmetric way onto the target and deposits its energy in the aluminium pusher layer of the mass of 120mg, P_p rearches the value of 7×10^{12}Pa at several nano seconds after the start of energy deposition. In the case in which the increase in the pusher pressure is too steep, shock waves propagate in the solid fuel layer, heating the fuel and supressing the fuel from the further compression. With the controlled temporal shapes of the beam power, however, the fuel can be accelerated in the adiabatic way.[7] On the conditions that the fuel mass is $M_{DT}=20$mg and the pusher pressure $P_p=10^{12}$Pa, the accelaretion

α of the fuel arrives at $\alpha=7.2\times10^{12}m/s^2$ and the implosion velocity U becomes $U=3\times10^5m/s$ after 40ns.

The most important parameter for compressing the fuel is the momentum of the fuel implosion. In the real target, the inner part of the pusher implodes accompanied with the fuel. Effectively one thirds of the pusher mass can be regarded as the mass to contribute to increasing the fuel momentum which implodes with the velocity U. Thus the fuel mass here is over-weighted to be $M_{DT}=100mg$ in this article, the pusher motion being discarded. The analysis will be given for the final implosion motion after the fuel of $M_{DT}=100mg$ obtains the average implosion velocity of $U=3\times10^5m/s$.

§8. Implosion of Fuel near Inner Boundary

As the description was given in the preceeding section, the pressure p_i of the inner boundary of the fuel layer is assumed to be constant. In this section, the inner boundary is shown to be accelerated toward the target centre inversely proportional to the fifth power of the radius ξ of the inner boundary, when the fuel layer approaches the centre. To support this large acceleration, a steep pressure gradient appears in the thin layer connecting the inner boundary like a longitudinal boundary layer. The pressure and hence the density of the fuel increase sharply across this thin layer.

At the inner boundary $r=\xi(t)$, the boundary conditions are given by

$$p=p_i=7\times10^7Pa, \tag{15}$$

$$\rho=\rho_i=1.9\times10^2kg/m^3. \tag{16}$$

The variables in this boundary layer are transformed to

$$r=\xi+x', \tag{17}$$

$$u=u_i+u', \tag{18}$$

$$\rho=\rho_i+\rho', \tag{19}$$

$$p=p_i+p', \tag{20}$$

where the variables with prime are assumed to be small of the order of ε. The operator $\partial/\partial x'$ increases the order of operand by $1/\varepsilon$. Equations (17)-(20) are substituted into eqs.(12)-(14). Then term of $O(1/\varepsilon)$ in eq.(12) leads to

$$\partial/\partial x'.(\xi^2\rho_i u_i)=0,$$

the flow is related with the radius r through

$$r_s/r=M^{1/2}[2/(\gamma+1).\{1+(\gamma-1)M^2/2\}]^{-(\gamma+1)/4(\gamma-1)} \quad (26)$$

where the suffix s is attached to the sonic state. At $r_o=3\times10^{-3}$m, $u_o=3\times10^5$m/s, $\rho_o=1,9\times10^2$kg/m^3 and $p_o=7\times10^7$Pa are assumed to be held. The sound velocity c is given by $c=(\gamma\rho_o/p_o)^{1/2}=7.8\times10^2$m/s and hence the Mach nunber is $M_o=3.85\times10^2$. The real high dense fuel is not an ideal gas and the Mach number is roughly estimated as $M_o=10$. Then eq.(26) derives

$$r_s=1.17\times10^{-3}\text{m}.$$

For the adiabatic flow, the density ρ and the velocity u are given by

$$\rho_s/\rho_o=[2/(\gamma+1).\{1+(\gamma-1)M_o^2/2\}]^{1/(\gamma-1)}, \quad (27)$$

$$u_s/u_o=1/M_o.[2/(\gamma+1).\{1+(\gamma-1)M_o^2/2\}]^{1/2}. \quad (28)$$

With $M_o=10$, we have $\rho_s=131\rho_o=2.49\times10^4$kg/m^3, $u_s=0.507u_o=1,52\times10^5$m/s.

At the sonic surface $r_s=1.17\times10^3$m, the density ρ_s is cpmpressed to more than one hundred times the solid density.

After the fuel arrives at the sonic surface, the flow of the fuel is in the subsonic state and is chocked by the decreasing cross-section. Thus the fuel flux is assumed to be a function of time, that is

$$r^2\rho u=c(1-t/\tau') \quad (29)$$

where a constant $c=5.18\times10^3$kg/s is chosen for the values at the sonic surface. The nonation τ' is the time interval in which the fuel is chocked to zero velocity. Of course, eq.(29) is a rough approximation and not the strict solution. With the assumption (29), eq.(12) gives

$$\partial/\partial r(r^2\rho u)=0,$$

from which we can assume the folowing forms for ρ and u,

$$\rho=kr^{\beta}, \quad (30)$$

$$u=(1-t/\tau')\ell r^{\delta}, \quad (31)$$

where β and δ are constants. Equation (29) derives

$$\beta+\delta+2=0. \quad (32)$$

If eqs.(30) and (31) are substituted into eq.(13)', we have

$$-c/r^2\tau'-c^2q^2\ell\delta r^{\delta-3}=-\Gamma\delta\beta k^{\gamma}r^{2\beta-1}, \quad (33)$$

where $q=(1-t/\tau')$. Equating the exponent of r in the second term on the left hand side to that on the right hand side, we have

$$\delta-3=2\beta-1. \tag{34}$$

(If we put $\tau'\to r/u$, then the exponent of r in the first term on the left hand side is equal to that of the second term.) Equations (32) and (33) lead to $\beta=-3/2$, and $\delta=-2/1$. With the sonic conditions $r_s=1.1\times10^{-3}$m and t=0 s, we have $k=9.97\times10^{1}kgm^{2/3}$ and $\ell=2.81\times10^{4}m^{1/2}$. Thus at $r=2\times10^{-4}$m, for example, the density bocomes $\rho=3.52\times10^{5}kg/m^{3}=185\rho_s$. From eq.(33), where $\Gamma=1.11\times10^{4}Pa^{2}m^{5}/kg^{5/3}$, we have $\tau'=3.5\times10^{-3}$s for $q=1.6\times10^{-3}$.

It is turned out in this section that the fuel is in the supersonic flow at the outer part in the target with the rather large radus, and the contiuous compression is carried out accompanied with the chocking in the subsonic flow near the target centre.

§9. Final Implosion of Fuel near Outer Boundary

After the section 7, the motion of fuel near the outer boundary is analyzed in the similar way to that in section 7. At the outer boundary $r=\eta(t)$, the boundary conditions are

$$p=p_0=2.25\times10^{13}Pa, \tag{35}$$

$$\rho=\rho_0=3.83\times10^{3}kg/m^{3}, \tag{36}$$

Again the variables are developed as

$$r=\eta+x'', \tag{37}$$

$$\rho=\rho_0+\rho'', \tag{38}$$

$$p=p_0+p'', \tag{39}$$

$$u=u_0+u'', \tag{40}$$

when the quantities with double primes are of order ε and the operator $\partial/\partial x''$ increases the order of operand by $1/\varepsilon$. If eqs.(37)-(40) are substituted into eqs.(12)-(14), the terms of $O(1/\varepsilon)$ in eqs.(1) give

$$u_0=d\eta/dt=-c_1'/\eta^{2}. \tag{41}$$

where a constant c_1' is chosen as $c_1'=2.23\times10/ms$. The velocity u_0 of the outer boundary is related with its radius through

$$u_0=d\eta/dt=-c_1'/\eta^{2}.$$

Thus we have

$$\eta=(c_2'-3c_1't)^{1/3}, \tag{42}$$

where c_2' is chosen as $c_2'=(6\times10^{-3}m)^{3}=2.16\times10^{-7}m^{3}$. The terms of O(1) in

eq.(12) derive

$$u''=-2c_1'x''/\eta^3=-2c_1'/\eta^2+2c_1'r/\eta^3. \tag{43}$$

The terms of O(1) in eq.(13) lead to

$$\rho''=-2c_1'^2\rho_o x''/\gamma p_o\eta^5=-2c_1'^2\rho_o/\gamma p_o(1/\eta^4-r/\eta^5). \tag{44}$$

Equation (14) derives

$$p''=-c_1'^2x''/\eta^5=-2c_1'^2/\eta^4+2c_1'^2r/\eta^5. \tag{45}$$

It is clear from eqs.(43)-(45) that the gradients at the outer boundary are less steep than those at the inner boundary, because η is larger in comparison with ξ which tends to zero.

§10. Example of Numerical Result

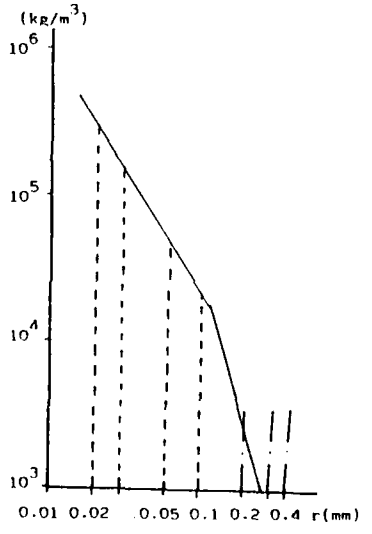

Fig.8. Fuel density versus radius. continuous line from eq.(19) for main fuel. Dotted lines from eq.(13) for inner boundary. Chain lines from eq. (33) for outer boundary.

The density ρ of the fuel obtained in the preceeding sections are plotted in Fig.8 versus the radius. The boundary layer formed near the inner boundary of the fuel is quite sharp due to the large acceleration. After the fuel is once accelarated to the supersonic flow with the Mach number of order 10 at the half way of implosion, the decreasing cross-sectional area of the fuel path in the spherical target causes the large compression (about one hundred times). After the flow of fuel arrives at the sonic surface, the chocking occurs in the subsonic region in which again the fuel compression occurs (about ten times). Formally speaking, the velocity of the inner boundary is infinite at $\xi=0$. After the void closure, this large fuel velocity stops at the target centre and hence a strong diverging shook will heat the central spot of the fuel to ignite the fusion reaction.

§11. Target Structure and Optimization of Target Parameter

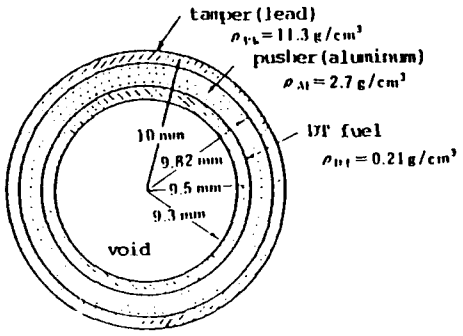

Fig.9 Target structure

The cryogenic target with one shell and three layers as is shown in Fig.9 is simple and practical to realize the high pressure of p= 5.72×10^{16}Pa at the fuel center. The target temperature is 8K before the implosion and forms the inner solid layer. The middle layer is called the pusher. The beam deposits the major part of its energy in this layer, whose temperature increases and hence whose pressure increases to accelerate the fuel layer to the target centre. It is hoped that the pusher absorbs the beam energy efficiently and does not occupy the large part of the kinetic energy of the implosion.

Let us consider the case that the beam with the intensity of 300TW deposits its energy in the pusher layer with the mass of $M_p=1.91\times10^{-4}$ kg. The pusher pressure p_p increases rapidly and arrives at $p_p=10^{12}$Pa after 10ns. The the pusher pressure remains constant because the deposited beam energy in the pusher layer is in balance with the work done on the fuel layer. As a strong acceleration ($\alpha=10^{12}$m/s^2) acts inward on the fuel from the pusher side, the density of the pusher must be higher than that of the fuel, if we want to have no Rayleigh-Taylor instability.[4] On the other hand, the fuel is decelerated strongly due to the decrease in the cross-sectional area of the fuel path, when the fuel approaches the target centre. At this deceleration phase of the fuel, the gravity acts on the fuel in the oposit direction to that in the acceleration phase. In this deceleration phase, the density of the pusher must be lower than that of the fuel in order to escape from the Rayleigh-Taylor instability. In the optimized target given later, the pusher expands 40 times the initial volume. Therefore, no Rayleigh-Taylor instability occurs when the initial pusher density ρ_p is chosen as 1-20 times the initial fuel density ρ_f. Since ρ_f=189kg/m^3, the aluminium of the density of ρ_{Al}=270kg/m^3 satisfies the conditions described above.

The tamper layer plays a role to protect the target from blowing off, when the beam deposits the energy in the pusher layer, which expands rapidly. The lead, whose density is $\rho_{Pb}=1.13\times10^4$kg/m^3, is one of the

preferable materials as the tamper. From the point of view of small induced radioactivities, aluminium and lead are preferable materials, too, for the bombardments of energetic neutrons.

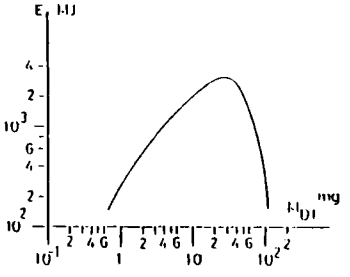

Fig. 10 E_f versus M_{DT}, for proton beam irradiation on the target. Parameters used are; E_b=6MJ, r_t=6mm, C_{Al}=0.85, δ_{Pb}=20.5μm (M_{Pb}=105mg), δ_{Al}=156μm, (M_{Al}=191mg) and e_p=5.1MeV.

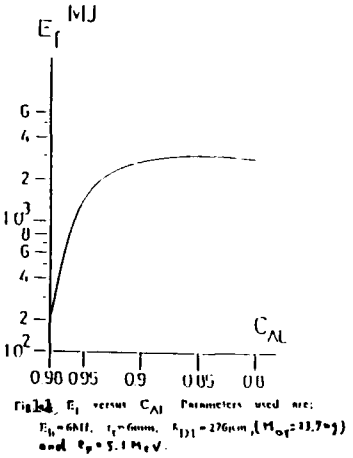

Fig. 11 E_f versus C_{Al}. Parameters used are; E_b=6MJ, r_t=6mm, δ_{DT}=276μm (M_{DT}=23.7mg) and e_p=5.1MeV.

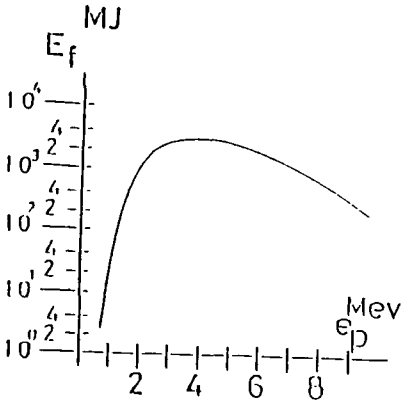

Fig. 12 E_f versus e_p. Parameters used are; E_b=6MJ, r_t=6mm, δ_{DT}=276μm (M_{DT}=23.7mg) and C_{Al}=0.85.

Figure 9 shows the fusion output energy E_f versus the fuel mass M_{DT} for the case that the target radius is r_t=6mm, the thickness of the tamper layer made of lead is δ_{Pb}=20.5μm (the mass of the tamper is M_{Pb}=150mg), the thickness of the pusher layer made of aluminium is δ_{Al}=156μm (the mass of the pusher is M_{Al}=191mg). The rate of the beam energy deposited in the pusher to the total input beam energy is C_{Al}=0.85, the particle energy of the proton beam is e_p=5.1MeV and the total beam energy is E_b=6MJ. In the figure, it turns out that M_{DT}=23.7mg is optimum to extract the maximum E_f.

The notation C_p shows the rate of the beam energy deposited in the pusher layer to the total beam energy. Figure 10 shows E_f versus C_p=C_{Al} for the same kind of the target and the proton beam with those for Fig.9.

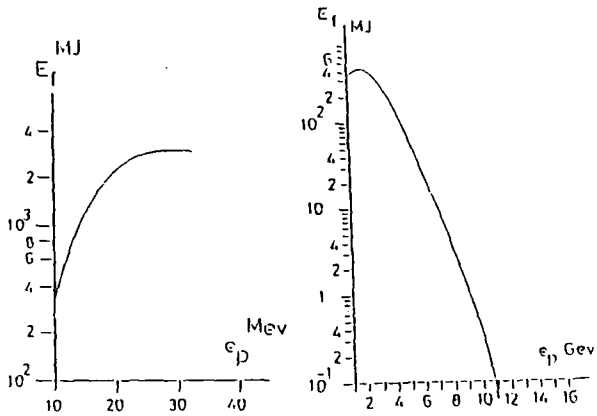

Fig.13 E_f versus e_p for Li beam. Parameters used are: Γ_{fb}=6kJ, r_t=6mm, A_{DT}=250g/cm^2 (ρR_{DT}=21.5mg/cm^2), A_{Al}=83.8g/cm (ρR_{Pb}=102mg/cm^2), A_{Pb}=73.9g/cm (ρR_{Pb}=91.1mg/cm^2) and C_{Al}=0.85

Fig.14 E_f versus e_p for Pb beam. Parameters used are: Γ_{fb}=4kJ, r_t=5mm, A_{DT}=54.6g/cm^2 (ρR_{DT}=3.26mg/cm^2) and C_{Al}=0.87.

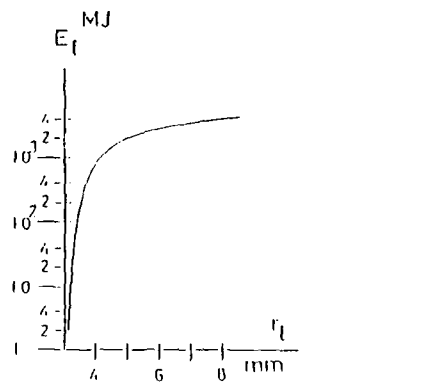

Fig.15 E_f versus r_t. Parameters used are: Γ_{fb}=6kJ, A_{DT}=276g/cm^2 (ρR_{DT}=21.7mg/cm^2), A_{Al}=156g/cm (ρR_{Pb}=191mg/cm^2), A_{Pb}=20.5g/cm (ρR_{Pb}=105mg/cm^2), C_{Al}=0.85 and e_p=3.5MeV.

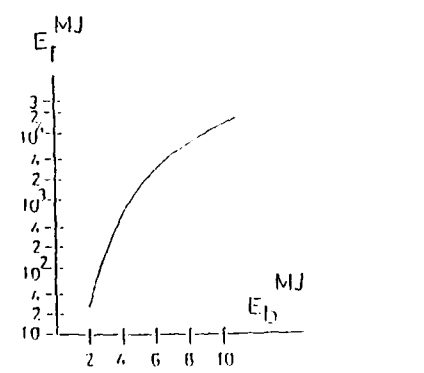

Fig.16 Γ_f versus Γ_b. Parameters used are: r_t=6mm, A_{DT}=276g/cm^2 (ρR_{DT}=21.7mg/cm^2), A_{Al}=156g/cm (ρR_{Pb}=191mg/cm^2), A_{Pb}=20.5g/cm (ρR_{Pb}=105mg/cm^2), C_{Al}=0.85 and e_p=3.5MeV

When C_{Al}=0.85, E_f is maximum.

There is the optimum value for the particle energy e_p. Figure 12 shows E_f versus e_p for the proton beams. From this figure, it turns out that e_p=4MeV is optimum. For the Li beam, E_f is plotted versus e_p in Fig.13. The optimum particle energy for ^{13}Li beam is e_p=30MeV. The optimum particle energy is e_p =3GeV for the ^{208}Pb beam as Fig.14 indicates. The distance along which the fuel is accelerated becomes long and the implosion velosity to compress the fuel reaches a large value when the target radius r_t is large. Figure 14 shows E_f versus r_t.

Figure 16 shows E_f versus the input energy E_b of the driver beam. The scientific breakeven is achieved at E_b=2MJ. The

fusion output energy E_f increases rapidly with the increase of E_b if E_b >2MJ.

§12. Summary

Let us imagine that the proton beam with e_p=4MeV and E_b=6MJ impinges on the three layer, cryogenic, hollow shell target which has δ_{Pb}=23.4μm (M_{Pb}=120mg), δ_{Al}=151μm (M_{Al}=184mg) and M_{DT}=21.5mg and r_t=6mm. Since the time duration of the implosion is about 60ns, the pulse width of the beam is required to be τ_b=30ns. Thus the beam power is 200TW. The pusher pressure increases with the deposition of the beam energy. The pressure arrives at $p_p=10^{13}$Pa (T_p=200eV) after 10ns of the beam irradiation on the target and the pressure saturates at this value during 20ns, being in balance with the beam energy distribution and the work to accelerate the fuel toward the target centre. The fuel mass of M_{DT}=21.5mg has an acceleration of $\alpha=5\times10^{12}$m/s^2, being pusher by the pusher pressure of $p_p=10^{12}$Pa and the implosion velocity reaches U=3×10^5m/s after the implosion time of 60ns. After the void closure, the fusion parameter reaches R =70kg/m^2 and the fuel temperature is heated to T_f=4keV by a strong shock wave which propagates outward from the target centre after the fuel collides with each other at the target centre. The self-heating of the fuel occurs since the stopping range of the α-particle as the fusion product is much smaller than R. The average reaction rate of the fuel reaches F=34% and the fusion reactions releases the output energy of E_f =2.5GJ.

References

1) K. Niu and S. Kawata: Fusion Tech. **11** (1987) 365.
2) T. Aoki and K. Niu: Laser and Particle Beams **5** (1987) 481.
3) P. C. Soures: Lawrence Livermore Laboratory UCRL-22628 (1979).
4) M. Tamba, N. Nagata, S. Kawata and K. Niu: Laser and Particle Beams **1** (1983) 121.
5) J. P. Morreeuw and Y. Sailard: Nucl. Fusion **18** (1978) 1263.
6) S. Kawata, T. Abe and K. Niu: J. Phys. Soc. Jpn **50** (1981) 3497.
7) R. E. Kidder: Nucl. Fusion **16** (1976) 405.
8) J. Meyer-ter Vehn: MPQ **103** (1985).
9) SESAME-Library: Los Alamos Scientific Laboratory (1981).
10) T. Abe, K. Kasuya, K. Niu and M. Tamba: J. Phys. Soc. Jpn **47** (1979) 1975.

Numerical Analysis for Effects of Irradiation Nonuniformities on Target Implosion

Hiroshi Takeda and Keishiro Niu

Department of Energy Sciences, The Graduate School at Nagatsuta, Tokyo Institute of Technology, Midori-ku, Yokohama 227

Synopsis

Effects of irradiation nonuniformities on target implosion and ignition conditions for inertial-confinement fusion with ion beams are studied by using a 2-dimensional code. The following results are then obtained. When the beam energy is 5 MJ which is 1.6 times the threshold beam energy (= 3.2 MJ) in the spherical symmetric case, ignition occurs if the peak-to-valley nonuniformity rate is smaller than 0.05. On the other hand, this value rises up to 0.1 when the beam energy is 7 MJ, i.e., it is 2.2 times the threshold beam energy in the spherical symmetric case. Furthermore, the ignition condition is the severest for the nonuniformity with the largest spatial scale.

§1. Introduction

For achievement of inertial-confinement fusion (ICF) with ion beams or lasers, it is necessary, at least, to compress the deuterium-tritium (DT) fuel up to 10^3 times the solid density and to raise the temperature of ignitors up to more than 4 keV.[1, 2] Many 1-dimensional (1-D) simulations have shown that energy drivers with the order of Mega Joule are required to attain such ignition conditions.[3-6] However, such results should be regarded to correspond to the most optimistic case because spherical symmetric motions are assumed in 1-D simulations. For real target implosion, spherical symmetric motions cannot be realized so far as infinite number of the same beams do not irradiate the completely spherical symmetric target. In other words, nonuniform motions exist all the time in practical implosion and explosion processes. On the other hand, targets during implosion are in the conditions where the Rayleigh-Taylor instabilities are likely to occur. It is, therefore, thought that nonuniform motions are

enlarged in the implosion process and have great influences on ignition conditions obtained in the spherical symmetric case.

For the past several years analyses for such nonuniformities have often been made using 2-D codes; the results have shown that nonuniformities may be very severe problems in realizing ICF.[5, 7-9] However, quantitative analyses for nonuniformity effects have yet not been made very much. Especially in ICF with ion beams, it has hardly been known how nonuniformities affect the ignition conditions. The purpose of the present study is, therefore, to estimate nonuniformity effects on the ignition conditions and the energy gain quantitatively when ion beams are used as a driver.

Roughly speaking, there are two kinds of nonuniformities. One is irradiation nonuniformity and the other is target structure nonuniformity. In the present paper we only consider the former and will remain the latter as a future work. The irradiation nonuniformity can be further classified into two kinds. One is the nonuniformity generated by the fact that finite number of the same separate beams irradiate the target. This nonuniformity has the same symmetry as that of beam irradiation. Utilizing this symmetry, we can, in some cases, analyze such nonuniformity effects in terms of a 3-D code with efforts as much as in the case of 2-D codes. This will be considered in part II. The other kind is the irradiation nonuniformity except that stated above. It includes the nonuniformity due to the cross section of one beam not being symmetric about the axis and that due to the incident direction of the beams diffracting from the target center, and so on. This kind of nonuniformities are supposed to be spatially random and must be analyzed in terms of 3-D simulations. However, 3-D simulations for the whole sphere require so much computational time that they are difficult to be performed actually even if supercomputers are used. Hence, in the present paper we look only at the axi-symmetric and bilateral symmetric modes and analyze them by using a 2-D code.

§2. Target structure and basic equations

In the present simulation we use a spherical target consisting of the lead, the aluminium and a fuel of the DT solid as shown in Fig.1. The mass of the DT fuel is 2 mg. Among the three layers the lead layer plays a

role of the tamper. On the other hand, the aluminium layer has two roles; an outer part is the pusher and the other inner part the radiation shield.

The plasma motions in the implosion and explosion processes can be well described by the two-temperature, one-fluid model.[1] On the other hand, the radiation field and the motion of α-particles may be described approximately by the diffusion model, and influences of neutrons on the fluid motions may be neglected.[1] Thus we have, as the starting point to derive the basic equations, the following conservation form of equations:

$$
\begin{aligned}
&\frac{\partial n_i}{\partial t} + \nabla\cdot n_i \mathbf{v} = -2S_n, \\
&\frac{\partial n_{\alpha 0}}{\partial t} + \nabla\cdot n_{\alpha 0}\mathbf{v} = \nu_\alpha n_{\alpha 1}, \\
&\frac{\partial n_{\alpha 1}}{\partial t} + \nabla\cdot n_{\alpha 1}\mathbf{v}_{\alpha 1} = S_n - \nu_\alpha n_{\alpha 1}, \\
&\frac{\partial \rho v_j}{\partial t} + \frac{\partial \rho v_k v_j}{\partial x_k} = -\frac{\partial p_t}{\partial x_j} - 2S_n m_i v_j + m_\alpha v_{\alpha j} \nu_\alpha n_{\alpha 1} + \frac{\partial (s_i + s_e)_{jk}}{\partial x_k} \qquad (j, k = 1, 2, 3), \\
&\frac{\partial E_i}{\partial t} + \nabla\cdot(E_i + p_i)\mathbf{v} \\
&= -2S_n\left(\varepsilon_i + \frac{m_i |\mathbf{v}|^2}{2}\right) + \varepsilon_{\alpha 1}\nu_{\alpha i} n_{\alpha 1} + n_i \nu_{ei}(T_e - T_i) + \frac{\partial (s_i)_{jk} v_j}{\partial x_k}, \\
&\frac{\partial E_e}{\partial t} + \nabla\cdot(E_e + p_e)\mathbf{v} \\
&= -2S_n \frac{n_e}{n_i}\varepsilon_e + \varepsilon_{\alpha 1}\nu_{\alpha e} n_{\alpha 1} + n_i \nu_{ei}(T_i - T_e) + c\kappa_R E_r - 4\kappa_P \sigma T_e^4 + \frac{\partial (s_e)_{jk} v_j}{\partial x_k}, \\
&\frac{\partial E_r}{\partial t} = \nabla\cdot(D_r \nabla E_r) + 4\kappa_P \sigma T_e^4 - c\kappa_R E_r, \qquad (1)
\end{aligned}
$$

where subscripts i, e, α and r indicate ions, free electrons, α-particles and radiation, respectively, m and ε represent mass and internal energy of one particle ($\varepsilon_{\alpha 0}$ is the energy of the α-particle moving together with the ions and electrons, and $\varepsilon_{\alpha 1}$ = 3.5 MeV; hereafter, we will represent variables for the α-particles with the energies $\varepsilon_{\alpha 0}$ and $\varepsilon_{\alpha 1}$ by subscripts α0 and α1,

respectively), σ is the Stefan-Boltzmann constant, n represents the number density, D the diffusion coefficient,

$$\rho = m_i n_i + m_\alpha n_{\alpha 0}$$

is the density of the fluid, v is the fluid velocity,

$$\mathbf{v}_{\alpha 1} = \mathbf{v} - D_\alpha \nabla n_{\alpha 1}$$

is the macroscopic velocity of the α-particles with the energy $\varepsilon_{\alpha 1}$,

$$E_i = \varepsilon_i n_i + \varepsilon_{\alpha 0} n_{\alpha 0} + \frac{\rho |\mathbf{v}|^2}{2},$$

$$E_e = \varepsilon_e n_e,$$

$$E_r = \frac{4\sigma T_r^4}{c}$$

are the energies per unit volume, p represents the pressure ($p_t = p_i + p_e + p_r$ is the total pressure),

$$S_n = \langle \sigma v \rangle n_D n_T$$

is the nuclear reaction rate per unit volume (with $\langle \sigma v \rangle$ being the reaction cross section), κ_P and κ_R are the Planck and Rosseland opacities, respectively, $\nu_{\alpha i}$, $\nu_{\alpha e}$ and ν_α are the collision frequencies between the α-particle with the energy $\varepsilon_{\alpha 1}$ and the ion, the free electron and the both, respectively ($\nu_\alpha = \nu_{\alpha i} + \nu_{\alpha e}$), ν_{ei} the electron-ion collision frequency, and s represents the stress tensor due to the molecular viscosity. In addition, the tensor form of description was used for the momentum equation and the viscous terms in the energy equations. In deriving the above equations, we assumed

$$m_e << m_i, \quad |\mathbf{v}|^2 << |\mathbf{v}_{\alpha 1}|^2, \quad |\mathbf{v}| << c,$$

and neglected energy exchange between the ions and the free electrons accompanied by variation of the ionization rate. This is because the ionization rate is nearly 1 and the energy exchange is negligible for such high temperature as discrepancies between the ion- and the electron-temperatures are distinguished.

For implosion and explosion motions the viscosity coefficient is very small and widths of shock waves are much narrower than the target size. In addition, integrals of the viscous terms in the momentum and energy equations in eq.(1) within an infinitesimal interval including a shock wave are zero at the inviscid limit. As a result, we may assume $s_i = s_e = 0$ if we discretize the conservation form of equation (1) as the basic equations. This is one of merits when the conservation form of equations are used. On the other hand, to use the conservation form of equation has some disadvantages as follows. If we use eq.(1), we cannot utilize a merit of using the staggerd mesh system, i.e., we must represent first order derivatives by using values at not two, but three grid points. As a result, computational modes appear in numerical results and they may cause computational instabilities. For this reason we will not use the conservation form of equation (1) as the basic equations in the present study regardless of the advantage stated above, but use the flux form of equations.

The continuity equations of ions and α-particles can be easily transformed into the flux form as follows:

$$\frac{Dn_i}{Dt} + n_i \nabla \cdot \mathbf{v} = -2S_n, \tag{2a}$$

$$\frac{Dn_{\alpha 0}}{Dt} + n_{\alpha 0} \nabla \cdot \mathbf{v} = \nu_\alpha n_{\alpha 1}, \tag{2b}$$

$$\frac{Dn_{\alpha 1}}{Dt} + n_{\alpha 1} \nabla \cdot \mathbf{v} = \nabla \cdot D_\alpha \nabla n_{\alpha 1} + S_n - \nu_\alpha n_{\alpha 1}, \tag{2c}$$

where D/Dt represents the Lagrangian derivative. On the other hand, the momentum equation is transformed into the flux form by using eq.(2a);

$$\rho \frac{D\mathbf{v}}{Dt} = -\nabla p_t + m_\alpha \nu_\alpha D_\alpha \nabla n_{\alpha 1} + \frac{\partial (s_i + s_e)_{jk}}{\partial x_k}. \tag{3}$$

Note that S_n does not appear in the flux form of equation (3). The energy equations for ions and electrons can be transformed into the flux form by using eqs. (2a) and (3);

$$(n_i c_{vi} + n_{\alpha 0} c_{v\alpha 0}) \frac{DT_i}{Dt} = -p_i \nabla \cdot \mathbf{v} + \nabla (p_e + p_r) \cdot \mathbf{v}$$
$$+ \varepsilon_{\alpha 1} \nu_{\alpha i} n_{\alpha 1} + n_i \nu_{ei} (T_e - T_i) + \frac{\partial (s_i)_{jk} v_j}{\partial x_k} - \frac{\partial (s_i + s_e)_{jk}}{\partial x_k} v_j, \tag{4a}$$

$$n_e c_{ve} \frac{DT_e}{Dt} = -p_e \nabla \cdot \mathbf{v} - \nabla p_e \cdot \mathbf{v}$$
$$+ \varepsilon_{\alpha 1} \nu_{\alpha e} n_{\alpha 1} + n_i \nu_{ei} (T_i - T_e) + 4\sigma \kappa_0 (T_r - T_e) + \frac{\partial (s_e)_{jk} v_j}{\partial x_k}, \tag{4b}$$

where c_v represents the specific heat of one particle at constant volume and $\kappa_0 = \kappa_P T_e^3 = \kappa_R T_r^3$ [10]. Note that S_n does not appear also in the flux form of energy equation (4) as in the momentum equation. The radiation equation in eq.(1) has already been of the flux form as a result that $|v|$ has been neglected compared with c. Here, making transformations only for the dependent variables, we obtain, after some rearrangement,

$$T_r^3 \frac{\partial T_r}{\partial t} = \nabla \cdot (D_r T_r^3 \nabla T_r) + \frac{c\kappa_0}{4} (T_e - T_r), \tag{5}$$

using the relation $E_r = 4\sigma T_r^4 / c$. In the present study we adopt eqs. (2)-(5) as the basic equations and the SESAME library[12] as the equation of state. When we discretize the flux form of equations, we can utilize merits of the staggered mesh system, in which boundary conditions are comparatively easy to be applied and almost all of the first order derivatives can be approximated by using values at two grid points. As a result, no computational mode exists and computational instabilities hardly occur. The flux form of equations have a disadvantage too. Integral of the second viscous term in eq.(4a) within an infinitesimal interval including a shock wave does not become zero even at the inviscid limit being different from the case of the conservation form of equations. This term originally comes from the viscous term in the momentum equation and physically represents the shock heating. Due to the integral being not zero, we cannot put $s_i = s_e = 0$ in the flux form of equation. In actual simulations we use an artificial viscosity instead of the molecular viscosity as will be stated in the next section.

As the equation governing the energy of one beam particle, e_b, we use the following approximation equation:

$$\frac{\partial e_b}{\partial r} = -\frac{h}{e_b + e_B},$$

where

$$h = \frac{e^4 m_b Z_{eff}^2 A n_i}{8\pi\varepsilon_0^2 m_e} \ln\frac{2m_e e_{b0}}{m_b I},$$

$$e_B = \frac{1}{2} m_b v_B^2 A_{pusher}^{4/3}, \tag{6}$$

and r denotes the radial direction. Furthermore, e is the electron charge, ε_0 the dielectric constant in the vacuum, m_b represents the mass of the beam particle, A the atomic number, Z_{eff} the effective charge, v_B the Bohr velocity, and e_{b0} is the energy of one beam particle before incidence. Equation (6) can be obtained by simplifying and modifying the Bethe equation[13] so that no Bragg peak exists. If we consider the beam stopping only in the 2-D case, we may use more complicated and accurate equations. Such equations will, however, be difficult to be used in 3-D simulations which will be performed in part II. Hence, in the present study we will further simplify eq.(6) and use it as the equation governing the stopping of beam particles. In eq.(6) h is a function of the time and the space and cannot be integrated analytically. However, if we approximate h by its average in each layer, h_{av} (which only includes the time as a parameter), we can integrate eq.(6) and obtain

$$e_b(r, \theta; t) = -e_B + \sqrt{(e_{b0}' + e_B)^2 - 2h_{av}r'}, \tag{7}$$

where θ denotes the azimuthal direction, e_{b0}' the particle energy at the outer edge of the layer concerned, and r' the distance from the outer edge to the point concerned.

As for the irradiation nonuniformity, we assume the beam intensities of the form

$$\text{const} \times \left(1 + \frac{a}{2}\cos(m\theta)\right),$$

where a (≥ 0) corresponds to the peak-to-valley nonuniformity rate and $|m|$ ($= 2, 4, 6, \ldots$) represents the mode in the azimuthal direction.

§3. Method of computation

When the flux form of equations (2)-(5) are used in actual computation, the viscous terms cannot be omitted within shock waves as stated in §2. If, however, we use the molecular viscosity itself in computation, we must use very small mesh widths because the shock widths are much narrower than the width of each layer in the present case. Hence, such a way requires so much computational time that it is almost impossible to be actually performed. In the present computation, therefore, we put $s_i = s_e = 0$, and instead, use the Neumann artificial viscosity,[14] i.e., replace the ion pressure as

$$p_i \rightarrow p_i' = p_i + b\rho(\Delta r^2 \delta_r u\,|\delta_r u| + \Delta\theta^2 \delta_\theta v\,|\delta_\theta v|), \tag{8}$$

where u and v denote the r- and the θ-components of the fluid velocity $\boldsymbol{v}$, δ_r and δ_θ represent the finite difference operators corresponding to $\partial/\partial r$ and $\partial/\partial\theta$, Δr and $\Delta\theta$ are the mesh widths, and b is a constant of O(1). The value of b used in the present study will be considered in §4.

In discretizing eqs. (2)-(5), we use the finite difference method. It is difficult, however, to apply it to eqs. (2)-(5) themselves because forms of the free boundaries and the contact surfaces of different materials vary with time. The Euler-Lagrange transformation[1] has often been made so far to avoid such difficulties. However, there still remain some problems in using the Euler-Lagrange transformation. One is that mesh widths in the physical space vary rapidly before and behind of shock waves; such a rapid variation of mesh widths often generates numerical errors and causes a numerical instability. The second is that mesh widths in the physical space become smaller for higher temperature because the sound velocity, v_s, is proportional to the square root of the fluid temperature; this fact is no good for computational efficiency because the time interval, Δt, is restricted by the Courant condition, $\Delta t \le \sqrt{\Delta r^2 + (r\Delta\theta)^2}/v_s$. The last is a problem at contact surfaces between different materials. When eqs. (2)-(5) with the artificial viscosity (8) are used as the basic equations, tangential velocities on the both sides at the contact surfaces are different because no shear stress is included in the equations. As a result, fluid particles that were at the same point initially on the surface are at different points after time

elapsed. In other words, the grid points do not necessarily coincide on the both sides of the surface; this fact makes treatment of boundary conditions at the contact surfaces complicated and is likely to cause numerical instabilities. For these reasons we will use another transformation in the present study instead of the Euler-Lagrange transformation;

$$
\begin{aligned}
&x = \frac{r - r_0}{l} \qquad (0 \le x \le 1), \\
&\theta' = \theta, \\
&t' = t,
\end{aligned} \tag{9}
$$

where $l(\theta,t) = r_1 - r_0$, and $r_0(\theta,t)$ and $r_1(\theta,t)$ $(r_0 < r_1)$ represent the r-coordinates of the points that are on, respectively, the inner and the outer contact surfaces of the layer concerned and have the same θ- (θ'-) coordinate as r (i.e., the point concerned). When using the above transformation, we have, in computation, no such problems as stated above. Variable transformation (9) has been verified to work very well in a run-up simulation of tsunami whose governing equations are very similar to the present ones.[15] Writing eqs. (2)-(5) with the artificial viscosity (8) instead of the molecular one in the polar coordinates (r, θ) and applying (9) to them, we have, after some rearrangement,

$$
\begin{aligned}
&\frac{Dn_i}{Dt'} + n_i \nabla\cdot\mathbf{v} = -2S_n, \\
&\frac{Dn_{\alpha 0}}{Dt'} + n_{\alpha 0} \nabla\cdot\mathbf{v} = \nu_\alpha n_{\alpha 1}, \\
&\frac{Dn_{\alpha 1}}{Dt'} + n_{\alpha 1} \nabla\cdot\mathbf{v} = \nabla\cdot D_\alpha \nabla n_{\alpha 1} + S_n - \nu_\alpha n_{\alpha 1}, \\
&\frac{Du}{Dt'} = -\frac{1}{\rho}\frac{\partial p_t'}{\partial r} + \frac{v^2}{r} + \frac{m_\alpha \nu_\alpha D_\alpha}{\rho} + \frac{\partial n_{\alpha 1}}{\partial r}, \\
&\frac{Dv}{Dt'} = -\frac{1}{\rho r}\frac{\partial p_t'}{\partial \theta} - \frac{uv}{r} + \frac{m_\alpha \nu_\alpha D_\alpha}{\rho r} + \frac{\partial n_{\alpha 1}}{\partial \theta}, \\
&(n_i c_{vi} + n_{\alpha 0} c_{v\alpha 0})\frac{DT_i}{Dt'} = -p_i'\nabla\cdot\mathbf{v} + \nabla(p_e + p_r)\cdot\mathbf{v} \\
&+ \varepsilon_{\alpha 1}\nu_{\alpha i} n_{\alpha 1} + n_i \nu_{ei}(T_e - T_i) + \frac{\partial (s_i)_{jk} v_j}{\partial x_k} - \frac{\partial (s_i + s_e)_{jk}}{\partial x_k} v_j, \\
&n_e c_{ve}\frac{DT_e}{Dt'} = -p_e \nabla\cdot\mathbf{v} - \nabla p_e \cdot \mathbf{v}
\end{aligned}
$$

$$+ \varepsilon_{\alpha 1}\nu_{\alpha e}n_{\alpha 1} + n_i\nu_{ei}(T_i - T_e) + 4\sigma\kappa_0(T_r - T_e) + \frac{\partial(s_e)_{jk}v_j}{\partial x_k},$$

$$T_r^3\frac{\partial T_r}{\partial t'} = \nabla\cdot D_r T_r^3 \nabla T_r + \frac{c\kappa_0}{4}(T_e - T_r),$$

where

$$\frac{\partial}{\partial r} = \frac{1}{l}\frac{\partial}{\partial x},$$

$$\frac{\partial}{\partial \theta} = \frac{\partial}{\partial \theta'} + \frac{\partial x}{\partial \theta}\frac{\partial}{\partial x},$$

$$\frac{D}{Dt'} = \frac{\partial}{\partial t'} + \left(\frac{u - u_1 x - u_0(1 - x)}{l} + \frac{v}{r}\frac{\partial x}{\partial \theta}\right)\frac{\partial}{\partial x} + \frac{v}{r}\frac{\partial}{\partial \theta'},$$

$$\frac{\partial x}{\partial \theta} = -\left(\frac{\partial r_0}{\partial \theta}(1 - x) + \frac{\partial r_1}{\partial \theta}x\right)/\, l,$$

$$p_t' = p_i' + p_e + p_r, \tag{10}$$

and u_0 and u_1 denote u at $x = 0$ and 1, respectively. In addition, ∇, $\nabla\cdot v$ and so on can be easily transformed using the above transformation equations. We next derive finite difference equations corresponding to eq.(10). As for the space, we use the staggered mesh system as stated in §2 and apply the centered finite difference to the derivatives. On the other hand, we apply, for the time, the most appropriate scheme among the leap-frog, the Crank-Nicolson and the backward Euler schemes according to properties of terms in the finite difference equations. In addition, the path-line method[15] is used for the advection terms in order to suppress computational instabilities due to the aliasing errors. Thus, the finite difference equations are obtained as follows:

$$(n_i^{n+1} - n_{i*}^{n-1})/2\Delta t + \frac{1}{2}(n_i^{n+1} + n_{i*}^{n-1})(\delta\nabla\cdot v)_*^n = -2S_n, \tag{11a}$$

$$(n_{\alpha 0}^{n+1} - n_{\alpha 0*}^{n-1})/2\Delta t + \frac{1}{2}(n_{\alpha 0}^{n+1} + n_{\alpha 0*}^{n-1})(\delta\nabla\cdot v)_*^n = (\nu_\alpha n_{\alpha 1})_*^n, \tag{11b}$$

$$(n_{\alpha 1}^{n} - n_{\alpha 1*}^{n-1})/\Delta t + n_{\alpha 1}^{n}(\delta\nabla\cdot v)^n = (\delta\nabla\cdot D_\alpha\delta\nabla n_{\alpha 1})^n + S_n^n - \nu_\alpha^n n_{\alpha 1}^n, \tag{11c}$$

$$(u^{n+1} - u_*^{n-1})/2\Delta t = -\left(\frac{\delta_r p_t'}{\rho}\right)_*^n + \left(\frac{v^2}{r}\right)_*^n + \left(\frac{m_\alpha\nu_\alpha D_\alpha}{\rho}\delta_r n_{\alpha 1}\right)_*^n, \tag{11d}$$

$$(v^{n+1} - v_*^{n-1})/2\Delta t = -\left(\frac{\delta_\theta p_t'}{\rho r}\right)_*^n - \frac{u_*^n}{2}\left(\frac{v^{n+1}}{r^{n+1}} + \frac{v_*^{n-1}}{r_*^{n-1}}\right) + \left(\frac{m_\alpha \nu_\alpha D_\alpha}{\rho r}\delta_\theta n_{\alpha 1}\right)_*^n, \qquad (11e)$$

$$(n_i c_{vi} + n_{\alpha 0} c_{v\alpha 0})_*^n (T_i^{n+1} - T_{i*}^{n\,1})/2\Delta t$$

$$= (-p_i' \delta_\nabla \cdot v + \delta_\nabla (p_e + p_r)\cdot v)_*^n + (\varepsilon_{\alpha 1} \nu_{\alpha i} n_{\alpha 1})_*^n + (n_i \nu_{ei})_*^n (T_e^{n+1} - T_i^{n+1}), \quad (11f)$$

$$(n_e c_{ve})_*^n (T_e^{n+1} - T_{e*}^{n-1})/2\Delta t = -(p_e \delta_\nabla \cdot v + \delta_\nabla p_e \cdot v)_*^n$$

$$+ (\varepsilon_{\alpha 1} \nu_{\alpha e} n_{\alpha 1})_*^n + (n_i \nu_{ei})_*^n (T_e^{n+1} - T_i^{n+1}) + 4\sigma \kappa_{0*}^n (T_r^{n+1} - T_e^{n+1}), \qquad (11g)$$

$$(T_{r*}^n)^3 (T_r^{n+1} - T_{r*}^n)/\Delta t = \delta_\nabla \cdot ((D_r T_r^3)_*^n \delta_\nabla T_r^{n+1}) + \frac{c\kappa_{0*}^n}{4}(T_e^{n+1} - T_r^{n+1}), \qquad (11h)$$

where

$$\delta_r = \frac{1}{l}\delta_x,$$

$$\delta_\theta = \delta_\theta' + \delta_\theta x \delta_x,$$

$$\delta_\nabla = (\delta_r, \frac{1}{r}\delta_\theta),$$

$$\delta_\nabla \cdot v = \delta_r u + \frac{2u}{r} + \frac{1}{r}\delta_\theta v + \frac{v}{r\tan\theta},$$

$$\delta_\nabla \cdot f\delta_\nabla = \delta_r(f\delta_r) + \frac{2f}{r}\delta_r + \frac{1}{r^2}\delta_\theta(f\delta_\theta) + \frac{f}{r^2\tan\theta}\delta_\theta \qquad (f = D_\alpha, D_r T_r^3),$$

$$p_i'^n = p_i^n + b\rho(\Delta r^2 \delta_r v\,|\,\delta_r v\,| + \Delta\theta^2 \delta_\theta v\,|\,\delta_\theta v\,|)^{n-1}.$$

Here, superscripts n-1, n and n+1 indicate time steps, subscript * refers to values on the path-line (defined in the transformed coordinate system), and $\delta_\theta x$ represents the finite difference corresponding to $\partial x/\partial\theta$ in eq.(10). When Δt is changed during computation, the simplified Runge-Kutta (i.e., Heun) scheme is used instead of the leap-frog scheme. Note that $\nabla \cdot v$ and the diffusion terms have been discretized in the form of the parentheses having been taken off (i.e., the non-conservation form). The reason is to keep the accuracy of the finite differences to the same order even near the center of the polar coordinates (see Appendix for details). In eq.(11) variables at $n+1$ step (n step in eq.(11c)) appear in more than one term in each equation

except eq.(11d). However, eqs. (11a), (11b) and (11e) can be easily solved explicitly by rewriting them as

$$(1 + \Delta t\delta\nabla\cdot\mathbf{v}_*^n)n_i^{n+1} = (1 - \Delta t\delta\nabla\cdot\mathbf{v}_*^n)n_{i*}^{n-1} - 4\Delta t S_{n*}^n,$$

$$(1 + \Delta t\delta\nabla\cdot\mathbf{v}_*^n)n_{\alpha 0}^{n+1} = (1 - \Delta t\delta\nabla\cdot\mathbf{v}_*^n)n_{\alpha 0*}^{n-1} + 2\Delta t(\nu_\alpha n_{\alpha 1})_*^n,$$

$$(1 + \frac{\Delta t u_*^n}{r^{n+1}})v^{n+1} = (1 - \frac{\Delta t u_*^n}{r_*^{n-1}})v_*^{n-1} + 2\Delta t(\frac{-\delta\theta p_t' + m_\alpha \nu_\alpha D_\alpha \delta\theta n_{\alpha 1}}{\rho r})_*^n. \qquad (12)$$

On the other hand, eqs. (11f), (11g) and (11h) can be rewritten, after some rearrangement, as

$$(\frac{(T_{r*}^n)^3}{\Delta t} + b_r - b_{er}b_r c_e)T_r^{n+1} = \delta\nabla\cdot((D_r T_r 3)_*^n \delta\nabla T_r^{n+1}) + (a_e + \frac{a_i b_{ei}}{c_i})\frac{b_r}{c_e},$$

$$c_e T_e^{n+1} = a_e + \frac{a_i b_{ei}}{c_i} + b_{er}T_r^{n+1},$$

$$c_i T_i^{n+1} = a_i + b_{ie}T_e^{n+1},$$

where

$$a_i = (-p_i'\delta\nabla\cdot\mathbf{v} + \delta\nabla(p_e + p_r)\cdot\mathbf{v} + \varepsilon_{\alpha 1}\nu_{\alpha i}n_{\alpha 1})_*^n,$$

$$a_e = (-p_e\delta\nabla\cdot\mathbf{v} - \delta\nabla p_e\cdot\mathbf{v} + \varepsilon_{\alpha 1}\nu_{\alpha e}n_{\alpha 1})_*^n,$$

$$b_i = (n_i\nu_{ei})_*^n,$$

$$b_{ei} = (n_i\nu_{ei})_*^n,$$

$$b_{er} = 4\sigma\kappa_{0*}^n,$$

$$b_r = \frac{c\kappa_{0*}^n}{4},$$

$$c_i = \frac{(n_i c_{vi} + n_{\alpha 0}c_{v\alpha 0})_*^n}{2\Delta t} + b_i,$$

$$c_e = \frac{(n_e c_{ve})^n_*}{2\Delta t} b_{ei} + b_{er} - \frac{b_{ei} b_i}{c_i}. \tag{13}$$

Using eq.(13), we may only solve T_r implicitly and can calculate T_e and T_i explicitly. In solving matrices for eq.(11c) and the radiation equation in eq.(13), we use a ICCG type of method. Number of meshes used in computation is 10, 20 and 20 in the Pb, the Al and the DT layers, respectively, in the r-direction and $2|m|$ in the θ-direction.

§4. Results

Before showing computational results of 2-D simulation, we check the code and determine the value of b in transformation (9) by solving 1-D problems. Figure 2 shows the profiles of T, ρ and u for b = 1 and 2 at 100 steps when the left wall began to move suddenly rightward with a constant velocity for the Mach number 10. The exact solution[16] has also been shown by the dotted line for comparison. It can be seen in the figure that the result for b = 1 represents the exact solution better than that for b = 2. Figure 3 shows numerical solutions for T, ρ and u representing Kidder's similar solution[17] (dotted line) at 180 steps. Also in this problem the numerical solution for b = 1 gives a better result as naturally expected. From these results we will, hereafter, use the value of b = 1.

Next, we will show computational results of target implosion. As a driver, proton beams with the particle energy of 5 MeV are used and assumed to irradiate the target with a constant intensity during 15 nsec. For the present parameters, the beam particles deposit their energy in the Pb layer (tamper) and about 2/5 part of the Al layer (pusher).

Table I shows the burning fraction (rate of nuclear reaction), f, the maxima of $\rho R = \int \rho_{DT} dr$, and the time, t_c, at which the target collides at the center versus representative values of the total incident beam energy, E_b, in the spherical symmetric case . Output energy by the nuclear reaction can be obtained by multiplying f by 1,325 MJ. It is found from the table that ignition occurs for beam energy greater than or equal to 3.2 MJ, i.e., the threshold beam energy for the spherical symmetric case is E_b^{th} = 3.2 MJ for the present situation. For E_b = 9 MJ, moreover, the values of f and ρR_{max} are found to decrease; this is supposed to be due to the fact that the preheat

occured as a result that the temperature in the pusher became high. As for ρR_{max}, it is seen to have exceeded the values, 20 ~ 40 kg/m^2, enough for ignition even in the case where no ignition occured. This indicates that for beam energies less than E_b^{th} = 3.2 MJ, no ignition occured as a result that ion temperature in the hot spot (i.e., ignitor) could not exceed the temperature, 4 ~ 5 keV, necessary for ignition.

Table II shows the burning fraction, f, the maximum of $\rho R = \int d\Omega \int \rho_{DT} dr / \int d\Omega$ (with Ω being the solid angle), and t_c versus representative values of the nonuniformity rate, a, for E_b = 5 MJ and m = 2, i.e., for the mode with the beam energy 1.6 times E_b^{th} and the largest scale. It is seen that no ignition occurs and the energy gain is nearly zero if the nonuniformity rate, a, exceeds 0.04. Hereafter, we will call this value the critical value of a for m = 2 and E_b = 5 MJ, and write a_{cr} = 0.04. On the other hand, the maximum of ρR does not decrease so much even in the case of no ignition. This means that when a is greater than a_{cr}, ion temperature in the hot spot could not rise up to the temperature necessary for ignition, as in the case of table II, owing to the nonuniformity effects. The values of t_c hardly depend on the nonuniformity rate.

Figure 4 shows the maximum of T_i (solid line), that of T_r (dotted line), ρR and the burning fraction, f, as a function of the elapsed time after the time, t_c, at which the target collides at the center for E_b = 5 MJ, m = 2 and a = 0.04, 0.05. Comparing the figures for a = 0.04 and 0.05, we can conclude that a slight difference in T_i determines whether ignition occurs or not and cause a large difference in the burning fraction.

Figure 5 shows contours of T_i and ρ when E_b = 5 MJ, m = 2, a = 0.04 and $t - t_c$ = 1 nsec (before the ignition; see Fig.4) and 1.5 nsec (after the ignition). It is seen in the figure at $t - t_c$ = 1 nsec that the contours fairly deform due to the nonuniformity effect. On the other hand, this deformation can be seen to have been mostly recovered at $t - t_c$ = 1.5 nsec, i.e., during the explosion process after the ignition.

Table III shows the critical values of a for m = 2, -2, 4, -4, 6, 8 and E_b = 5 MJ and 7 MJ. It is seen in the case of E_b = 5 MJ that a_{cr} takes the smallest value for the m = 2 mode. In other words, the ignition condition is the severest for the nonuniformity with the largest spatial scale. It should be noted, moreover, that a_{cr} has different values for the same $|m|$. This means that strength of nonuniformity effects on the ignition conditions is a

function of not only the growth rate in the linear stability theory, but also that in the nonlinear theory. The reason is why the modes with the same $|m|$ have the same growth rate in the linear theory. When E_b = 7 MJ (i.e., E_b is 2.2 times E_b^{th}), the value of a_{cr} for m = 2 is found to rise up to 0.09.

§5. Conclusions

Using the 2-D axi-symmetric code, we analyzed how implosion motions and the ignition conditions for the ion-beam fusion were affected by irradiation nonuniformities except those due to the target being irradiated by finite number of the same separate beams. We then obtained the following two main results. The first result is that the critical value of the peak-to-valley nonuniformity rate is the lowest for the m = 2 mode. In the present simulation the left-right symmetry has been assumed as well as the spherical symmetry. Consequently, the m = 2 mode corresponds to motions with the largest scale in the present simulation. This result, therefore, implies that the value of a_{cr} may be smaller for the m = 1 mode, i.e., the ignition condition may be severer if simulations are performed without assuming the left-right symmetry. This is a future problem.

The second is the result that the critical value of the nonuniformity rate is a_{cr} = 0.04 when E_b = 5 MJ, i.e., the beam energy is 1.6 times the threshold beam energy, E_b^{th} = 3.2 MJ, in the case of spherical symmetric irradiation. On the other hand, a_{cr} rises up to 0.09 when E_b = 7 MJ, i.e., E_b is 2.2 times E_b^{th}. These results indicate that the critical value of a may further increase if beams with larger energy may be applied on the target. It is, however, difficult to apply the beam energy greater than 7 MJ so far as the target with the present parameters is used. The reason is as follows. When more beam energy is applied on the target, temperature in the pusher becomes higher and the propagation velocity of radiation becomes faster. As a result, we must use targets with a wider radiation shield to avoid preheat and make the pulsed width shorter. In such target implosion, however, the hydrodynamic efficiency is expected to decrease and the implosion velocity and the temperature in the ignitor may not increase; it is questionalbe, therefore, whether ignition occurs or not even when larger energies are applied.

In the present simulation no ignition occurred when the nonuniformity rate exceeded a certain value not as a result that the value of ρR became smaller than that necessary for ignition, but as a result that ion temperature in the ignitor could not exceed the ignition temperature. This is due to the fact that the mass of the DT fuel used here was comparatively large, or rather too large. If, therefore, we lessen the target size and the fuel mass, we may obtain a_{cr} with a larger value because the implosion velocity and the temperature in the ignitor are expected to increase for such a target. For smaller targets, however, preheat effects should be taken into consideration as in the case where beams with larger energy are applied. The reason is that the target closure time is shorter for smaller targets and the pulse width must be shortened for such targets. As a result, temperature in the pusher increases and preheat will be easy to occur.

To summarize these results, we may conclude that we can obtain sufficient pellet gains if we can control the peak-to-valley rate of irradiation nonuniformities except those due to finite number of separate beams irradiating targets to be within 10%. If such a control is difficult, therefore, it will be necessary to look for other conditions in which a_{cr} becomes greater by changing various parameters concerning the target and the beam. It may not necessarily be easy to look for such conditions, and we will remain it as a future work.

Appendix: Estimation of Finite Difference Errors for $\nabla\cdot\boldsymbol{v}$ and $\nabla\cdot\kappa\nabla T$

For simplicity, we take $\nabla\cdot\boldsymbol{v}$ as an example, and assume $\boldsymbol{v}$ to be a function of r alone. In this case, since $\nabla\cdot\boldsymbol{v}$ can be written in the conservation and the non-conservation forms as

$$\nabla\cdot\mathbf{v} = \frac{1}{r^2}\frac{\partial r^2 u}{\partial r} = \frac{\partial u}{\partial r} + \frac{2u}{r},$$

the two finite difference forms can be considered as follows:

$$\nabla\cdot\mathbf{v} = \frac{\delta_r r^2 u + O(\Delta r^2)}{r^2} = \frac{\delta_r r^2 u}{r^2} + \frac{O(\Delta r^2)}{r^2}, \tag{A1}$$

$$\nabla\cdot\mathbf{v} = \delta_r u + \frac{2u}{r} + O(\Delta r^2), \tag{A2}$$

assuming the finite difference errors for the first-order derivatives to $O(\Delta r^2)$. The above equations show that the conservation form of finite difference (A1) has an error of O(1) when $r \sim \Delta r$. On the other hand, the finite difference error can always be kept to $O(\Delta r^2)$ when the non-conservation form (A2) is used.

As for $\nabla \cdot \kappa \nabla T$, we can also show, in a similar way, that the finite difference error may be of O(1) when the conservation form of finite difference is used and it can be kept to $O(\Delta r^2)$ when the non-conservation form is used.

References

1) J.J. Duderstadt and G.A. Moses: *Inertial Confinement Fusion* (John Willey & Sons, New York, 1982).

2) C. Deutch: Ann. Phys. **11** (1986) 1.

3) R.O. Bangerter, J.W.-K. Mark and A.R. Thiessen: Phys. Lett. **88A** (1982) 225.

4) N.A. Tahir and K.A. Long: Atomkernergie-Kerntechnik **48** (1986) 105.

5) R.S. Craxton, R.L. McCrory and J.M. Soures: Sci. America (1986) 60.

6) K. Niu and S. Kawata: Fusion Tech. **11** (1987) 365.

7) J.D. Lindl and W.C. Mead: Phys. Rev. Lett. **34** (1975) 127.

8) M.H. Emery, J.H. Orens, J.H. Gardner and J.P. Boris: Phys. Rev. Lett. **48** (1982) 253.

9) M.C. Richardson, P.W. McKenty, R.L. Keck, F.J. Marshall, D.M. Roback, C.P. Verdon, R.L. McCrory and J.M. Soures: Phys. Rev. Lett. **56** (1986) 2048.

10) Y.B. Zel'dovich, Y.P. Raizer, W.D. Hayes and R.F. Probstein: *Physics of Shock Waves and High-Temperature Hydrodynamic Phenomina* (Academic Press, NewYork, 1966) Vol. 1.

11) G.S. Fraley, E.J. Linnebur, R.J. Mason and R.L. Morse: Phys. Fluids **17** (1974) 474.

12) N.G. Cooper (ed.): *An Invitation to LASL-EOS Library* (Los Alamos, 1979) LASL-79-62.

13) H. Bethe: Ann. Phys. **5** (1930) 325.

14) J. von Neumann and R. Richtmyer: J. Appl. Phys. **21** (1950) 232.

15) H. Takeda: J. Oceanogr. Soc. Jpn. **40** (1984) 271.

16) L.D. Landau and E.M. Lifshitz: *Fluid Mechinics* (Pergamon, New York, 1959).

17) R.E. Kidder: Nucl. Fusion **16** (1976) 3.

Table I. The values of the burning fraction (the rate of nuclear reaction), f, the maximum of $\rho R = \int \rho_{DT} dr$, and the time, t_c, at which the target collides at the center versus representative values of the total incident beam energy, E_b, in the spherical symmetric case.

E_b (MJ)	f	ρR_{max} (kg/m^2)	t_c (nsec)
3.1	0.0003	73.8	22.1
3.2	0.547	74.5	21.8
4	0.560	79.5	19.8
5	0.569	81.4	18.0
6	0.573	82.3	16.6
7	0.570	83.8	15.5
8	0.554	83.2	14.4
9	0.408	25.2	13.3

Table II. The values of the burning fraction, f, the maximum of $\rho R = \int \rho_{DT} dr$, and the time, t_c, at which the target collides at the center versus representative values of the nonuniformity rate, a, for $E_b = 5$ MJ and $m = 2$.

a	f	ρR_{max} (kg/m^2)	t_c (nsec)
0	0.569	82.4	18.0
0.01	0.568	81.4	18.0
0.02	0.568	80.0	18.0
0.03	0.566	76.7	18.0
0.04	0.561	71.9	17.9
0.05	0.0006	66.9	17.9

Table III. The critical values of the nonuniformity rate, a_{cr}, versus representative values of the incident beam energy, E_b, and the mode in the θ-direction, m.

E_b (MJ)	m	a_{cr}
5	2	0.04
5	4	0.07
5	6	0.05
5	8	0.07
5	-2	0.07
5	-4	0.05
7	2	0.09

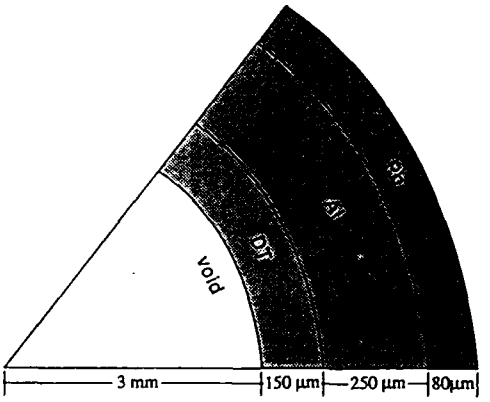

Fig.1. Target structure used in the computation.

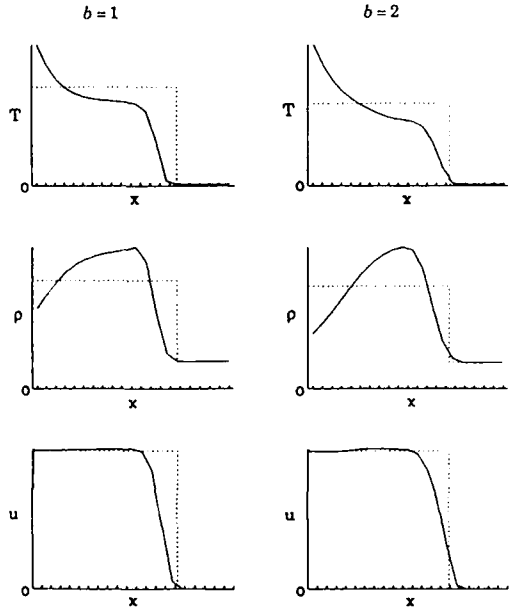

Fig.2. Distributions of T, ρ and u for $b = 1$ and 2 at 100 steps when the left wall began to move suddenly rightward with a constant velocity for the Mach number 10. The exact solution[16] has also been shown by the dotted line for comparison.

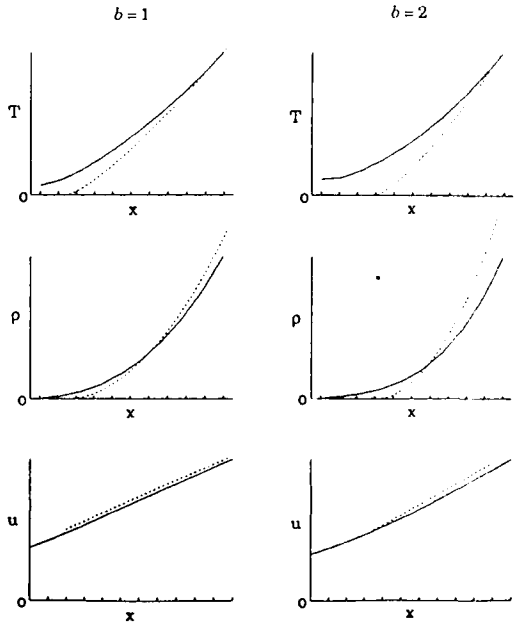

Fig.3. Finite difference solutions for T, ρ and u with $b = 1$ and 2 representing Kidder's similar solution[17] (dotted line) at 180 steps.

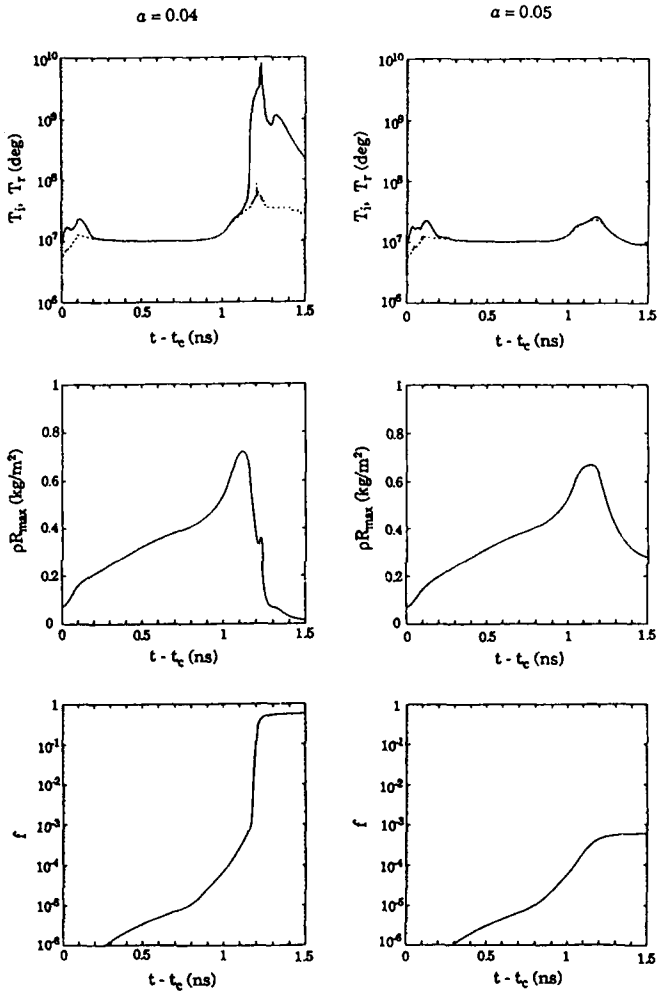

Fig.4. Plot of the maximum of T_i (solid line), that of T_r (dotted line), ρR and the burning fraction, f, as a function of the elapsed time after the time, t_c, at which the target collides at the center for E_b = 5 MJ, m = 2, and a = 0.04, 0.05.

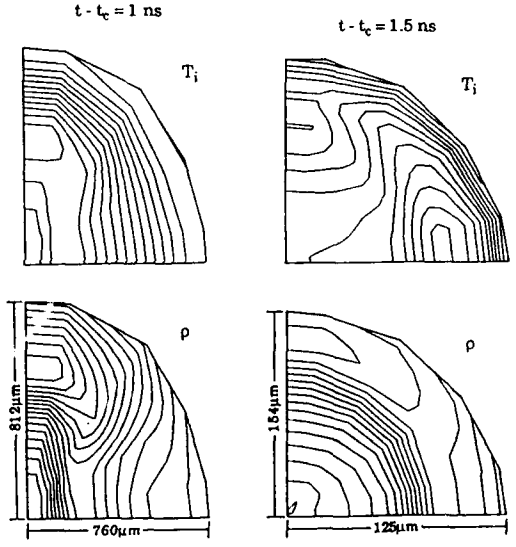

Fig.5. Contours of T_i and ρ when E_b = 5 MJ, m = 2, a = 0.04, and $t - t_c$ = 1 nsec (before the ignition; see Fig.4) and 1.5 nsec (after the ignition).

Development of Electromagnetic PIC Code for LIB Diode

Katsuhiko Ozaki and Keishiro Niu
Department of Energy Sciences,
Tokyo Institute of Technology,
Nagatsuta, Midori-ku, Yokohama 227, Japan

We are developing a 2.5 - dimensional Particle - in - Cell Code to design High Intensity LIB Diode for Inertial Confinement Fusion. The fundamental equations consist of three wave equations, one Poisson equation for determing the electromagnetic field and Newton - Lorentzs equations for moving particles. In this code , Cylindrical coordinate is used . The first step, this PIC Code try to simulate a simple model which is parallel cicular plane Diode , and to investigate Ion current density at cathode .

§1 Introduction

In LIB ICF , it is required that the several MJ Energy is injected into a Target with the radius of several milimeters during the time interval of several nanosecond. For generating such High Energy Ion Beam , we can use the high

voltage pulsed power techniques . The main problem connected with ion beam production is that application of a high voltage to an anode - cathode gap candraw both an electron beam from the cathede and an ion beam from the anode . Due to the larger ion mass , the ion current will bebe smaller than the electron current .[1] And the power delivered to the ion beam will be smaller than the power to the electron beam. To improve the efficiency of the ion beam production, it is necessary to prevent the electrons from cathode ,because electrons will take up the most of energy delivered to the diode. To prevent the electron current from the cathode , we apply the magnetic field at the anode - cathode gap. This diode type is the Magnetically Insulated Diode .

At generating the ion beam , The stability of electron sheath is very important problem . Therefore , we make the P. I. C. Code to simulate ion and electron motion in the diode . In this code, Assuming axial symmetry in cylindrical coordinate .

§ 2 Model

[A] Field Equations

If we employ the relations

$$\mathbf{B} = \nabla \times \mathbf{A}$$

$$\mathbf{E} = -\nabla\Phi - (\partial \mathbf{A} / \partial t)$$

$$\nabla \cdot \mathbf{A} = 0$$

with Maxwell's equations, the electromagnetic field are obtained by solving three wave equations for the vector potential and one Poisson equation for the scalar potential.

$$\nabla^2\Phi = -\rho / \varepsilon_0$$

$$\nabla^2 \mathbf{A} - (1/c^2)(\partial^2 \mathbf{A} / \partial t^2) = -\mu_0 \mathbf{J} + \nabla(\partial\Phi / \partial t)$$

where $\mathbf{A}$ and Φ are the vector and scalar potential. J and ρ are current and charge density. The current and charge densities is interpolated by area-weighting. The model is circular plane diode. Assuming axial symmetry in cylindrical coordinate. $(\partial / \partial \theta = 0)$

[B] Equations of Motion

Ion motion are determined by this equations

$$\frac{dr}{dt} = v$$

$$\frac{d\mathbf{v}_i}{dt} = q_i / m_i \left(\mathbf{E} + \mathbf{v}_i \times \mathbf{B} \right)$$

Electron motion are determined by this relativistic equations[3]

$$\frac{d\mathbf{r}_e}{dt} = \mathbf{v}_e$$

$$\frac{d\left(M_e \mathbf{v}_e\right)}{dt} = q_e \left(\mathbf{E} + \mathbf{v}_e \times \mathbf{B} \right)$$

$$\frac{d\left(M_e c^2\right)}{dt} = q_e \left(\mathbf{E} \cdot \mathbf{v}_e \right)$$

A particle position is treated in 2 - dimensional. (r - z) But velocity is treated in 3 - dimensional. (V_r, V_θ, V_z)

§ 3 Simulation

The field equations are solved on a finite difference meah. The mesh spacing is given by Δr, Δz. The position on the mesh is given by $r_j = j\Delta r$, $z_k = k\Delta z$. And given time is denoted by $n\Delta t$, $n = 0, 1, 2, \cdots$

The difference approximation that we use in solving

the field eqs. and motion eqs. is implicit method.

To simulate the diode ,we used this parameters

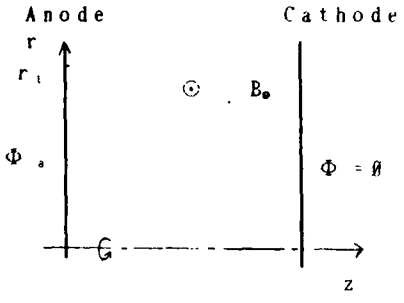

A - K Gap	: 0.01	[m]
Anode radius r_1	: 0.1	[m]
Applied B_e	: 4.0	[T]
Voltage Φ_a	: 5.0	[MV]
Super particles	: 10^{4}	

§ 4 Results

In this research , we simulated a very simple model . But we need more detailed calculation of this model and more development of this code to design LIB diode for I. C. F.

The ion current density at the cathode is shown in Figure 1.(at 0.7 nsec) The ion and electron maps are shown in Figure 2 ~ 3. The Scalar potential is shown in Figure 4. The electric and magnetic field is shown in figure 5 ~ 7.

According to the simulation results , the electron sheath is unstable . We need a method of stabilizing the electron sheath.

References

(1) Langmuir , Phys. Rev. 33, 954 (1929)

(2) Charles K. Birdsall , A. Bruce Langdon , PLASMA PHYSICS VIA COMPUTER SIMULATION (1985)

(3) Buneman, O., J. Comput. Phys. 1. 517 535 (1967)

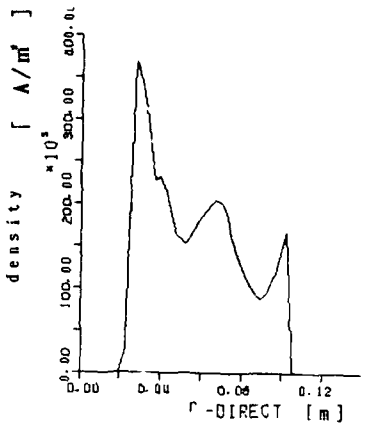

ion current density

0.7 nsec

Figure 1.

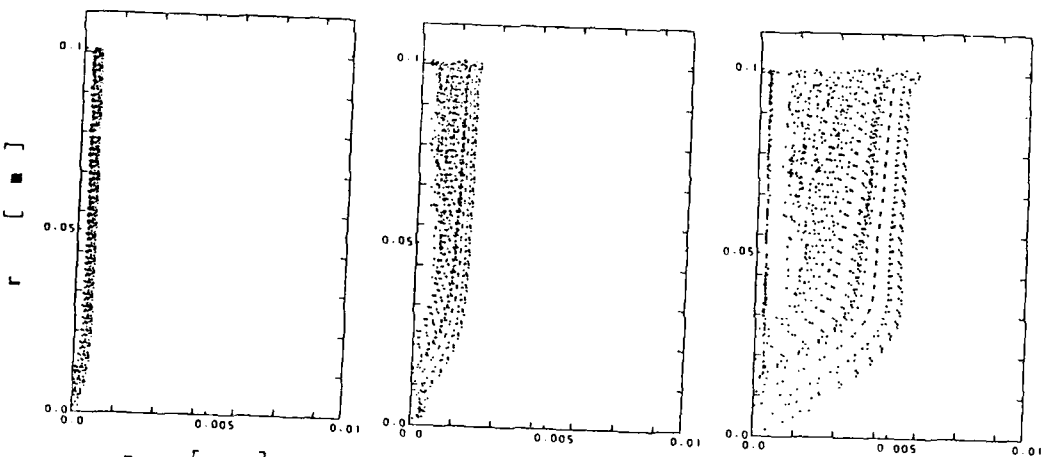

Ion Map

Figure 2.

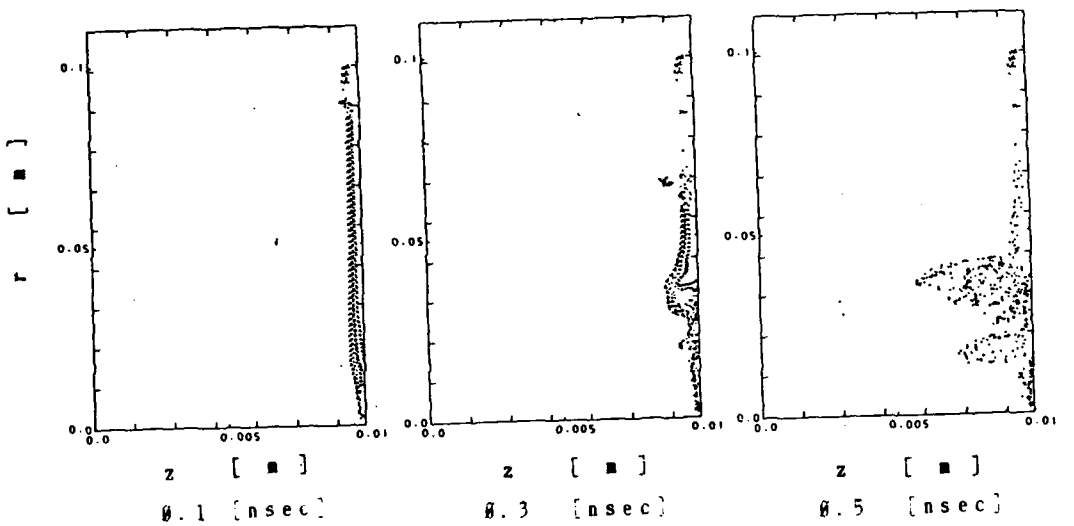

Electron Map

Figure 3

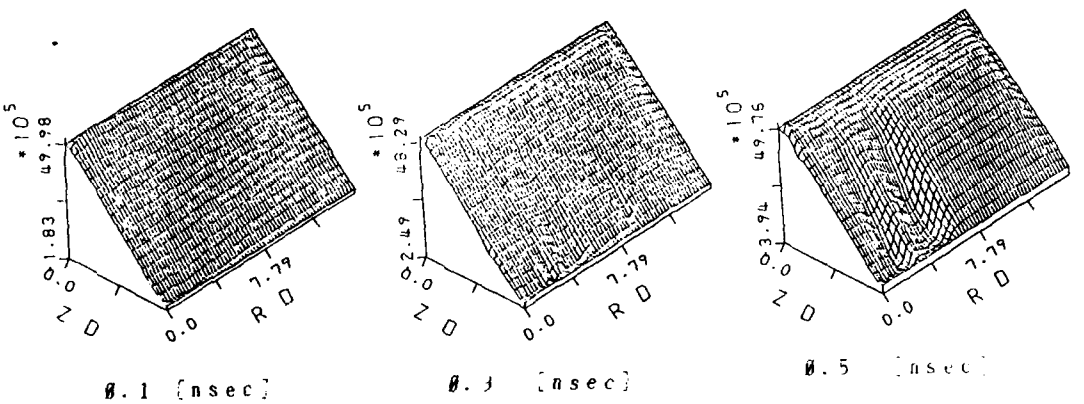

The Scalar potential

Figure 4.

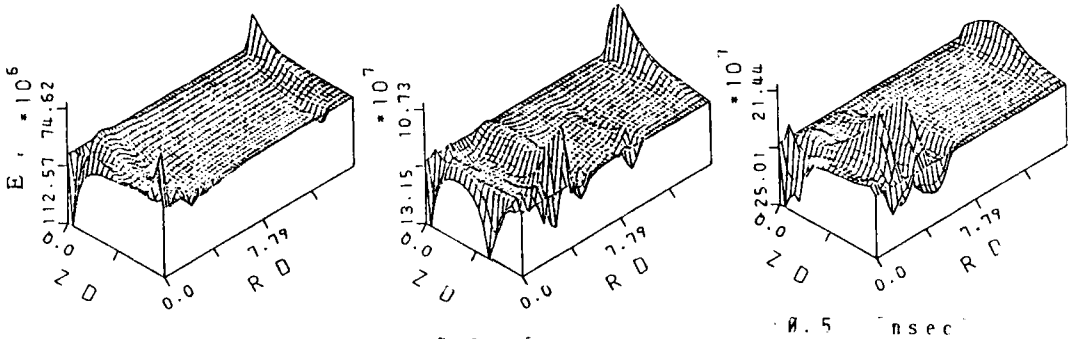

0.1 [nsec] 0.3 [nsec] 0.5 [nsec]

Electric field ~ E_r

Figure 5.

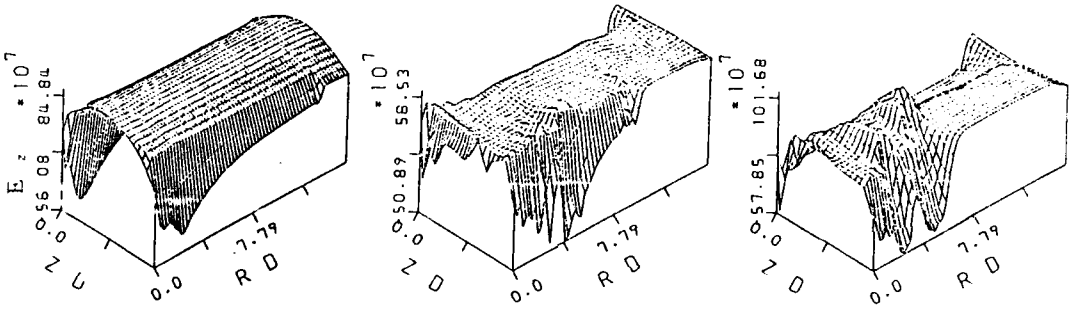

0.1 [nsec] 0.3 [nsec] 0.5 [nsec]

Electric field ~ E_z

Figure 6.

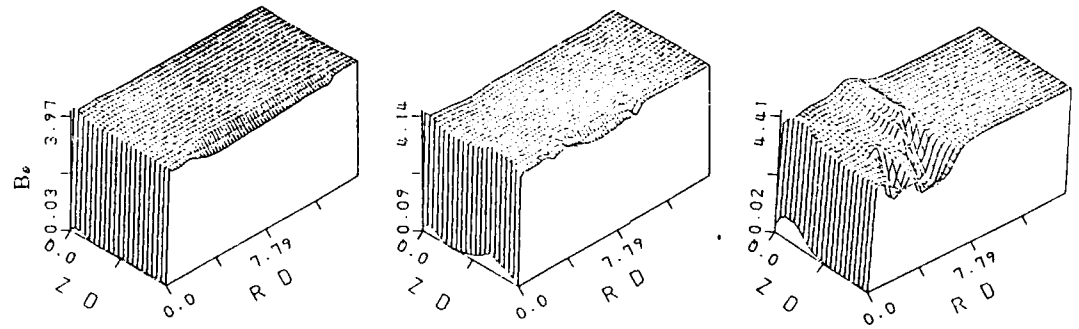

0.1 [nsec] 0.3 [nsec] 0.5 [nsec]

Magnetic field ~ B_θ

Figure 7.

Kinetic Theoretical Analysis for Propagation of Rotating Ion Beam in ICF

T. Kaneda and K. Niu

Department of Energy Sciences, the Graduate School at Nagatsuta,
Tokyo Institute of Technology, Nagatsuta, Midori-ku, Yokohama 227, Japan

Abstract

It is proposed that self-magnetic field of the beam can stabilize and pinch itself, without complete neutralization of the beam current. This situation is achieved in the back ground plasma which density is about 1/10 of the beam. The beam produces the strong azimuthal self-magnetic field by the axial motion. This field makes the beam pinch. The axial self-magnetic field is induced by the beam azimuthal motion and stabilizes the beam propagation.

In this paper, the rotating light ion beam is discussed on the basis of kinetic theory. The velocity distribution function for the beam ions f_{b0} is obtained as an exact solution of the Vlasov-Maxwell equation for the steady state. That is, f_{b0} is an arbitrary function with respect to Hamiltonian H, canonical angular momentum P_θ and canonical axial momentum P_z ; $f_{b0}=f_{b0}(H, P_\theta, P_z)$. Here, the subscript "$_0$" denotes the steady state. The macroscopic physical quantities are obtained by integration in v-space. Hence, in order to obtain the steady state solution of beam-plasma system, these equations must be solved numerically with Maxwell equations simultaneously. The distribution function f_{b0} is assumed by considering the condition to extract the beam in the diode.

Introduction

The choice of the energy driver is one of the most important subject of the study to realize the inertial confinement fusion at the present stage. Many kinds of energy drivers have been proposed until now. To use the light ion beam as an energy driver is one method, but the propagation from the diode to the target must be studied still in detail. The plasma channel method has been proposed for stable propagation of the light ion beam. But such a method has many difficult problems in order to design the actual fusion reactor. The rotating beam has been proposed recently as an another method to propagate the light ion beam from the diode to the target. The azimuthal (θ- direction) motion of the beam stabilize itself. The beam particles receive the Lorentz force to the azimuthal direction by appling the radial (r-direction) magnetic field in the diode, so the rotating motion of the beam particles is induced. The axial (z-direction) magnetic field is induced by this rotating motion of the beam particles. The axial self-magnetic field stabilizes the beam propagation and the azimuthal self-magnetic field makes the beam pinch. Considering the condition to extract the beam in the diode, the velocity distribution function of the beam particles is decided and the macroscopic physical quantities are solved numerically in this paper.

General Solution of The Vlasov-Maxwell Equations

The governing equations of beam-plasma system are given as following equations.

Boltzmann equations

$$\frac{\partial f_x}{\partial t}+\dot{q}\cdot\frac{\partial f_x}{\partial q}+\ddot{q}\cdot\frac{\partial f_x}{\partial \dot{q}}=\left(\frac{\partial f_x}{\partial t}\right)_c \quad (x;b,e,i) \tag{1}$$

Maxwell equations

$$\nabla \times B = \mu_0 \int_{-\infty}^{\infty} \sum_x e_x \hat{v}_x f_x \, d^3\hat{v} + \mu_0 \epsilon_0 \frac{\partial E}{\partial t} \quad (x;b,e,i) \tag{2}$$

$$\nabla \times E = -\frac{\partial B}{\partial t} \tag{3}$$

$$\nabla \cdot B = 0 \tag{4}$$

$$\epsilon_0 \nabla \cdot E = \int_{-\infty}^{\infty} \sum_x e_x f_x \, d^3\hat{v} \quad (x;b,e,i) \tag{5}$$

Here, f_x is a velocity distribution function. The subscript "$_x$" denotes a sort of particles. t is time, **q** (**q**=(r,θ,z)) is generalized co-ordinate, superscript "·" denotes the time derivative and "^" denotes the microscopic velocity. Because the mean free path is exceedingly long compare to the beam radius as to the beam particles, the assumption of collisionless holds to a fairly good approximation.

$$\frac{\partial f_b}{\partial t} + \dot{q} \cdot \frac{\partial f_b}{\partial q} + \ddot{q} \cdot \frac{\partial f_b}{\partial \dot{q}} = 0 \tag{6}$$

Based on a few assumptions ($\frac{\partial}{\partial t} = \frac{\partial}{\partial \theta} = \frac{\partial}{\partial z} = 0$), equation (6) can be written as follows:

$$\hat{v}_r \frac{\partial f_{b0}}{\partial r} + (r\dot{\theta}^2 + \frac{1}{m_b} F_r) \frac{\partial f_{b0}}{\partial \hat{v}_r} + \{ \frac{\frac{1}{m_b} F_\theta - 2\dot{r}\dot{\theta}}{r} \} \frac{\partial f_{b0}}{\partial \dot{\theta}} + \frac{F_z}{m_b} \frac{\partial f_{b0}}{\partial \hat{v}_z} = 0. \tag{7}$$

Here, $\mathbf{F} = (F_r, F_\theta, F_z)$ is external electro-magnetic force. This external force is written by scalar potential Φ and vector potential **A**. Equation (7) has the form of Lagrange's partial differential equation. From the characteristic

equation of this equation, following three integrals of motion are obtained.

$H = e_b\Phi + \frac{1}{2}m_b(\hat{v}_r^2 + \hat{v}_\theta^2 + \hat{v}_z^2)$: Hamiltonian

$P_\theta = m_b r\hat{v}_\theta + e_b r A_\theta$: canonical angular momentun

$P_z = m_b\hat{v}_z + e_b A_z$: canonical axial momentum

Then, the general solution of Eq.(7) is an arbitrary function with respect to these three integrals of motion.

$$f_{b0} = f_{b0}(H, P_\theta, P_z) \tag{8}$$

Furthermore, the range of the motion of a beam particle is given by the following condition.

$$H - U(r) \geq 0 \tag{9}$$

Here, the function U(r) is given by

$$U(r) = e_b\Phi + 1/2m_b\{(\frac{P_\theta - e_b r A_\theta}{m_b r})^2 + (\frac{P_z - e_b A_z}{m_b})^2\}.$$

Equilibrium Solution of The Beam

The steady solutions of the rotating ion beam can be obtained by the before basic equations. It is assumed that the canonical angular momentum P_θ has the scatter and the Hamiltonian H and the canonical axial momentum P_z have constant value H_0 and P_{z0} respectively on each particle. Then the velocity distribution function f_{b0} can be approximated by following equation.

$$f_{b0}(H,P_\theta,P_z) = A\ \delta(H-H_0)\ \delta(P_z-P_{z0})\ S(P_\theta; P_{\theta 1}, P_{\theta 2}) \tag{10}$$

Here, A is constant, $\delta(x\text{-}x_0)$ is a delta function. The function $S(x;x_1,x_2)$ takes unity between x_1 and x_2 , and the value corresponding to the another x values is zero. Such a distribution function f_{b0} expresses a hot plasma propagating to z-direction with the betatron motion. The integration appeared in the Maxwell equation (2) and (5) can be calculated as follows:

$$n_{b0} = \frac{2A}{m_b^3 r}\int_{P_{\theta 1}}^{P_{\theta 2}} \frac{1}{G}\, dP_\theta \tag{11}$$

$$V_{br0} = 0 \tag{12}$$

$$V_{b\theta 0} = \frac{2A}{n_{b0} m_b^3 r}\int_{P_{\theta 1}}^{P_{\theta 2}} \frac{1}{G}\frac{P_\theta - e_b r A_{\theta 0}}{m_b r}\, dP_\theta \tag{13}$$

$$V_{bz0} = \frac{P_{z0} - e_b A_{z0}}{m_b}. \tag{14}$$

The beam temperature T_{b0} is not an unknown function of the Maxwell equations, however, which can be written as follows:

$$T_{b0} = \frac{2A}{n_{b0} m_b^2 k_B r} \int_{P_{\theta 1}}^{P_{\theta 2}} G dP_\theta . \tag{15}$$

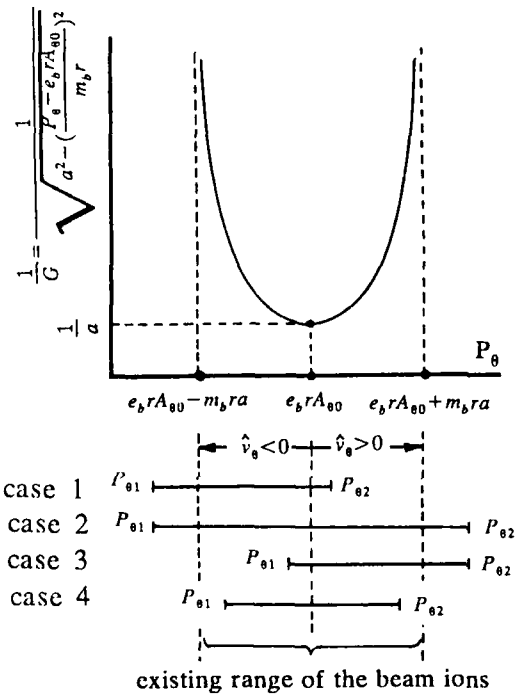

Fig.1 Classification of the ranges of the integral

The integral from $P_{\theta 1}$ to $P_{\theta 2}$ of P_θ in the Eq.(11),(13) and (15) can be integrated analytically by sorting out into following four cases.

For example, beam number density (Eq.(11)) is calculated as following way.

By comparing the singular points ($P_\theta = e_b r A_{\theta 0} \pm m_b r a$) of the curve 1/G and the range of integral ($P_{\theta 1} \leq P_\theta \leq P_{\theta 2}$) , the solutions are classified into four cases. Here, a is defined as follows:

$$a = \sqrt{\frac{2}{m_b}(H_0 - e_b \Phi_0) - (\frac{P_{z0} - e_b A_{z0}}{m_b})^2} .$$

As to the other physical quantities, in the same manner as number density, the analytical solutions are obtained by the classification into four cases.

Table 1 The analytical solutions classified into four cases

	case 1	case 2	case 3	case 4
n_{b0}	$\frac{2A}{m_b^2}(Arcsin\frac{t_2}{a}+\frac{\pi}{2})$	$\frac{2A}{m_b^2}\pi$	$\frac{2A}{m_b^2}(\frac{\pi}{2}-Arcsin\frac{t_1}{a})$	$\frac{2A}{m_b^2}(Arcsin\frac{t_2}{a}-Arcsin\frac{t_1}{a})$
$V_{b\theta 0}$	$-\frac{2Aa}{n_{b0}m_b^2}\sqrt{1-(\frac{t_2}{a})^2}$	0	$\frac{2Aa}{n_{b0}m_b^2}\sqrt{1-(\frac{t_1}{a})^2}$	$\frac{2Aa}{n_{b0}m_b^2}(\sqrt{1-(\frac{t_1}{a})^2}-\sqrt{1-(\frac{t_2}{a})^2})$
T_{b0}	$\frac{Aa^2}{n_{b0}m_bk_B}\{\frac{t_2}{a}\sqrt{1-(\frac{t_2}{a})^2}+Arcsin\frac{t_2}{a}+\frac{\pi}{2}\}$	$\frac{Aa^2\pi}{n_{b0}m_bk_B}$	$\frac{Aa^2}{n_{b0}m_bk_B}\{\frac{\pi}{2}-\frac{t_1}{a}\sqrt{1-(\frac{t_1}{a})^2}-Arcsin\frac{t_1}{a}\}$	$\frac{Aa^2}{n_{b0}m_bk_B}\{\frac{t_2}{a}\sqrt{1-(\frac{t_2}{a})^2}-\frac{t_1}{a}\sqrt{1-(\frac{t_1}{a})^2}+Arcsin\frac{t_2}{a}-Arcsin\frac{t_1}{a}\}$

where $t_1=\frac{P_{\theta 1}-e_brA_{\theta 0}}{m_br}$ and $t_2=\frac{P_{\theta 2}-e_brA_{\theta 0}}{m_br}$

The *Arcsin* denotes the principal value of the *arcsin*. Here, one should note that these physical quantities n_{b0},$V_{b\theta 0}$ and T_{b0} are not decided as functions of r. Because in the above solutions, the functional forms of $\Phi_0(r)$,$A_{\theta 0}(r)$ and $A_{z0}(r)$ are not decided. Hence, in order to obtain the steady state solution of beam-plasma system, these equations must be solved numerically with Maxwell equations simultaneously. At each point of r, the "case" must be

decided to calculate the n_{b0},$V_{b\theta 0}$ and T_{b0}.

The results are shown in Fig.2-Fig.7 in the case of $E_r = 0, V_i = V_e = 0$. The following parameters are used in this calculation.

$$H_0 = 1.3 \times 10^{-12}\ \mathrm{J}$$
$$P_{\theta 1} = -0.3 \times 10^{-22}\ \mathrm{kg\ m^2/s}$$
$$P_{\theta 2} = 1.5 \times 10^{-22}\ \mathrm{kg\ m^2/s}$$
$$P_{z0} = 6.5 \times 10^{-20}\ \mathrm{kg\ m/s}$$

References

(1) R.B.Miller: Intense Charged Particle Beams (Plenum, New York, 1982) p.26.

(2) Ronald C.Davidson: Theory of Nonneutral Plasmas (W.A.BENJAMIN, Inc., 1974) p.92.

(3) H.Murakami: Jpn.J.Appl.Phys.23 (1984) 1227.

(4) T.Kaneda and K Niu: Proc.2nd Int. Topic. Symp. on Inertial-Confinement Fusion Research by High-Power Particle Beams, 1986, pp.133-142.

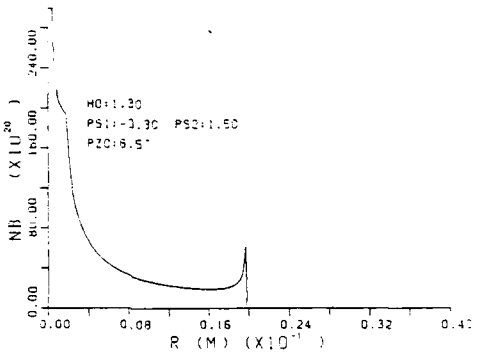

Fig.2 Beam number density profile

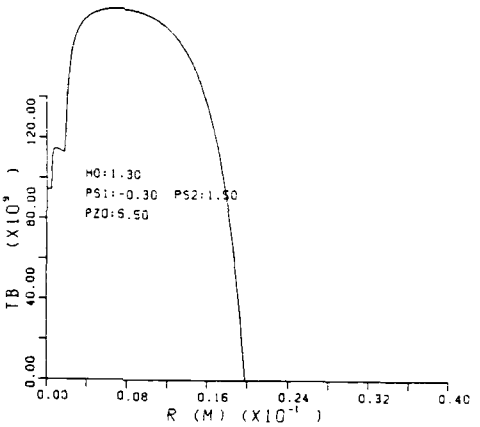

Fig.3 Beam temperature profile

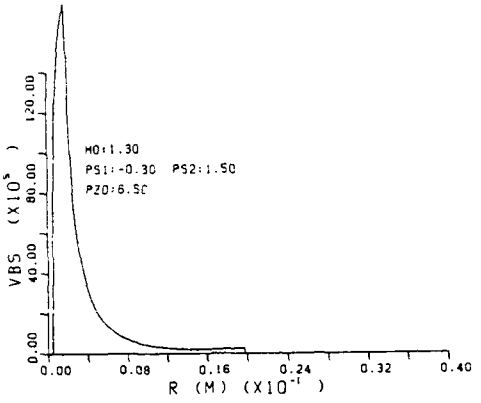

Fig.4 Beam azimuthal velocity profile

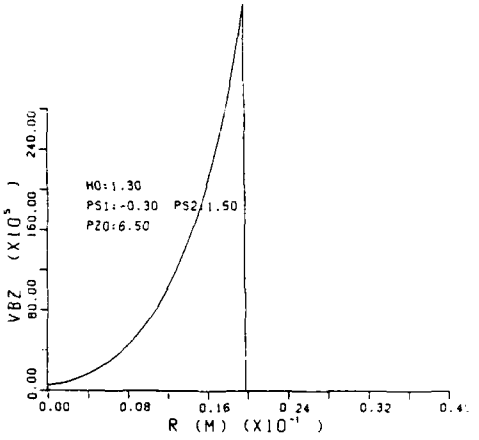

Fig.5 Beam axial velocity profile

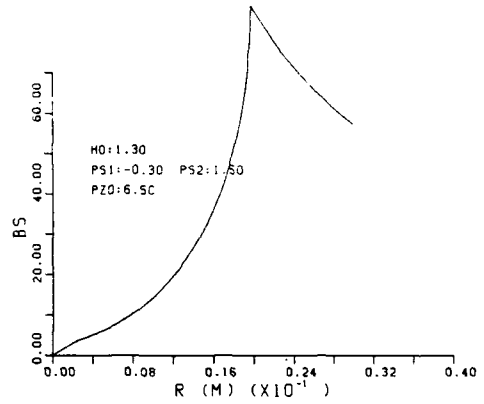

Fig.6 Azimuthal magnetic field profile

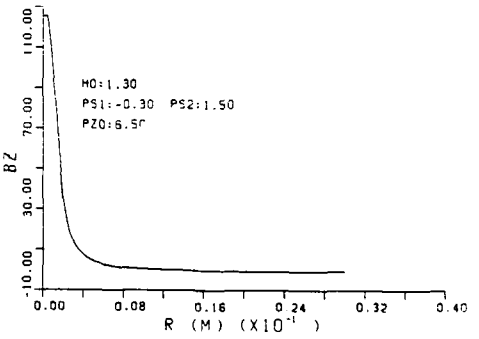

Fig.7 Axial magnetic field profile

Hybrid Particle Simulation for Focusing of Rotating and Propagating LIB

Takayuki AOKI and Keishiro NIU
Department of Energy Sciences, the Graduate School at Nagatsuta,
Tokyo Institute of Technology, Nagatsuta, Midori-ku, Yokohama 227

Abstract

The focusing processes of a rotating and propagating light ion beam in the drift region are studied numerically by using a hybrid particle code. Initially an intense ion beam with the current density of 8 kA/cm^2 and the total current of 2.5 MA, which is extracted from the diode, passes through the applied magnetic field to make the beam rotate in the azimuthal direction. The beam is focused owing to the anode geometry and the induced self-magnetic field. The phenomena of the beam focusing strongly depend on both the background plasma pressure of the drift region and the applied magnetic field. In the case that the plasma pressure is 3.0 Torr and the 0.2-Tesla magnetic field is applied in the distance of 2.0 cm, the self-magnetic field is induced in the vicinity of the focal spot, and the rotating and propagating beam with the intensity of 108 TW/cm^2 and the beam radius of 3.5 mm is formed after the focal spot.

1. Introduction

Inertial Confinement Fusion (ICF) schemes require the intensity of more than 100 TW/cm^2 and the beam energy of several MJ for light ion beam (LIB) drivers in order to extract enough energies from DT fuel targets.[1] Recent experiments[2] of the beam generation resulted that the beam current density was 6 kA/cm^2 before focusing and the diode voltage was 1.4 MV. Beam focusing experiments[3,4] reported that the focal intensity was 1.5 TW/cm^2, because the flashover anode plasma was inhomogeneous and the cathod

electron sheath could not make a spherical equi-potential. Furthermore, the self-magnetic field induced in the drift region had bending effects on the beam trajectories. A recent approach is to use an ion with a larger mass-to-charge ratio than a proton, that is, to accelerate Li^+ ions.[5] However, these types of experiments assumed that the target was located at the focal spot, and the beam transport in the reactor chamber was not taken into consideration. The transport experiments using the *z*-discharge plasma channel[6] were made, while there were a few cumbersome problems. used for the beam transport from the focal spot to the target.

Recently a rotating and propagating LIB has been proposed[1,7] in order to improve the focusing properties and stably transport the beam to the target over the distance of several meters. A beam current of a intense LIB is not neutralized adequately in a low-density plasma comparable to the beam density.[8] This beam makes use of the pinch effect of the azimuthal self-magnetic field induced in the focusing phase in addition to the diode geometry. In the propagation phase, the beam is confined by this magnetic field and the Lorentz forces balance with both the beam pressure gradient and the centrifugal force in the radial direction. At this stage, beam trajectories are not straightforward and beam particles oscillate with a betatron frequency in the radial direction. A beam brightness and beam optics become meaningless in such a situation. The beam propagation is stabilized by the beam rotational motion and induced axial magnetic field. In the macroscopic equilibrium state, the beam is stable on the condition that the ratio of the beam rotating velocity to the propagating one is more than the value of 0.6.[9] In this paper, the phenomena of the beam focusing are simulated by the hybrid particle code in which beam ions are represented by a particle model and a background plasma is treated as a fluid model. We investigate the optimum density of the background plasma and the optimum strength of the applied field to rotate a beam for a well-focused rotating and propagating LIB.

2. Self Focusing and Formation of Rotating and Propagating LIB

The beam particles with the injection angles and the local divergence

angles due to the diode structure are injected into the drift region. In this paper, it is assumed that the specie of a beam is a proton and each particle has the energy of 5.6 MeV in the entrance. The structure of the drift region and the system of the cylindrical coordinate (r,θ,z) are shown in Fig. 1. This region is filled with a low-density plasma and the applied field coils setting up in the entrance continue to the anode of the diode. The magnetic-field structure made by these coils is shown in Fig. 1.

In the applied magnetic field, the beam particles begin to rotate in the θ-direction owing to the Lorentz force. A small percentage of the axial momentum of the beam is transferred to the angular momentum by the applied magnetic field. The space charge of the beam is perfectly neutralized by the background electrons in this region, however, the current neutralization fraction strongly depends on the density of the background plasma. The beam current is mostly neutralized on the condition that the plasma density is much higher than the beam density. It is assumed that the plasma pressure of the drift region is a few Torr (at 273K), that is, the plasma density is the order of 10^{23} m^{-3}. If there are no field and no interaction among each particle, the beam is focused at the focal point z_f, which is determined by the injection angles and the spot radius of the beam depend on the local divergence angles. When the beam is focused within the 1 cm-radius owing to the injection condition, the density of the beam becomes comparable to that of the plasma and the strong magnetic field is induced in the vicinity of the focal spot. Because the angular momentum is conserved, the beam velocity in the θ-direction becomes large near the focal spot. The beam θ-current induces the magnetic field in the z-direction to stabilize the beam propagation. After the focal point z_f, the strong induced magnetic field confines the beam within a small radius. Thus far the configuration of a rotating and propagating beam is formed.

3. Hybrid particle code

In order to simulate the focusing process of a rotating and propagating LIB, we have developed a hybrid particle code. In this code, the beam motions

are solved by using a particle in cell (PIC) model, because the mean free path of the beam particle is much larger than the scale of the region. The particle description is given by the following Newton's equations,

$$\frac{d\mathbf{v}_b}{dt}=\frac{e}{m_b}\left(E+\mathbf{v}_b\times B\right) , \tag{1}$$

$$\frac{d\mathbf{r}_b}{dt}=\mathbf{v}_b , \tag{2}$$

where $\mathbf{v}_b$ and $\mathbf{r}_b$ represent the velocity and the position of the beam particle, respectively. Other symbols obey the standard notation.

The background plasma is collisional and is treated as two fluids (electron − ion) model. We are not interested in the phenomena occurring on the time scale of the electron plasma frequency, ω_{pe} and the electron cyclotron frequency, Ω_{ce}. In this regime, the inertia term in the momentum equation can be neglected[10] and the quasineutrality holds good, i.e., $n_e=Z_i n_i+n_b$, where n is the number density and Z is the charge state. The subscripts e, i and b denote the electron, the ion and the beam, respectively. The basic equations describing the electron fluid are as follows,

$$-en_e(E+u_e\times B)-m_e n_e \nu_{ei}(u_e-u_i)-\nabla p_e=0 , \tag{3}$$

$$\frac{3}{2}n_e k\left[\frac{\partial}{\partial t}+u_e\cdot\nabla\right]T_e=-p_e\nabla\cdot u_e+\nabla\cdot\kappa_e\nabla T_e+Q_e , \tag{4}$$

$$Q_e=\frac{3m_e}{m_i}\nu_{ei}n_e k(T_i-T_e)+\eta J_{plasma}^2 + Q_{stopping}-Q_{Bremsstrahlung} , \tag{5}$$

where ν_{ei} is the electron-ion collision frequency, κ is the thermal conductivity and η is the electrical resistivity. $Q_{stopping}$ is collisional deposition of the beam energy and $Q_{Bremsstrahlung}$ is the cooling due to Bremsstrahlung radiation. The plasma is assumed to be optically thin.

For the ions of the background plasma, the full sets of fluid equations are used as follows:

$$\frac{\partial n_i}{\partial t}+\nabla\cdot(n_i u_i)=0 \ , \tag{6}$$

$$m_i n_i\left[\frac{\partial}{\partial t}+u_i\cdot\nabla\right]u_i=Z_i e n_i(E+u_i\times B)-\nabla P_i - m_e n_e \nu_{ei}(u_i-u_e) \ , \tag{7}$$

$$\frac{3}{2}n_i k\left[\frac{\partial}{\partial t}+u_i\cdot\nabla\right]T_i=-p_i\nabla\cdot u_i+\nabla\cdot\kappa_i\nabla T_i+Q_i \ , \tag{8}$$

$$Q_i=\frac{3m_e}{m_i}\nu_{ei}n_i k(T_e-T_i) \ . \tag{9}$$

By using the scalar and vector potentials, the electric and magnetic fields are represented as follows,

$$E=-\nabla\phi-\frac{\partial A}{\partial t} \ , \tag{10}$$

$$B=\nabla\times A \ . \tag{11}$$

Choosing the Coulomb gauge, $\nabla\cdot A=0$, Maxwell's equations are reduced to

$$\Delta\phi=-\frac{e}{\epsilon_0}(Z_i n_i+n_b-n_e) \ , \tag{12}$$

$$\frac{1}{c^2}\frac{\partial^2 A}{\partial t^2}-\Delta A=\mu_0 e(Z_i n_i u_i+n_b u_b-n_e u_e)-\frac{\partial\nabla\phi}{\partial t} \ . \tag{13}$$

Here, u_b represents the local mean velocity of the beam particles. Under the quasineutral condition, however, it is impossible to use Poisson's equation (12). Solving Eq. (3) for E and taking divergence, we have

$$\Delta\phi=\nabla\cdot\left(u_e\times B+m_e\nu_{ei}(u_e-u_i)+\frac{1}{n_e}\nabla P_e\right) \ . \tag{14}$$

Equations (13) and (14) are used to obtain the scalar and vector potential.

In the above formulation, the existence of neutral atoms and atomic physics including such effects as ionization, collisional excitation, radiative decay and

so on are ignored.

4. Dependency of Background Plasma

The current-neutralization fraction of the beam depends on the background-plasma density. When a beam is injected into the drift region, the beam current induces the self-magnetic fields. Because these fields vary temporally and spatially associated with the beam motion, the induced electric fields are generated in directions inverse to the beam propagation. The electrical conductivity of the plasma determine the electron current corresponding to the electric field. If the plasma pressure is homogeneous, equation (3) is reduced to the following Ohm's law,

$$J_{\text{electron}} = \sigma_{\parallel} E_{\parallel} + \frac{1}{1+\omega_{ce}^2 \tau_{ei}^2} \sigma_{\perp} E_{\perp} + \frac{\omega_{ce}\tau_{ei}}{1+\omega_{ce}^2 \tau_{ei}^2} \sigma_{\perp} \boldsymbol{b} \times \boldsymbol{E}_{\perp} \quad , \quad \boldsymbol{b} = \boldsymbol{B}/B \quad , \quad (15)$$

$$\sigma_{\parallel} = 2\frac{e^2 n_e \tau_{ei}}{m_e} \quad , \qquad \sigma_{\perp} = \frac{e^2 n_e \tau_{ei}}{m_e} \quad , \qquad (16)$$

where the subscripts $\parallel$ and $\perp$ mean to be parallel and perpendicular to the magnetic field. The parameter $\omega_{ce}\tau_{ei}$ depends on both the plasma density and the magnetic field. If the plasma is rarefied and coupled strongly with the magnetic field, $\omega_{ce}\tau_{ei} >> 1$, the effective conductivity decrease rapidly.

The focusing processes are simulated on the condition that the incident-beam current density and particle energies increase with a rising time of 10 nsec as shown in Fig. 2. The injection angles are chosen such as the beam is focus at the point of z_f=28 cm, and the local divergence angles are all 30 mrad. In the case that the background is a 20-Torr Argon plasma, we can show the temporal precesses in Fig. 3 and beam emittances in Fig. 4, respectively. The ionization state of the Argon plasma is assumed to be single constant'y. In any cases simulated in this Section, the applied magnetic field is the same strength of 0.25 Tesla in the entrace of this region.

The numerical results show that the beam current is almost neutralized and the self-magnetic field is hardly generated, because the density of the plasma is

much higher than that of the beam even in the focal spot. After the focal spot, the beam diverge and cannot form a rotating and propagating LIB. The trajectories of the beam particle are almost straightforward except the vicinity of the focal spot. It can be found that the beam emittance is conserved along the z-axis according to the beam optics theory.

In the case that the background plasma is 3 Torr, the Map of the beam ion in the vicinity of the focal spot and the beam emittance are shown in Figs. 5 and 6, respectively. The beam becomes such a situation as maintained in Sec. 2. The map of beam steering angles[5], i.e., steering angle$=\tan^{-1}(u_{radial}/u_{axial})$ can be shown in Fig. 7. Because the steering angles are distributed broadly in both negative and positive sides, it can be confirmed that the particles are oscillating the betatron motion in the r-direction. In Fig. 8, we show the map of the rotation ratio[9] which is defined as the ratio of the beam particle velocity in the θ-direction to that in the z-direction. After the focal spot, the average value of the rotation ratio is about 0.5. We can find that a rotating and propagating LIB is formed under these conditions. The background plasma is heated up to 200 eV mainly by the Joule heating effect of the electron current. The plasma is expanded by the $J_{return}\times B_{self}$ force and the temperature gradient, however, the spatial profile of the plasma density changes hardly.

In the case of a 1-Torr background plasma, the map of the beam ions, the beam emittance, the steering angle and the rotation ratio are shown in Figs. 9 ~ 12. If the background-plasma density is equal or less than 1 Torr, the large induced electric fields are generated and deflect the particle trajectories from the central axis from the early stage of the focusing. Because the beam density cannot become high, the force due to the strong induced electric field overwhelms the Lorentz pinch force and diverges the beam. The position of the beam focal spot changes and cannot form a rotating and propagating LIB.

If the background is 3-Torr Hydrogen plasma, the plasma is blew off in the r-direction mainly by the strong $J_{return}\times B_{self}$ force, because the mass of the plasma ion is too small. The plasma density near the focal spot decrease and the induced magnetic fields become large.

To be summarized, a 3-Torr Argon plasma is the most suitable for the focusing and the formation of a rotating and propagating LIB configuration.

5. Optimum Applied Field

In order to rotate a beam propagating in the z-direction, the magnetic field has to be applied in the r-direction. The strength of this field has a strong effect on the beam focusing processes as well as the background-plasma density. We can estimate the strength B_{applied} and the distance Δz which the field should be applied to. After passing through this field and before focusing, the beam particle has the rotational velocity, Δu_θ, which is calculated as follows;

$$\Delta u_\theta = \frac{e}{m_b} u_{bz} B_{\text{applied}} \Delta t = \frac{e}{m_b} B_{\text{applied}} \Delta z \ , \tag{17}$$

where u_{bz} is the beam injection velocity in the z-direction and Δt is the propagating time for the distance Δz. Because the system is cylindrically symmetry, the angular momentum is conserved,

$$L_\theta = m_b r u_\theta + e r A_\theta = \text{const} \ . \tag{18}$$

After the beam is focused, the beam density $n_b{}^a$ and the beam azimuthal velocity $u_\theta{}^a$ are required to be $\sim 10^{22}$ m^{-3} and $\sim 10^7$ m/s, respectively. From Eq.(13), we have

$$A_\theta \sim \mu_0 e n_b{}^a u_\theta{}^a r^{a\,2} \ , \tag{18}$$

where r^a is the beam mean radius The angular momentums between before focusing and after focusing are equal and we have

$$B_{\text{applied}} \Delta z = \frac{m_b u_\theta{}^a r^a}{e r^b} \left(1 + \frac{n_b{}^a e^2}{m_b \epsilon_0} \frac{r^{a\,2}}{c^2}\right) \ , \tag{19}$$

here r^b is the beam velocity before focusing and is approximately equal to the diode radius of 10 cm. In the case of $r^a = 5$mm, the value of $B_{\text{applied}} \Delta z$ is 10^{-2} Tesla·m. In the case investigated in Sec. 2, we chose the applied magnetic field such as $B_{\text{applied}} \Delta z = 4 \times 10^{-2}$ Tesla·m and the simulation resulted that beam was

focused well.

In the case of non-applied magnetic field, the results of the simulation are shown in Figs. 13 and 14. In this Section, the background is assumed to be a 3-Torr Argon Plasma. It can be found that the rippling occurs after the focal spot. The focused-beam intensity increases only up to 50 TW/cm^2 and This rippling may trigger instabilities. According to the stability analysis[9], non-rotating beams confined by the self-magnetic field are subject to Sausage instability.

In the case of $B_{applied}\Delta z = 0.1$ Tesla·m, the results are shown in Figs. 15 ~ 18. After the particles pass through the applied field, they have too large rotational velocity. Because the centrifugal force becomes large coming near the center, the particles are deflected. Therefore, there is the optimum strength of the applied magnetic field and $B_{applied}\Delta z \sim 0.04$ Tesla·m is the most suitable for the beam focusing.

6. Conclusion

By using the hybrid particle code, we could simulate the focusing and formation phenomena of a rotating and propagating LIB in the drift region. We assumed that the proton beam with the current density of 8 kA/cm^2, the rising time of 10 nsec, the beam radius of 10 cm and the local divergence angle of 30 mrad was injected into the drift region. When the density of the background plasma was 3 Torr and the magnetic field was applied such as $B_{applied}\Delta z = 0.04$ Tesla·m, we had the results of the beam maximum intensity of 108 TW/cm^2 and the beam minimum radius of 3.5 mm after focusing. Furthermore, the beam tended to the equilibrium state and propagated forming a rotating and propagating LIB configuration. The background of a Argon plasma which is heavier than a Hydrogen plasma, is suitable for the beam focusing to keep the density constant.

It is easy and highly efficient to extract intense proton beams, and there are a lot of advantages to a use proton beam. If the focusing experiments of a rotating and propagating proton beam, which have not made ever, coincide the simulation results of this paper, a proton beam is still promising candidate for

the energy driver of ICF.

References

1) K. Niu and S. Kawata: Fusion Tech. **11** (1987) 365.
2) J. P. VanDevender et al.: Laser and Particle Beams **3** (1987) 93.
3) D. J. Johnson et al.: J. Appl. Phys. **58** (1985) 12.
4) J. Maenchen et al.: Proc. 6th Intl. Conf. High Power Particle Beams, Kobe (1986) p.85.
5) J. P. VanDevender et al.: Laser and Particle Beams **5** (1987) 439.
6) P. F. Ottinger, D. Mosher and S. A. Goldstein: Phys. Fluids **23** (1980) 909.
7) K. Niu et al.: Proc. 14th Int. Symp. Rarefied Gas Dynamics, Tsukuba Science City, 1984, Vol. 2, p.1023.
8) T. Aoki and K. Niu: Laser and Particle Beams 5 (1987) 481.
9) T. Aoki and K. Niu: J. Phys. Soc. Jpn. **56** (1987) 3525.
10) A. Mankofsky, R. N. Sudan and J. Denavit: J. Comp. Phys. **70** (1987) 89.

Figure Captions

Fig. 1 Cross sectional view of the drift region. The dash lines mean the magnetic field lines and the mesh structure is used for the simulation.

Fig. 2 Time dependence of the incident beam current density and the beam particle density.

Fig. 3 Temporal variations of the beam-ion map in the focusing process. Dots are the beam ions. (a) time=6.6 nsec, (b) time=9.9 nsec and (c) time=13.2 nsec. After time=13.2 nsec, the beam-ion maps are almost same as (c). The background-plasma pressure is 20.0 Torr (273K).

Fig. 4 Spatial variations of the beam emittances along the z-direction. (a) z=7.0 cm, (b) z=18.0 cm, (c) z=23.0 cm, (d) z=26.0 cm, (e) z=28.5 cm and (f) z=31.0 cm.

Fig. 5 Map of the beam ions near the focal spot at time=26.4 nsec. The background-plasma pressure is 3.0 Torr.

Fig. 6 Beam emittance at z=30.0 cm. The background-plasma pressure is 3.0 Torr.

Fig. 7 Beam steering angle versus axial position of the drift region at time=26.4 nsec.

Fig. 8 Rotation Ratio versus axial position at time=26.4 nsec.

Fig. 9 Map of the beam ions near the focal spot at time=26.4 nsec. The background-plasma pressure is 1.0 Torr.

Fig. 10 Beam emittance at z=30.0 cm. The background-plasma pressure is 1.0 Torr.

Fig. 11 Beam steering angle versus axial position of the drift region at time=26.4 nsec. The background-plasma pressure is 1.0 Torr.

Fig. 12 Rotation Ratio versus axial position at time=26.4 nsec. The background-plasma pressure is 1.0 Torr.

Fig. 13 Map of the beam ions near the focal spot at time=26.4 nsec. There is no applied magnetic field in the drift region.

Fig. 14 Beam steering angle versus axial position of the drift region at time=26.4 nsec without applied magnetic field.

Fig. 15 Map of the beam ions near the focal spot at time=26.4 nsec in the case of $B_{applied}\Delta z=0.01$ Tesla·m.

Fig. 16 Beam emittance at $z=30.0$ cm in the case of $B_{applied}\Delta z=0.01$ Tesla·m.

Fig. 17 Beam steering angle versus axial position of the drift region at time=26.4 nsec in the case of $B_{applied}\Delta z=0.01$ Tesla·m.

Fig. 18 Rotation Ratio versus axial position at time=26.4 nsec in the case of $B_{applied}\Delta z=0.01$ Tesla·m.

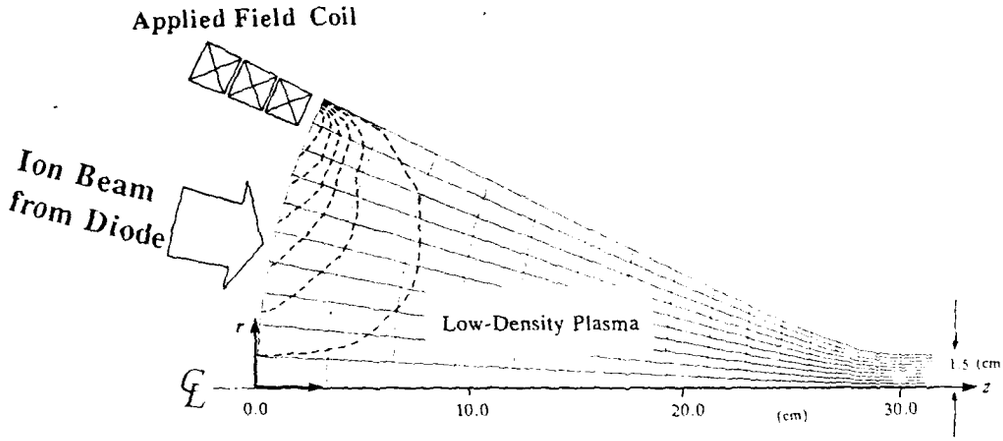
Applied Field Coil
Ion Beam
from Diode
Low-Density Plasma
r
z
0.0
10.0
20.0
(cm)
30.0

Fig. 1

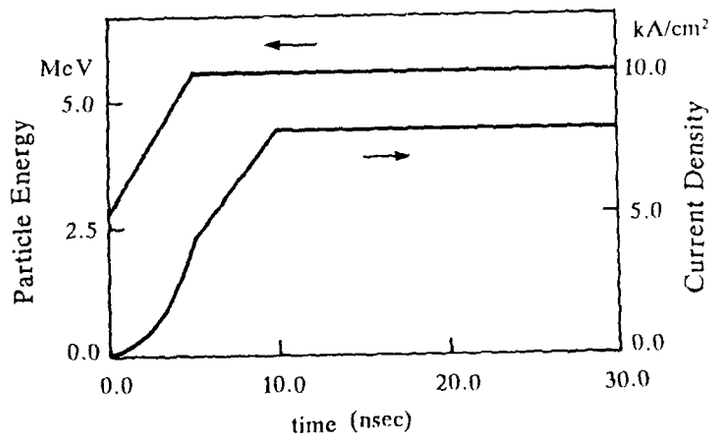
MeV
5.0
2.5
0.0
Particle Energy
kA/cm²
10.0
5.0
0.0
Current Density
0.0
10.0
20.0
30.0
time (nsec)

Fig. 2

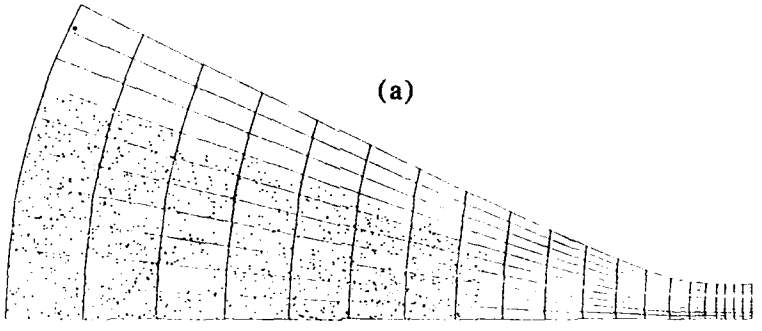

time = 6.6 (nsec)

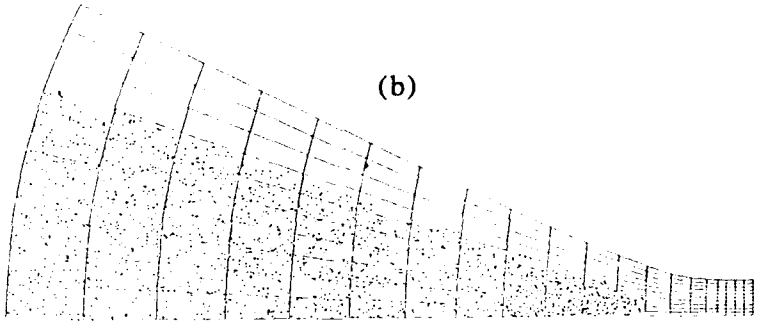

time = 9.9 (nscc)

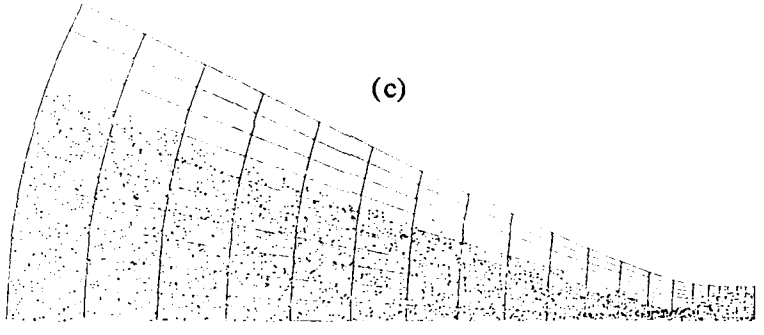

time = 13.2 (nsec)

Fig. 3

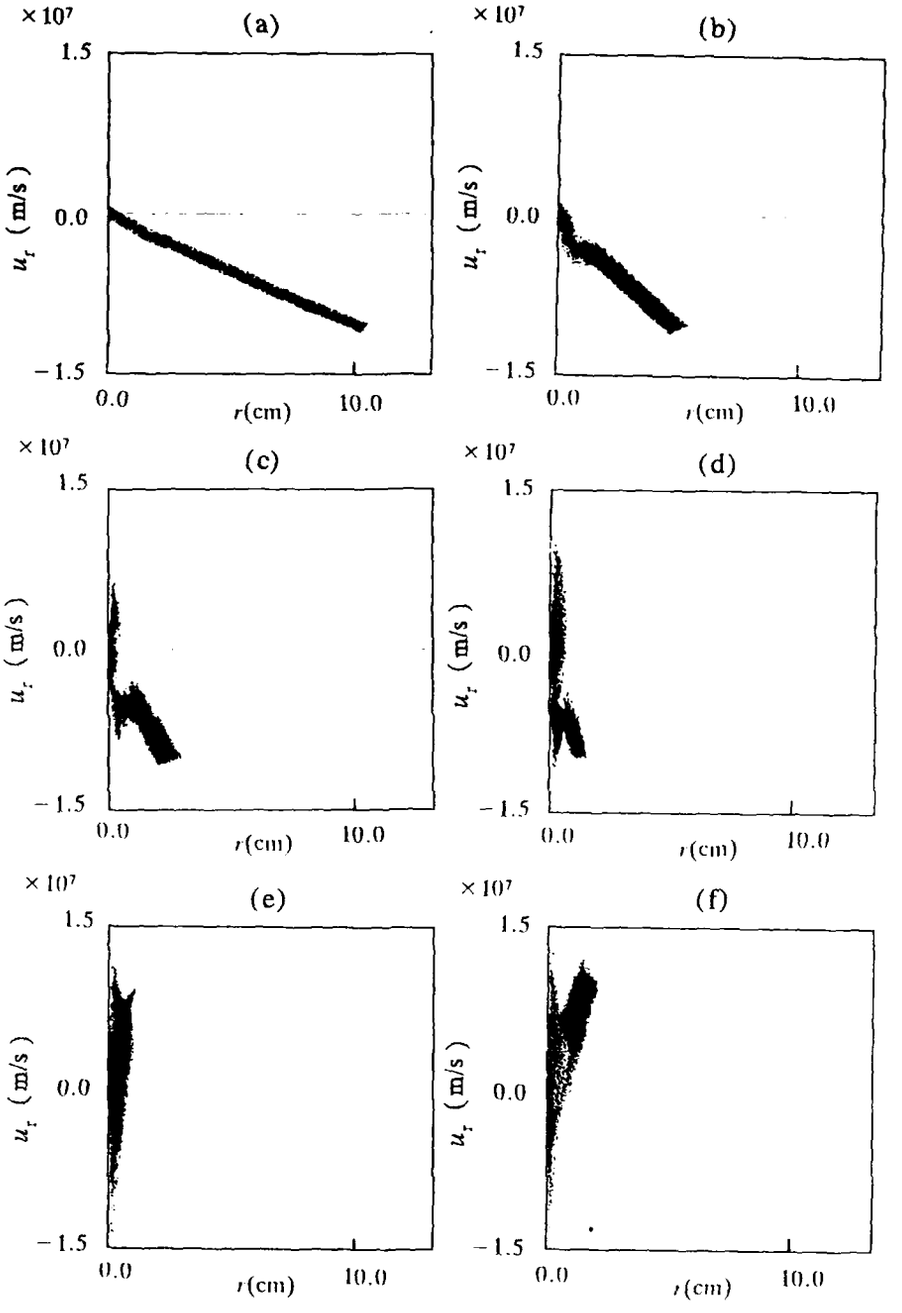

Fig. 4

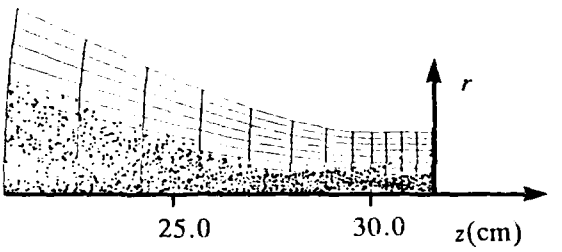

Fig. 5

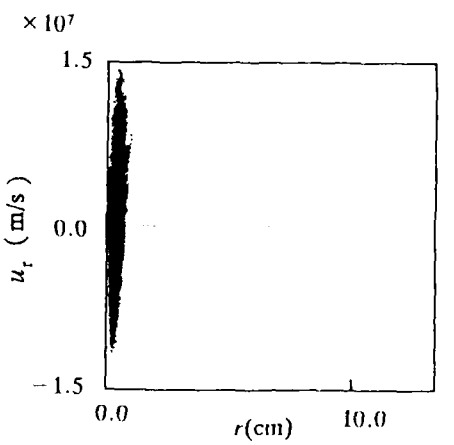

Fig. 6

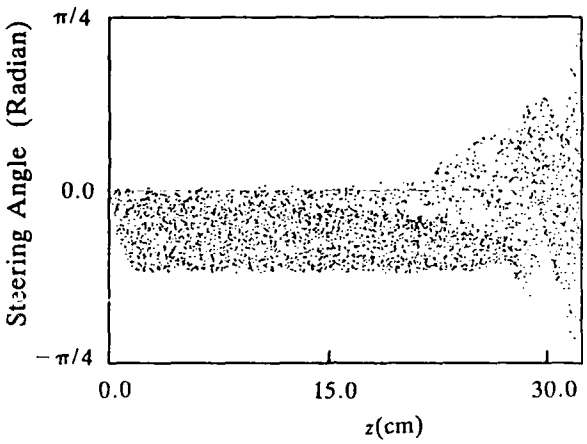
π/4
0.0
−π/4
Steering Angle (Radian)
0.0
15.0
30.0
z(cm)

Fig. 7

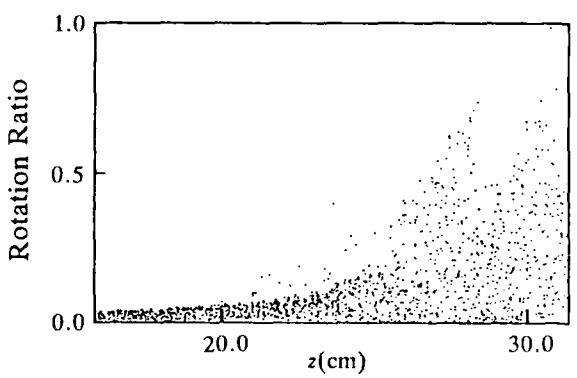
1.0
0.5
0.0
Rotation Ratio
20.0
30.0
z(cm)

Fig. 8

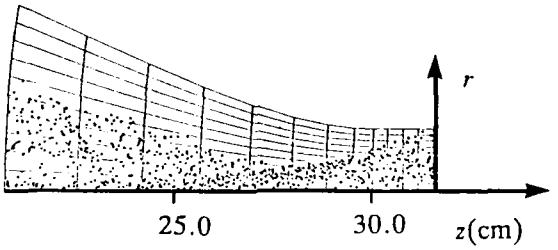

Fig. 9

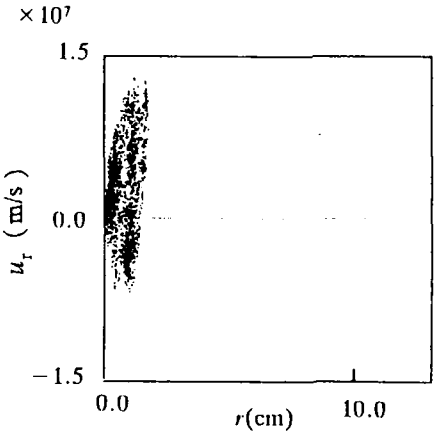

Fig. 10

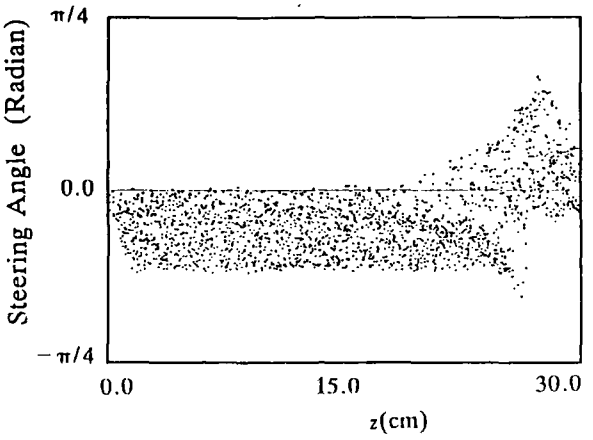
π/4
0.0
−π/4
Steering Angle (Radian)
0.0
15.0
30.0
z(cm)

Fig. 11

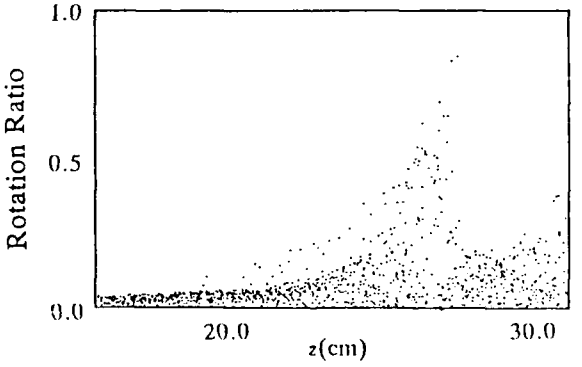
1.0
0.5
0.0
Rotation Ratio
20.0
30.0
z(cm)

Fig. 12

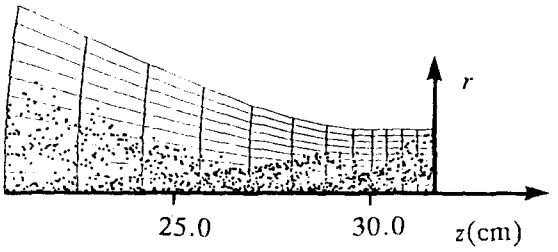

Fig. 13

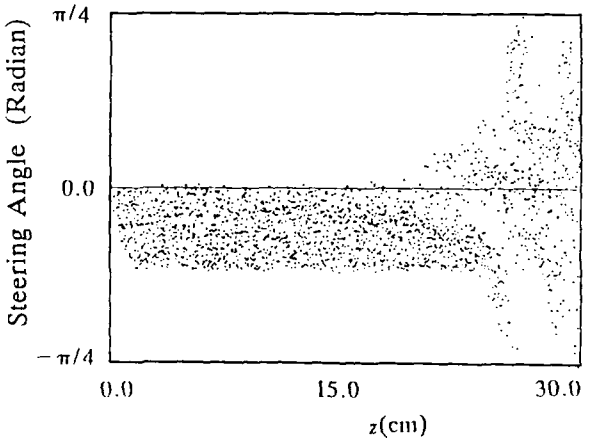

Fig. 14

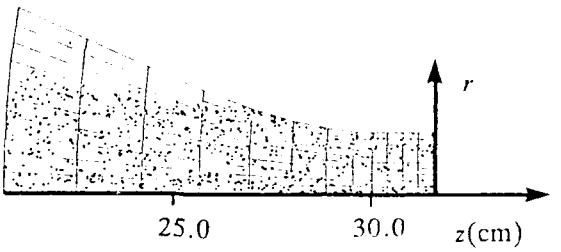

Fig. 15

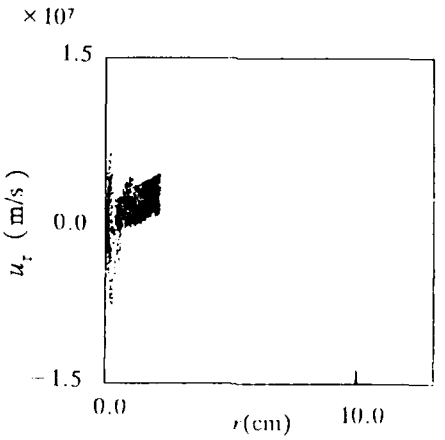

Fig. 16

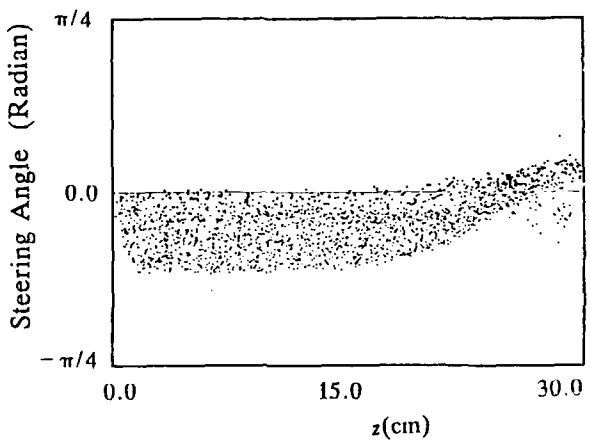
π/4
0.0
−π/4
Steering Angle (Radian)
0.0
15.0
30.0
z(cm)

Fig. 17

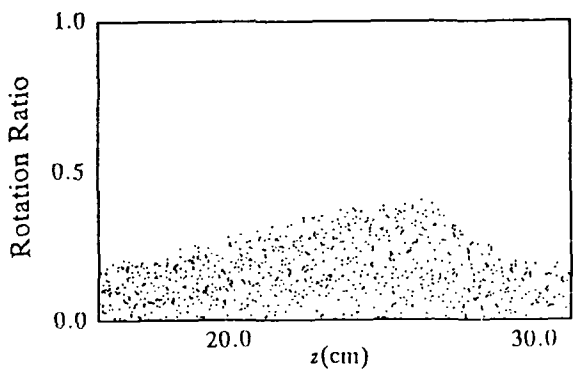
1.0
0.5
0.0
Rotation Ratio
20.0
30.0
z(cm)

Fig. 18

Elctron Current Effect on Stability of Plasma Channel

Tomokazu Kato and Tetsuya Ishimoto
Depertment of Applied Physics, School of Science and Engineering
Waseda University, Ohkubo 3-Chome, Shinjuku-ku, Tokyo, 160

§1. Abstract

We investigate the density profile of each species when the beam propagates in a plasma channel. Assuming the cylindrical symmetry and uniformity in the z-direction for the ion beam and the plasma channel, the profile depends only on the radial distance from the axis of symmetry. We treat the channel ion is at rest, and there are two flow in the channel, electron return current and beam flow. They build the magnetic field. Only this field contributes to the density profile because of charge neutrality. We consider the two cases, one is that the pressure balances with Lorentz force (in equilibrium) and the other is that the profile is constant (before equilibrium). So the considerable combination of the electron and the beam profile is as follows. (1) Both the ion beam and the electron current are in equilibrium. (2) The ion beam is in equilibrium and the electron density profile is constant. (3) The beam density profile is constant and the electron is in equilibrium. (4) Both profiles are constant. Case (1) is mentioned by Bennett[1], and case (4) by Alfven[2]. Then we investigate case (2) and (3) in Sec.§2. In Sec.§3, we discuss the validity of the assumption of thermal equilibrium.

§2. Analysis of the density profile

We first consider case (2). As the beam is in thermal equilibrium, the profile is given by the Boltzmann factor. Ampere's law, expressed in terms of the z component of vector potential A , is written as follows,

$$\frac{\partial^2 A_z}{\partial r^2} + \frac{1}{r}\frac{\partial A_z}{\partial r} = -\frac{4\pi e V_b}{c} n_{b0} \exp\left(\frac{eV_b A_z}{T_b c}\right) + \frac{4\pi e n_e V_e}{c} \qquad (1)$$

We assume $eV_b A_z / cT_b \ll 1$ and expand the exponential into the

Taylor series up to the second terms. The linearized equation is

$$\frac{\partial^2 A_z}{\partial r^2} + \frac{1}{r}\frac{\partial A_z}{\partial r} + \frac{V_b^2}{c^2}\frac{1}{\lambda_b^2}A_z = \frac{4\pi e n_b(0) V_b}{c}(\alpha - 1) \qquad (2)$$

where α is the fraction of current neutralization ($n_e V_e = \alpha n_b V_b$, $0 < \alpha < 1$) and λ_b is the Debye length defined on the ion beam ($\lambda_b = \left(\frac{T_b}{4\pi n_b(0) e^2}\right)^{1/2}$). The solution of Eq.(2) is

$$A_z(r) = \frac{cT_b}{eV_b}(1-\alpha)\left\{J_0\left(\frac{V_b}{c}\frac{1}{\lambda_b}r\right) - 1\right\} \qquad (3)$$

and

$$n_b(r) = n_b(0)\left\{J_0\left(\frac{V_b}{c}\frac{1}{\lambda_b}r\right) + \alpha\left(1 - J_0\left(\frac{V_b}{c}\frac{1}{\lambda_b}r\right)\right)\right\} \qquad (4)$$

From the assumption of charge neutrality, the beam charge density cannot change rapidly in the channel. Hence the argument of Bessel function is restricted within small region, and we expand J_0 to the second term. Then Eq.(4) becomes

$$n_b(r) = n_b(0)\left\{1 - (1-\alpha)\frac{1}{4}\frac{V_b^2}{c^2}\frac{r^2}{\lambda_b^2}\right\} \qquad (5)$$

The only requirement for the validity of the present treatment is

$$(1-\alpha)\frac{1}{4}\frac{V_b^2}{c^2}\frac{a^2}{\lambda_b^2} < 1 \qquad (6)$$

where a is the channel radius.

This method is similarly applied to case (3). In this case the electron density profile (corresponding to Eq.(5)) is

$$n_e(r) = n_e(0)\left\{1 + \left(\frac{1}{\alpha} - 1\right)\frac{1}{4}\frac{V_e^2}{c^2}\frac{r^2}{\lambda_e^2}\right\} \qquad (7)$$

where λ_e is the electron Debye length of the plasma channel. The condition, corresponding to Eq.(6), is

$$\left(\frac{1}{\alpha} - 1\right)\frac{1}{4}\frac{V_e^2}{c^2}\frac{a^2}{\lambda_e^2} < 1 \qquad (8)$$

§3. Conclusion

We consider the parameter of ICF using LIB experiment: $n_e=10^{18}$ cm^{-3}, $n_b=10^{16}$ cm^{-3}, T_b=0.1MeV, T_e=10eV, $V_b=4.4*10^9$ $cm\ s^{-1}$, a=0.5 cm. The condition of Eq.(6) requires $\alpha > 0.996$, and Eq.(8) requires $\alpha \leq 1$. Hence, in the plasma channel of LIB experiment, the assumtion of thermal equilibrium does not be valid, unless current is fully neutralized. A similar quantity to Debye length in electric charge distribution does not play a role in the magnetic interaction between electric currents.

References

1) W.H.Bennett: Phys.Rev **45** (1934) 890

2) H.Alfven: Phys.Rev **55** (1939) 425

NUMERICAL SIMULATION FOR PARTICLE ACCELERATION AND TRAPPING BY AN ELECTROMAGNETIC WAVE

Shigeo KAWATA, Masami MATSUMOTO and Yukio MASUBUCHI
Faculty of Engineering, The Technological University of Nagaoka,
Kamitomioka, Nagaoka 940-21, Niigata, Japan

Abstract

The interaction between particles and an electromagnetic (EM) wave is investigated numerically in the system of particle V_pxB acceleration by the EM wave. Numerical simulations show that the particle acceleration mechanism works well in the case of the appropriate number density of the imposed particles. When the interaction between particles and the wave is too strong, a part of the trapped and accelerated particles is detrapped. A condition is also presented for the efficient particle acceleration and trapping by the EM wave.

1. Introduction

Recently many researches have been done for the high energy particle acceleration[1] based on the electrostatic wave and the electromagnetic one. For example, the particle acceleration has been studied by using an electrostatic wave propagating perpendicular to a static magnetic field (B_0) theoretically[2,3] and experimentally[4].

In addition, another type of particle acceleration has been proposed in these days by using an electromagnetic (EM) wave propagating perpendicular to B_0[5,6]. In the references of 5 and 6 the basic idea for the mechanism of particle acceleration by an EM wave was presented by a simple analysis.

Following the proposal[5,6], this paper shows a further investigation about the interaction between the particles and the EM wave in the mechanism of the particle acceleration and trapping by an EM wave perpendicular to B_0. In the situation as shown in Fig.1, electrons introduced near the B_z=0 point (or sheet) of A, can be trapped in the x direction by the magnetic force of $-e/cV_yB_z$. In addition, near the B_z=0 sheet the trapped electrons feel the electric field of the EM wave to be accelerated in the -y direction. First the mechanism of particle acceleration and trapping is checked by a particle simulation[7]. Then the particle-wave interaction is discussed: the numerical simulation presents that the detrapping of the trapped particles occur when the interaction is strong. Finally a condition is also discussed for the efficient particle acceleration and trapping in the mechanism.

2. Interaction between electrons and an EM wave

The purposes of this paper are to check the mechanism and to clarify the particle-wave interaction in the system. For those purposes one-dimensional numerical simulations are performed. The used code is an particle-in-cell (PIC) code and is just the same with the ZOHAR code[7]. The Maxwell equations and the relativistic equation of motion are solved in the code. As is described in the references 5 and 6, the EM wave must be a slow one in order for particles to couple with the wave. The slow wave is realized by a wave guide with a dielectric presented in the references 5 and 6. In the simulation the slow wave is introduced by changing the dielectric constant in the Maxwell equations. For our purposes this approximation or technique in the simulation is enough accurate.

In this paper the wave speed is 0.85xc. Here c is the light speed. The dielectric constant is 1.38. The magnitude of the electric field E_y is $2.73\times10^4/(\lambda\ (cm))$ volt/cm and λ the wave length in cm. The applied magnetic field (B_{zapp}) is small compared with the wave magnetic field (B_{z0}) by the factor of 6.9, that is $B_{zapp} = B_{z0}/6.9$. The averaged velocity of imposed electrons is 0.85c in the x direction and -0.2c in the y direction (see Fig. 1). The electrons are distributed uniformly in the real space. In the velocity space the electrons are distributed by the Maxwell distribution function with the temperature of 5.45 kev. In the paper only the electrons are movable. The number density of imposed electrons is a changeable parameter. The employed boundary condition in the simulation is the cyclic one.

Figures 2 show one of the simulation results in the case of $1\times n_0$ of the electron number density, where n_0 is $5.58\times10^8/(\lambda^2 cm))\ cm^{-3}$. The initial condition is presented in Fig.2-1: Fig.2-1-a shows the distribution function versus the momentum in

the y direction, Fig.2-1-b the diagram of the relativistic factor versus the real space x, Fig.2-1-c the electron map in the momentum space and Fig.2-1-d the space profiles of electric and magnetic fields (E_y and B_z). In each figures the trapping and B_z=0 point (sheet) is indicated by an arrow. Figure 2-2 presents a rather beginning stage of particle trapping and acceleration. A part of introduced particles starts to be trapped by the magnetic field and accelerated by the electric field. Figure 2-3 shows the efficient acceleration of electrons. In this case the energy of the EM wave is large significantly compared with the particle one. This simulation results show that the trapping and acceleration mechanism by an EM wave works well.

Figures 3 present other results for the case of the higher density of $5xn_0$. Other initial conditions are the same with those in the former case. Figure 3-1 shows that a part of electrons is trapped and accelerated like in the Fig.2. But Fig.3-2 presents that the acceleration efficiency is lower than that in the former case. In addition the back ground particles are also accelerated. Figure 3-2 also shows that the trapped particles start to be detrapped. In this case the EM wave has not so large energy compared with the particle energy as shown in Fig.4 because of the higher density of electrons. Figure 4 shows the time sequences of the wave and particle energies, and that the particles gain the wave energy as the increase of time. Near the detrapping time, that is 2000 in the normalized time, the wave looses its energy much. Figures 5 and 6 show the profiles of magnetic field B_z and electric one E_y, respectively for the case. The decrease of electric field E_y is significant at the trapping region. At the later time the electric field is nearly zero at the trapping region. Therefore the trapped particle can not be accelerated any more at the later time in this case (see Fig.3).

The density profiles are shown in Fig.7 for the case of $1xn_0$ and $5xn_0$ at the normalized time 2000. In the figure the density is normalized by the initial density. As shown in the figure the density of the trapped particles is higher than the initial one because of the bunching or focusing effect by the magnetic field as is expected. In addition Fig.7 presents that the density peak moves to the -x direction in the case of the higher density. The wave propagates to the +x direction. This fact means the start of the detrapping in the case of the higher density of electrons. It is clear from the numerical results shown in Fig.3-2. The reason why the detrapping occurs, comes from the self electric field of the beam in the x direction. In the simulation the Maxwell equation is solved even in the x direction in order to include the self electric field of the beam. Roughly the electric field E_x is estimated by the Maxwell equation as the following:

$$\delta E_x \simeq -4\pi J_x \delta t, \tag{1}$$

where t is the acceleration time interval. If the relation

$$|\delta E_x| < |v_y B_z/c| \tag{2}$$

is violated, the trapping force disappears in the x direction and the trapped particles start to be detrapped. Therefore the trapping condition becomes

$$n_{trap}\delta t < 1/(4\pi q\, c)\ (v_y/v_x)\ B_z. \tag{3}$$

Here n_{trap} is the trapped-particle number density. For the efficient trapping and acceleration of particles, this condition must be kept. Actually the simulation results show that the detrapping occurs at the higher density than $3 \sim 5x10^9/(\lambda^2(cm))$

cm^{-3} at the normalized time 2000 for our case. The estimated condition shows that $n_{trap} < 4.65 \times 10^9 / (\lambda^2(cm))\ cm^{-3}$. We believe that the condition (3) is a good estimation for the efficient particle acceleration and trapping.

In addition to these results there is another remarkable feature in the computed results. That is the acceleration of the untrapped background particles in the case of the higher density, as shown in Fig.3. The result is explained by using Fig.8. Figure 8 shows the fourier components of E_y. Only the basic component and the k=0 (or flat) one are presented in Fig.8. The flat component appears from the particle-wave interaction as shown in the figure. The background particles moves through the wave in the x direction and feel the flat component of E_y. Then they are accelerated by it. On the other hand the acceleration of the trapped particles is saturated, because the electric field becomes zero at the trapping region as shown in Fig.6.

3. Discussions

The interaction between particles and the wave is studied in this paper by the numerical simulations. The numerical analyses show that the mechanism of the particle acceleration and trapping by an EM wave works well. The condition is also derived for the efficient particle acceleration and trapping.

In the real situation a slow mode of elctromagnetic wave is realized by the dielectric material presented in the references 5 and 6, and the actual structure of the wave fields is slightly different from one which is employed in the analyses of this paper. In order to simulate such the complicated structure, we need the simulation in the multi dimension. In addition particles move in the three-dimensional real space in the actual situation. But the multi dimensionality is not the essential

point in the system. The essential points are included in the analyses. This multi dimensionality will be included in the next work.

In the next stage of the analyses we will also work on parameter study in order to find the optimal parameter values for the efficient particle acceleration by an EM wave and the application to the ion acceleration in the near future.

Acknowledgement

This work is partly supported by the cooperation program of Institute of Plasma Physics at Nagoya University. Authors would like to present the acknowledgement to Dr. Takashi Yabe at Osaka University for his great help, to Dr. Satoshi Takeuchi at Yamanashi University and Prof. Ryo Sugihara at Nagoya University for their fruitful discussions. The authors also would like to express our thanks to Prof. Keishiro Niu for his invitation to this symposium from our deep mind.

References

1)IEEE Trans. on Plasma Science PS-15, (1987).
2)J. M. Dawson, V. K. Decyk, R. W. Huff, I. Jechart, T. Katsouleas, J. N. Leboeuf, B. Lembege, R. M. Martinez, Y. Ohsawa ans S. T. Ratliff, Phys. Rev. Lett. 50, 1455(1983).
3)R. Sugihara and Y. Midzuno, J. Phys. Soc. Japan 47, 1290(1979). R. Sugihara, S. Takeuchi, K. Sakai and M. Matsumoto, Phys. Rev. Lett. 52, 1500(1984).
4)Y. Nishida, M. Yoshizumi and R. Sugihara, Phys. Lett. A 105, (1984).
5)S. Takeuchi, K. Sakai, M. Matsumoto and R. Sugihara, Phys. Lett. A 122, 257(1987).
6)S. Takeuchi, K. Sakai, M. Matsumoto and R. Sugihara, IEEE Trans. on Plasma Science PS-15, 251(1987).
7)A. B. Langdon and B. F. Lasinski, Meth. Comp. Physics 16, 327.

Figure captions

Fig. 1

Mechanism of the particle trapping and acceleration by an electromagnetic wave. A static magnetic field is applied so that there is a finite electric field at the point A (B_z=0). Near the point A the magnetic field acts to trapp electrons. The electric field accelerates the trapped electrons.

Fig. 2

Simulation results in the case of electron number density of $1xn_0$, here n_0 is $5.58x10^8/(\text{wave length } \lambda(\text{cm}))^2$ cm^{-3}. Figure 2-1 shows the initial state, in which Fig. 2-1-a shows the distribution function veresus the momentum in the y direction, Fig. 2-1-b the diagram of the relativistic factor versus the real space X, Fig. 2-1-c the electron map in the momentum space and Fig. 2-1-d the space profiles of electric and magnetic fields. Figure 2-2 shows a rather beginning stage of the trapping and acceleration. A part of electrons starts to be trapped and accelerated. Figure 2-3 shows the efficient acceleration. In this case the wave energy is much larger than the particle one.

Fig. 3

Result for the case of $5xn^0$. Figures show the acceleration efficiency is lower than that in Fig.2. Figure 3-2 shows that a part of trapped electrons start to be detrapped and the back ground particles are also accelerated.

Fig. 4

Time sequences of the wave and particle energies for the case in Fig. 3.

Fig. 5

Profiles of magnetic field at the times of 0, 600 and 1600 for the case shown in Fig. 3.

Fig. 6

Profiles of electric field at the times of 0, 600 and 1600 for the case shown in Fig 3.

Fig. 7

Density profiles for the cases of $1xn_0$ and $5xn_0$ at time 2000. The indicated density is normalized by the initial one. The trapped particles are focused near the trapping point by the magnetic field. The peak of density moves to the -x direction in the case of the higher density. For the case of higher density the plotted state is at just the detrapping time. The detrapping comes from the induced electric field E_x in the x direction. At the time of the detrapping the electric force by the induced electric field starts to overcome the trapping force by the magneitic field.

Fig. 8

Fourier component of E_y. Only the basic and k=0 components are presented. By the k=0 component the back ground particles are accelerated as shown in Fig.3-2.

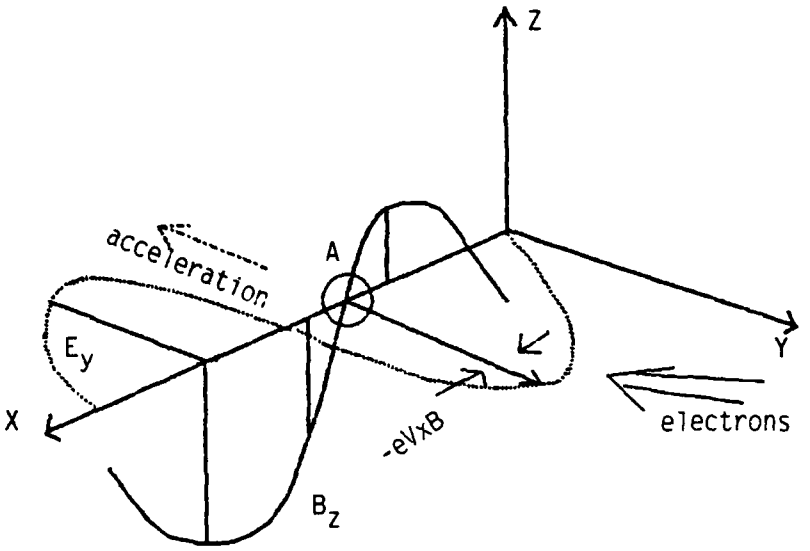

Fig. 1 Mechanism of the particle trapping and acceleration by an electromagnetic wave.

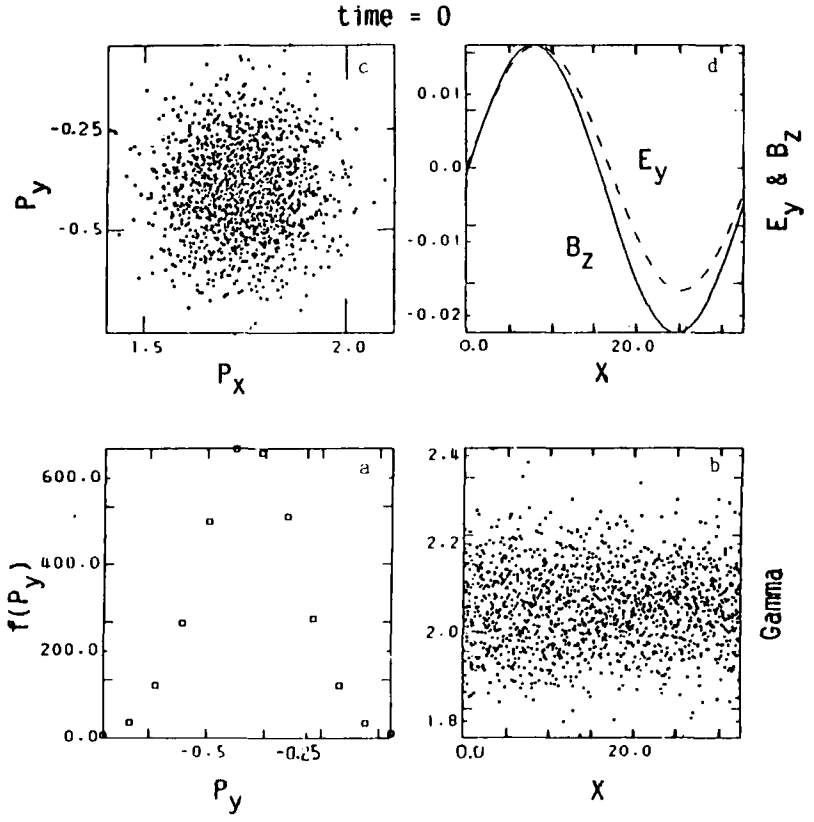
time = 0
c
d
a
b
P_y
P_x
E_y
B_z
E_y & B_z
X
$f(P_y)$
Gamma
0.01
0.0
-0.01
-0.02
-0.25
-0.5
1.5
2.0
0.0
20.0
600.0
400.0
200.0
2.4
2.2
2.0
1.8

Fig. 2-1

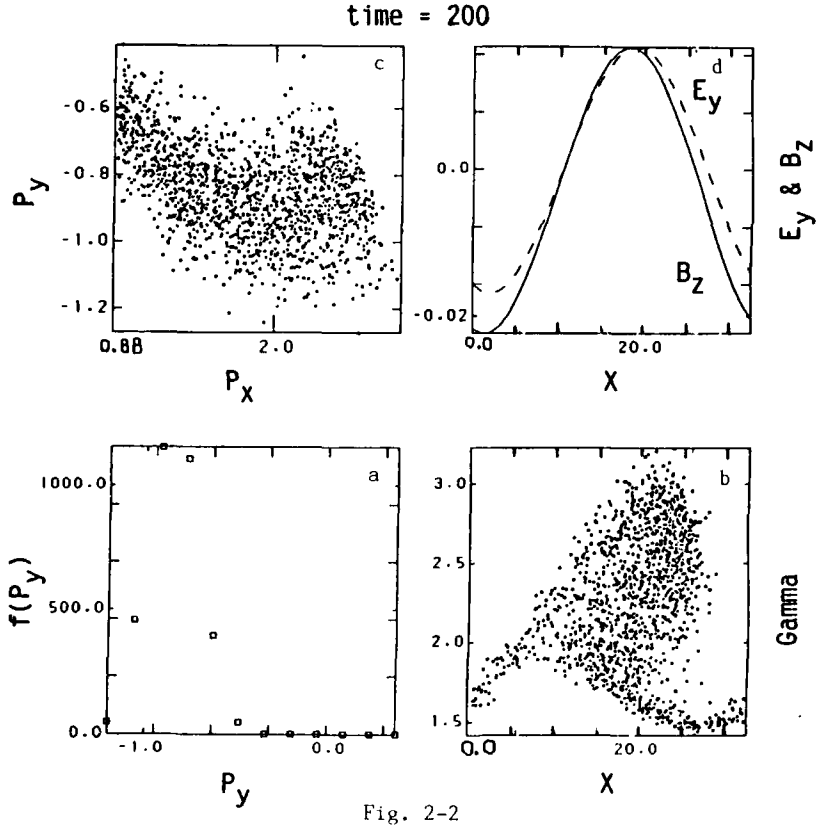
time = 200
c
-0.6
-0.8
-1.0
-1.2
P_y
0.88
2.0
P_x
d
E_y
B_z
0.0
-0.02
0.0
20.0
X
E_y & B_z
a
1000.0
500.0
0.0
$f(P_y)$
-1.0
0.0
P_y
b
3.0
2.5
2.0
1.5
0.0
20.0
X
Gamma

Fig. 2-2

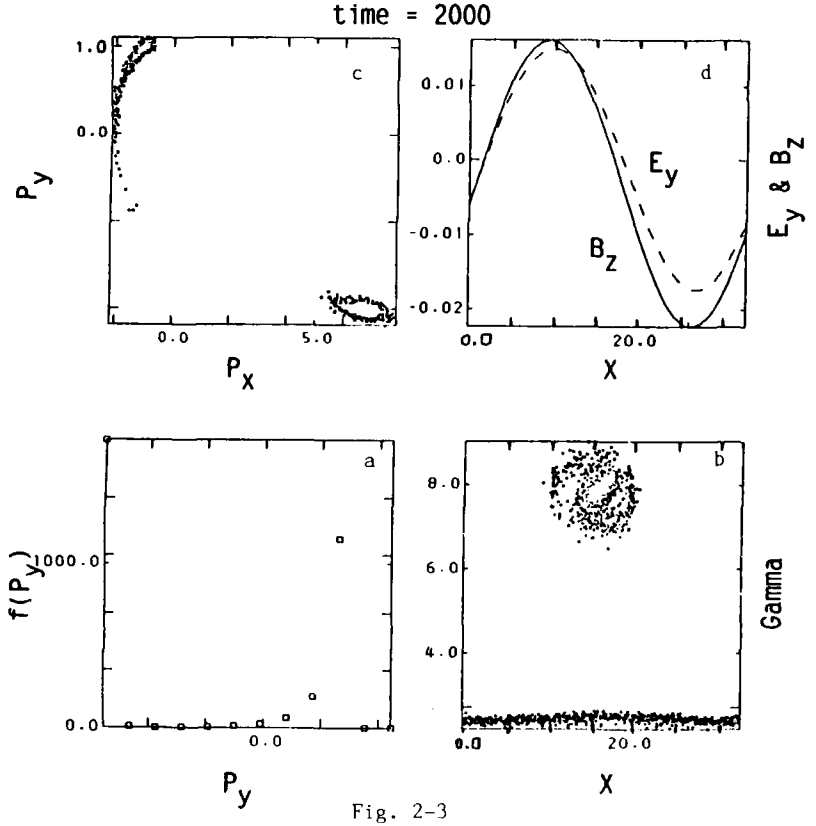
time = 2000
c
d
a
b
1.0
0.0
5.0
P_y
P_x
0.01
-0.01
-0.02
20.0
X
E_y
B_z
E_y & B_z
1000.0
$f(P_y)$
8.0
6.0
4.0
Gamma

Fig. 2-3

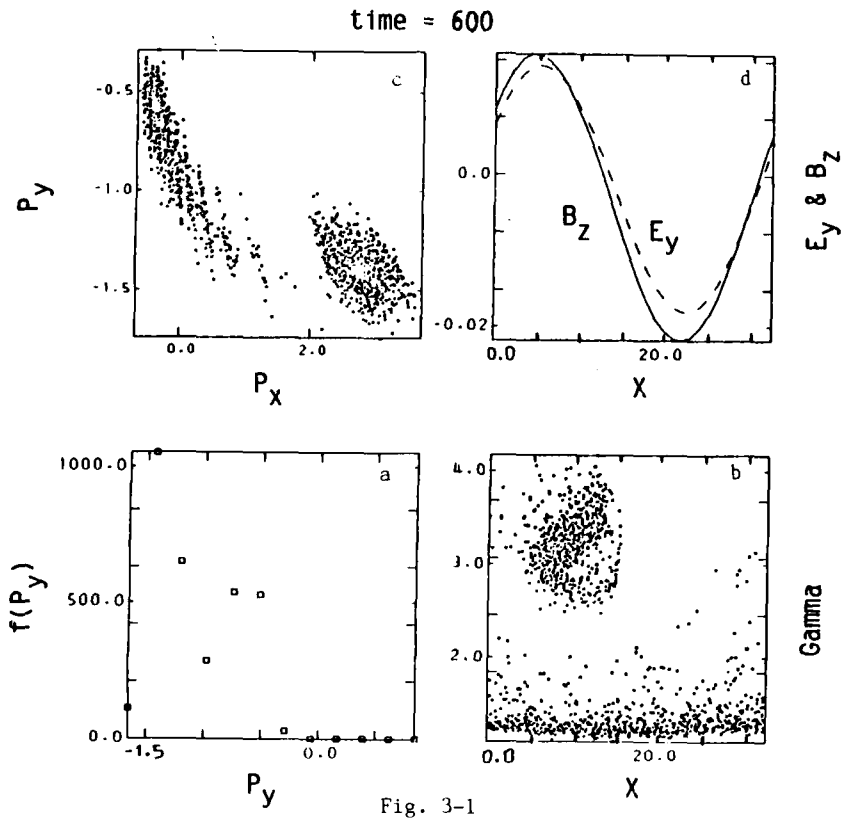
time = 600
c
d
a
b
P_y
P_x
B_z
E_y
E_y & B_z
X
$f(P_y)$
Gamma
-0.5
-1.0
-1.5
0.0
2.0
-0.02
20.0
1000.0
500.0
-1.5
4.0
3.0
2.0

Fig. 3-1

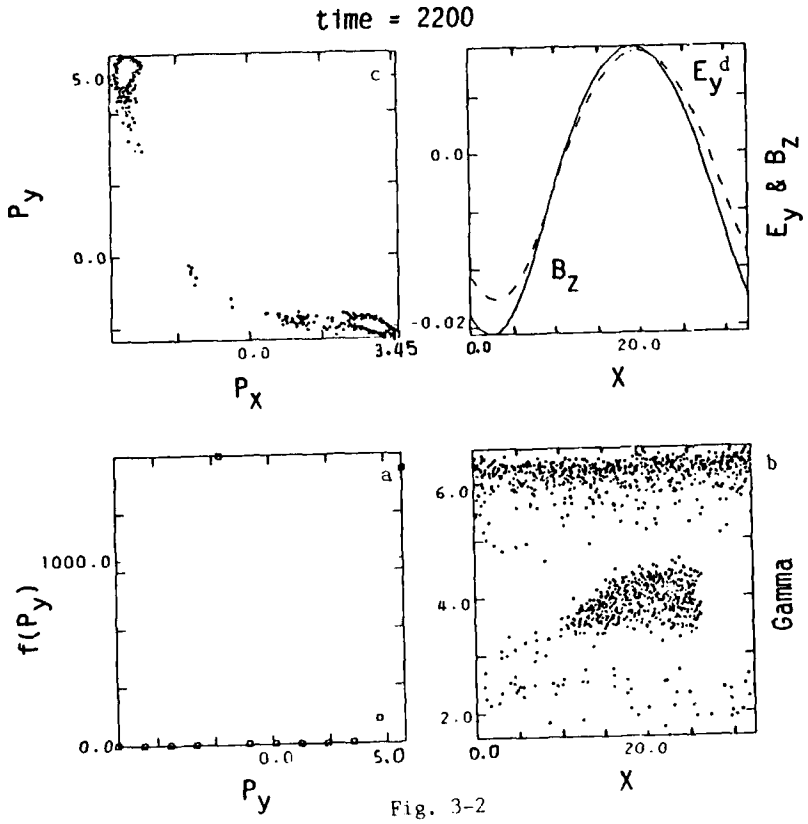
time = 2200
c
5.0
0.0
3.45
P_y
P_x
E_y^d
B_z
0.0
-0.02
0.0
20.0
X
E_y & B_z
a
1000.0
0.0
0.0
5.0
$f(P_y)$
P_y
b
6.0
4.0
2.0
0.0
20.0
X
Gamma

Fig. 3-2

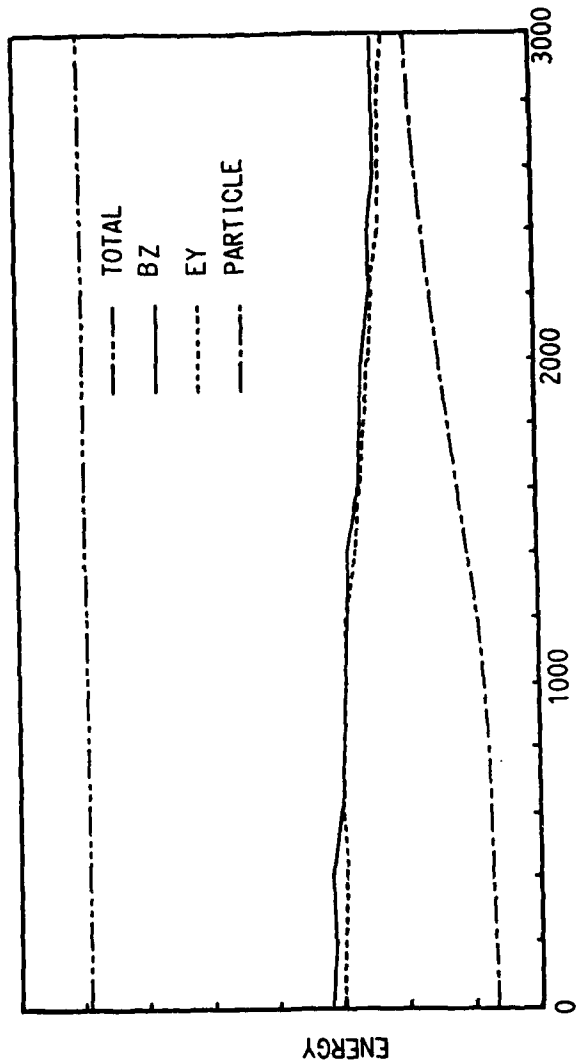

Fig. 4 Time sequences of the wave and particle energies.

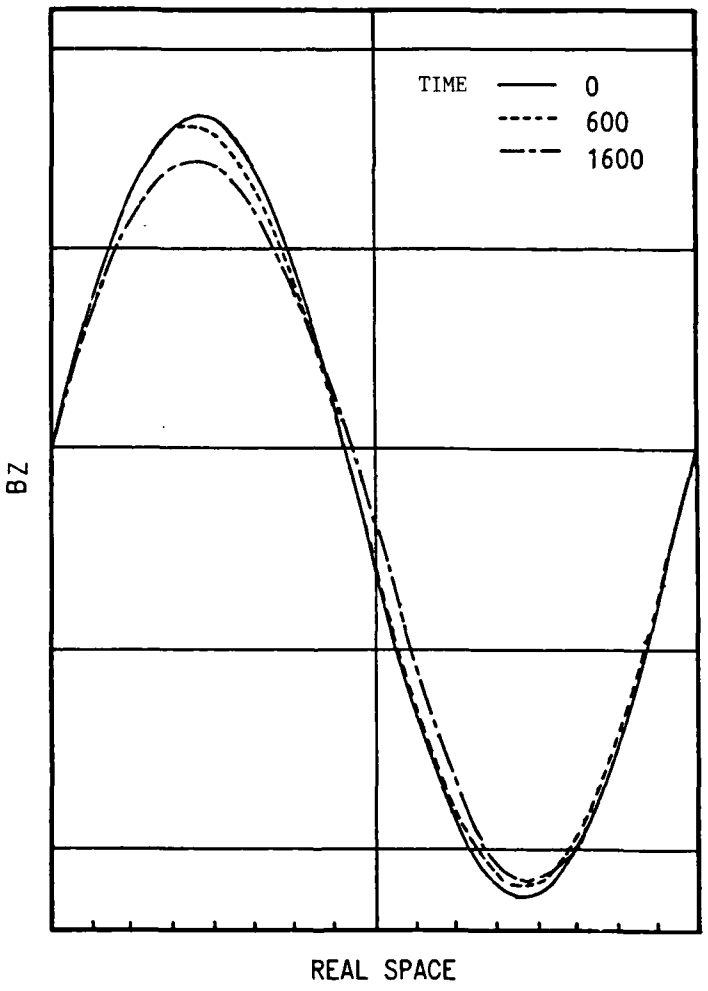

Fig. 5 Profiles of Magnetic field.

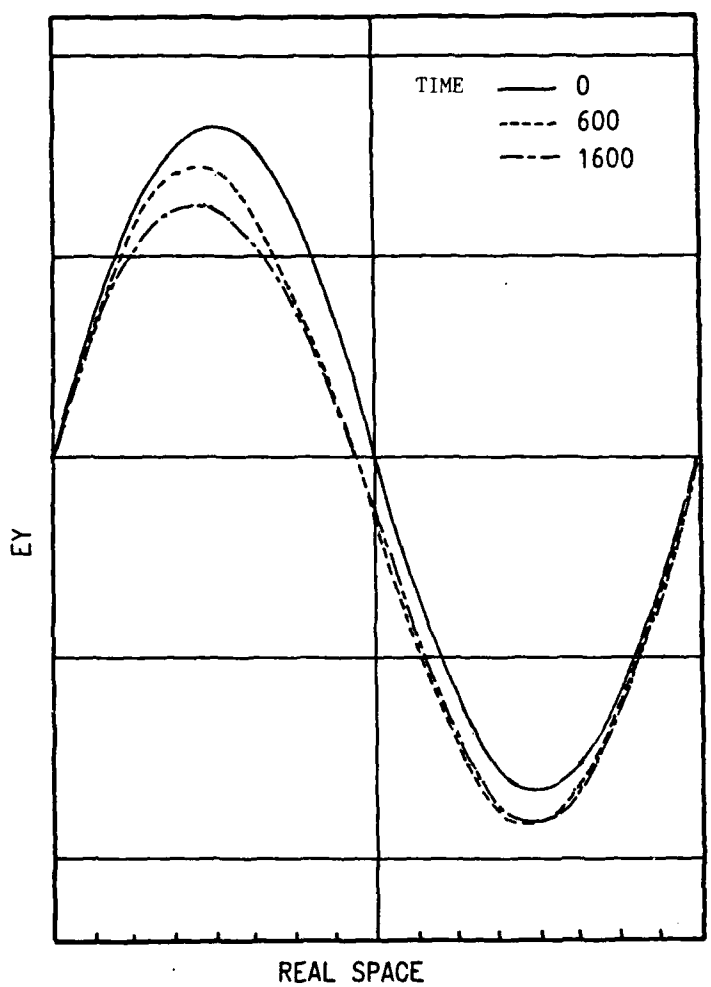

Fig. 6 Profiles of electric field E_y.

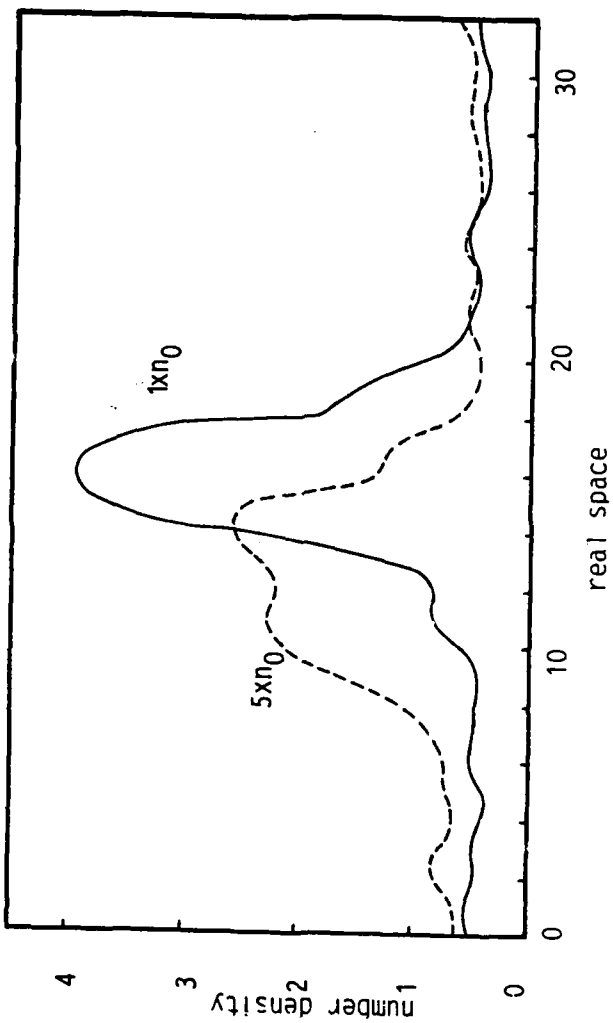

Fig. 7 Density profiles.

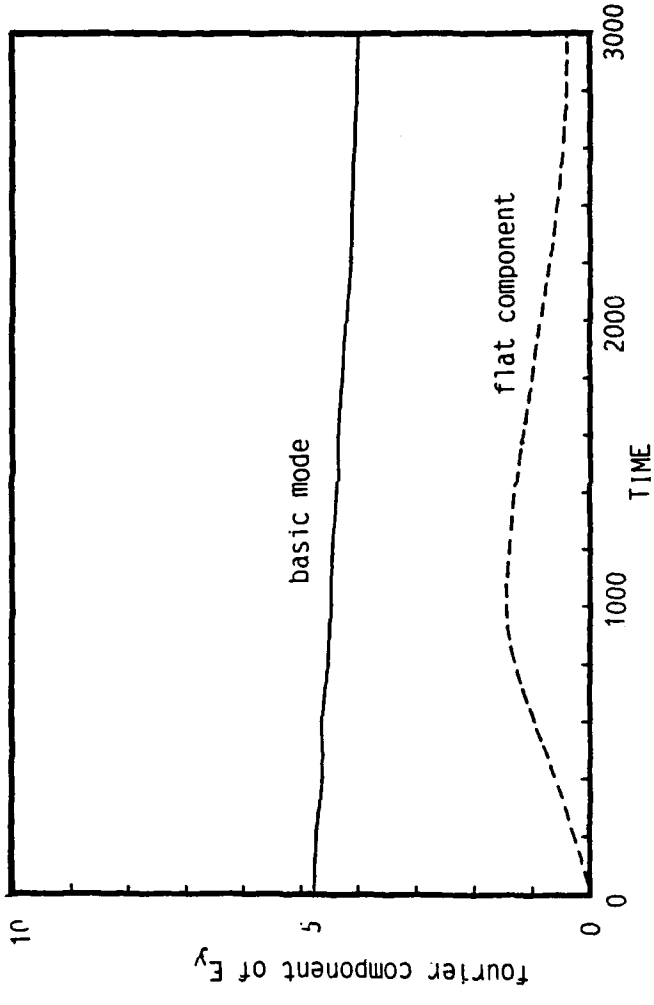

Fig. 8 Fourier components of E_y.

SIMULATION CODE FOR ICF INCLUDING RADIATIVE ENERGY TRANSFER

G. Velarde, J. M. Aragonés, J. J. Honrubia, J. M. Martínez-Val,
E. Mínguez, J. L. Ocaña, J. M. Perlado

Instituto de Fusión Nuclear (DENIM)
Universidad Politécnica de Madrid

ABSTRACT

New improvements in the atomic physics environment of our ICF code NORMA, together with new algorithms for radiation transport are presented. Using that code, results on LHAR targets of ILE are reported and compared with ILESTA and HISHO-1D codes.

LOW-Z OPACITY CALCULATIONS

The opacity calculations are divided in three parts. The first one is the computation of the atomic orbital quantities, such as: orbital populations, orbital energies and oscillator strengths, for each plasma condition. The second one is the calculation of the ion distributions occurring in the real plasma, which can be obtained via rate equations or by a binomial distribution [1]. Finally, the extinction coefficients (absorption plus scattering) for each ionic species are determined, using the formalism for bound-bound, bound-free and free-free transitions, and for the scattering processes.

The first step is the calculation of bound electron populations, orbital energies transition probabilities, effective charges and free electron densities for each plasma component. Besides, the atomic calculation will take into account the excited states and ground states, for each ionic state, that contribute to the extinction coefficient, according to their actual abundances in the plasma.

This level of calculation is performed by using average atom models (AA) or detailed configurations (DC). The second way is obtained after an AA calculation followed by a calculation of ion abundances through a binomial distribution.

In order to know the atomic structure and the atomic line transitions, the radial Dirac wave equation is solved, using a self-consistent central potential, which includes bound and free electron contributions. A Thomas-Fermi potential, externally calculated, can also be provided.

The frequency dependent photoabsorption coefficients versus density and temperature for each low-Z element, for about 2000 energy discrete

Paper presented at the Symposium on Physics of Target Implosion and Pulsed Power Techniques, Tokyo Institute of Technology, Tokyo (1987).

values can thus be determined. These coefficients weighted in an appropiate manner provide the multigroup opacities, which are employed in radiation transport codes.

Several of our previous works [2, 3] show the results for aluminium and other materials, which were found out by using the aforementioned methodology. By comparing these results with those from the Astrophysical Library [4], some small differences are observed in the Rosseland mean opacity for ranges of temperatures higher than 300 eV, but the differences are larger at lower temperatures.

These differences have been reduced when the following phenomena are taken into account: non-hydrogenic oscillator strength, collisional line broadening due to electrons besides the Doppler line broadening, and with the most detailed structure of the configurations in the real plasma.

To check these results, aluminium plasma at 100 eV and 0.187 $g.cm^{-3}$ has been selected, because at these plasma conditions the aluminium is not fully ionized.

In figures 1.a, b & c, the extinction profiles for the Astrophysical Library, and those for the AA model calculation and for the DC one are shown. Looking at the results, the AA model gives a rather good results in Rosseland mean opacity, although the extinction profile is not really reproduced, such as it is obtained with the use of DC.

HYDRODYNAMICS WITH MULTIGROUP RADIATION TRANSPORT.

Recently, we have developed a one-dimensional radiation-hydrodinamics code called SARA (Synthetically Accelerated Radiation Transport Algorithm) that includes the multigroup radiation capability. The main goals to write this code have been, first, to test the numerical techniques to be used in two-dimensional ICF codes and, second, to perform a more detailed analysis of the ICF capsules in a one-dimensional frame.

The radiation-hydrodynamics equations are solved following the time-splitting technique. In the first step, the hydro equations are solved by means of the Flux Corrected Transport (FCT) algorithm of Boris [5]. In the second step, the S_n multigroup radiation equation is solved by a second order positive scheme and the convergence of the radiation source is largely improved by a synthetic acceleration method [6, 7]. Finally, the electron conduction is advanced in the third step.

By this time-splitting procedure, the radiation transport equation is greatly simplified, resulting after time differencing and linearization the following equation for the specific radiation intensity

$$\Omega.\nabla I^{\ell+1/2}+\sigma_t I^{\ell+1/2}=\eta\chi(E)\int_0^\infty dE\sigma(E)I_0^{\ell}(E)+Q \qquad (1)$$

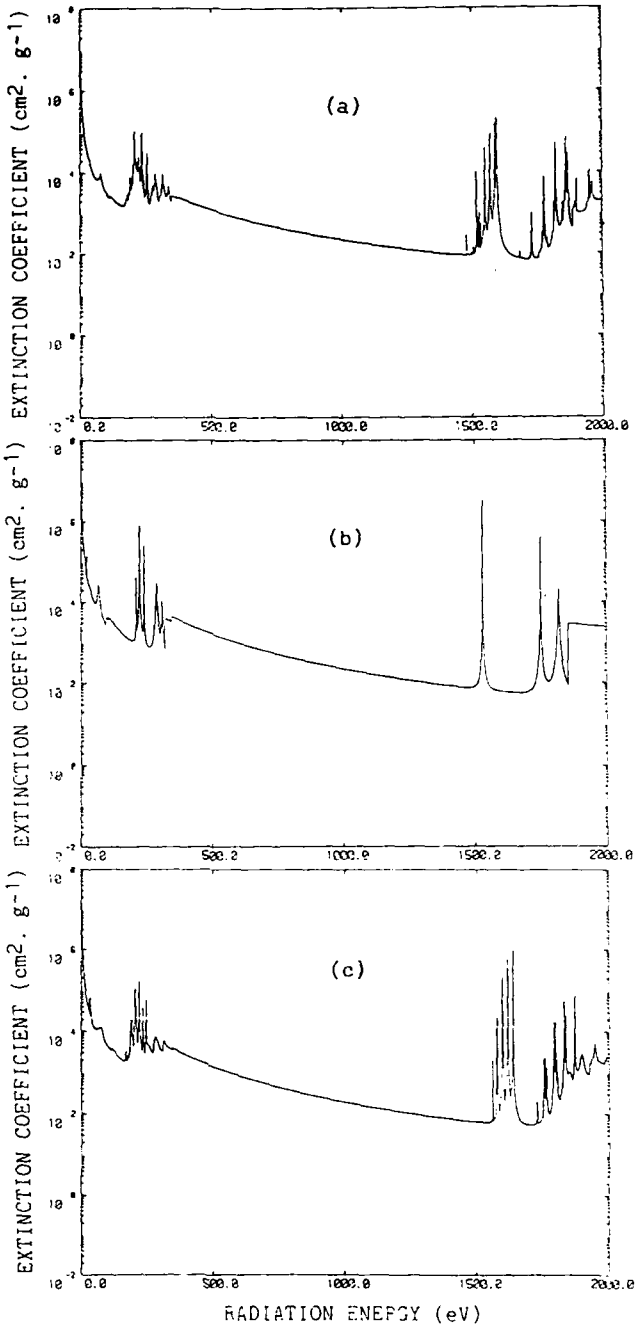

Figure 1.- Extinction coefficient versus radiation energy for aluminium at 100 eV, 0.187 g.cm^{-3}. from:
(a). Astrophysical library (K_R = 923.6 cm^2. g^{-1})
(b). Average atom model (K_R = 943.0 cm^2. g^{-1})
(c). Detailed configuration model (K_R = 922.3 cm^2. g^{-1})

where σ stands for the opacity, $\sigma_t = \sigma + 1/c\Delta t$, I_0 for the scalar intensity (zeroth moment in angle) and η and X are standard parameters [7]. In the radiation transport equation, all the terms should be evaluated implicitly. This can be effectively done by the source iteration technique, that consists on taking the radiation source from the last iteration (ℓ) and solving Eq. (1) to obtain the next estimate ($\ell+1/2$) for the radiation intensity. In unaccelerated schemes $I^{\ell+1} = I^{\ell+1/2}$, whereas in synthetically accelerated schemes the radiation intensities are updated for the next iterate by means of solving a simpler form of Eq. (1) (low order operator).

In radiative transfer applications, one finds that the opacities can reach very high values, in such a manner that the optical thickness of a cell can be extremely high. In these circumstances, the numerical schemes to discretize the S_n equations present two major problems. First, the solution can become unstable, and second, the cell-centered or cell-edge specific intensities do not fulfill the asymptotic (very high optical thickness) diffusion limit [8]. The linear dicontinuous scheme (LD) [9], as well as other high order methods [8], solves both problems, but is not fully positive and it is expensive from a computational viewpoint, specifically in 2D-settings.

Based on the LD scheme Honrubia & Morel [10], have developed a new Weighted Diamond with Slopes (WDS) scheme that is positive, second order accurate, verifies the asymptotic diffusion limit and is cheaper than the LD scheme.

The Fourier analysis of the convergence process of Eq. (1) shows that for optically thick cells and large time steps, the asymptotic (after many iterations) convergence rate can be unacceptably slow (spectral radius close to 1). Thus, to solve the radiation transport equation in the hydrodynamics time scale, with a suitable computational effort, requires to improve this rate by using the synthetic acceleration method. Specifically, following the Alcouffe et al. [6] and Morel et al. [7] prescriptions we have used the S_2-synthetic method to accelerate the convergence of the S_n iterates at two levels. In the first level, the S_n equations are accelerated with high efficiency by the multigroup S_2 equations. However, the convergence rate of the multigroup S_2 equations can be also unacceptably slow. Then, the second step accelerates the multigroup S_2 equations convergence by a one-group (or grey) S_2 equation. By this procedure, one can obtain the implicit radiation intensities with reasonable calculational resources.

In conclusion, our WDS discretization scheme and the S_2-synthetic method are highly effective for radiation transport calculations. In Fig. 2 the results obtained for a Marshak wave benchmark problem proposed by Alcouffe et al. [6] are presented. The problem consists on a homogeneus slab at initially 1eV with the temperature raising in the left boundary up to 1KeV in 0.1 ns. From this picture, the excellent agreement with the work of Alcouffe et al. [6] is noticeable.

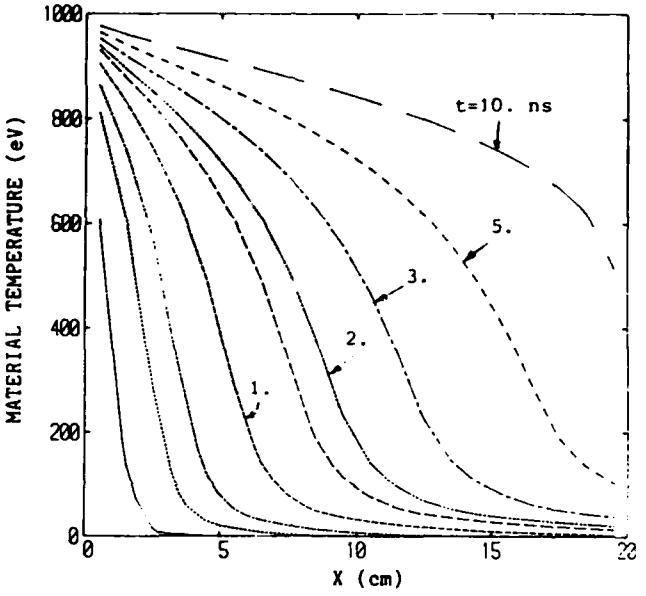

Figure 2.- Marshak wave propagation in a homogeneous slab with $\sigma(v)=2.7\ 10^{10}\ (1-\exp(-v/KT))/v^3(cm^{-1})$ (v in KeV) and $\rho c_v=8.1\ 10^9$ erg. cm^{-3}. eV^{-1}.t

ONE-DIMENSIONAL SIMULATION OF LHAR TARGETS

During the last years the Institute of Laser Engineering (ILE) of Osaka has been very active in the design and experimentation of Large High Aspect Ratio Targets (LHART). The main idea was to obtain a very high velocity ($\simeq 10^8$ cm/sec) which makes able to obtain a high neutron yield. Preliminary proposals in this sense were made by Afanas'ev, [11] and the first experimental results were conducted at ILE [12] but using a glass microballoon without fuel. The actual experimental results have been produced again in ILE and reported in the 11th Conference on Plasma Physics and Controlled Nuclear Fusion in Kyoto [13], using in this case fuel filled glass microballoon. In addition to the experimental results, numerical simulations with the 1-D ILESTA-BG code were reported [13, 14].

The experiments were driven with GEKKO XII at green, delivering 13KJ with a FWHM of 1ns, and focusing conditions of f=3 lenses, and a relation between the distance of the focusing point from the target center (d) and initial radius of the target (R) of d/R = -5. The imploded targets have had diameters in the range $700 \leq \phi \leq 1500$ μm and thickness $0.9 < \Delta R < 2.5$ μm which cover aspect ratios (AR) between $200 < AR < 700$. The experimental and simulation results of the neutron yield versus aspect ratio are plotted in figure 3.

From this figure 3 we conclude that only in a range between 400 and 500 of aspect ratios, the discrepancies between those results could be considered minor ones (½ to ½). But, for aspect ratios lower and higher

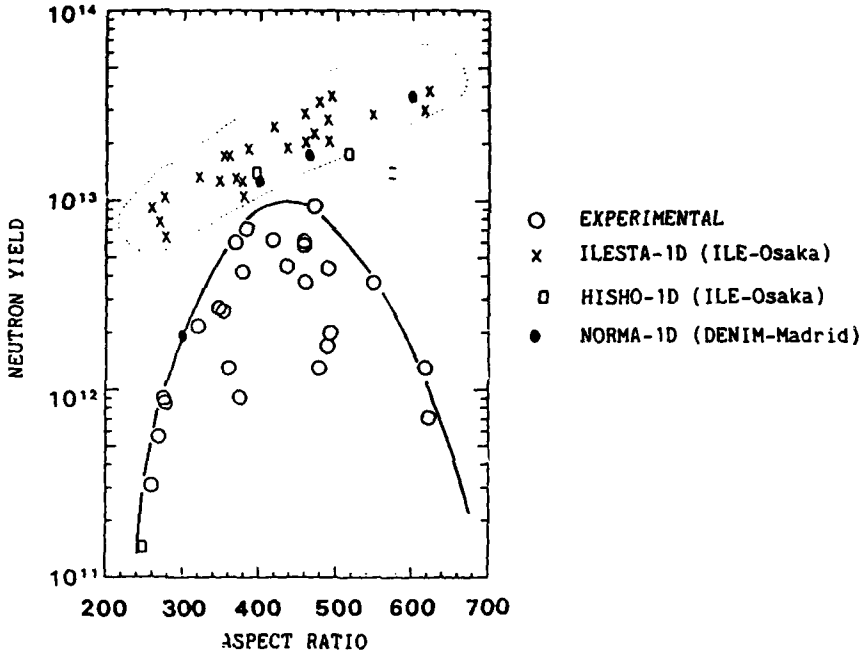

Figure 3.- Neutron yield vs. aspect ratio

of that mentioned range the discrepancies appears to be dramatic in the neutron yield. Some explanations have been reported [14], for these large discrepancies. It is explained the effect for lower aspect ratios due to the dominant of stagnation dynamics which gives a larger number of neutrons in simulation. That stagnation phase is supossed to be not stable in experiments because of not good enough uniformity of GEKKO XII. For higher aspect ratios two reasons are mentioned: poor modelling of the electron conduction through the flux limited Spitzer conductivity with no consideration of non local heating, and the shell break-up due to nonuniformity in laser intensity. It seems to be clear that these hypothesis must be carefully analyzed in the future with the use of 2-D modelling and perturbation codes.

The interesting physics explored with these targets, which arrived to a gain of 0.2%, and the well possed conditions of the experiments, diagnosis and simulations makes them particularly useful to give a comparison and criticism of the 1-D numerical simulation codes, their algorithms and involved physics. In that sense, some 1-D calculations using our NORMA code have been performed using the mentioned experiments. The main characteristics of the code are pointed out below, and the simulations have been carried out with a description of the target which includes 32 meshes for SiO_2 and 50 meshes for DT.

The standard version of NORMA used for target calculations includes a 3T model with implicit conduction solver and variable coefficients. EOS and opacity data are from DENIM library (SESAME plus analytical calculations wherever necessary). The energy source coming from laser deposition is calculated with the ray-tracing package [15, 16]. Absorption coefficients model the collisional and resonant absorption. The attemps to reproduce SRS and SBS have been rather a failure. In addition to that, when tracking the ray path, linear intepolation is used. But, hydro codes use a few zones for the coronal region (10 ~ 20) in 1D, and proportionally a lesser number in 2D. Moreover, the gradient of the density is discontinous. Parabolic interpolation cannot be used because it is overdeterminated and gives oscillations. The cubic one is enough except with strong density gradients. It is possible to design a general monotonic interpolation [16] paying a high overhead time. In 2D, linear interpolation lets follow only perturbations over 2-3 cells if the code is not too dissipative. In this case absorption coefficients have to be corrected (about 10%) because the density is rather exponential.

In addition to the results of NORMA code [17], some calculations have been performed [18], and reported partially here using the ILE code HISHO-1D [19] with the same simulation parameters than NORMA and using a multigroup (50) description of the radiation transport.

Observing the neutron yield results, Fig. 3, the same tendency is given for NORMA and ILESTA simulations except in the point of lower aspect ratio. Two reasons could be argued for that: the different spatial meshes description (40 SiO_2, 100 DT in ILESTA), and the different radiation transport treatment. In the case of HISHO-1D the results show discrepancies at lower and higher aspect ratios, but it was observed a different absorption percentage of laser energy in every case to that of ILESTA and NORMA, which are in good agreement.

The attention is now devoted to the implosion dynamic characteristic in the case of closer coincidence among the experimental and simulation results. This point is described in NORMA simulations as that of aspect ratio $\simeq$ 470 in Table I. Internal pressure of DT gas is 6 atm. and initial temperature in all the materials T = 1ev.

In Fig. 4, the absorption percentage efficiency versus time is represented with a total value of 71.1% in good agreement with ILESTA code which gives a 73% [14]. In the case of HISHO-1D this absorption percentage is $\simeq$ 56% as is pointed out in Table II.

When analyzing the neutron yield versus time, two different points must be considered corresponding to the time when the first shock wave collapse to the center, that can be considered as the starting of stagnation phase, and the final implosion time. That difference is important when the number coming out from experiments is compared [14]. In NORMA calculations those times correspond to $\simeq$ 2.2 ns and $\simeq$ 2.4 ns

TABLE I. Configurations selected for NORMA simulation of the LHAR Targets

ASPECT RATIO R/ΔR	EXTERNAL RADIUS (μm)	THICKNESS SiO_2 (μm)
300	619.56	2.058
400	619.04	1.543
470	618.81	1.310
600	618.53	1.030

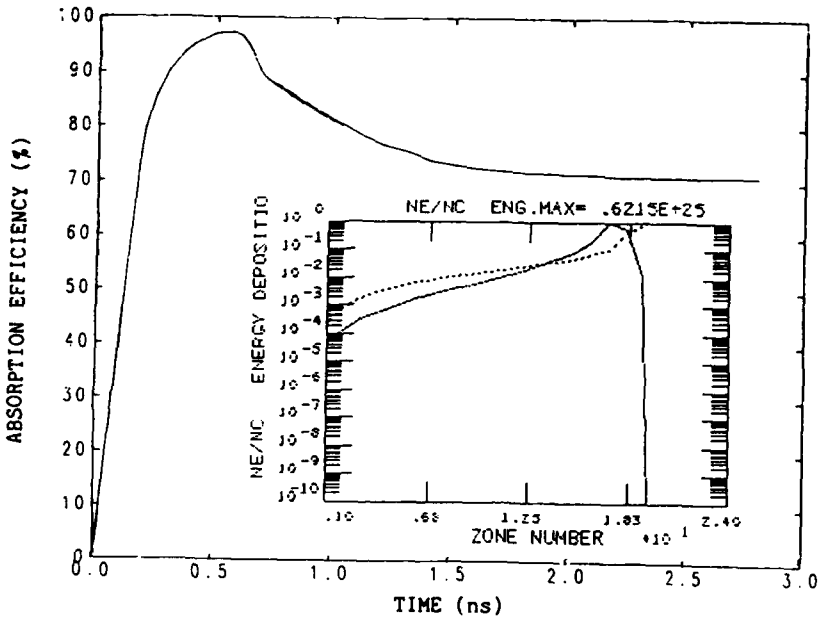

Figure 4.- Absorption efficiency vs. time, and spatial profile of energy deposition and critical density

whose spatial hydrodynamic (T,ρ) descriptions are presented in Figures 5.a and 5.b.

In comparing the ionic temperature from the weighted areal emission rate (not average) of the first time with that of the experiments and ILESTA simulation 13, 14), it is observed an almost good agreement, ≃ 9 KeV. Well understood that the time when it is produced has a slightly difference of ≃ 0.2 ns. This shift in time is also consequently observed in the final implosion time. Minor differences are noted in the ρR values when comparing with the experimental points and ILE simulation curves, and larger in the average density (ρ). If the neutron yield is compared for that AR between the experimental and the NORMA results, we

TABLE II. NORMA-1D and HISHO-1D comparison for the main interaction and average hydrodinamic values (AR = 470)

		NORMA-1D (DENIM)	HISHO-1D (ILE)
#	Input energy (KJ)	13	13
	Absorbed energy (KJ)	9.15	7.2
	Radiation out (KJ)	1.15	—
	Implosion time (ns)	2.4	2.4
	η_a (%)	71.1	56.17
	η_u (%)	10.85	14.18
	η_c (%)	7.71	4.37
#	Max. average ionic T. (KeV)	3.76	3.87
	tine (ns)	2.29	2.28
	average electronic T (KeV)	1.92	2.71
	density (g/cm^3)	0.52	0.56
	ρR (mg/cm2)	3.85	3.45
#	Max. average density (g/cm^3)	0.95	1.31
	time (ns)	2.4	2.4
	average ionic T (KeV)	2.94	2.54
	average electronic T (KeV)	2.02	1.97
	ρR (mg/cm^2)	7.56	6.921
#	Max. average ρR (mg/cm^2)	7.56	9.22
	time (ns)	2.4	2.36
	average ionic T (KeV)	2.94	3.28
	average electronic T (KeV)	2.02	2.30
	density (g/cm^3)	0.95	1.16

obtain the following values Y_N(exp) $\simeq 9\times10^{12}$ and Y_N(simulation) $\simeq 8\times10^{12}$. The total number of neutrons is 1.88×10^{13} when the final implosion occurs which is larger than the experimental result and slightly lower than ILESTA calculations.

It can be concluded that a good agreement is generally obtained among the numerical simulations of ILESTA and NORMA codes, specially in the range of AR closer to the experimental ones. Slightly differences are found in average results between NORMA and HISHO-1D, but these similarities under a different laser absorption should be explained in the future. The comparison with the available experimental data for the AR of maximum neutron yield show an acceptable agreement in the

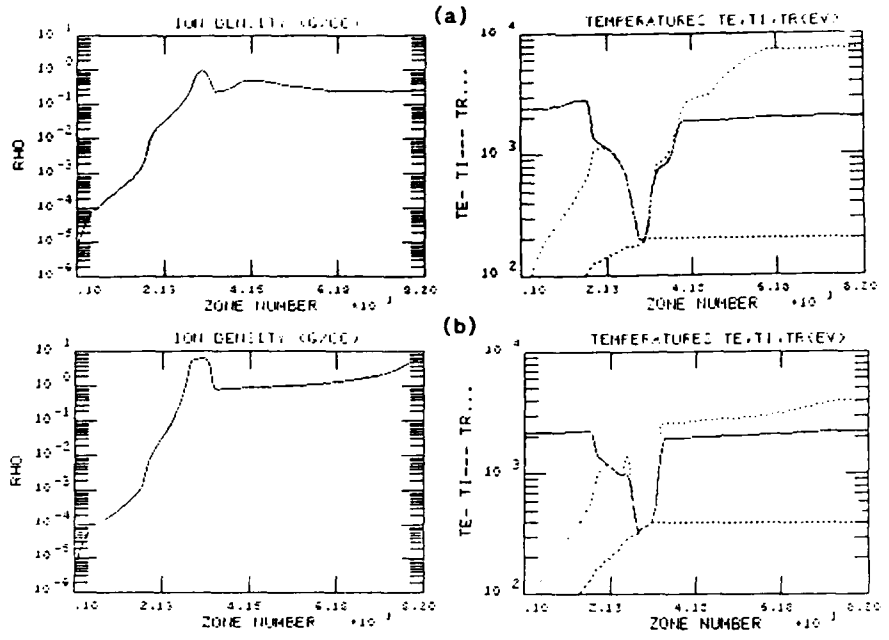

Figure 5.- Temperatures (ionic, electronic, radiation) and density spatial profiles at:
(a) t=2.26 ns (after first shock collapses to the center)
(b) t=2.41 ns (implosion time)

implosion dynamic parameters that need a deeply analysis when other physics mechanisms are included in the code (NLTE atomic physics, ...).

Acknowledgments

One of the authors (J.M.P.) ackowledges specially Professor C. Yamanaka for the support of the LHART work at ILE, and Professor K. Nishihara for his help in using HISHO-1D and many discussions and suggestions of future works. He also thanks to Dr. H. Takabe and Mr. M. Murakami for their help and information.

This work has been partially supported by the CAICYT and UNESA-OCIDE.

REFERENCES

1) M. F. Argo, W. F. Huebner, J. Quant. Spectrosc. Radiat. Transfer, **16**, 1091 (1976)

2) G. Velarde et al., European Space Agency & Scientific and Technical. Publication Branch **207**, 201 (1984)

3) G. Velarde et al., Laser & Particle Beams **4**, 349 (1986 a)

4) W. F. Huebner et al., Los Alamos National Laboratoy Report No LA-6760-M (1977)

5) J. P. Boris, NRL Memorandum Report 3237 (1976)

6) R. E. Alcouffe, B. A. Clark, E. W. Larsen, Multiple Time Scales, Academic Press (1985)

7) J. E. Morel, E. W. Larsen, M. K. Matzen, J. Quant. Spectrosc. Radiat. Transfer, **34**, 3 (1985)

8) E. W. Larsen, J. E. Morel, W. F. Miller, J. Comput Phys, **69**, 2 (1987)

9) J. J. Honrubia, J. M. Aragonés, Nucl. Sci. Eng. **93**, 386 (1986)

10) J. J. Honrubia, J. E. Morel, Proc. Int. Topl. Mtg. on Adv. Reac. Mat. and Comp. 1, 377 (1987)

11) Yu. Afanas'ev et al., JETP Lett. **23**, 566 (1976)

12) C. Yamanaka et al., Tenth Int. Conf. Plasma Phys. Contr. Nucl. Fus. Res. London, IAEA-CN-44/B-I-1 (1984)

13) C. Yamanaka et al., Eleventh Int. Conf. Plasma Phys. Contr. Nucl. Fus. Res. Kyoto, IAEA-CN-47/B-I-4 (1986)

14) H. Takabe, ILE Quarterly Report, ILE-QPR-86-20, 3 (1987)

15) G. Velarde et al., DENIM Annual Report 1985 (1986 b)

16) P. M. Velarde, DENIM Annual Report 1986 (1987)

17) J. L. Pérez-Torres, Master Thesis, Universidad Politécnica de Madrid (September 1987)

18) J. M. Perlado, private communication of unpublished work performed during visiting scientist stay at ILE (1986)

19) M. Murakami and K. Nishihara, ILE Quarterly Report, ILE-QPR-83-6, 34 (1983)

NUMERICAL ANALYSIS OF TARGET IMPLOSION IN LIB ICF

Yukio MASUBUCHI and Shigeo KAWATA

The Technological University of Nagaoka
Nagaoka, Niigata 940-21, Japan

Abstract

The paper presents the numerical analysis for the target implosion using uniform and non-uniform beams. In the analysis we assume very simple model and use the 2-dimensional hydrodynamic code called HALLEY.

1. Introduction

The implosion of a spherical target for inertial confinement fusion(ICF) has been investigated for the light ion beam.[1,2] In order to achieve a high target gain, it is necessary to realize the spherically symmetric implosion. Up to the present there are some reports[3-6] for the implosion simulation. A few works[3,4] on the symmetric target implosion suggest that the non-uniformity of the implosion pressure must be suppressed under 1-4%. But the requirements for the uniformity of the target implosion is not clear at the present stage. To clear this problem, the target implosion is simulated in this paper as the first stage.

2. HALLEY Code

The code using in this calculation is based on HALLEY code developed by Prof. Niu laboratory at Tokyo Insutitute of Technology. This code uses the r-θ polar coodinate and the MEL(Mixed Eulerian Lagrangian) method.[7]

The basic equations are follows,

$$\frac{\partial \rho}{\partial t} = -\nabla \cdot \tilde{u}\rho \tag{1}$$

$$\frac{\partial (\rho \tilde{u})}{\partial t} = -\nabla \cdot \tilde{u}(\rho \tilde{u}) - \nabla P \tag{2}$$

$$\frac{\partial (\rho e)}{\partial t} = -\nabla \cdot \tilde{u}(\rho e) - \nabla \cdot (P\tilde{u}) + S_E \ . \tag{3}$$

where ρ is the density, P the plessure, e the internal energy, S_E the sink energy and $\tilde{u}$ the vector of the fluid velocity. These basic equations can be represented by the following cell equations,

$$\frac{dM}{dt} = -\int_S d\tilde{S} \cdot (\tilde{u}-\tilde{w})\rho \tag{4}$$

$$\frac{d\tilde{P}}{dt} = -\int_S d\tilde{S} \cdot (\tilde{u}-\tilde{w})(\rho \tilde{u}) - \int_S d\tilde{S} \cdot P \tag{5}$$

$$\frac{dE}{dt} = -\int_S d\tilde{S} \cdot (\tilde{u}-\tilde{w})(\rho e) - \int_V dV \cdot P\nabla \cdot \tilde{u} + \int_V S_E dV \ . \tag{6}$$

where $\tilde{w}$ is the vector of the mesh velocity and $\tilde{S}$ is the vector of the normal direction. The target region is devided by the mesh and it is assumed that the meshes in the θ direction are the Euler meshes and in the r direction are the Lagrange meshes. The Lagrange meshes move with the fluid. Namely they need the following condition (Lagrange condition):

$$d\tilde{S} \cdot (\tilde{u}-\tilde{w}) = 0 \ . \tag{7}$$

The Euler meshes do not move. So they need the following condition (Euler condition):

$$\tilde{w} = 0 \ . \tag{8}$$

3. Simulation Model

For the very simple model we assume several physical phenomena, that is the ideal EOS (equation of state), no radia-

tion, and no heat conduction. By way of example we use the pellet showing in Fig.1. The Mesh structure is shown in Table 1. The initial condition of the pellet is presented in Table 2. The Incident beam is perpendicular to the spherical surface (Fig.1). Table 3 shows beam values. The energy of the coming beam increases power in the manner shown in Fig.2. The rising time is 15[nsec] and the duration time is 40[nsec] for this beam pulse.

4. Simulation Results

At first we show the results of the simulation using the uniform beam. Figure 3 shows the stream lines. The void closure time is 57.9[nsec]. From now on, we explain about four stages which are indicated in Fig.3. From the biginning they present the initial state, the middle of implosion, the void closure

Table 1. The mesh structure

Number of cell
θ direction 29
r direction 30
. Pb layer ... 5
. Al layer ...15
. DT layer ...10

Table 3. The beam parameter values

.Species	Proton
.One particle energy	8 [Mev]
.Beam velocity	3.9×10^{7} [m/sec]
.Total energy	2 [MJ]
.Duration time	40 [nsec]
.Rising time	15 [nsec]

Table 2. The initial condition

Layer	Atomic weight	Thickness[mm]	ρ[kg/m³]	T[kev]
Pb	207.2	0.030	1.134×10^{4}	1.0×10^{-4}
Al	27.0	0.135	2.690×10^{3}	1.0×10^{-4}
DT	2.5	0.160	1.870×10^{2}	1.0×10^{-4}

and the expansion stages.

Figure 4 shows the implosion pattern. The grayish zone is the D-T layer. Figure 5 is the density profile. At the middle of implosion the density of the outer D-T layer is higher than that of the inner layer. At the void closure the density of the D-T layer is about 100 times as much as the initial state. When the pellet expands, the density becomes flat.

This simulation of the uniform beam is no more than the check of this code. The essential matter is to examine the influence of the non-uniform beam. We use very simple method shown in Fig.5 in order to introduce the non-uniform beam. The beam number density changes by a cosine curve. The amplitude of the non-uniformity are 0.2% and 0.5%. Figure 6 shows the stream lines. These lines indicate maximum position in the same number mesh of θ direction. One of the innermost D-T meshes reaches at the center of the target at 58.0[nsec] and 58.7[nsec] respectively in these two cases. We assume this time to the void closure time. We show about four stages indicated in Fig.6 at the case of the 0.2% non-uniformity. Figure 7 shows the implosion pattern and Figure 8 shows the density profile. At the middle of the implosion, it is hard to see the non-uniformity. At the void closure and the expansion states, we can find a little non-uniformity. But there are so much influence of non-uniform beam. Table 4 shows the degree of this influence, that is the ratio of

Table 4. The degree of the influence

Non-uniformity	0.2%	0.5%
Density	29.0%	32.4%
Temperature	12.9%	13.6%
Radius	23.7%	26.0%
ρR	27.0%	29.1%

maximum and minimum physical values at innermost D-T layer meshes. Up to the present there is a research[5] of the influence non-uniformity after the void closure time using the 3-dimensional implosion code. We connect this result with its research. Its result indicates that maximum ρR is 27.0% and 29.1% decrease respectively in these two cases. It is clear that just the little non-uniformity of beam have fairly influence on ρR, temperature, density, radius and so on.

5. Conclusions

This report uses very simple model of physical phenomena. At the present it is underway to include some physical phenomena which are thermal conductivity, two temperature and the realistic EOS. We include more real phenomena.

Another future ploblem is to find how we can smoothe the non-uniformity.

Acknowlegment

The HALLEY code was supported by professor Niu Laboratory at Tokyo Institute of Technology. The authors appreciate Prof. Niu.

This work is partly supported by the cooperation program of Institute of Plasma Physics at Nagoya University.

References

1) K. Niu and S. Kawata: Fusion Tech. 11 (1987) 365.
2) J. P. Vandevender and D. L. Cook: Science 232 (1986) 83.
3) M. H. Emery, J. H. Orens, J. H. Gardner and J. P. Boris: Phys.Rev.Lett. 25 (1982) 253.
4) T. Yabe, A. Nishiguchi and N. Ueda: Appl.Phys.Lett. 39 (1981) 222.
5) S. Kawata and K. Niu: Jpn.J.Appl.Phys.Soc. 53 (1984) 4316.
6) K. A. Long and N. A. Tahir: Phys.Rev. A35 (1987) 2631.
7) R. M. Frank and R. B. Lazarus: Methods in Computational Physics vol.3 (Academic Press, 1946).

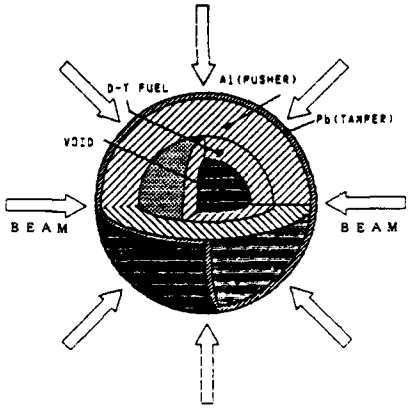

Fig.1 The target structure

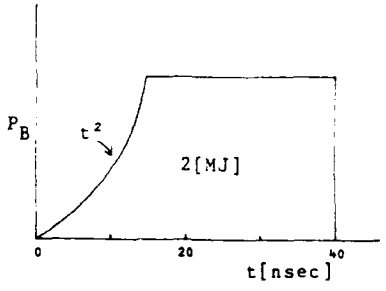

Fig.2 The pulse shape

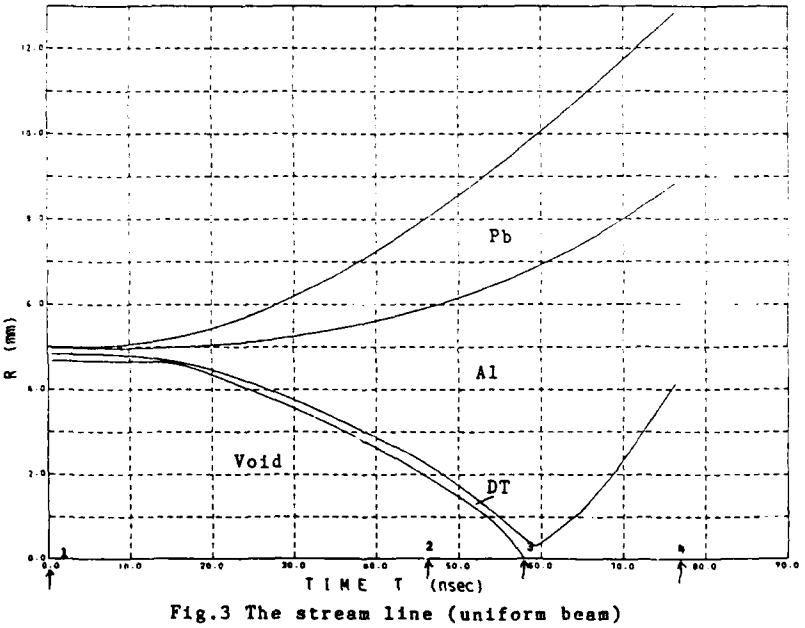

Fig.3 The stream line (uniform beam)

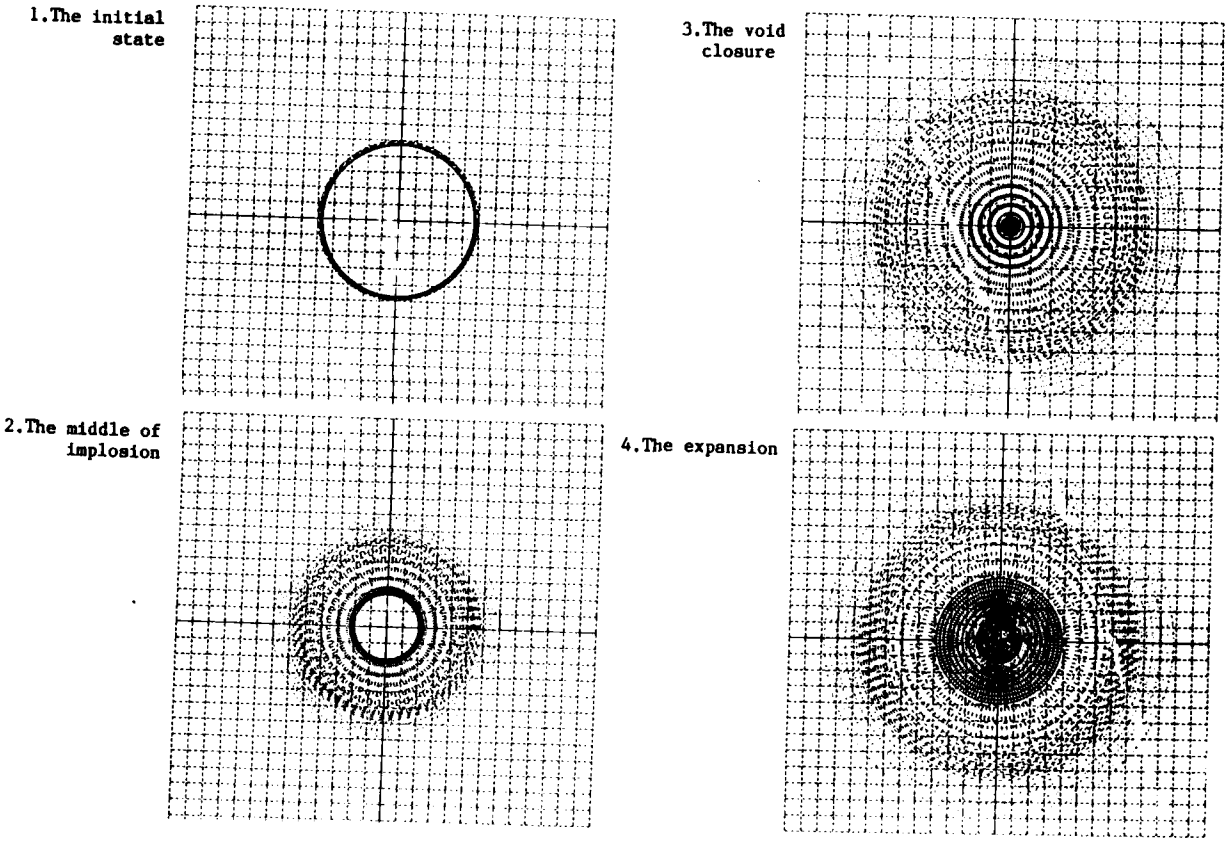

Fig.4 The implosion pattern (uniform beam)

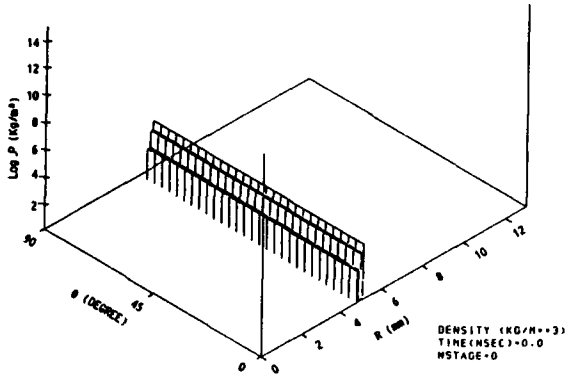

1.The initial state

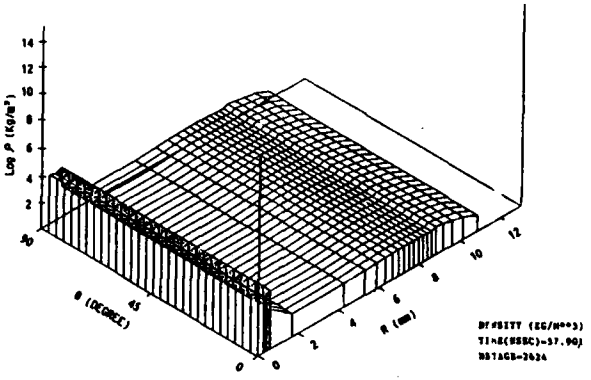

3.The void closure

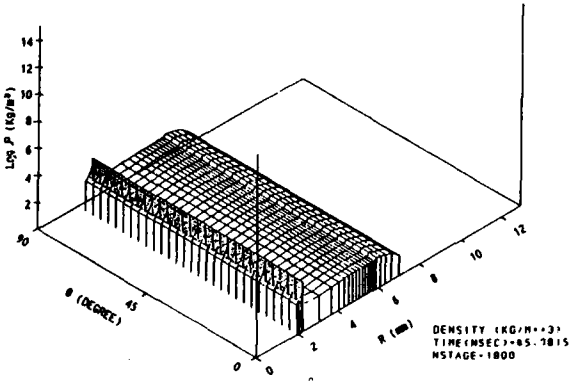

2.The middle of implosion

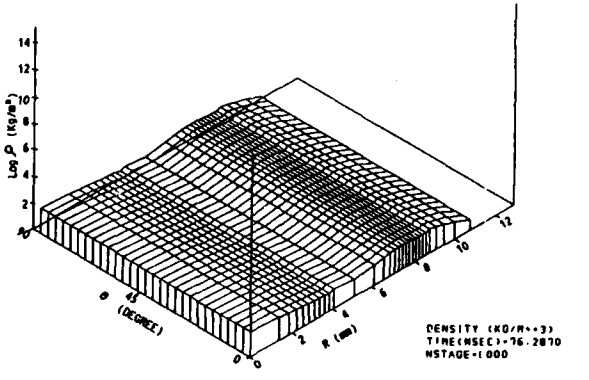

4.The expantion

Fig.5 The profiles of density (uniform beam)

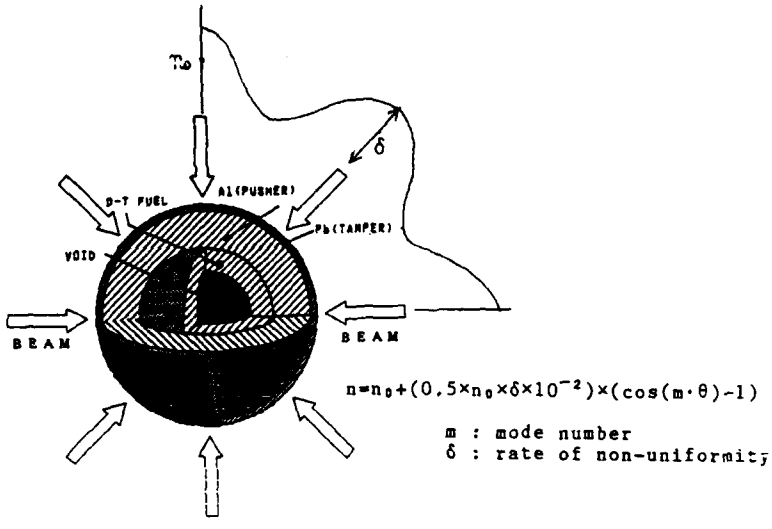

Fig.6 The non-uniform beam

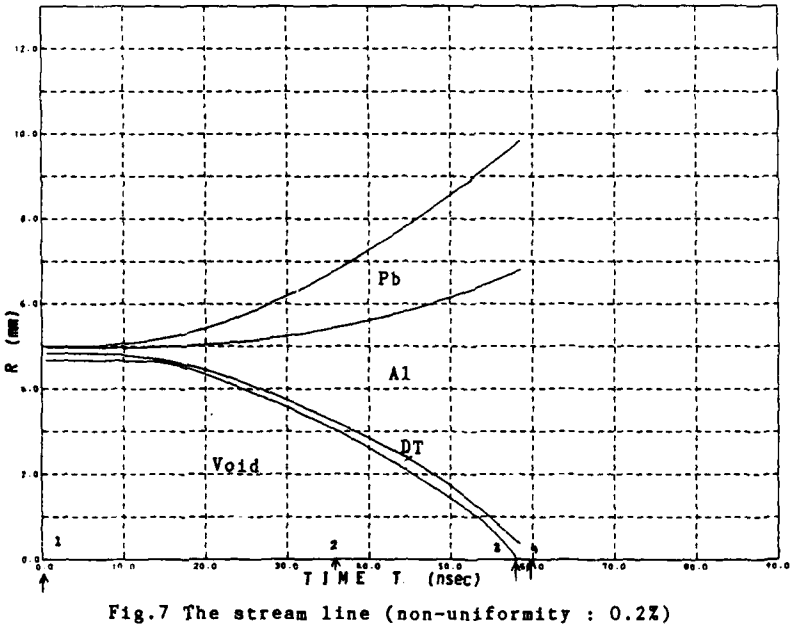

Fig.7 The stream line (non-uniformity : 0.2%)

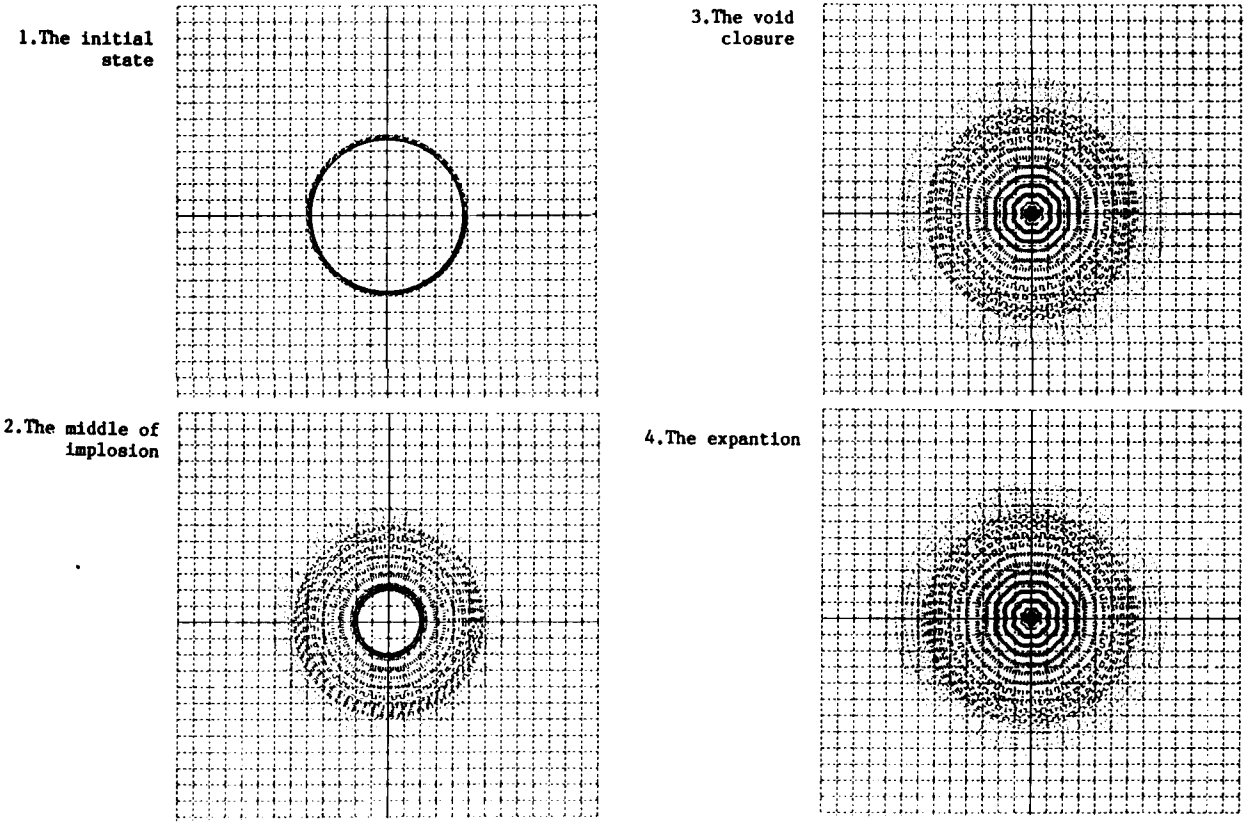

Fig.8 The implosion pattern (non-uniformity : 0.2%)

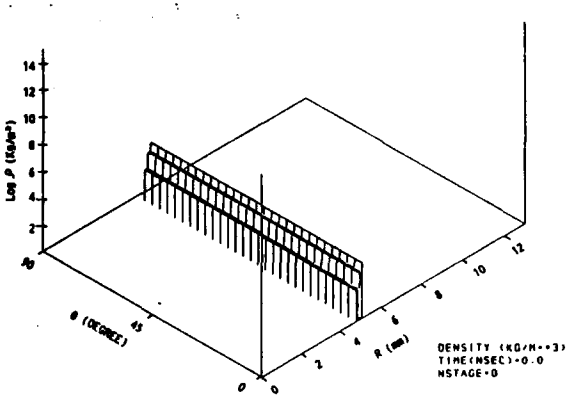

1.The initial state

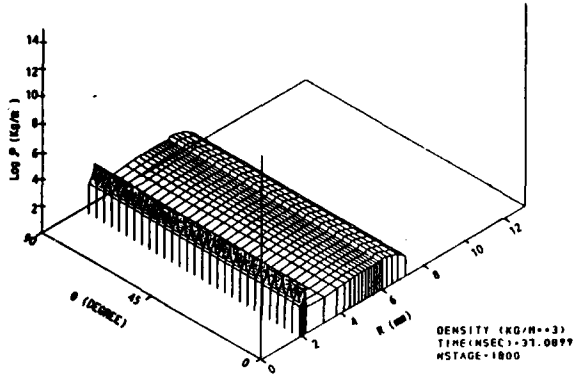

2.The middle of implosion

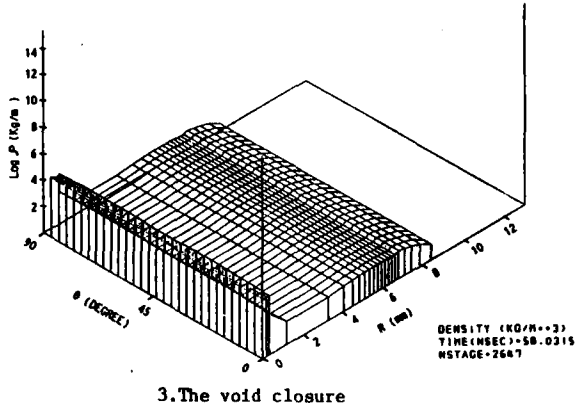

3.The void closure

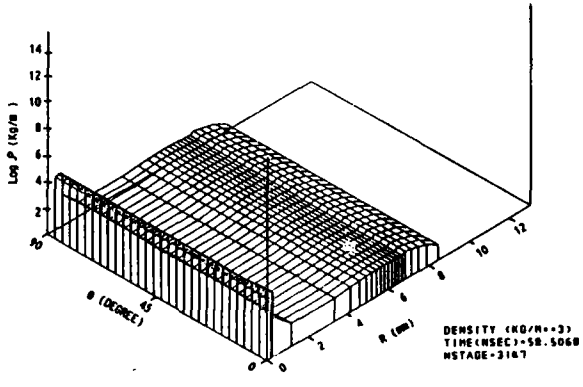

4.The expansion

Fig.9 The profiles of density (non-uniformity : 0.2%)

Pusherless Implosion, Pulse Tailoring and Ignition Scaling Law for Laser Fusion

K. Mima, H. Takabe and S. Nakai

Institute of Laser Engineering, Osaka University, Suita, Osaka 565 Japan

Abstract

The conventional implosion scheme for high gain and high density compression depends upon piston action of an accelerated heavy pusher. However, the contact surface between the pusher and the fuel layer is very unstable in the stagnation phase. In this report, the laser pulse tailoring and the scaling laws for pellet gain, fuel ρR and so on are discussed under the condition of very weak piston action of the pusher. The scaling laws indicate that the fuel will be ignited by 100kJ, 0.35μm wavelength laser irradiation.

1. Introduction

In the conventional implosion scheme, a heavy pusher is ablatively accelerated together with a fuel layer. Since the pusher mass density is much higher than the DT fuel density, the accelerated pusher has higher energy density than the fuel layer, which generates a very high pressure at the pellet center. Therefore, the fuel is expected to be highly compressed by piston action of the pusher. However, the contact surface between the pusher and the fuel layer is strongly unstable in the stagnation phase.[1~2] Therefore, it is very difficult to compress the fuel to a very high pressure by the pusher stagnation.

Let perturbations of the contact surface grow as $\exp\left[\int_0^t dt\ \Gamma\right]$, where Γ is the growth rate which is approximated by $\sqrt{kg}$. The wavenumber, k and the acceleration, g increase as ℓ/r and $1/r^3$ respectively according to self-similar

analysis for adiabatic compression and a fixed mode number, ℓ. Therefore, Γ increases as $1/r^2$ and the perturbations grow explosively when the contact surface converges.[3] As the results, the contact surface will be highly distorted and the pusher kinetic energy will not be converted into the fuel internal energy. Therefore, the hydrodynamic energy has to be accumulated in the fuel shell instead of the pusher. In that case, the contact surface instability will not be serious for compression and heating of the fuel.

Recently, a new target fabrication technique, namely a foam cryogenic target has been proposed to fabricate a thick DT shell target. The DT shell thickness of the foam cryogenic target can be thick enough for constructing both of the ablator-pusher and the fuel layer. Since the foam cryogenic shell density, $0.2 g/cm^2$ is significantly lower than those of the other solid materials, the laser ablation pressure generates a very strong shock wave to cause the shell disassembly when the ablation pressure rises up rapidly. Therefore, it is necessary to shape the laser pulse carefully for pressure pulse tailoring.[4~6]

In this paper, we report theory and simulation studies on the pusherless implosion hydrodynamic and discuss the realistic scaling laws for designing an ignition target.

2. Contact Surface Stability

Let us consider the stability of the contact surface at $r=r_c$ in a typical density profile of a stagnating plasma as shown in Fig. 1. The stagnation process is well described by a self-similar solution in which temporal evolutions of density and pressure are given by [1,2]

$$\rho(r,t) = \rho_0(rf_0/f)[f_0/f(t)]^{-3},$$

and $$P(r,t) = P_0(rf_0/f)[f_0/f(t)]^{-5}, \qquad (1)$$

respectively, where $\rho_0(r_0)$ and $P_0(r_0)$ are the initial density and pressure profiles respectively, $f_0 = f(t_0)$ and

$$f(t) = [1 + (t/\tau)^2]^{1/2}. \tag{2}$$

Here, we assume that the stagnation starts at $t = -t_0$ and the maximum compression occurs at $t = 0$. The maximum compression ratio by the stagnation is given by $[1 + (t_0/\tau)^2]^{3/2}$ and the initial implosion velocity, v_0 of the contact surface is related to r_c, t_0 and τ by,

$$v_0 = r_c t_0/(\tau^2 + t_0^2). \tag{3}$$

Preturbations of the spherical harmonics, $\ell = 10$, 20 and 40 are added on the contact surface. The temporal evolutions of the perturbations are analytically calculated.

The analytical results are shown in Fig. 2.[3] In this case, the volume compression is suppoued to be 70 which corresponds to $f_0 = 4.12$ and $t_0 = -4\tau$. The growth rates of Fig. 2 are well approximated by

$$\sqrt{\frac{\rho_p - \rho_f}{\rho_p + \rho_f}}\, kg \simeq \sqrt{\frac{\rho_p - \rho_f}{\rho_p + \rho_f}}\, \ell/(\tau f^2), \tag{4}$$

where we used the relations

$$k = \ell/r = \ell f_0/(r_c f),$$

and $$g = |d^2r/dt^2| = r_c/(\tau^2 f_0 f^3). \tag{5}$$

Namely, the growth rate increases in proportion to $1/r^2$. Therefore, when the Attwood number, $\frac{\rho_p - \rho_f}{\rho_p + \rho_f}$ is order unity, the surface distortions are amplified strongly when the compression ratio is more than 10 in the stagnation phase. This concludes that the fuel should be compressed without piston action of the pusher.

As for the stability of an actual DT gas filled GMB (glass micro balloon), the linearized equations for the perturbations have been investigated numerically by a simulation code 'ILESTA' which consists of 1D implosion hydrodynamic code and the perturbation code.[7]

The r-t diagrams of 1-D simulations and the temporal evolutions of the perturbations on the contact surface are shown in figures 3(a), (b) and 4(a), (b) respectively. The initial aspecto ratios of the glass shell are 450 and 340 for Figs. 3(a) and 4(a) (Case 1) and Figs. 3(b) and 4(b) (Case 2) respectively. In the case 1, the glass shell is almost burned through and the glass shell density is significantly reduced by the ablation. However, the glass shell for the case 2 is a little thicker than the ablation depth for the present laser and target parameters. Therefore, the high density pusher layer remains to stagnate at the center. As the results, ρ_p/ρ_f for the case 2 is significantly greater than that for the case 1. Actually, at the time when the first reflection shock from the target center hits the inner surface of the imploding S_iO_2 pusher, ρ_p/ρ_f are less than unity for the case 1, namely, the Attwood number is negative. On the other hand, ρ_p/ρ_f is greater than unity for the case 2.

Therefore, the perturbations grow strongly in the stagnation phase in Fig 4(b), while they do not grow in Fig. 4(a). In Figs. 4, the perturbations are generated by the laser irradiation nonuniformity, δI_L and the amplitudes, $\zeta r/R_0$ and $\zeta_\perp/R_0$ are the radial and the transverse displacements of the fluid element due to perturbation respectively. They are normolized by $|\delta I_L/I_L|$. Therefore, the Fig. 4(a) indicates that the contact surface rippling amplitude

grows to 10 percents of the initial target radius, R_0 for $|\delta I_L/I_L| = 0.1$. Since the minimum radius of the contact surface is about 0.15 R_o in Fig. 3(a), the case 1 implosion seems not to be affected much by the irradiation nonuniformity. On the other hand, the final perturbation amplitude in the case 2 is larger than R_0 even if a very uniform irradiation is assumed, say, $|\delta I_L/I_L| \lesssim 0.01$. This amplitude is greater than the ten times of the contact surface radius at the maximum compression. Namely, the case 2 implosion can never be described by the one dimensional simulation. Actually, the experimental neutron yields for the case 2 type targets are always lower by one or two orders of magnitude than the simulation yields. On the other hand, the experimental neutron yields of the case 1 type targets agree reasonably well with the simulation results.[8)]

3. Pusherless Implosion and Pulse Tailoring

According to the previous discussions, the plastic or the S_iO_2 ablator has to be thin enough to be burned through. In particular, when there is no high Z ablator layer, the ablation pressure directly drives a strong shock wave in the fuel layer. Therefore, the shock heating is too strong to compress the fuel to high density, when the laser pulse is gaussian. In the Figs. 5(a) and (b), r-t diagrams for a gaussian pulse and a tailored pulse implosions are compared, where the target has no layer other than a foam cryogenic fuel layer and the total input laser energy is 100kJ. The tailored pulse is assumed to consist of four stacked gaussian pulses and the prepulse intensity is set to be one fifth of the main pulse. The propagation velocity of a rare faction wave on the inner surface is sufficiently small for the tailored pulse in comparison with that for the single gaussian pulse. Actually, the propagation velocities are 2×10^7cm/sec and 5×10^7cm/sec for the tailored and gaussian pulses respectively. Namely, the shock front pressure on the rear surface for the

tailored pulse is 1/6 of that for the gaussian pulse. Note that a high Z ablator layer moderates the first shock and the pulse tailoring is not necessarily required. Since ρR has to be greater than 0.3g/cm^2 for ignition, the high density compression, say, more than 1000 times solid density is required for laser energy less than 100kJ. Therefore, the pulse tailoring is invevitable for ignition experiments when the cryogenic foam target is applied.

After the imploded fuel shell collapses at the center, the fuel is compressed only by the reflection shock. Since the compression ratio by the Guderley shock[9] is 33, we can assume the final fuel density, ρ_{final} to be

$$\rho_{final} = \rho_{acc} \times 33, \tag{6}$$

where ρ_{acc} is the density compressed by the pulse tailoring. After the first shock passes through the fuel shell, the density, ρ and the pressure, P are given by

$$\rho_{shock} = 4\rho_{DT} \text{ and } P = P_P \tag{7}$$

where ρ_{DT} is the solid density and P_P is the ablation pressure generated by the prepulse. Using the adiabatic relation, $\rho \propto P^{0.6}$, the density during the acceleration is given by

$$P_{acc} = 4\rho_{DT} (P_{max}/P_P)^{0.6} \tag{8}$$

Using the empirical scaling law, $P \propto I^{2/3}$, we obtain

$$P_{acc} = 4\rho_{DT} (I_{max}/I_P)^{0.4} \tag{9}$$

where I_{max} and Ip are the maximum and prepulse absorbed laser intensities respectively.

When we require $\rho_{final} > 10^3 \times$ solid DT density, ρ_{acc} has to be greater than 30 ρ_{DT}. Namely, $I_{max}/I_p \gtrsim 150$. Even if we take into account the spherical convergence effects of the ablation surface, the maximum input laser power has to be more than 50 times of the prepulse power.

Since the low power and long pulse irradiation causes the various fluid and plasma instabilities, it is better to set the prepulse power as high as possible. For that purpose, we investigate effects of the ablator layer of which density is sufficiently higher than the DT solid density, 0.2g/cm^3. The ablator layer is regarded as a piston which drives a shock in the fuel. This situation is essentially the same as that for the DT gas filled GMB. Namely, a rare faction wave on the ablator rear surface reduces the contact surface pressure. When the ablator layer velocity is v_0, the pressure behind the shock, P_S is given by

$$P_s = \frac{4}{3}\rho_{DT} v_0^2 , \tag{10}$$

for a strong shock. The piston is accelerated by the ablation pressure as follows,

$$\frac{dV_0}{dt} = g = \frac{P_p}{(\rho\Delta r)_{effec.}} . \tag{11}$$

Here, $(\rho\Delta r)_{effec.}$ is the effective area mass density which increases from $(\rho\Delta r)_{abl.}$ to $(\rho\Delta r)_{abl.} + (\rho\Delta r)_{DT}$, where $(\rho\Delta r)_{abl.}$ and $(\rho\Delta r)_{DT}$ are the ablator and fuel area mass density. We approximate $(\rho\Delta r)_{effec.}$ by the constant, $(\rho\Delta r)_{abl.} + 0.5(\rho\Delta r)_{DT}$. Integration of Eq. (11) yields $3\Delta r_{DT}/4 = g\tau_s^2/2$, where

Δr_{DT} is the fuel layer thickness. Note that the ablator-fuel contact surface traverses $3\Delta r_{DT}/4$, when the shock front reaches the rear side of the fuel layer.

Since the piston velocity is given by $g\tau_s$, Eq. (11) and $\tau_s=(3\Delta r_{DT}/2g)^{1/2}$ yield,

$$v_0=\left[\frac{3}{2}\frac{P_p\Delta r_{DT}}{(\rho\Delta r)_{abl.}+0.5(\rho\Delta r)_{DT}}\right]^{1/2}. \tag{12}$$

Let the ablator be plastic (CH) and the density and the thickness be ρ_{CH} and Δr_{CH} respectively. The equations (10) and (12) yield the shock pressure,

$$P_s=\frac{2\rho_{DT}}{\rho_{CH}}\frac{\Delta r_{DT}}{\Delta r_{CH}+0.1\Delta r_{DT}}P_p. \tag{13}$$

Since the hydrodynamic efficiency is maximum, when $\rho_{CH}\Delta r_{CH}=0.8(\rho_{CH}\Delta r_{CH}+\rho_{DT}\Delta r_{DT})$, Eq. (13) yields $P_s\simeq 0.4P_p$. This reduces the intensity ratio, I_{max}/I_P from 150 to 40.

4. Simulations for Ignition Experiments

We discuss the possibility of igniting fusion burn by using a foam cryogenic target covered with a high density ablator. As we discussed in the previous section, the high density ablator relaxes the pulse tailoring condition. By the implosion simulations, it turns out that a gaussian pulse of 100kJ and an appropriate pulse width is good enough for high compression to increase ρr to more than $0.3 g/cm^2$.

In order to see the laser energy dependence of the pellet gain, we scale the target radius and the thickness as follows. The specific laser energy which is defined by,

[Total Laser Energy ; E_L] / [Total Target Mass]

is required to be constant. Furthermore, aspect ratios are determined by maximizing the hydrodynamic efficiency. In the present simulation, the aspect ratio is kept constant. Therefore, the total target mass is proportional to R_0^3 (R_0; target radius) and $R_0 \propto E_L^{1/3}$. The simulation results for the above target scaling show that the maximum fuel ρR, the neutron yield and the pellet gain are proportional to $E_L^{1/3}$, $E_L^{4/3}$ and $E_L^{1/3}$ respectively, before the ignition. After the ignition, Y_N and the pellet gain are proportional to E_L^2 and E_L respectively because of the alpha-particle heating. In Fig. 6, the laser energy dependences of T_i and ρR are shown, where T_i and T_i^c are the main fuel and the central spark ion temperatures respectively. The broken lines which indicate the cases without alpha-particle heating separate from the solid lines around 50~100kJ. This indicates that the fusion burn is ignited around this range of laser energy. Finally, a typical exmaple of target and laser parameters and the implosion results is summarized in the table 1.

Reference

1) R.E. Kidder, Nucl. Fusion 16, 3(1976).

2) D.L. Book and I.B. Bernstein, J. Plasma Phys. 23, 521(1980).

3) F. Hattori, H. Takabe and K. Mima, Phys. Fluids 29, 1719(1986).

4) R.E. Kidder, Nucl. Fusion 19, 223(1979).

5) R.E. Kidder, Nucl. Fusion 14, 53(1974).

6) S.M. Pollaine and J.D. Lindl, Nucl. Fusion 26, 1719(1986).

7) H. Takabe, ILE Quarterly Progress Report, ILE-QPR-84-12, 24(1985).

8) H. Takabe, ILE Quarterly Progress Report, ILE-QPR-86-20, 3(1987).

9) G. Guderlye, Luftfahrtforschung 19, 302(1942).

Table 1. An example of ignition

Target Parameters		Laser Parameters	
Diameter	1 mm	Total Energy	100 kJ
CH Shell Thickness	12 μm	Wavelength	0.35 μm
DT Thickness	9.4 μm	Pulse Width (FWHM)	2 ns
Simulation Results			
Neutron Yield	10^{17}	Total ρR	0.8 g/cm^2
		Spark ρR	0.5 g/cm^2
Gain	3		
		maximum density	
Hydrodynamic Efficiency	7 %	Spark	200 g/cm^3
		Cold Fuel	600 g/cm^3

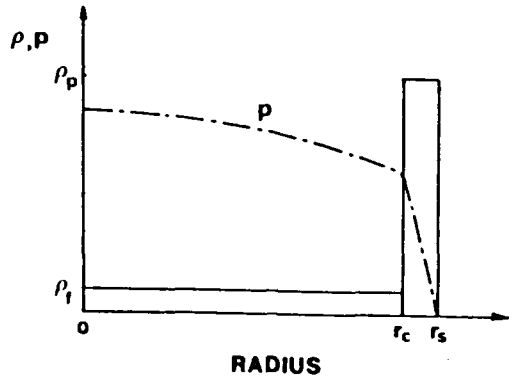

Fig. 1. Spatial profiles of density and pressure of background plasmas for the case with $\rho_p/\rho_f = 10$ and $r_c/r_s = 0.9$.

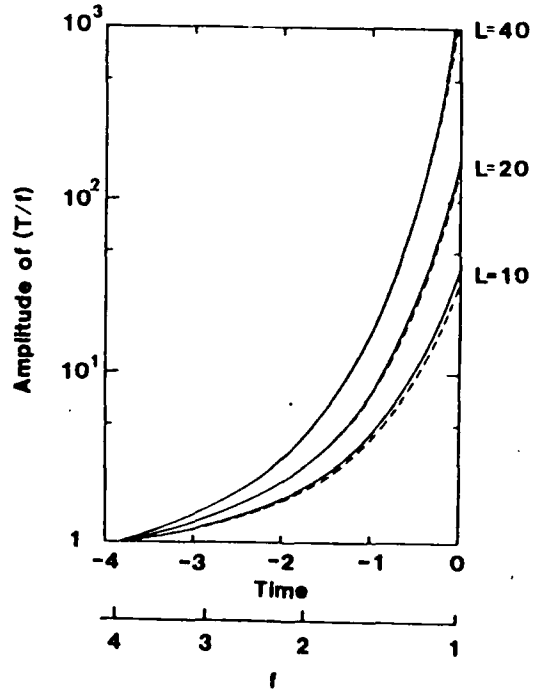

Fig. 2. Temporal evolutions of perturbation amplitudes for $\ell = 10$, 20, and 40. The broken lines show the approximated growth rate.

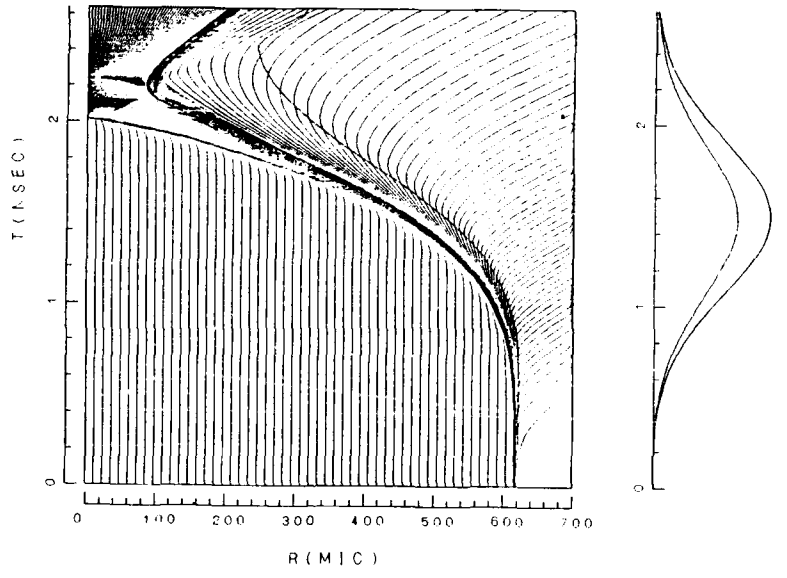

(a)

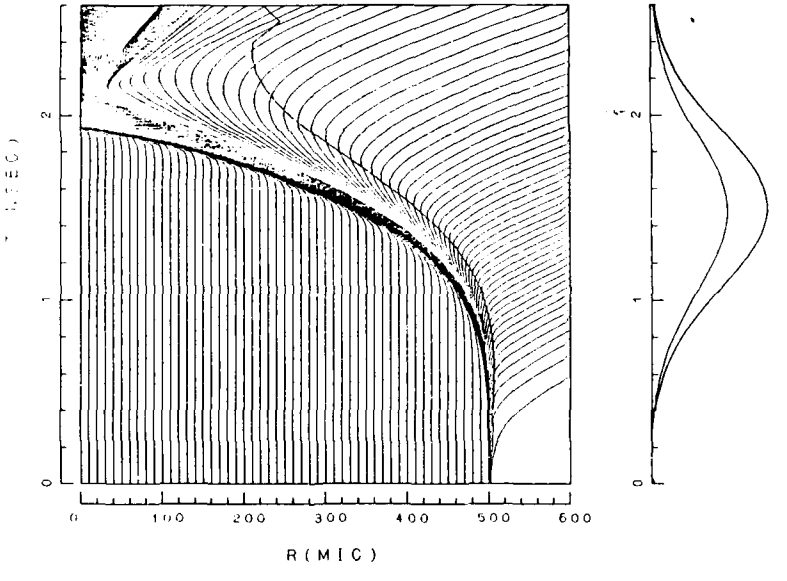

(b)

Fig. 3. r-t diagrams of large high aspect ratio target implosions. (a) target radius; $R_0 = 618\mu m$, thickness; $\Delta R = 1.3\mu m$ and DT gas pressure; $P_f = 6.2atm$ (b) $R_0 = 500\mu m$, $\Delta R = 1.5\mu m$, and $P_f = 2atm$. In the right hand sides of the figures, the laser pulse shape and the absorbed laser power are shown.

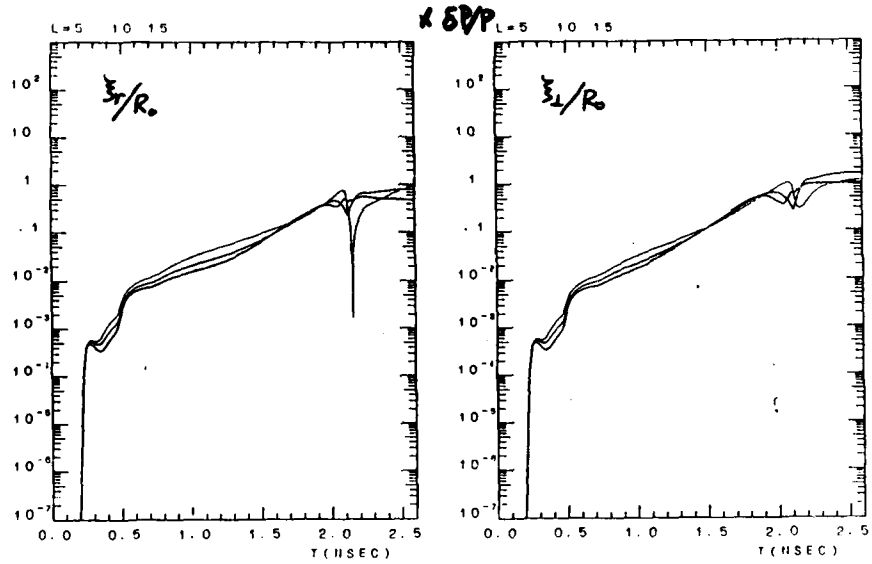

(a)

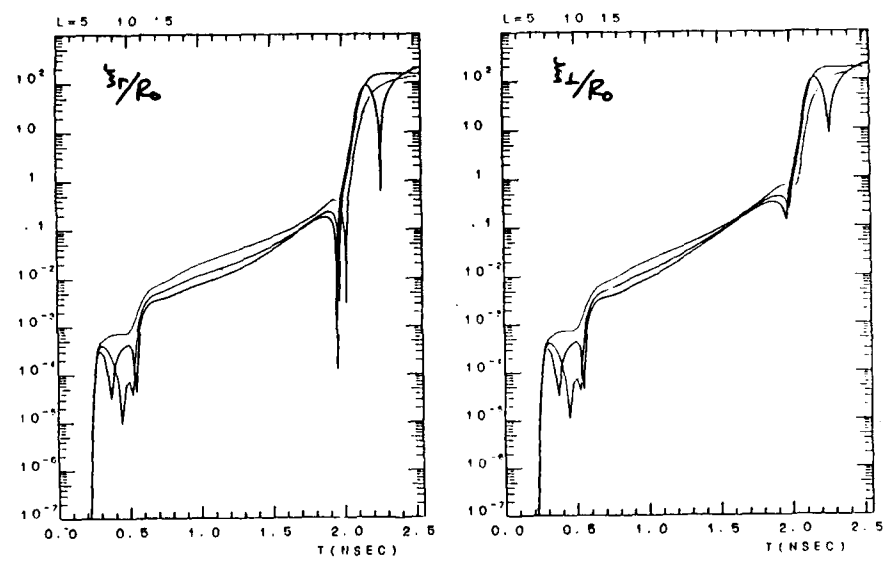

(b)

Fig. 4. Perturbation amplitudes of Rayleigh-Taylor Modes on the contact surface. (a) and (b) correspond to Figs. 3(a) and (b) respectively.

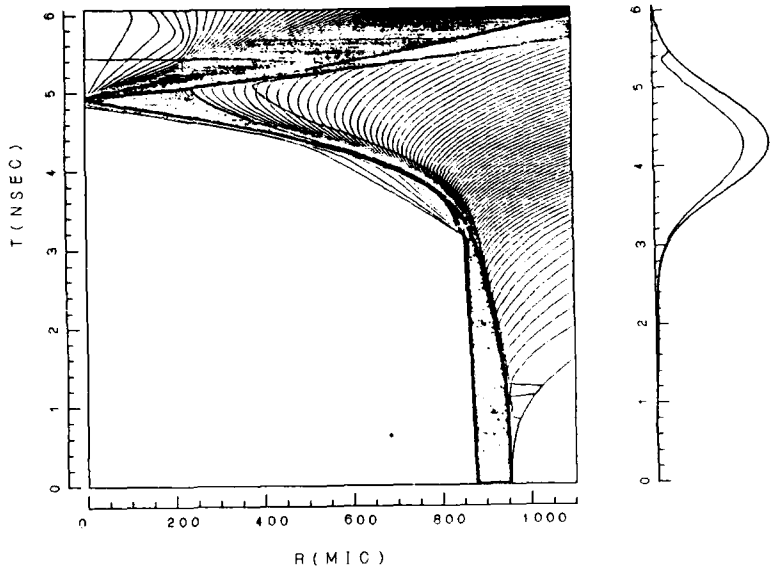

(a)

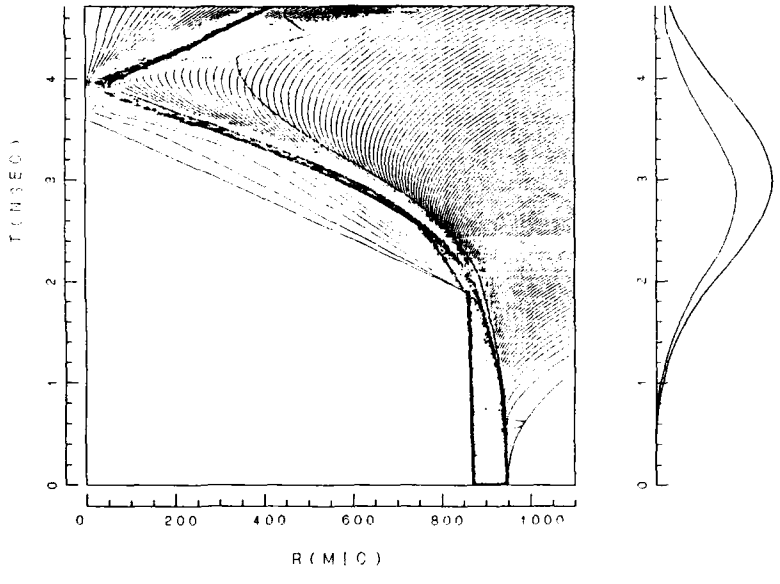

(b)

Fig. 5. r-t diagrams of a tailored pulse (a) and a gaussian pulse implosions (b) of foam cryogenic targets.

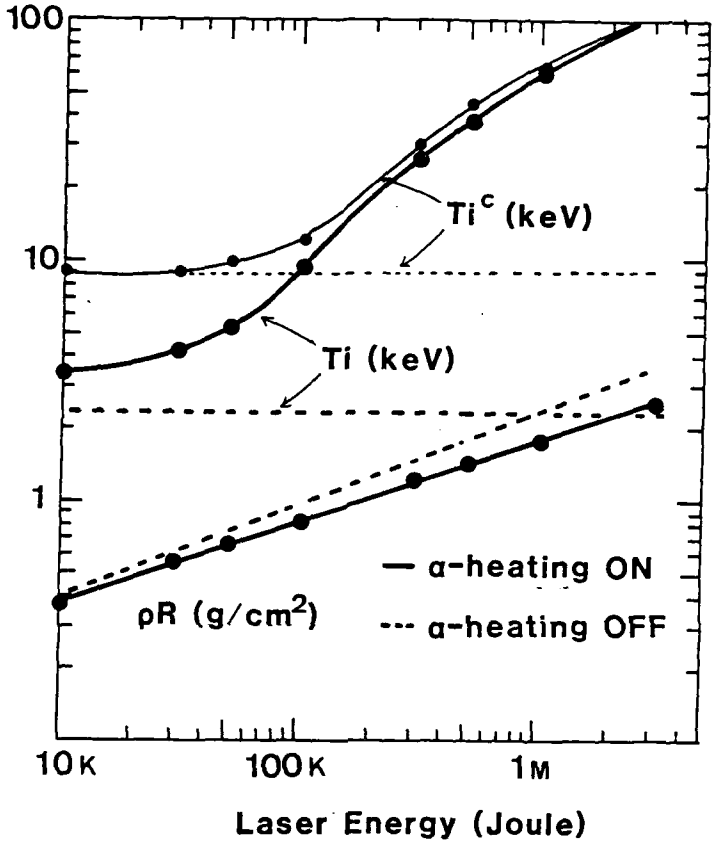

Fig. 6. Laser energy dependence of the fuel ρR and the averaged fuel temperature (T_i) and the temperature of the hot spark (T_i^c). The solid and dotted lines show the simulation results with and without alpha-particle heating respectively.

Efficient Shell Implosion and Target Design

M.Murakami, K.Nishihara, and H.Takabe

Institute of Laser Engineering, Osaka University
2-6, Yamada-Oka, Suita, Osaka, 565, Japan

I. INTRODUCTION

The optimization of the laser and thermonuclear target system is of great interest in inertial confinment fusion (ICF). Spherical compressions have crucial problems such as the Rayleigh-Taylor (R-T) instability or fuel+pusher mixing at stagnation phase. Recently, by careful choice of the implosion mode, neutron yields as high as 10^{13} have been achieved at Institute of Laser Engineering (ILE), Osaka University, by using the twelve-beam green GEKKO XII laser[1]. In the experiments, large-high-aspect-ratio targets[1-3] (LHART) were used so that the stagnation phase is less important for neutron production. Thus, the optimum aspect ratio is one of key variables in the design of ICF pellet.

In Sec.II, we show that the coupling efficiency is essentially a function of the aspect ratio. Then, in Sec.III, we develop a simple model to estimate plasma parameters at peak compression, and show its validity by comparing with a large amount of experimental data. In Sec.IV, we discuss how nonuniformities of absorption and/or shell thickness affect the neutron production. In Sec.V, a scaling for an optimum initial radius versus the laser energy is derived. In Sec.VI,we show the comparison between the theory and experiments for CD shell targets. Sec.VII is devoted to a summary.

Thus a main point of this paper is that the model analysis leads to a simple, qualitative, physical picture of ablative implosions of high-aspect-ratio targets. The theoretical understanding of these implosions has been

obtained mainly from many expensive numerical simulations. Therefore, the simple analytic modeling presented here may be used to assess scaling behavior based on experiments and simulations. The detailed simulation results will be discussed elsewhere.[1)]

II. SIMPLE MODEL FOR ABLATIVE IMPLOSION

To increase neutron yield, required is a target design leading to a maximum coupling efficiency,[4)] which is composed of absorption, hydrodynamic, and transfer efficiencies. In this section, we show that these efficiencies are predominantly controlled by the aspect ratio.

A. HYDRODYNAMIC EFFICIENCY

When we assume a constant mass ablation rate and a constant ablation velocity, the implosion dynamics of a spherical shell, such as the implosion velocity, is found to be determined only by the implosion parameter given by[5,6)]

$$\alpha = \frac{1}{\chi} \frac{\rho_{C-J}}{\rho_0} \frac{R_0}{\Delta R_0} , \qquad (1)$$

where $\chi \equiv P_a/P_{C-J}$ (P_a: ablation pressure, P_{C-J}: pressure at the Chapman-Jouguet (C-J) point) is a constant, and ρ_{C-J} and ρ_0 are the mass density at the C-J point and that of initial state, and $R_0/\Delta R_0$ the initial aspect ratio. ρ_{C-J} can be taken as the critical density in use of 0.53μm-light* (0.013 g/cm^3) and $\chi = 1.4$, which are confirmed by the simulations.

---

* In use of shorter wavelength laser than 0.53μm, ρ_{C-J} becomes less than the critical density, since the bulk of laser energy will be absorbed by underdense plasma before the laser light reaches the critical point.

Although the mass ablation rate and ablation velocity are not always constant, this simple modeling does not, as a rule, alter the qualitative picture of the ablative implosion dynamics. Moreover, the hydrodynamic and transfer efficiencies intrinsically depend on the total exhaust mass rather than the time history of the mass ablation rate and ablation velocity. When the shell reaches the center, unablated mass normalized by the initial mass, $\tilde{M} = M/M_0$, is obtained by the implosion parameter through the following equation,

$$\tilde{M}(1 - \ln\tilde{M}) = 1 - \alpha/3 \ . \qquad (2)$$

The hydrodynamic efficiency, which is a fraction of absorbed energy converted into the kinetic energy of the shell, is then given by[6)]

$$\eta_h = \frac{(1/2)\chi^2 \tilde{M} \ln^2 \tilde{M}}{(\chi^2 - \chi + 3 + Z^2 I_H/3T)\tilde{\Delta M} + (\chi^2 - \chi)\tilde{M}\ln\tilde{M}}, \qquad (3)$$

where $\tilde{\Delta M} = 1 - \tilde{M}$, and $Z^2 I_H/3T$ represents ionization loss of ablated plasma (Z: ionization state, I_H: ionization energy of a hydrogen atom, T: temperature behind the C-J point). Numerical simulations for glass microballoon (GMB) targets in use of 0.53μm-light show that the analytic formulation, eq.(3), with a value of $Z^2 I_H/3T = 2$ excellently reproduces the simulation results. Thus, with those values mentioned above, eqs.(1),(2) and (3) are reduced to the following expressions:

$$\tilde{M}(1 - \ln\tilde{M}) = 1 - \frac{1}{800}\frac{R_0}{\Delta R_0} \qquad (4)$$

and

$$\eta_h = \frac{\tilde{M}\ln^2\tilde{M}}{5.7\Delta\tilde{M} + 0.57\tilde{M}\ln\tilde{M}} \quad . \qquad (5)$$

Eqs.(4) and (5) show that the hydrodynamic efficiency is a function of the aspect ratio.

B. TRANSFER EFFICIENCY

The transfer efficiency, which is a fraction of the shell kinetic energy converted into the thermal energy of the fuel, can also be expressed by the aspect ratio as follows. At peak compression, the kinetic energy of an imploding shell, E_{sk}, is assumed to be all converted into thermal energy of both the shell and the fuel. In such stage, reflected weak shock waves within unablated matter smooth out the pressure profile to a constant P, to mass density of the shell ρ_s, and the fuel ρ_f. Then, the energy conservation law leads to

$$E_{sk} = (M/\rho_s + M_f/\rho_f)P/(\gamma - 1) \ ,$$

where γ (=5/3) is the specific heats ratio and $M_f = (4\pi/3)R_0^3\rho_{f0}$ is the constant fuel mass (ρ_{f0} is the initial mass density of the fuel). Further, due to the thermal conduction, the plasma temperatures of the fuel and the pusher are of the same order of magnitude. We can then simply assume that the number densities of them are the same, i.e., $\rho_s/\rho_f \simeq A_s/A_f$, where A_s and A_f denote the average mass number of the shell and the fuel. The transfer efficiency is therefore given by

$$\eta_t = \frac{M_f/\rho_f}{M/\rho_s + M_f/\rho_f} = \left(3\tilde{M}\frac{\rho_0}{\rho_{f0}}\frac{A_f}{A_s}\frac{\Delta R_0}{R_0} + 1\right)^{-1}, \qquad (6)$$

where the relation, $M_0 = 4\pi R_0^2 \Delta R_0 \rho_0$, was used. As a result, when using a GMB target and DT fuel (A_s/A_f=8) with the initial pressure p_{f0} (atm) at room temperature, eq.(6) is reduced to

$$\eta_t = \{4.7\times10^3\tilde{M}(p_{f0}R_0/\Delta R_0)^{-1} + 1\}^{-1} . \qquad (7)$$

Thus, the transfer efficiency is also a function of the aspect ratio (see eq.(4)).

Figure 1 shows the hydrodynamic and transfer

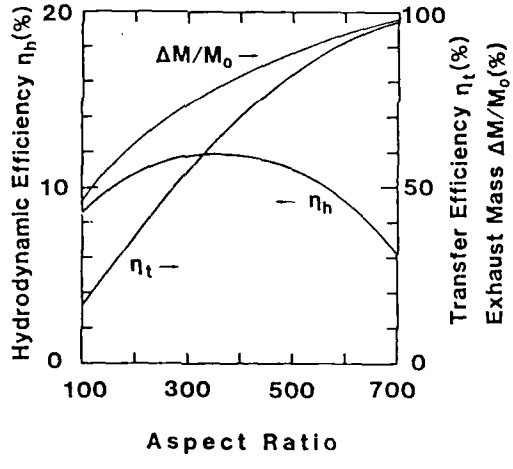

Fig. 1 Hydrodynamic and transfer efficiencies and shell mass at maximum compression as functions of the aspect ratio for a green laser and a glass microballoon target filled with a DT gas fuel of 5 atm pressure.

efficiencies and normalized exhaust mass as a function of the aspect ratio obtained from eqs.(4),(5) and (7), where p_{f0}=5atm is used for the transfer efficiency. As can be seen in Fig.1, the transfer efficiency and the exhaust mass increase with the aspect ratio, while the hydrodynamic efficiency has a peak value of 12 % at $R_0/\Delta R_0$ = 350 and $\Delta M/M_0$ = 0.77.

C. COUPLING EFFICIENCY AND ION TEMPERATURE

The coupling efficiency η_c, which is a fraction of the input energy E_L converted into the thermal energy of the fuel, is defined as

$$\eta_c = \eta_a \eta_h \eta_t \ , \qquad (8)$$

where η_a is an absorption efficiency and has values of 50-70 % in use of 0.53μm-light[3]. Thus, we easily find that the coupling efficiency is a function of the aspect ratio from eqs.(4)-(8).**

** In ref.1, the coupling efficiency is given in a form: $\eta_c \propto M_f/M_T$ ($M_f=(4\pi/3)R_0^3\rho_{f0}$ is the fuel mass, and $M_T \simeq M_0=4\pi R_0^2\rho_0$ is the target mass). It has the same proportionality as eq.(8) in a limited case as follows. Since the hydrodynamic efficiency little depends on the aspect ratio ($200<R_0/\Delta R_0<500$, see Fig.1)in our model, the coupling efficiency changes with the transfer efficiency when the absorption efficiency is constant. Therefore, the coupling efficiency, eq.(7), can be expressed, when the aspect ratio is relatively low, as $\eta_c \propto \eta_t \propto \hat{M}^{-1} p_{f0} R_0/\Delta R_0 \propto \hat{M}^{-1} M_f/M_0$.

Plasma temperature averaged over the ions and electrons of the fuel is then calculated with the coupling efficiency as

$$T = \eta_c E_L/3N_0 \ , \qquad (9)$$

where $N_0 = M_f/\mu_{DT}$ (μ_{DT} is the average DT atomic mass) is the

total ion number of the fuel.

Figures 2(a) and (b) show the coupling efficiency and ion temperature, thus obtained, as a function of the aspect ratio; the dashed-dotted, solid and dashed lines correspond to the gas pressures of 3, 5 and 10 atm, respectively (these notations are the same for the figures shown below). For the theory, in Fig.2(a), the fixed parameter is only the absorption efficiency, η_a = 0.65; in addition, in Fig.2(b), E_L=10kJ and R_0=0.5mm are used. Solid circles represent various experimental results obtained at ILE; the targets were DT gas-filled GMB with aspect ratios of 110-625, diameters of 0.70-1.5 mm, gas pressures of 2-13 atm; the laser outputs at 0.53μm in Gaussian pulse were 6-15 kJ in 1 ns. In the experiments, the ion temperatures were measured by the method of neutron time of flight. The energy balance among the beams was within 5% deviation. The targets were dodecahedrally irradiated with F/3 lenses under a focusing condition of D/R_0 = -5, where D is the displacement of the focal point from the target center. The sphericity and wall nonuniformity of the targets were better than 1% and 5%, respectively. In Figs.2(a) and (b), the analytic lines reproduce well the experimental results as an envelope line. The maximum coupling efficiency by the theory is obtained with aspect ratio of 450-550 at corresponding values of gas pressure of 10~3 atm. It should be noted here that ion temperature in the hot core, after the collapse of a convergent shock, is appreciably higher than that of electron; this is due to the difference of thermal conductivity between them. Simulation results show that the ion temperature is roughly twice the electron temperature[1]. Therefore, when taking account of $T_i = 2T_e$, the ion temperatures in Fig.2(b) (lines) are higher than those obtained by eq.(9) by 4/3-fold.

III. PLASMA PARAMETERS AT PEAK COMPRESSION

In contrast with the coupling efficiency and ion temperature, plasma parameters at peak compression such as

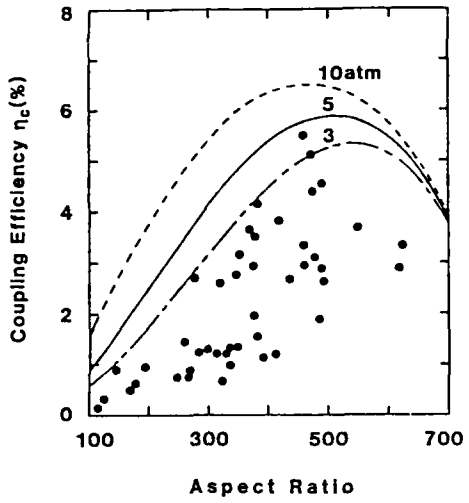

Fig.2(a) Experimental target coupling efficiencies (dotts) estimated from measured ion temperatures (Fig.8) Analytical values are calculated with the assumption of η_e=0.65. The solid line is for P_{fo}=5 atm, the dotted line for 10atm and dash-dotted line for 3 atm.

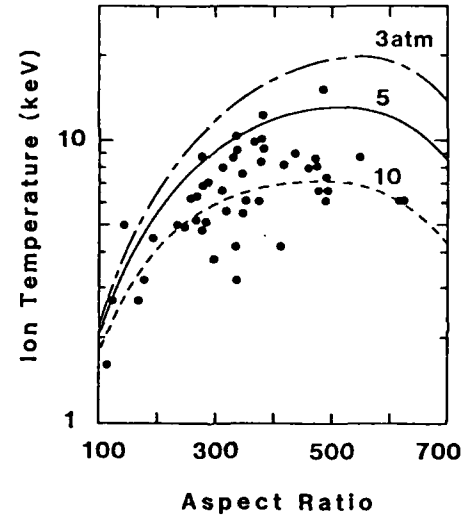

Fig.2(b) Ion temperatures (dotts) observed from neutron time of flight measurements versus target aspect ratios for the LHART. Analytical values (lines) are estimated from the coupling efficiencies and the assumptions of T_i=2T_e, E_L=10kJ and R_o=500μm with various initial DT fuel pressures, solid line for P_{fo}=5 atm, dotted line 10 atm and dash-dotted line 3 atm.

fuel ρ and ρR and resultant neutron yield, remarkably depend on a compression scheme. Recent experiments performed at ILE have demonstrated that high neutron yields can be achieved by using very thin high-aspect-ratio targets; the first half of a Gaussian pulse is utilized as a tailored pulse, which synchronizes well with the shell implosion. In the following, we develop a simple model to estimate the plasma parameters, which are produced at peak compression as a result of successive weak shocks and sequential adiabatic compression. It is shown schematically in Fig.3. The solid line is the shell/fuel contact surface. The dotted line shows how the shock wave is transmitted into the fuel, and collapses at $t = t_1$. In our interesting case, with those target and laser parameters mentioned earlier, a reflected shock wave will not be formed after the collapse of the convergent shock. This is due to ion-preheating of the fuel[7]; the ion mean free path becomes comparable to the size

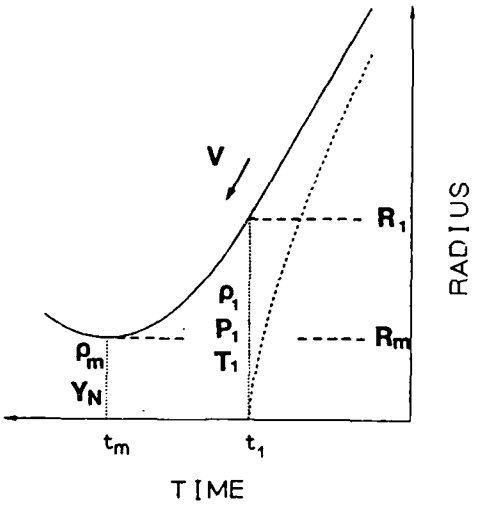

Fig.3 A schematic picture of ablative implosion of a high-aspect-ratio target. The solid line is the fuel/pusher contact surface. The dotted line shows how the shock wave is transmitted in the fuel.

of the compressed fuel. Thus, we can assume that the fuel is adiabatically compressed from $t = t_1$ to t_m (peak compression). When the ion mean free path becomes much shorter than the fuel core size, we must interpolate another compression process including the reflected shock wave .

By following the scaling law of the absorption efficiency,[8] the absorbed intensity I_a is expressed as

$$I_a = \eta_a I = (0.9 - 0.5\log_{10} I_{14})I \ , \qquad (10a)$$

and

$$I = P_L/4\pi R_0^2 \ . \qquad (10b)$$

where I is the irradiated laser intensity, P_L the peak laser power, and the subscript "14" denotes normalization by 10^{14} W/cm^2. The mass ablation rate $\dot{m}$ is also given by the scaling law experimentally obtained for 0.53μm-light[9],

$$\dot{m} = 4.5\times10^5 \ I_{a14}^{0.5} \ (g/cm^2.s) \ . \qquad (11)$$

The ablation pressure P_a is related to the mass ablation rate by the relations, $\dot{m} = \rho_{C-J}u$, and $P_a = \chi\rho_{C-J}u^2$, where u is the ablation velocity, and χ is a scaling factor as mentioned previously and χ=1.4. We can thus obtain

$$P_a = \chi\dot{m}^2/\rho_{C-J} \ . \qquad (12)$$

After the shell passes around the one third of its initial radius, it almost finishes the mass ablation and reaches an imploding velocity,

$$V = \chi u \ln\tilde{M} \ . \qquad (13)$$

At $t = t_1$, the pressure of shock-compressed fuel P_1, induced by the imploding shell with the velocity V, is estimated with the aid of eqs.(12) and (13):

$$P_1 = \{(\gamma + 1)/2\} \ \rho_{f0}V^2$$

$$= 1.9(\rho_{f0}/\rho_{C\text{-}J})P_a \ln^2\tilde{M} \quad . \tag{14}$$

The fuel density at $t = t_1$,

$$\rho_1 = \tilde{\rho}_1 \rho_{f0} \quad , \tag{15}$$

depends much on the way how the shell is accelerated by the tailored pulse ($\tilde{\rho}_1$ is the density compression rate), and simulation results have shown $\tilde{\rho}_1 \simeq 30$ in the regime concerned. Thus, the temperature T_1 at $t = t_1$ averaged over the electrons and ions is given with the aid of eqs.(14) and (15) by

$$T_1 = P_1/(2\rho_1/\mu_{DT})$$

$$= 0.19(P_a/1\text{Mbar})\tilde{\rho}_1^{-1} \ln^2\tilde{M} \quad (\text{keV}), \tag{16}$$

We note here that the temperature of eq.(16) does not depend on the initial gas pressure.

As mentioned before, the adiabatic compression follows the shock compression leading to the maximum density at $t = t_m$,

$$\rho_m = \rho_1(\eta_c E_L/3N_0T_1)^{3/2} \quad . \tag{17}$$

Consequently, we can evaluate the neutron yield,

$$Y_N = (4\pi/3)R_m^3(n_m/2)^2\langle\sigma v\rangle R_m/4c_s$$

$$= 2.0\times10^{-9}\, n_m N_0^{4/3}\langle\sigma v\rangle T_i^{-1/2} \quad , \tag{18}$$

where $n_m = \rho_m/\mu_{DT}$, and $R_m = R_0(\rho_{f0}/\rho_m)^{1/3}$ is the core radius; $\langle\sigma v\rangle$ and c_s are Maxwellian-averaged fusion reaction rate and the sonic speed at $t = t_m$ (cgs units), as a function of the ion temperature (keV), respectively. Here, we postulated the relation, $T_i = 2T_e = (4/3)T$ (see eq.(9)).

Figures 4(a), (b) and (c) show the comparison between the theory and the experiments for the neutron yield, and fuel ρ and ρR; fuel ρR were measured from x-ray pinhole image, and then ρ were estimated with the ρR values by the mass conservation assumption. Fixed parameters for the theory are R_0 = 0.5 mm, E_L = 10 kJ, P_L = 10 TW, and $\tilde{\rho}_1$ = 30. The solid circles represent the experimental results, of which laser and target conditions are the same as those depicted in Figs.2(a) and (b). In paticular, Fig.4(a) includes the neutron yields obtained by the simulations as open circles, and shows fairly good agreement with the analytic estimation. In the model, the maximum neutron yields are obtained at $R_0/\Delta R_0 \sim 400$, and this figure agrees well with the experimental results.

IV. NONUNIFORMITY AND REDUCTION OF NEUTRON YIELD

As can be seen in Fig.4(a), the absolute values of neutron yields obtained by the experiments are much smaller than those of the theory and simulations. This is probably because the R-T instability and/or fuel+pusher mixing during the deceleration phase from $t = t_1$ to t_m lead to a drastic reduction of neutron yield. In the following, we evaluate the reduction of neutron yield due to the R-T instability during the deceleration phase.

Hattori et al.[10] studied the R-T instability on the fuel/pusher contact surface by modeling the stagnation dynamics with the self-similar motion, and the R-T instability is found to grow as (γ = 5/3),

$$\delta = \delta_0 f \exp\{\mu^{1/2}(\pi/2 - \arcsin f)\} , \qquad (19a)$$

and

$$\mu = \{\ell(\ell + 1) + 1)^{1/2} + 1 , \qquad (19b)$$

where δ_0 and ℓ are the perturbation amplitude of the contact surface at $t = t_1$ and the mode number, respectively. In addition, f represents the reciprocal of radial compression rate,

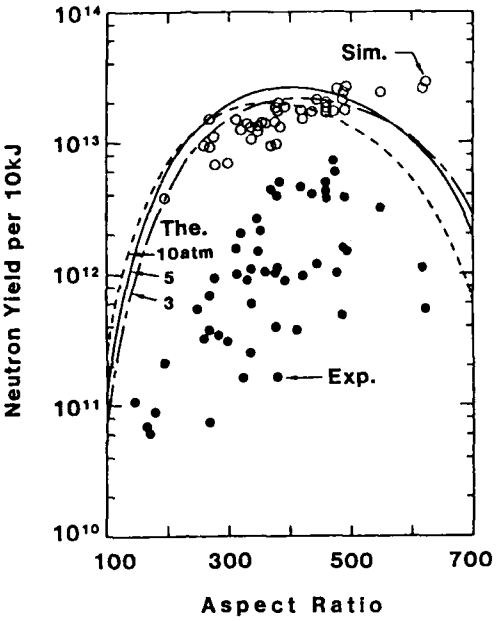

Fig.4(a) Comparison of neutron yields per 10 kJ between the experiments (solid circles), the simulations (open circles), and the model (lines). For the analytic lines (3, 5 and 10 atm), fixed parameters are P_L = 10 TW and R_0 = 0.5 mm.

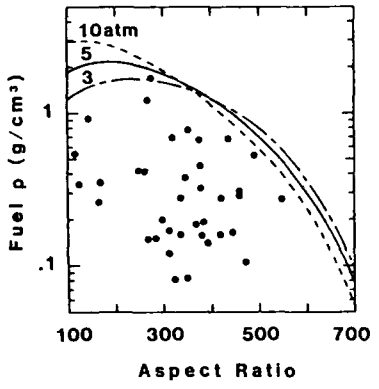

Fig.4(b)

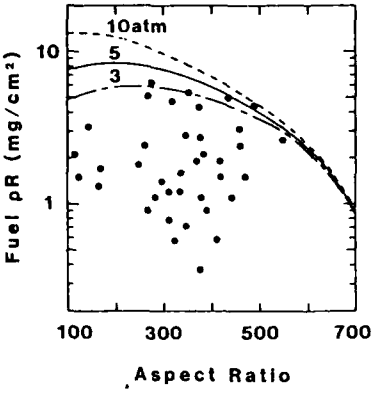

Fig.4(c)

$$f = R_m/R_1 = (3N_0T_1/\eta_c E_L)^{1/2} , \qquad (20)$$

where R_1 and R_m are the shell radius at $t = t_1$ and t_m. Moreover, we can relate the amplitude, δ_0, to the wall nonuniformity of the shell at initial state, $d/\Delta R_0$, and/or the laser absorption, $\Delta I_a/I_a$. With the aid of eq.(11), the nonuniformity ε is expressed as

$$\varepsilon = d/\Delta R_0 = \Delta\dot{m}/\dot{m} = 0.5\Delta I_a/I_a . \qquad (21)$$

We consider that the nonuniform acceleration of the shell, which is induced by the nonuniformities of wall thickness and/or of absorption, results in the amplitude δ_0. Therefore, δ_0 can be a function of the aspect ratio and the nonuniformity ε; δ_0 is numerically calculated by solving the rocket equation. By assuming that the neutrons are effectively generated inside of the mixing layer (the width of which can be taken to be $\delta/2$), we obtain the effective neutron yield in the form;

$$Y_N(\text{eff})/Y_N(\text{ana}) = \{1 - (\delta/2)\}^3 , \qquad (22)$$

where Y_N(eff) and Y_N(ana) are an effective neutron yield, which is expected to be equal to the experimental one, and that of the model analysis under the symmetry assumption given by eq.(18), respectively. Figure 5 shows a schematic picture describing eq.(22); the shaded area is the effective core region at $t = t_m$. In Fig.6, solid circles denote the values of the neutron yields, experimentally obtained, devided by the analytic ones, where the theory is applied to all targets irradiated with different laser energies. The solid lines denote the reduction of neutron yield estimated with eqs.(19)-(22) as a function the aspect ratio with ε = 2 to 8%, where fixed parameters are R_0 = 0.5mm, E_L = 10kJ, P_L = 10TW, and p_{f0} = 3atm. In addition to these parameters, we selected ℓ = 6, which results from the irradiating

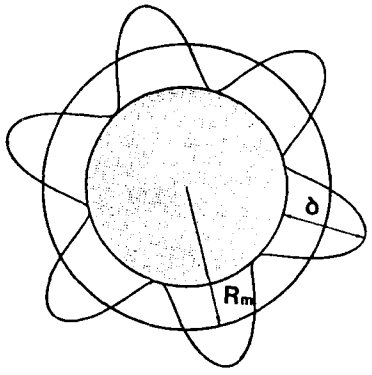

A schematic picture showing reduction of neutron yield due to the R-T instability. R_m is the averaged radius of the contact surface at peak compression, and δ is the amplitude of the R-T instability. The shaded area is taken to be an effective core region.

Fig.5

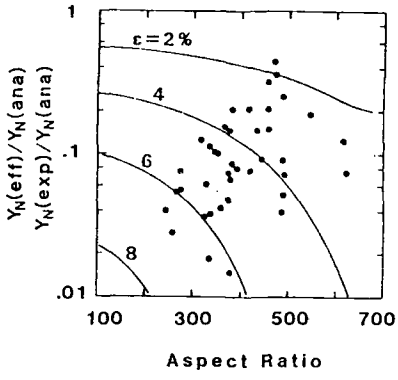

Solid circles show the comparisons of neutron yields between the experiments and the theory as a function of the aspect ratio. The solid lines are obtained from the model as a function of the nonuniformity of the wall thickness and/or absorption, where fixed parameters are R_0 = 0.5 mm, E_L = 10 kJ, P_L = 10 TW, p_{f0} = 3 atm, and the mode number ℓ = 6 is used.

Fig.6

configuration of the GEKKO XII laser system[11]. As seen in Fig.6, a higher aspect ratio can lead to a drastic reduction of neutron yield in the model.

Alternatively, we can estimate the nonuniformity from Fig.6 corresponding to each experimental result. Figure 7 shows the histgram, thus obtained, when we attribute the reduction of neutron yield only to the absorption nonuniformity. The solid line is a Gaussian profile with standrd deviation obtained from the histgram, and 10% of absorption nonuniformity on an average can be concluded.

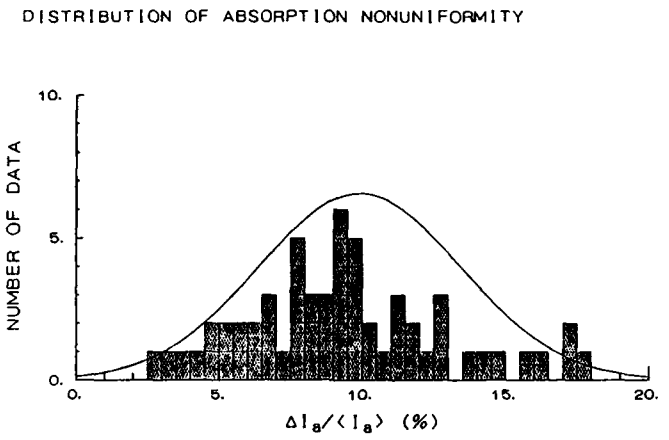

Fig.7 Histgram for absorption nonuniformity obtained by applying the model to all experimental results.

V. OPTIMUM INITIAL RADIUS

Finally, let us estimate the optimum scaling of the target radius regarding the laser energy. Here we fix the pulse duration τ_L of 1 ns. Then, with the aid of eqs.(10) and (11) and the relations, $E_L = P_L\tau_L$, and $R_0 = u\tau_L$, which is obtained at $\Delta M/M_0 = 0.85$, we can obtain the optimum initial radius as

$$R_0/1\ \text{mm} = 0.31(\eta_a E_L/1\ \text{kJ})^{0.25} . \qquad (23)$$

Thus, eq.(20) predicts a target diameter of 0.97 mm with E_L = 10 kJ and η_a = 0.6, which is quite close to an optimim one obtained through the experiments.

VI. CD Shell Targets

It is hard to obtain a high density compression by using a gas fuel target. High density and ρR can be achieved

by using the cryogenic or foam cryogenic targets instead of the gas fuel targets. The foam cryogenic target is free from the Rayleigh-Taylor instability in the deceleration phase because of no pusher-fuel contact surface. The mass density of the foam cryogenic target may be of the order of 0.2 g/cm^3. Thus the optimum aspect ratio of the foam cryogenic target is much smaller than that of the glass microballoon target. This also reduces the growth rate of the Rayleigh-Taylor instability at the ablation front in the acceleration phase.

To study the implosion properties of the shell target we have used CD plastic targets, of which mass density is approximately 1.1g/cm^3. The experimental conditions are summarized as

$$8 < E_L < 10 \text{ kJ} \quad \text{Laser Energy:}$$
$$600 < 2R_0 < 1050 \ \mu m \quad \text{Target Diameter:}$$
$$4 < \Delta R_0 < 14 \ \mu m \quad \text{Thickness:}$$

The pulse duration is 1ns, and focusing condition is d/R=-5.

Because of the low Z compared with the GMB, the laser absorption is slightly smaller than that for GMB, about 40 to 65%. However the optimum radius does not change much from the LHART, because of its weak dependence on the absorption efficiency. On the other hand, the optimum aspect ratio is approximately 2/5-fold of that for the LHART, i.e., ∂160, because of the low mass density.

Fig.8(a) and (b) show the comparison between the theory and experiments of the CD shell targets, for the implosion velocity and ion temperature, respectively. The implosion velocities are measured from x-ray streak image data. In the theory, the ion temperatures are estimeted from the implosion velocity assuming that $T_e/T_i=0.3$. As clearly seen in the Figure, they are in good agreement.

VII. SUMMARY

We have developed an analytic model describing the implosion property of high-aspect-ratio targets. As a result, we have shown that the hydrodynamic and transfer

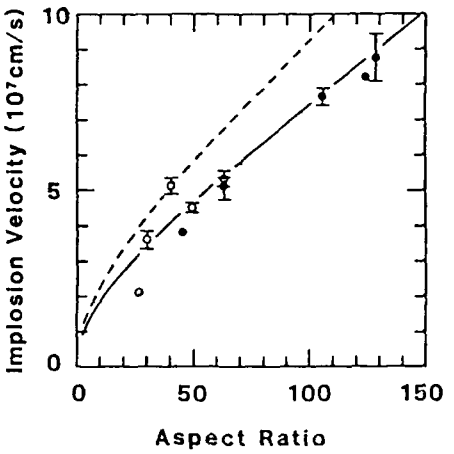

Fig.8(a) Implosion velocities of CD shell targets measured from streak camera images: Open circles for diameter of 600∿700μm, closed circles 900∿1000μm. Analytical implosion velocities and shell mass at maximum compression are obtained for $2R_o$=700μm (dotted line), and $2R_o$=1000μm (solid line).

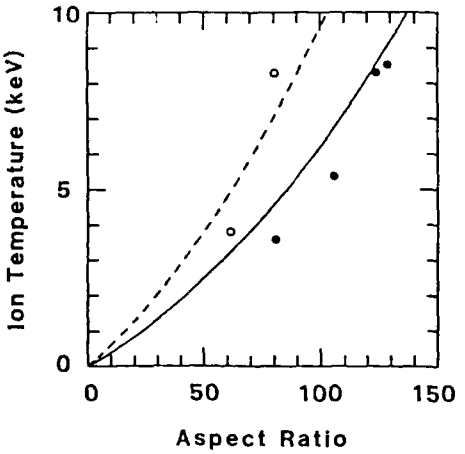

Fig.8(b) Ion temperatures observed from neutron time of flight measurements versus target aspect ratios for the CD shell: Open circles for diameter of 600∿700μm and closed circles for 900∿1000μm. Analytical values are estimated from the implosion velocities (Fig.10) with $T_i=3T_e$ dotted line for 600∿700μm in diameter, and solid line for 900∿1000μm.

efficiencies, and consequent coupling efficiency and ion temperature can be expressed as a function of the aspect ratio. Optimum target design, regarding the aspect ratio and the initial radius, can be found with this theory. Furthermore, we have examined this theory by comparing with a large amount of experimental data to show the validity of the theory. Also, the theory developed here well reproduce the simulation results. The modeling to obtain the plasma parameters at peak compression, which is composed of shock and adiabatic compressions, is a simple one and not especially new. However, the unique and important point is that eq.(17), which determines the final condition of plasma, includes the coupling efficiency as a function of the aspect ratio. That is why such plasma parameters as neutron yield, and fuel ρ and ρR are obtained explicitly as a function of the aspect ratio. The reduction of neutron yields from one dimensional analysis can be explained by considering the R-T instability in the deceleration phase[10], which is related to the nonuniformities of the shell thickness and/or the absorption.

References

1)H.Takabe et al., submitted to Phys.Fluids.

2)M.C.Richardson, P.W.McKenty, R.L.Keck, F.J.Marshall, D.M.Roback, C.P.Verdon, R.L.McCrory, J.M.Soures, and S.M.Lane, Phys.Rev.Lett.56, 2048(1986).

3)C.Yamanaka, S.Nakai, T.Yabe, H.Nishimura, S.Uchida, Y.Izawa, T.Norimatsu, H.Azechi, M.Nakai, H.Takabe, T.Jitsuno, K.Mima, M.Nakatsuka, T.Sasaki, M.Yamanaka, Y.Kato, T.Mochizuki, Y.Kitagawa, T.Yamanaka, and K.Yoshida, Phys.Rev.Lett.56, 1575(1986).

4)H.Takabe, ILE Quarterly Progrees Report, Osaka Univ. ILE-QPR-86-18, p2(1986).

5)M.Murakami and K.Nishihara,Jpn.J.Appl.Phys.25, L257(1986).

6)M.Murakami and K.Nishihara,Jpn.J.Appl.Phys.26, 1132(1987).

7)T.Yabe, ILE Reserch Report, Osaka Univ., ILE8708P(1987).

8)For example, H.Nishimura et.al., Can.J.Phys.64, 986(1986).

9)N.Miyanaga, private communication.
10)F.Hattori, H.Takabe and K.Mima, Phys.Fluids 29, 1719(1986).
11)K.Mima, K.Sawai and H.Takabe, ILE Quarterly Progress Report, Osaka Univ., ILE-QPR-83-7, p28(1983).
12)B.Ahlborn, M.H.Key and A.R.Bell, Phys.Fluids25, 541(1982).

MICROINSTABILITIES IN ION BEAM PROPAGATION

Toshio Okada and Keishiro Niu*
Department of Applied Physics, Tokyo University of Agriculture and Technology, Naka-machi, Koganei-shi, Tokyo 184
*Department of Energy Sciences, The Graduate School at Nagatsuta Tokyo Institute of Technology, Nagatsuta, Midori-ku, Yokohama 227

Microinstability for a rotating light ion beam (LIB) fusion system is investigated. Stability conditions including the effects of fractional current neutralyzation, rotation of LIB and beam temperature are derived for propagation through a background plasma. The results are illustrated by examining the various parameters of a rotating proton beam propagating in a plasma.

§1. Introduction

In the investigation of inertial confinement fusion by high power light ion beams, it is one of the most important problems to propagate the LIB stably through the chamber to the target. There has been many investigations[1)-3)] of a stability analysis of LIB propagation through a plasma. However, previous theoretical analysis of the propagation has been carried out mostly for a model in which the ion beam is completely neutralized and does not rotate. In recent paper[4)] a rotating light ion beam which is assumed to be symmetric about the rotation and propagation is proposed as a energy driver of inertial confinement fusion. In our previous paper[1)] it is pointed out that the filamentation instability is the most deleterious one for LIB propagation in a plasma. To investigate the influence of current neutralization, rotation of LIB and beam temperature on the filamentation instability, we make use of the Vlasov-Maxwell equations including the self magnetic field and the constant magnetic field perpendicular to the direction of the electromagnetic waves. The magnetic field in the propagation direction induced by the rotation of LIB and the fractional current neutralization have the tendency to stabilize the filamentation instability.

§2. Stability analysis

We assume that equilibrium and perturbed beam space charge field are completely neutralized by the plasma. We introduce a cylindrical polar coordinate system (r, Θ, z) with z-axis along the axis of symmetry. To obtain a dispersion relation for the filamentation instability, we adopt the linearized Vlasov equation for the j-th component perturbed distribution function $\delta f_j(x,p,t)(j=b,p)$ of the form

$$\left(\frac{\partial}{\partial t} + \mathbf{v}\cdot\frac{\partial}{\partial \mathbf{x}} + e_j \frac{\mathbf{v} \times (B_0^z \mathbf{e}_z + B_0^\theta \mathbf{e}_\theta)}{c} \cdot \frac{\partial}{\partial \mathbf{p}} \right) \delta f_j(\mathbf{x},\mathbf{p},t)$$

$$= -e_j \left(\delta \mathbf{E}(\mathbf{x},t) + \frac{\mathbf{v}\times\delta\mathbf{B}(\mathbf{x},t)}{c}\right) \cdot \frac{\partial}{\partial \mathbf{p}} f_j^0(H,P_\theta,P_z) \qquad (1)$$

where $B_0^z \mathbf{e}_z$ is a uniform magnetic field in the direction of beam propagation, $B_0 \mathbf{e}_\theta$ is an azimuthal self-magnetic field, e_j is the charge of the j-th component, H is the total energy, P_θ is the canonical angular momentum, P_z is the axial canonical momentum. The equilibrium distribution function in (1) can be approximated in the beam-plasma system by

$$f_b^0(H,P_\theta,P_z) = \frac{n_b}{(2\pi m_b T_b)^{3/2}} \exp\left(- \frac{1}{2m_b T_b} \left(p_r^2 + (p_\theta - m_b r \Omega_{rb})^2 + (p_z - m_b V_{zb})^2\right)\right) \qquad (2)$$

$$f_p^0(H,P_\theta,P_z) = \frac{n_p}{(2\pi m_p T_p)^{3/2}} \exp\left(- \frac{1}{2m_p T_p} \left(p_r^2 + (p_\theta - m_p r \Omega_{rp})^2 + (p_z - m_p V_{zp})^2\right)\right) \qquad (3)$$

where n_b is the beam density, T_b is the beam thermal energy, m_b is the beam ion mass, Ω_{rb} is the beam angular velocity, V_{zb} is the axial velocity of the beam, n_p is the background electron density, T_p is the plasma electron mass, Ω_{rp} is the plasma angular velocity and V_{zp} is the axial velocity of the plasma. To obtain the most unstable mode, we consider the interaction between beam ions and background electrons. From equation (1),(2),(3) and linearized Maxwell's equations, we obtain the linear dispersion relation for the filamentation instability of the form[5)]

$$0 = \omega^2 - c^2k_\perp^2 - \sum_{j=b,p} \frac{4\pi n_j e_j^2}{m_j} + \sum_{j=b,p} \frac{4\pi e_j^2}{m_j}$$

$$\times \sum_{n=-\infty}^{\infty} \frac{n(\Omega_{rj}^+ - \Omega_{rj}^-)}{\omega - l\omega_{rj} - n(\Omega_{rj}^+ - \Omega_{rj}^-)}$$

$$\times 2\pi \int_0^\infty dp_\perp p_\perp \int_{-\infty}^{\infty} dp_z \, J_n^2\left(\frac{k_\perp p_\perp / m_j}{\Omega_{rj}^+ - \Omega_{rj}^-} \right) \frac{p_z^2}{p_\perp} \frac{\partial}{\partial p_\perp} f_j^0 \, . \qquad (4)$$

In (4), l is the azimuthal harmonic number, $J_n(x)$ is the Bessel function of the first kind order n and

$$\Omega_{rj}^+ - \Omega_{rj}^- = -\varepsilon_j \omega_{cj} \left(1 - \frac{8\pi e_j}{m_j \omega_{cj}^2} \sum_k n_k e_k \left(1 - \frac{V_{zj} V_{zk}}{c^2} \right) \right)^{1/2} \qquad (5)$$

where $\varepsilon_j = \mathrm{sgn}(e_j)$ and $\omega_{cj} = |e_j| B_0^z / m_j c$.
In obtaining (4), we have introduced the perpendicular momentum variable in the rotating frame, $p_\perp = (p_r^2 + (p_\theta - m_j r \Omega_{rj})^2)^{1/2}$. Assuming that $k^2(T_j/m_j)/(\Omega_{rj}^+ - \Omega_{rj}^-)^2 << 1$, $n_b << n_p$ and $\omega_b^2 V_{zb}^2 >> \omega_p^2 V_{zp}^2$, equation (4) reduces to (for l=0 and $|\omega|^2 << c^2k^2$)

$$\omega^2 = (\Omega_{rb}^+ - \Omega_{rb}^-)^2 - \frac{\omega_b^2 k^2}{\omega_p^2 + c^2 k_\perp^2} (V_{zb}^2 + T_b/m_b) \qquad (6)$$

where

$$(\Omega_{rb}^+ - \Omega_{rb}^-)^2 = \omega_{cb}^2 \left(1 + 2(\omega_b V_{zb})^2 / (\omega_{cb} c)^2 (1 - f_m) \right). \qquad (7)$$

$f_m = -(n_p e_p V_{zp})/(n_b e_b V_{zb})$ is the fractional current neutralization by the background electron plasma for a charge neutralized system. The maximum growth rate of the filamentation instability is given by

$$\delta_{max} = \left(\frac{\omega_b^2 (V_{zb}^2 + T_b/m_b)}{c^2} - \omega_{cb}^2 \left(1 + \frac{2\omega_b^2}{\omega_{cb}^2} \frac{V_{zb}^2}{c^2} (1 - f_m) \right) \right)^{1/2}. \qquad (8)$$

From (8), we expect that there may be a range of density for which LIB can propagate without triggering the filamentation instability or have sufficiently slow filamentation growth.

§3. Results and discussion

If we assume that the magnetic field in the propagation direction

is induced by the rotation of the ion beam, the field has the tendency to stabilize the filamentation instability. The fractional current neutralization has a stabilizing influence on the instability but the drift velocity and the temperature of the beam enhance the instability. From (8), the stability condition results in

$$\frac{1}{2f_m - 1} > \frac{V_{zb}^2}{V_{\theta b}^2} \frac{R^2}{c^2} \omega_b^2 \quad . \tag{9}$$

In (9), we have assumed that $V_{zb}^2 >> T_b/m_b$ and $V_{\theta b} = R\omega_{cb}$ where R is the typical beam radius. Table 1 shows the upper limit current for a rotating light ion beam which propagate through a plasma without triggering filamentation instability.

TABLE 1. The upper limit current I for a rotating light ion beam is given in the cases of the total beam energy $E_b = 10$ MeV and current neutralization factor $f_M = 0.8$.

$V_{\theta b}/V_{zb}$	0.2	0.4	0.6	0.8
I(MA)	0.8	3	7	12

References

1) T. Okada and K. Niu : J. Phys. Soc. Japan 50 (1981) 3845.
2) T. Okada and W. Schmidt : J. Plasma Physics 37 (1987) 373.
3) P.F. Ottinger, D. Mosher and S.A. Goldstein : Phys. of Fluids 24 (1981) 164.
4) H. Murakami, T. Aoki, S. Kawata and K. Niu : Laser and Particle Beams 2 (1984) 1.
5) R.C. Davidson : Basic Plasma Physics II (North-Holland Press 1984)

Some aspects of the unified model of non-ideal high-parameter plasmas: electron EOS and conduction coefficients

L. Ľalka Krouský[1,2]

Faculty of Nuclear Science and Physical Engineering,
Technical University of Prague,
Brehova 7, 115 19 Prague 1, Czechoslovakia

In the paper two partial models applied in atomic physics subpackage used in numerical simulations of pulsed-power-driven, non-ideal high-parameter plasmas are presented: electron EOS model and the model for electron conductivity coefficients calculations. The EOS model uses Dharma-Wardana exchange and correlation correction depending on both electron density and temperature. The electron thermal and electrical conductivity calculations are based on the Balescu-Lenard equation.

[1]Present adress : Department of Electrical Engineering, Technological University of Nagaoka, Kamitomicka, Nagaoka 940-21, Japan

[2]Supported by the Japan Society for the Promotion of Science

1. Introduction

During the past years in many laboratories the physics of matter states produced by powerful pulsed sources (lasers, particle beams, impact systems etc.) is being investigated both theoretically and experimentally. In these studies matter is found in very different and rather extreme conditions (More 1986).

In most cases of interest system behaviour can be described by numerical codes (Nicholas 1983), following the evolution of two separate fluids (ion fluid and electron fluid), each being characterized by its own temperature. The two fluids interact with each other, with non-thermal particles and with radiation of various origin.

The codes require data on physical properties of matter with mass densities from values well below atmospheric density up to about one thousand times that of the solids and with temperatures from thousandths of eV to hundreds of kev.

The core of the simulation package MIRIAM (Drska et al, 1986), representing an effort to develop reasonably consistent and self-contained model of pulsed-source-driven high-parameter non-ideal plasma systems is characterized by the following essential features:

(1) One-dimensional Lagrangian hydrodynamics of systems with variable mass of subsystems; formulation of equations assures the total energy conservation.

(2) Lagrange formulation of particle kinetic equations and equation of radiation transport.

(3) Energy and momentum deposition rates of heavy particles based on simultaneous solution of kinetic equations.

(4) Radiation transport calculated in multigroup new diffusion approximation with consistent emissivity/opacity estimation.

(5) Unified description of medium and high-Z ion physics, equation of state, radiation characteristics, conduction coefficients and energy-exchange characteristics.

To achieve self-contained simulation program which requires no or at least minimum external data, atomic physics subpackage has been developed. Its specific features can be summarized as follows:

(1) Unified treatment of atomic physics based on consistent solution of Thomas-Fermi Corrected equation, Schrodinger and Balescu-Lenard equations.
(2) Improved TFC model with exchange and correlation potential corrections.
(3) Schrodinger equation solved in WKB approximation, radiation characteristics calculated by using screened hydrogenic model.
(4) Conduction coefficients obtained via expansion of Balescu-Lenard equation in Legendre polynomials with truncation after two first terms; electron degeneracy taken into account by using Fermi-Dirac distribution as the first term of the expansion.
(5) Consistent evaluation of high-frequency electrical conductivity (in progress), free/bound electron stoping and electron-ion heat exhange.

The work reported in this article concentrated on the formulation of two specific models used in our atomic physics subroutines:
(1) Electron equation of state (EOS) calculations.
(2) Electron thermal and electric conductivities calculation.

Our approach to the electron EOS model is characterized by using the exchange and correlation corrections presented in (Dharma-Wardana 1981). The reasons for this approach are:
(1) Simple formulation, including the dependence on both electron density and temperature.
(2) Correct behaviour of the correction in limit cases.

Where electron conduction coefficients is concerned, we decided to formulate the problem on the basis of classical Balescu-Lenard equation. We stress the following arguments for this choice:
(1) The theory can be formulated without using the Coulomb logarithm, there are no problems with upper cutoff.
(2) The model respects polarization effects; in perspective inelastic processes can be included.

2. Improved TFC Model

2.1 Thomas-Fermi Corrected Equation

In accordance with the standard cell model each atom is supposed to be enclosed in a spherical volume V which contains Z electrons (bound and free), where Z is the nuclear charge. The radius of each cell is the same, $R^3 = (3M/4\pi\rho)$, where ρ is the matter density and M is the mass of the atom. The electron density is given by

$$n_e(r) = \int_0^\infty \frac{8\pi}{h^3} \frac{p^2 dp}{\exp[p^2/2mkT + (V(r)-\mu)/kT] + 1} \qquad (1)$$

where kT is the temperature in energy units, m is the electron mass, r denotes the distance from the nucleus, μ is the chemical potential, V(r) is the electron potential given by

$$V(r) = -e\Phi(r) + V_{ex}(r) + V_{cor}(r) - V_{ex}(\infty) - V_{cor}(\infty) \qquad (2)$$

where V_{ex} and V_{cor} are the contributions from the exchange and correlation as described in (Dharma-wardana et al. 1981)

$$V_{ex}(r) = -0.4073 r_s^{-1} \tanh(\tau^{-1})$$

$$V_{cor}(r) = -0.5109 r_s^{-1} (-0.0061 + 1.127\tau^2 + 3.756\tau^4)/ \qquad (3)$$
$$(1.0 + 1.241\tau^2 + 3.543\tau^4) \tanh(\tau^{-1/2})$$

where

$$\tau = (4/9\pi)^{2/3} r_s kT, \qquad r_s^{-1} = (4/3\ \pi n_e)^{1/3}$$

and

$$V_{ex}(\infty) = V_{ex}(R)$$

$$V_{cor}(\infty) = V_{cor}(R)$$

V_{ex} and V_{cor} are evaluated in atomic unit system.

2.2 Electron Potential

Now, for the theory to be self consistent, the potential Φ and the charge density should be related through the Poisson equation

$$\nabla^2\Phi = en_e(r)/\epsilon_0 \qquad (4)$$

Further, as $r \to 0$, the potential will be essentially that due to the nucleus so that it will behave as $eZ_i/(4\pi\epsilon_0 r)$. Now, the electric field at the cell should vanish (because each cell is electrically neutral) and therefore at $r = R$

$$d\Phi/dr = 0$$

We introduce the dimensionless variable $\xi = r/R$ and new function Ψ as

$$\Psi(\xi) = (e\Phi + \mu)\xi/kT \qquad (5)$$

If we now use the Poisson equation (4) and transformation (5) we would get

$$d\Psi/d\xi = \Omega \qquad (6)$$

$$d\Omega/d\xi = \alpha\xi F_{1/2}[\Psi(\xi)/\xi - (V_{ex}(\xi)+V_{cor}(\xi)-V_{ex}(1)-V_{cor}(1))/kT]$$

with boundary conditions

$$\Omega(1) = \Psi(1) \qquad (7a)$$

$$\Psi(0) = \alpha \qquad (7b)$$

where

$$\alpha = e^2Z/(4\pi\epsilon_0 kT), \quad \beta = 4\pi e^2(2m_e kT)^{3/2}R^2/(h^3 kT)$$

and $F_{1/2}$ is the Fermi-Dirac integral. The system of differential equations (6) with boundary conditions (7) is solved using the Runge-Kutta-Fehlberg routine (Forsythe et al, 1977)

for solution of system (6) from right to left. We note that the left boundary condition must be transformed in the asymptotical form via Taylor expansion of Ψ at $\xi = 0$.

$$\Psi(0) \approx \Psi(\delta)+\Omega(\delta)\delta+a\delta^{3} \qquad (8)$$
$$+\tfrac{1}{2}[\Psi(\delta)/\delta-(V_{ex}(\delta)+V_{corr}(\delta)-V_{ex}(1)-V_{corr}(1))/kT]/2$$

where δ is choosen as $\delta = R_{core}/R$, R_{core} is the ion core radius.

2.3 Effective charge

Other relevant quantity is the effective nuclear charge Z_*. According to (Rozsnyai 1972) Z_* is given by

$$Z_* = \frac{4}{3}\pi R^{3} n_e(R) \qquad (9)$$

where $n_e(R)$ is given by the self consistent solution of (6), (7), (2), (3). Detailed Hartree-Slater calculation (Rozsnyai 1972) confirm that this is very good approximation of the average ion charge.

Figure 1 shows effective nuclear charge of aluminum versus mass density for various electron temperatures.

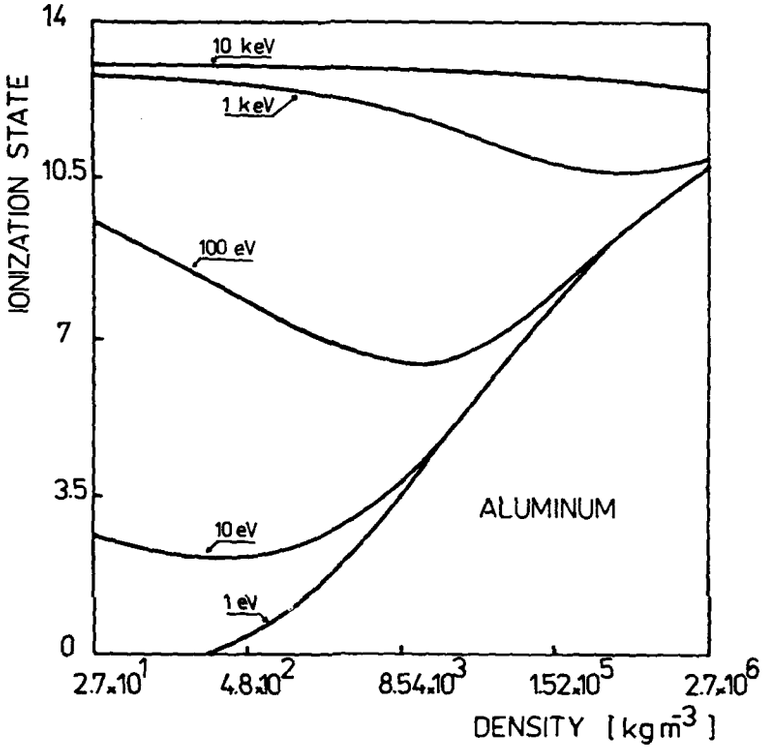

FIG. 1. Effective nuclear charge of aluminum versus mass density for various electron temperatures

3. Electron Equation of State

3.1 Electron Pressure

We are treating the electrons essentially as if they formed a classical gas that happens to have a momentum distribution given by

$$f(r,p)dp = \frac{8\pi}{h^3} \frac{p^2 dp}{\exp\left[\frac{p^2/2m + v(r) - \mu}{kT}\right] + 1} \qquad (11)$$

The pressure at the boundary is therefore just the rate of transfer of momentum at R. For an electron of momentum p, the momentum transfer would be 2p, and the rate will be one third of the velocity, p/m, since the electrons move randomly in all directions. Thus the total pressure exerted by all electrons at the boundary is

$$P = \frac{8\pi}{h^3} \int_0^\infty \frac{p^2 (2p)(p/3m)\, dp}{\exp\left[\frac{p^2/2m - \mu}{kT}\right] + 1} \qquad (11)$$

remembering that $v(R) = 0$.

In figure 2 electron pressure of aluminum as a function of mass density and electron temperature is displayed.

3.2 Electron Energy

The average kinetic energy is easily to be calculated by multiplying the kinetic energy of a single electron, $p^2/2m$, by the distribution function (11) and integrating over all p and over all r between 0 and R. The result (12) again be expressed in terms of Fermi-Dirac integral $F_{1/2}$ as

$$E_{kin} = \frac{4\pi R^3}{3} \frac{1}{(2mkT)^{3/2}} (2mkT)^{5/2} \int_0^\infty \varepsilon^{3/2} F_{1/2}\left[\varepsilon - \frac{v(\varepsilon)-\mu}{kT}\right] d\varepsilon \qquad (12)$$

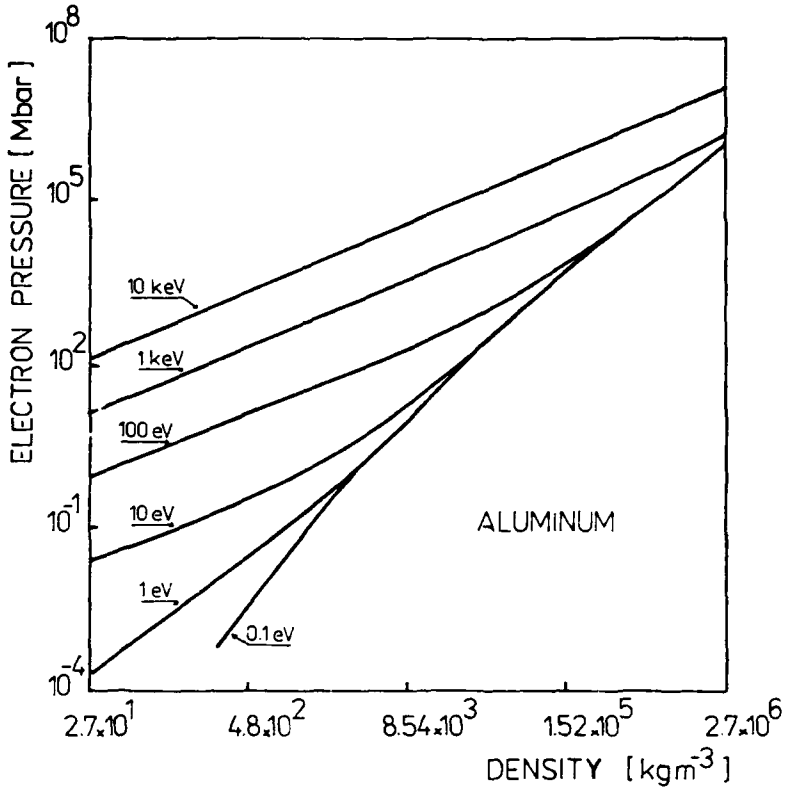

FIG. 2. Electron pressure of aluminum as a function of mass density and electron temperature

We can also calculate the potential energy of the electrons by using their motion integrals and their interaction with the nuclear field [Liberman 1979]. We have

$$E_{pot} = \frac{4\pi R^3}{3}\frac{2m}{h^3}(2mkT)^{5/2}\int_0^{\infty}\frac{x}{2}F_{1/2}\left[-\frac{\chi_{ion}+\psi(r_s)-e\psi(r_s)}{kT}\right]dx_s \qquad (13)$$

The expression for the exchange and correlation energy is very similar, and we get, after simplifications

$$E_{ex,cor} = \frac{4\pi R^3}{3}\frac{2m}{h^3}(2mkT)^{3/2}\int_0^{\infty}\frac{x}{2}F_{1/2}\left[-\frac{\chi_{ion}+\psi(r_s)}{kT}\right]\cdot \frac{V_{ex}(r_s)+V_{cor}(r_s)-V_{ex}(r_s)-V_{cor}(r_s)}{kT}dx_s \qquad (14)$$

The total electron energy is given by

$$E_{tot} = E_{kin} + E_{pot} + E_{ex,cor} \qquad (15)$$

More practical way to calculate the total energy can be via virial theorem [Geiger et al. 1985]

$$2E_{kin} + E_{pot} + E_{ex,cor} = 3PV \qquad (16)$$

Figure 3 represents electronic energy of aluminum as a function of mass density and electron temperature.

3.3 Normalization and chemical potential

We note that the total energy must be normalized on the total energy of an isolated atom (total binding energy). According to [Kalitkin 1978] the total binding energy is given by

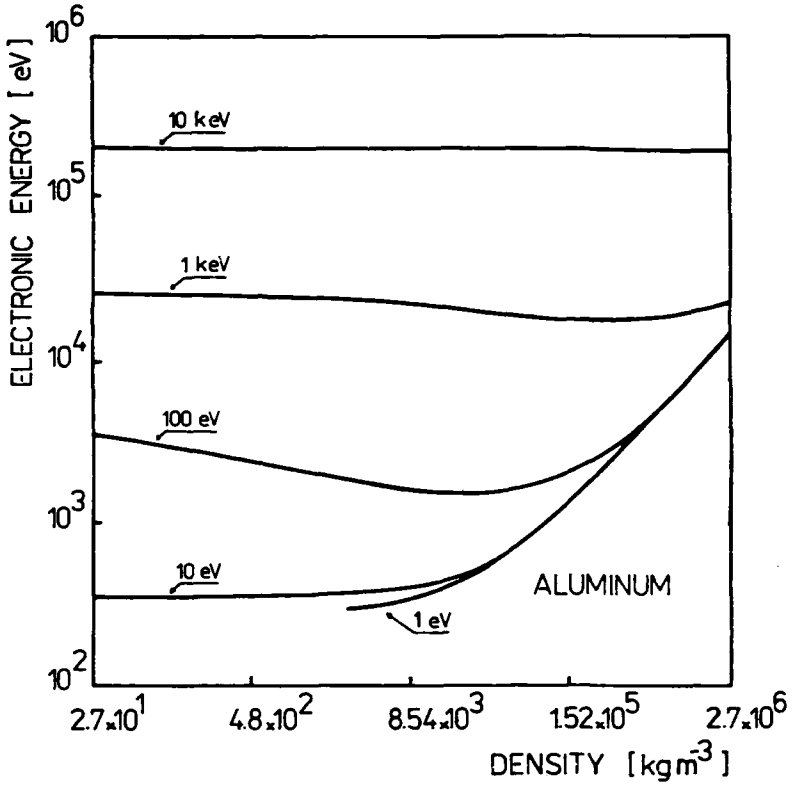

FIG. 3. Electronic energy of aluminum as a function of mass density and electron temperature

$$E_{ex} = -0.7387 \left(\frac{e^2}{4\pi\varepsilon_0 a_i}\right) N_i^{1/3} - 0.0744 \left(\frac{e^2}{4\pi\varepsilon_0 a_e}\right) N_e^{1/3} \quad (17)$$

The chemical potential μ is given by the formula

$$\mu = kT\Psi(1) \quad (18)$$

4. Conduction Coefficients

4.1 Electron Kinetic Equation (EKE)

The Balescu-Lenard kinetic equation (Klimontovich 1982) has been used for transport coefficients calculations. The coefficients are obtained from the solution of the Balescu-Lenard equation based on an expansion of distribution function in Legendre polynomials with truncation after the first two terms. The electron degeneracy effects on the transport coefficients are taken into account by using a Fermi-Dirac distribution for the electrons as the first term of the expansion. The partial ionization is also taken into account via effective nuclear charge obtained from self consistent solution of TFC equation (9). The chemical potential in Fermi-Dirac distribution we have also from the solution of TFC equation (18).

The electron kinetic equation is given by

$$\frac{\partial f}{\partial t} + v_i \frac{\partial f}{\partial r_i} - eE_i \frac{\partial f}{\partial p_i} = \frac{\partial}{\partial p_i}(A_i f) + \frac{\partial}{\partial p_i} D_{ij} \frac{\partial f}{\partial p_j} \quad (19)$$

where f is the electron distribution function, $\mathbf{E}$ is an electric field, and A_i, D_{ij} are the coefficients of Balescu-Lenard collision term. We note that we ignore the magnetic field effects here. According to (Klimontovich 1982) the coefficients A_i and D_{ij} are given as (in CGS units)

$$A_i(D) = \frac{e^2}{c\hbar^2} \int \delta(\omega - \mathbf{k}\cdot\mathbf{v}) \frac{k_i}{k^2} \frac{\mathrm{Im}[\varepsilon(\omega,\mathbf{k})]}{|\varepsilon(\omega,\mathbf{k})|^2} d\omega\, d\mathbf{k} \quad (20)$$

$$D_{ij}(p) = \frac{e^2}{16\pi^3} \int \delta(\omega - \mathbf{k}\cdot\mathbf{v}) \langle \delta E \delta E \rangle_{\omega,\mathbf{k}} \, d\mathbf{k} \qquad (1)$$

$$\langle \delta E_i \delta E_j \rangle_{\omega,\mathbf{k}} = \frac{A_i k_j}{k^2 |\epsilon(\omega,\mathbf{k})|^2} \frac{\omega^2}{\omega_p^2} \int \frac{4\pi e_\alpha^2}{m_\alpha} \frac{\partial f_\alpha / \partial v_i}{\omega - \mathbf{k}\cdot\mathbf{v} + i\eta} \, d\mathbf{p} \qquad (2)$$

where $\epsilon(\omega,\mathbf{k})$ is the dielectric function of the plasma, f_α is the distribution function of the αth plasma species, e_α is the electronic charge, and m_α is the absolute value of the particle charge. Next, as we consider the interaction between electrons and ions, the summation over α in the expression for $\epsilon(\omega,\mathbf{k})$ is broken into two parts, i.e.,

$$\epsilon(\omega,\mathbf{k}) = \lim_{\eta \to 0} \left[1 + \sum_\alpha \frac{4\pi e_\alpha^2}{k^2} \int \frac{\partial f_\alpha / \partial v_i}{\omega - \mathbf{k}\cdot\mathbf{v} + i\eta} \, d\mathbf{p} \right] \qquad (3)$$

After transformation of the electron velocity distribution into spherical coordinates and taking into account the rotational symmetry of f_e in ϕ, the Fokker-Planck equation for the electrons becomes

$$\frac{\partial f}{\partial t} + v_\parallel \frac{\partial f}{\partial z} - \frac{e_e E}{m_e} \frac{\partial f}{\partial v_\parallel} - \frac{e_e E}{m_e} \frac{1 - \mu^2}{v} \frac{\partial f}{\partial \mu} + \frac{1}{2} \frac{e_e^2 E^2}{m_e^2} \cdot$$

$$\frac{1}{v} \frac{\partial}{\partial v} v^2 D_{\mu\mu} \frac{\partial f}{\partial \mu} + \frac{D_{\mu\mu}}{v^2} \frac{\partial}{\partial \mu} (1-\mu^2) \frac{\partial f}{\partial \mu}$$

where the improved Balescu-Lenard collision term is given by

$$A_i(\mathbf{v}) = \sum_\beta \frac{e_\alpha^2 e_\beta^2 \ln \Lambda_{\alpha\beta}}{m_\alpha} \int \left[\frac{\delta_{ij}}{v^3} - \frac{3 v_i v_j}{v^5} \right] \frac{f_\beta(\mathbf{v}') - f_\beta(\mathbf{v})}{|\mathbf{v}' - \mathbf{v}|^3} \, d\mathbf{v}' +$$

$$- \frac{\partial f_\alpha}{\partial v_i} \left[\frac{m_\alpha}{m_\alpha + m_\beta} \right] \frac{e_\beta^2}{m_\beta^2} \cdot$$

$$D_{pp}(p) = \frac{2e^2}{v^3}\int_0^v x^2 \sum_n e_n^2 c_n(x)\left\{\frac{1}{2}\ln\left[\frac{k_m^2(k_m^2+a(x))}{a(x)^2+b(x)^2}+1\right] - \right.$$

$$\left. - \frac{a(x)}{b(x)}\left[\operatorname{arctg}\frac{k_m^2+a(x)}{b(x)} - \operatorname{arctg}\frac{a(x)}{b(x)}\right]\right\}dx \qquad (26)$$

$$D_{00}(p) = \frac{e^2}{v^3}\int_0^v \sum_n e_n^2 c_n(x)\left\{\frac{1}{2}\ln\left[\frac{k_m^2(k_m^2+a(x))}{a(x)^2+b(x)^2}+1\right] - \right.$$

$$\left. - \frac{a(x)}{b(x)}\left[\operatorname{arctg}\frac{k_m^2+a(x)}{b(x)} - \operatorname{arctg}\frac{a(x)}{b(x)}\right]\right\}dx - \frac{D_{pp}(p)}{2} \qquad (27)$$

with

$$a(x) = -\sum_n 16\pi^2 e_n^2 m_n^2 \int_0^\infty f_n(m_n w)\,\frac{w^2}{x^2-w^2}\,dw \qquad (28)$$

$$b(x) = 8\pi^3 \sum_n e_n^2 m_n^2 x f_n(m_n x) \qquad (29)$$

$$c_n(x) = (2\pi)^2 m_n^3 \int_0^\infty f_n\left(m_n(w^2+x^2)^{1/2}\right) w\,dw \qquad (30)$$

and

$$k_m = \min\left[kT/e, (mkT/\hbar^2)^{1/2}\right]$$

4.2 Linearization of EKE

The usual approach for deriving transport coefficients starts with a linearization of the kinetic equation for a plasma close to thermal equilibrium. This linearization may be accomplished by expanding the single-particle distribution function in Legendre polynomials and truncating the expansion after the first two terms, i.e.,

$$f = f^0(x,p,t)/4\pi + 3pf^1(x,p,t)\cdot\Omega/4\pi \qquad (31)$$

Substituting this expansion in to the Boltzmann equation and taking angular moments, we obtain two coupled differential equations in f^0 and f^1. Based on the assumption that the plasma is close to thermodynamic equilibrium, f^0 is set to be a Fermi-Dirac, f^1 is a small perturbation and f^1 have not dependence on the coefficients A_D, D_{pp}, E_{00}.

Now, after transformation in energy (in electronvolts), this two partial differential equations can be written in the form

$$\frac{\partial f^0}{\partial t} - \left(\frac{2e}{mE}\right)^{1/2} E \frac{\partial E f^1}{\partial E} + \left(\frac{2eE}{m}\right)^{1/2} \frac{\partial f^1}{\partial x} - \left(\frac{2e}{mE}\right)^{1/2} \frac{\partial}{\partial E} [E a^0 f^0 + E^{3/2} \delta_{pp} \frac{\partial f^0}{\partial E}] \quad (32)$$

$$\frac{\partial f^1}{\partial t} - \left(\frac{2eE}{m}\right)^{1/2} \frac{E}{3} \frac{\partial f^0}{\partial E} + \frac{1}{3} \left(\frac{2eE}{m}\right)^{1/2} \frac{\partial f^0}{\partial x} = \left(\frac{2e}{mE}\right)^{1/2} \frac{\partial}{\partial E} [E a^0 f^1 + E^{3/2} \delta_{pp} \frac{\partial f^1}{\partial E}] - 2\left(\frac{2eE}{m}\right)^{1/2} \frac{\delta_{00} f^1}{E^{2/3}} \quad (33)$$

where

$$a^0 = A_D (f^0)/e \quad (34)$$

$$\delta_{pp} = 2^{1/2} D_{pp} (f^0)/e^{3/2} m^{1/2}) \quad (35)$$

$$\delta_{00} = D_{00} (f^0)/12^{3/2} e^{3/2} m^{1/2}) \quad (36)$$

Equation (32) describes the energy conservation law, as may by shown by multiplying it by $p^2/(2m)p^2 dp$ (or in energy variable by $e/2(2emE)^{3/2} dE$) and integrating from $p=0$ to $p=\infty$ (assuming the mean plasma velocity to be zero). From energy conservation law we can shown, that the electrical current and heat flow are given as

$$j = -2e^3 m \int_0^\infty E f^1 dE \quad (37)$$

$$q_j = ce^3 m \int_0^\infty E^{2+j} dE \qquad (38)$$

Since we are interested in steady state transport processes, we equate the time derivative in eq. (38) to zero. Then we have

$$\frac{d}{dE}\left[Eq^0 f^1 + E^{3/2}\phi_{pp}\frac{df^1}{dE}\right] - \frac{c\phi_{00}f^1}{E^{1/2}} = \frac{E}{3}\frac{\partial f^0}{\partial\theta} - \frac{EE}{3}\frac{df^0}{dE} \qquad (39)$$

Equation (39) may now be solved and the heat flow and the current calculated as integrals given by (37), (38). Based on the assumption that $f^0/4\pi$ is set to be Fermi-Dirac distribution, the equation (39) becomes a linear differential equation. It is easy to shown that both j and q_T become linear function of the temperature gradient and electric field:

$$j = -s_{11}E - s_{12}v\Theta \qquad (40)$$

$$q_T = -s_{21}E - s_{22}v\Theta \qquad (41)$$

where Θ is electron temperature in ev and

$$s_{11} = -2e^3 m \int E L^{-1}[\Psi_2]\, dE \qquad (42a)$$

$$s_{12} = 2e^3 m \int E L^{-1}[\Psi_1]\, dE \qquad (42b)$$

$$s_{21} = 2e^3 m \int E^2 L^{-1}[\Psi_2]\, dE \qquad (42c)$$

$$s_{22} = -2e^3 m \int E^2 L^{-1}[\Psi_1]\, dE \qquad (42d)$$

and

$$\Psi_1 = \frac{E}{3}\frac{\partial f^0}{\partial\Theta} \qquad (43a)$$

$$\Psi_2 = \frac{E}{3}\frac{\partial f^0}{\partial E} \qquad (43b)$$

The differential operator $L[q]$ is defined by

$$L[\varphi] = \frac{d}{dE}\left[E\omega^{0}\varphi + E^{3/2}\sigma_{p1}\frac{d\varphi}{dE} \right] - \frac{\varphi\sigma_{p1}\sqrt{E}}{E^{3/2}} \qquad (44)$$

4.3 Electron Thermal and Electrical Conductivity

The thermal conductivity κ is defined as the ratio of q_T to $v\Theta$ for situation in which $i=0$ and the electrical conductivity σ is the ratio of i to E when $q_T=0$. The thermal conductivity can be calculated as follows: First must be solved the equation

$$L[\varphi_0] = \varphi_1 v\Theta \qquad (45)$$

with boundary condition $\varphi_0(E) \to 0$ for $E \to \infty$ and integral condition

$$j \approx \int E\,\varphi_0\,dE = 0$$

The coefficients s_{12} and s_{22} are obtained by substituting

$$\varphi_0 = L^{-1}[\varphi_1]v\Theta$$

into (42b),(42d). Second must be solved equation

$$L[\varphi_e] = -\varphi_2 E \qquad (46)$$

with boundary condition $\varphi_e(E) \to 0$ for $E \to \infty$ and integral condition

$$j \approx \int E\,\varphi_e\,dE = 0$$

The coefficients s_{11} and s_{21} are obtained similar by substituting

$$\varphi_e = L^{-1}[\varphi_2]E$$

into (42a),(42c). Using (40), (41) κ the thermal conductivity has been written as

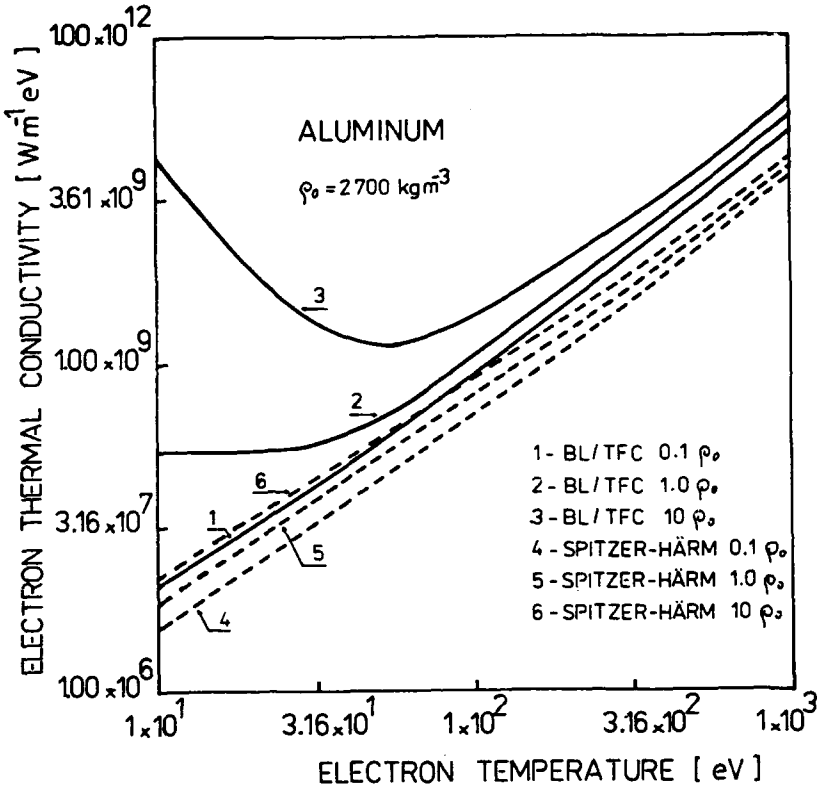

FIG. 4. The dependence of electron thermal conductivity of aluminum on the electron temperature and mass density

$$K = s_{22} - s_{21}\, s_{12}/s_{11} \qquad (47)$$

Numerical procedure for the solution of equations (45) and (46) is based on the finite differencing E within the interval $[E_{min}, E_{max}]$ in logarithmic scale. The integral conditions are evaluated via the trapezium rule.

Figure 4 shows the dependence of electron thermal conductivity on electron temperature where different theories are used in the conductivity model.

The electrical conductivity may be computed using the same way, but the integral condition must be changed by

$$q_T \approx \int E^2 \varphi_{0,e}\, dE = 0$$

The result is

$$\sigma = - s_{11} + s_{12}\, s_{21}/s_{22} \qquad (48)$$

5. Conclusion

Electron EOS and conduction coefficients based on consistent using of Thomas-Fermi Corrected model and Balescu - Lenard equation are clearly well applicable in systems chracterized by sufficiently high temperature (T > 10 eV). Highly non-ideal region of low temperatures and very high densities need to be treated different way.

Where medium non - ideal plasmas is concerned, we got acceptable agreement of our models with other, more empirical calculations (Atzeni et al. 1986, Lee et al. 1984). As an illustration, in figure 5 a comparison of our results for electrical conductivity with the data of (Lee et al. 1984) for a relatively dense system is presented.

Principially, our model could be relatively straight-way corrected to plasma-nonideality effects using consistently estimated structure factors (Vondrasek et al., to be published). The main advance of the model presented is its potential to be extended to the high-Z, partially ionized systems, being of interest in many study ex of high - energy - density systems.

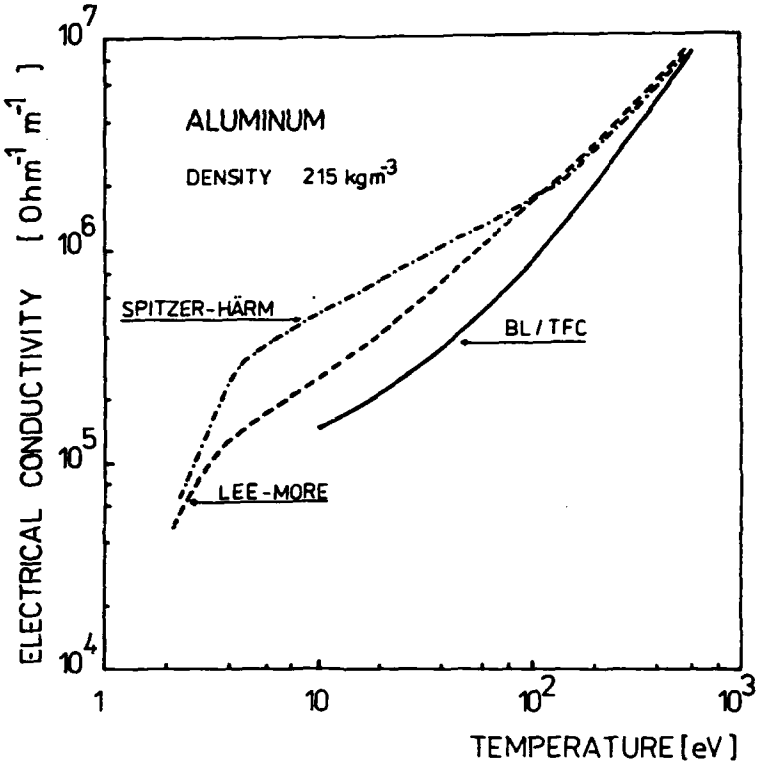

FIG. 5. The dependence of electron electrical conductivity of aluminum on the electron temperature ; comparison of several models

References

ATZENI, S., CARUSO, A. and PAIS V.A. 1986 Laser and Particle Beams **4**, 393.

DHARMA-WARDANA, M.W.C. and TAYLOR, R. 1981 J. Phys. C: Solid State Phys. **14**, 629.

DRSKA, L. and VONDRASEK, J. 1986 Proc. 6th Int. Conf. on High - Power Particle Beams, Kobe 1986 (edited by C. Yamanaka), p. 558.

FORSYTHE, G.E., MALCOLM, M.A. and MOLER, C.B. 1977 Computer Methods for Mathematical Computations, Prentice - Hall, Englewood Cliffs.

GEIGER, W., HORNBERG, H. and SCHRAMM, K.H. 1968 Springer Tracts in Modern Physisies, Springer-Verlag, Berlin, p. 1.

KALITKIN N.N. 1975 Tables of Thermodynamic Function of Matter at High Energy Densities (in Russian), Inst. Appl. Math., Moscow.

KLIMONTOVICH Yu.L. 1982 Statistical Physics (in Russian), Nauka, Moscow.

LEE, Y.T. and MORE, R.M. 1984 Phys. Fluids **27**, 1273.

MORE, R.M. 1986 Laser Plasma Interactions 3 (edited by H.B. Hooper), SUSSP Publications, Edinburgh, p. 157.

NICHOLAS, D.J. 1983 Laser Plasma Interactions 2 (edited by R.A. Cairns), SUSSP Publications, Edinburgh, p. 129.

ROZSNYAI, B.F. 1972 Phys. Rev. **145**, 1137.

SPITZER, L. 1962 Physics of Fully Ionized Gases, 2nd ed., Interscience, New York.

STABILITY REQUIRMENT FOT IGNITION AND HIGH GAIN IMPLOSION
= 2-D Simulation for High Neutron Yield Experiment =

H. Takabe

Institute of Laser Engineering, Osaka University
Yamada-oka 2-6, Suita, Osaka, Japan

Implosion stability is the essential problem for ICF scinerio, in which we expect to demonstrate the ignition by the use of 100 kJoule class driver and realize the pellet gain 100 with MJoule class driver. In order to study the stability requirment, we have developed a two dimensional fluid code, ILESTA-2D. In the present note, we report prerliminary results obtained by using the 2-D code to simulate the recent high neutron yield experiment by Gekko-XII. It is found that the neutron yield is rather insensitive to the implosion with relatively smaller wavenumber nonuniformity (ℓ = 6, 12).

I. Introduction

A uniformity of implosion dynamics is essential requirement for the inertial confinement fusion. Even for relatively low density compression which is seen in the recent high neutron yield experiment[1], nonuniformity of implosion plays important role on neutron production.

In Fig. 1, the neutron yields obtained by the implosion experiment with Gekko-XII green laser system are plotted as a function of the aspect ratio of the glass shell [=(radius)/ (thickness) of target] with the solid circles, while those obtained by the one dimensional simulation code ILESTA-BG are plotted with the plus signs. One dimensional simulation always provides higher neutron yield and even at the best agreement, the difference of a factor two is seen compared to the experimental results. Such discrepancy is mainly accused of the asymmetry of implosion dynamics, although a variety of physics not correctly included in the simulation can be enumerated; for example, nonlocal and non-maxwell effects of electron heat transport, non LTE radiation transport, etc.

The data shown in Fig. 1 are replotted in a different point of view. In Fig. 2, the neutron yields from the experiment divided by those from

the simulation are plotted with the solid circles as a function of a calculated convergence ratio, R_0/R_f, where R_0 is the initial radius of the fuel and R_f is its radius at the maximum compression obtained in the 1-D simulation. In this figure, the solid lines indicate the calculated effective neutron yields until the times defined in the schematic figure, where Y_N is the calculated full neutron yield. It is clearly seen that most of neutrons produced during the stagnation phase is not observed in the experiment. This is considered to be due to the Rayleigh-Taylor instability in the stagnation phase, which grows explosively in time[2].

In order to study the effect of low ℓ-number nonuniformity (ℓ=1-20) on the neutron production, where ℓ is the wavenumber in spherical geometry, a two dimensional fluid code ILESTA-2D has been developed. Our main purpose is to see whether the lower ℓ mode is more important compared to the higher ℓ mode nonuniformity, which is fairly hard to be simulated with conventinal two dimensional simulation code. If the latter is essential, we will be required to model theoretically the turbulent mixing phenomena due to micro scale perturbations.

II. Implosion Dynamics

In the present paper, we focus on the shot #3826 at which the neutron yield of 10^{13} was observed in the experiment. At this shot, a target with diameter 1235 μm and thickness 1.31 μm filled with 6.2 atm. DT gas is irradiated by a Gaussian shaped 0.53 μm laser with 13 kJoule/ 1 nsec. The calculated neutron yield with ILESTA-BG code was 2×10^{13} against 1×10^{13} neutrons in the experiment.

First of all, we have studied how much absorption nonuniformity is required to reduce the neutron yield from 2×10^{13} to 1×10^{13} in ILESTA-2D simulation. It is found that as for a nonuniformity of ℓ=6, the onuniformity of 35% is required for a reduction of a factor two. The snap shots of the implosion dynamics are shown in Fig. 3. In this simulation, 24 grids are used in $\pi/2$ of θ-direction and 100 grids are used in r-direction (20 for DT fuel and 80 for glass shell). The laser peak is located at t=1.5 nsec. The shock wave driven in the fuel gas collides at the center at t=2.2 nsec, and the maximum compression is seen at t=2.4 nsec. It is noted that the spatial scale is streached by a factor two from 2.0 nsec, and the thicker azimuthal line indicates the contact surface of the fuel and glass pusher.

It is seen through these snapshots that the nonuniformity of the

pusher grows with the convergence of the shell, while the shock wave front (see 2.0 nsec) is relatively uniform. In this implosion, the deformation of the contact surface near the maximum compression is improved due to the mass ablation of the pusher towards the fuel; therefore, the sphericity of the contact surface is eventually improved to allow sufficient neutron production. After the maximum compression, the DT plasma predominantly expands in $\theta=\pi/2$ direction. As the result, even under such nonuniform implosion, the difference of neutron yield is only a factor 2 compared to the corresponding 1-D simulation.

In the present simulation, the laser absorption is calculated for one beam irradiated on the north pole with d/R = -5 by f/3 lense. The ray tracing method is used to determine the ray trajectories and the calculated absorbed energy is redistributed in the θ-direction with 35 % nonuniformity of ℓ = 6 mode.

III. Ray-Tracing in 2-D Space

In order to include the coupling between the density nonuniformity and the resultant laser ray deflection effect, we modified the geometry from (θ,r) space to (ϕ,r) space in the spherical coordinate system. Then, the laser beams are irradiated in the plane of equator ($\theta=\pi/2$ plane). In this case, we have investigated an effective d/R value at which the neutron yield reduces by a factor 2 in 2-D simulation compared to 1-D simulation. We assumed uniform intensity pattern for each beam. At first, the case with d/R = -5 (experimental focusing condition) is studied, but the neutron yield in the 2-D simulation was almost equal to that in the 1-D simulation. We finally find that the case of d/R = -3 reduces the neutron yield by a factor 2.

In Fig. 4-(a), the trajectries of laser rays at the laser peak intensity (t=1.5 nsec) are shown for this case. In Fig. 4-(b), the irradiated (W_L) and absorbed (W_{abs}) laser intensities are plotted in TW unit, where the absorbed intensity by each radial Lagrangian zone are also plotted. In Fig. 4-(c) indicated is the standard deviation of the absorbed laser intensity integrated in the radial direction,

$$\sigma = \left[\int_0^{2\pi}\left(\int_0^{\infty} I(\phi,r)r^2 dr - \langle I\rangle\right)^2 d\phi/2\pi\right]^{1/2} / \langle I\rangle,$$

where

$$\langle I \rangle = \int_0^{2\pi} d\phi/2\pi \int_0^{\infty} I(\phi,r) r^2 dr,$$

and $I(\phi,r)$ is the absorbed laser intensity at time t. It is seen that about 20-30 % nonuniformity is induced due to the finiteness of the number of beams.

The nonuniformity of shell dynamics is driven by the absorption nonuniformity. In this case, the foundamental mode is $\ell = 6$ mode and the relatively strong absorption is seen in the beam overlapped region. On the other hand, the region heated by the component of normal incidence is also strongly heated, and the nonuniform mode of $\ell = 12$ is also seen, which is inferred from the shell deformation. The fluid dynamics affects the time development of the σ. As the radius of the critical surface decreases, the effective $|d/R|$ value increases. This effect helps the improvement of uniformity as seen in Fig. 4-(c).

IV. Neutron Poduction

In Fig. 5, the time developement of neutron emission rate, time integrated neutron yield, and the fuel density and temperature are shown for the (a) one dimensional simulation and (b) two dimensional simulation.

As seen in Fig. 5-(a), the density increases around t=2.2 nsec in 1-D simulation and this allows the production of neutron in this phase (stagnation phase). However, the density increase in this phase is not seen in the present 2-D simulation for d/R = -3 focusing. It is typical that in 1-D the neutron emission starts from the arrival time of the shock wave at the center and continues through the stagnation phase. On the other hand, in the two dimensional case the stagnation dynamics is not seen and the neutrons are not produced in this phase. Therefore, the time duration of neutron emission is reduced in the 2-D simulation and as the result the neutron yield is reduced by a factor 2.

V. Conclusion

We have developed a two dimensional fluid simulation code ILESTA-2D, in which a Lagrangian mesh scheme is used to solve the one-fluid, two-temperature fluid equation. This code has been used to simulate the recent high neutron yield implosion experiment with Gekko-XII green laser system. It is found that in the gas target implosion, the resultant neutron yields are almost insensitive to lower wavenumber nonuniformities

(ℓ = 6, 12) of laser absorption. For example, in order to obtain a 50 % reduction of neutron yield in two dimensional simulation compared to that in one dimensional simulation, we need to impose 35 % nonuniformity of ℓ = 6 mode.

Through the two dimensional simulations, we inferred that the discrepancy between the experimental and 1-D simulational neutron yields (usually one or two orders of magnitude difference) is mainly due to the mixing of fuel and pusher materials induced by relatively larger ℓ-mode perturbations.

References

[1] H. Takabe et. al., "Scalings of Implosion Experiment for High Neutron Yield", (submitted to Physics of Fluids).

[2] F. Hattori et. al., Physcs of Fluids 29, 1719 (1986).

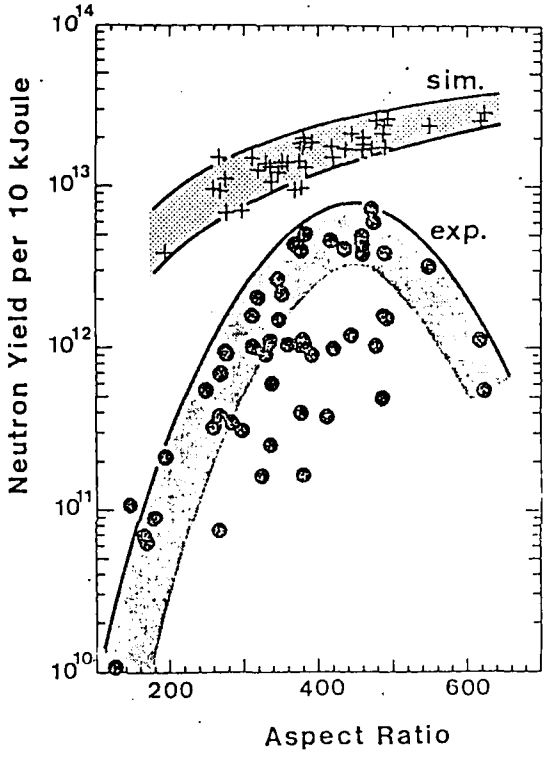

Fig. 1

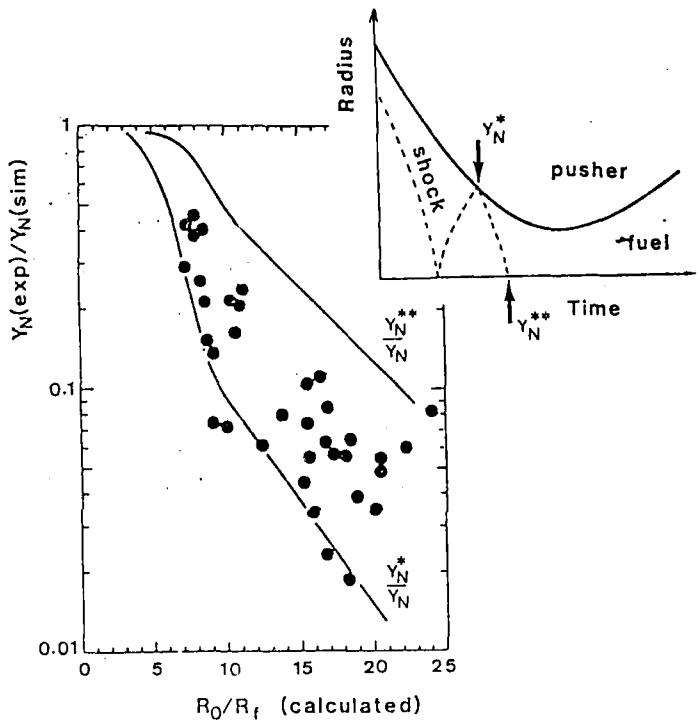

Fig. 2

Fig. 1 Neutron yields per 10 kJoule (0.53 μm laser) obtained from experiment (•) and 1-D fluid code "ILESTA-BG" (+) v.s. a target aspect ratio.

Fig. 2 Experimental neutron yield Y_N(exp) divided by 1-D simulational yield Y_N(sim) v.s. calculated convergence ratio. The solid lines indicate the effective neutron yields defined in the schematic r-t diagram, where Y_N is 1-D full neutron yield.

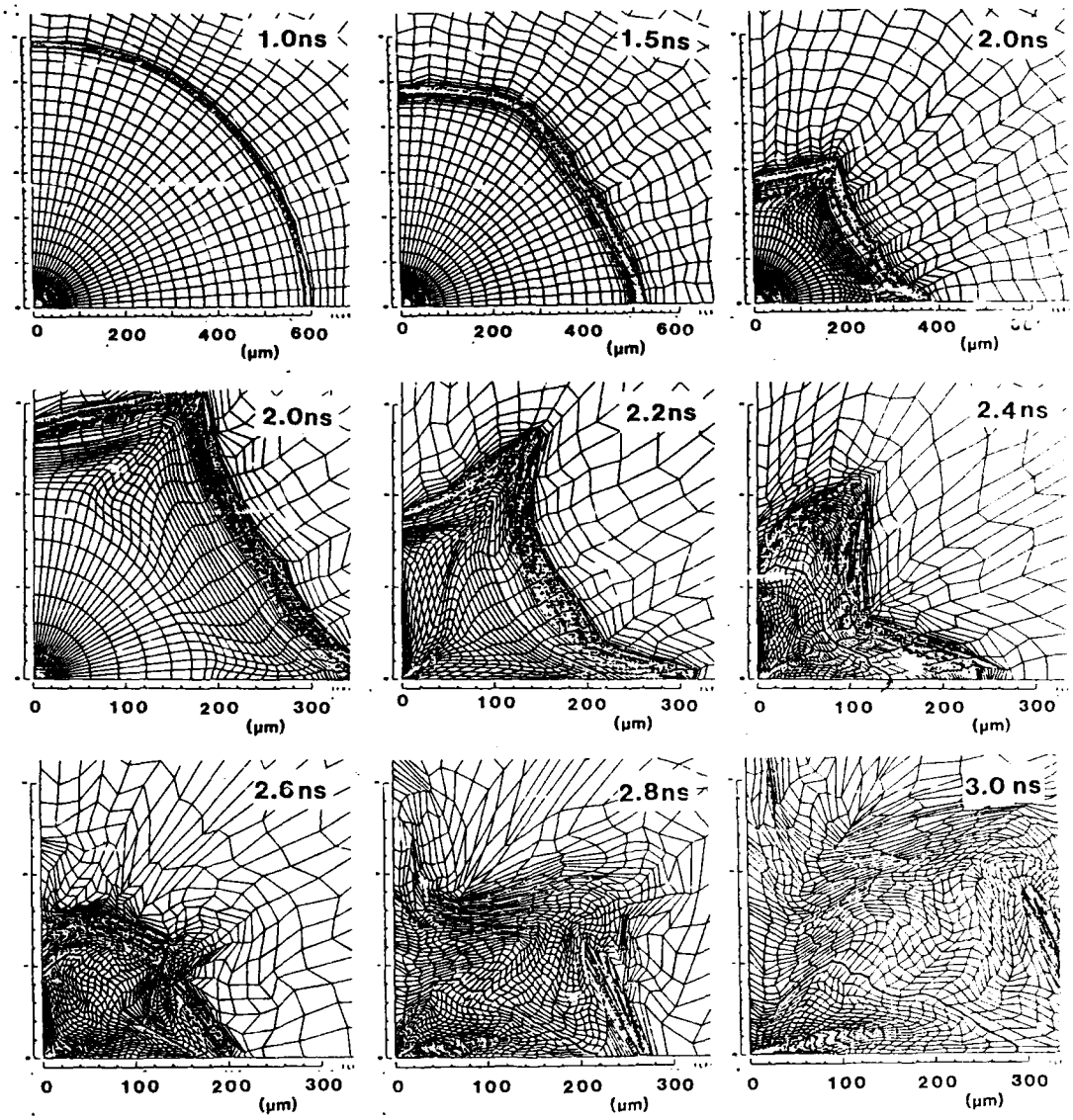

Fig. 3 Snap shots of 2-D simulation in which 35 % nonuniform absorption is imposed with the assumption of $\ell = 6$ nonuniform mode. The laser intensity has its peak at t=1.5 nsec and the maximum compression is seen at 2.4 nsec.

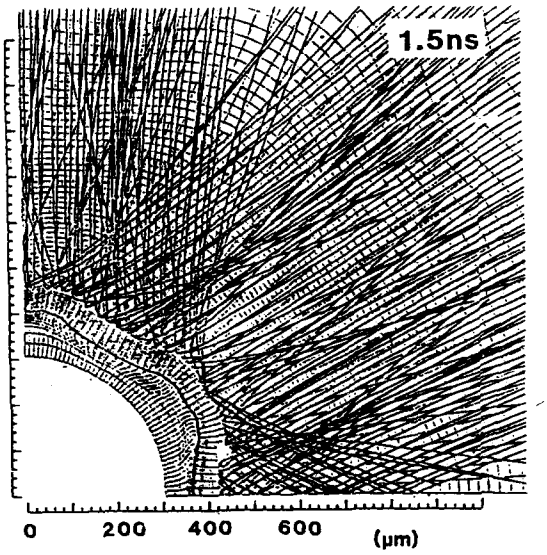

Fig. 4-(a)

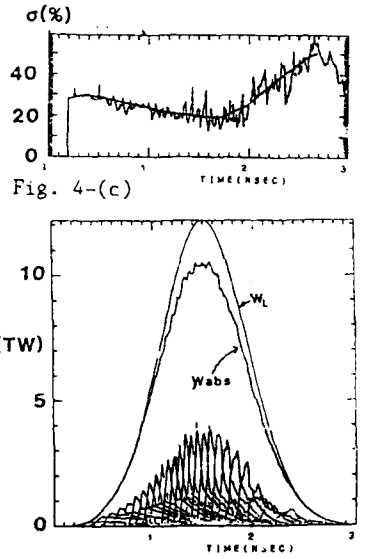

Fig. 4-(c)

Fig. 4-(b)

Fig. 4 (a) Laser ray trajectries in (ϕ,r) space at the time of peak intensity.

(b) Irradiated (W_L) and absorbed (W_{abs}) laser intensities in TW unit.

(c) The standard deviation of nonuniformity of absorbed laser intensity integrated in the radial direction.

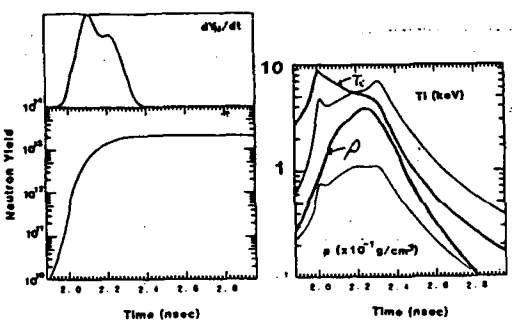

Fig. 5-(a)

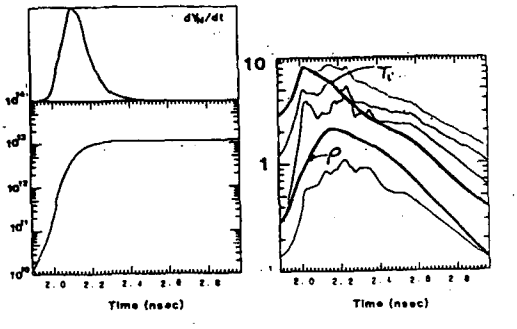

(b)

Fig. 5 The time development of neutron emission rate dY_N/dt, time integrated neutron yield, and the density and temperature of the fuel [(a): 1-D simulation, (b): 2-D simulation].

CORONAL FLUID-DYNAMICS IN LASER FUSION

Juan R. Sanmartín
E.T.S.I.Aeronáuticos, Universidad Politécnica, 28040-Madrid

The fluid-dynamics of the corona ejected by laser-fusion targets in the direct-drive approach (thermal radiation and atomic physics unimportant) is discussed. A two-fluid model involves inverse bremsstrahlung absorption, refraction, different ion and electron temperatures with energy exchange, different ion and electron velocities and magnetic field generation, and their effect on ion-electron friction and heat flux. Four dimensionless parameters determine coronal regimes for one-dimensional flows under uniform irradiation. One additional parameter is involved in two-dimensional problems, including the stability of one-dimensional flows, and the smoothing of non-uniform driving.

I. INTRODUCTION

We discuss here the fluid dynamics of the corona of fully ionized plasma ejected by a laser-irradiated target. The motivation of such a discussion is that, first, coronal flows make a special field in fluid dynamics, and, second, the variety of existing flow regimes need be explored prior to a full understanding of laser fusion, particularly of the compression of the imploding (part of the) target. We restrict our study to the direct-drive approach, for which thermal radiation and atomic physics play no dominant role.

The special features of the corona are elaborated in Sec. II. The equations involved in its analysis and the dimensionless parameters characterizing the coronal regimes are considered in Secs. III and IV respectively. In the following section we review limit regimes and time behaviours for uniform laser irradiation, leading to one-dimensional problems described by systems of ordinary differential equations; their solutions involve nonlinear eigenvalues determination and provide basic universal laws. In Sec. VI we consider weakly two-dimensional problems that include the stability of 1-D flows, and the coronal smoothing of weakly non-uniform irradiation of targets. Some effects not included in the model of Sec. III are discussed in Sec. VII.

II. CORONAL FEATURES

In the simplest case, the plasma is characterized by an ion charge number Z_i and mass $Z_i\bar{m}$, and the laser pulse by its peak power W_m, half-width τ_L, and frequency ω (with wavelength λ_L and cri-

tical density n_c then known in terms of universal constants m_e, e, and c). There is, in addition, a characteristic width R: if the target is a foil, R is the focal-spot radius; for a pellet, R is its radius.

The following basic features can now be noticed:

a) There are two widely disparate time-scales, ω^{-1} and $\tau_L >> \omega^{-1}$. The slow-scale flow, of dominant interest here, may be affected by the fast, oscillatory electron motion (light refraction, ponderomotive force).

b) The plasma expands into a vacuum.

c) Energy deposition takes place at electron densities $n_e < n_c$.

d) The mass critical density, $\rho_c = \bar{m} n_c$, is small compared with that of the imploding target, which will be larger than solid density ($770\rho_c$ for fully stripped aluminum and 1.06 μm light).

Consequent, additional, features are

1) The flow speed reaches sonic values, $v^* \sim (T_e^*/\bar{m})^{1/2} \equiv c_s^*$, somewhere in the expanding plasma (asterisk supercripts mark unknown characteristic values, say in the critical surface). The ion inertia enters the sound speed because the slow-scale motion is quasineutral

$$\lambda_D^* << \min(c_s^* \tau_L, R)$$

i.e.

$$(\bar{m}/m_e)^{1/2} << \omega\tau_L \quad \text{or} \quad \lambda_L << Rc/c_e^*$$

where $c_e \equiv (T_e/m_e)^{1/2}$.

2) Since energy must be taken from critical to target den-

sities, and energy convection has an outward direction, thermal conduction must play a dominant role in the overdense region.

3) Formally letting $\rho_{target}/\rho_c \to \infty$, and because i) pressure and mass flow rate remain finite and ii) plasma heat conduction is non-linear, one gets $T/T^* \to 0$ and $v/v^* \to 0$ at the target, which exhibits a well defined (ablation) surface lying at finite distance from the critical density. The slow recession of that surface may be neglected in the analysis of the plasma outside it -the corona-, which is thus uncoupled from the implosion process. (Results from that analysis, say the light absorption, or the pressure and flow rate at the ablation surface, might later be used to study the implosion).

4) The analysis of the corona requires a collisional two-fluid model. Indeed, if electron conduction and energy convection are to be comparable in the overdense region, its length must be

$$L_c \sim \lambda^*_{ei}(\bar{m}/m_e)^{1/2} >> \lambda^*_{ei}, \qquad (1)$$

λ_{ei} being the ion-electron scattering meen-free-path. From the ion energy equation one then gets

$$\frac{T^*_e - T^*_i}{T^*_i} \sim \frac{\lambda^*_{ei}}{L_c}\left(\frac{\bar{m}}{m_e}\right)^{1/2} \sim 1.$$

From the electron momentum equation the same result is found for $|\bar{v}^*_e - \bar{v}^*_i|/c^*_s$.

5) Ion conduction and viscosity, and electron viscosity, represent small corrections of order $(m_e/\bar{m})^{1/2} Z_i^{-5/2}$ and $Z_i m_e/\bar{m}$, respectively.

III. MODEL EQUATIONS

The two-fluid model consists of Maxwell equations

$$\nabla\cdot\bar{E} = 4\pi e(Z_i n_i - n_e), \qquad \nabla\wedge\bar{E} = -\frac{1}{c}\frac{\partial\bar{B}}{\partial t},$$

$$\nabla\cdot\bar{B} = 0, \qquad \nabla\wedge\bar{B} = \frac{1}{c}\frac{\partial\bar{E}}{\partial t} + \frac{4\pi}{c}\bar{J},$$

continuity, momentum, and energy (entropy) equations for either species ($\alpha = e,i$)

$$\frac{\partial n_\alpha}{\partial t} + \nabla\cdot n_\alpha\bar{v}_\alpha = 0$$

$$m_\alpha n_\alpha\left(\frac{\partial}{\partial t} + \bar{v}_\alpha\cdot\nabla\right)\bar{v}_\alpha = -\nabla(n_\alpha T_\alpha) + n_\alpha q_\alpha\left(\bar{E} + \frac{v_\alpha}{c}\wedge\bar{B}\right) +$$

$$+ \bar{R}_{\beta\alpha} + \text{viscous term}$$

$$n_\alpha T_\alpha\left(\frac{\partial}{\partial t} + \bar{v}_\alpha\cdot\nabla\right)\ln\frac{T_\alpha^{3/2}}{n_\alpha} = -\nabla\cdot\bar{q}_\alpha + Q_{\beta\alpha} +$$

$$+ \text{laser heating} + \text{viscous heating}$$

together with a description of light propagation and absorption. Note that $\bar{R}_{\beta\alpha}+\bar{R}_{\alpha\beta} = 0$, $Q_{\beta\alpha}+Q_{\alpha\beta}+\bar{v}_\alpha\cdot\bar{R}_{\beta\alpha}+\bar{v}_\beta\cdot\bar{R}_{\alpha\beta} = 0$.

Ion conduction and viscous terms are negligible as previously indicated. Quasineutrality requires $Z_i n_i = n_e$ and allows to neglect the displacement current and the electron inertia. It also leads to $\nabla\cdot\bar{J} = 0$ where $\bar{J} = eZ_i n_i\bar{v}_i - en_e\bar{v}_e \simeq -en_e\bar{u}$ ($\bar{u} \equiv \bar{v}_e - \bar{v}_i$). One then gets the following system of equations

$$\frac{\partial n_e}{\partial t} + \nabla\cdot n_e\bar{v}_i = 0 \tag{2}$$

$$\bar{m}n_e\left(\frac{\partial}{\partial t} + \bar{v}_i\cdot\nabla\right)\bar{v}_i = -\nabla\left(n_e T_e + \frac{n_e}{Z_i}T_i\right) - n_e\bar{u}\wedge\frac{e\bar{B}}{c} \tag{3}$$

$$\frac{n_e}{Z_i}T_i\left(\frac{\partial}{\partial t} + \bar{v}_i\cdot\nabla\right)\ln\frac{T_i^{3/2}}{n_i} = Q_{ei} \tag{4}$$

$$n_e T_e\left(\frac{\partial}{\partial t} + \bar{v}_i\cdot\nabla\right)\ln\frac{T_e^{3/2}}{n_e} = -n_e T_e\bar{u}\cdot\nabla\ln\frac{T_e^{3/2}}{n_e} - \nabla\cdot\bar{q}_e - \bar{u}\cdot\bar{R}_{ie} - Q_{ei} - \nabla\cdot\bar{S}_L \tag{5}$$

$$\nabla \wedge \left(\frac{e\bar{B}}{c}\right) = -\frac{k_L^2 m_e}{n_c} n_e \bar{u}, \qquad (k_L \equiv \omega/c). \tag{6}$$

In addition, the electron momentum equation is used in Faraday's law to obtain

$$\frac{\partial}{\partial t}\left(\frac{e\bar{B}}{c}\right) + \nabla \wedge \left(\frac{e\bar{B}}{c} \wedge (\bar{v}_i + \bar{u}) + \frac{\bar{R}_{ie}}{n_e}\right) = \nabla T_e \wedge \nabla \ln n_e . \tag{7}$$

The collisional results for electron heat flux, and ion-electron friction and energy exchange rate are[1]

$$\bar{q}_e = -n_e T_e \left(\frac{\tau_e}{m_e} \bar{\bar{\gamma}} \cdot \nabla T_e - \bar{\bar{\beta}} \cdot \bar{u}\right)$$

$$\bar{R}_{ie} = -n_e \left(\frac{m_e}{\tau_e} \bar{\bar{\alpha}} \cdot \bar{u} + \bar{\bar{\beta}} \cdot \nabla T_e\right)$$

$$Q_{ei} = \frac{3 m_e n_e}{Z_i \bar{m} \tau_e} (T_e - T_i),$$

where τ_e is some characteristic electron collision time

$$\tau_e = \frac{3}{4(2\pi)^{1/2}} \frac{m_e^{1/2} T_e^{3/2}}{e^4 Z_i n_e \ln \Lambda}$$

and $\ln \Lambda$ is a Coulomb logarithm.

The tensors $\bar{\bar{\alpha}}$, $\bar{\bar{\beta}}$, and $\bar{\bar{\gamma}}$ are dimensionless functions of Z_i and $\frac{eB}{c}\frac{\tau_e}{m_e} \equiv \omega_{ce}\tau_e$, ω_{ce} being the electron cyclotron frequency. Their symmetric and antisymmetric parts are even and odd in B respectively, and represent laws or effects well stablished in other fields of physics

$$\bar{\bar{\alpha}} = \bar{\bar{\alpha}}_s(\text{Ohm}) + \bar{\bar{\alpha}}_a(\text{Hall})$$

$$\bar{\bar{\gamma}} = \bar{\bar{\gamma}}_s(\text{Fourier}) + \bar{\bar{\gamma}}_a(\text{Righi-Leduc})$$

$$\bar{\bar{\beta}} = \bar{\bar{\beta}}_s \begin{Bmatrix} \text{Seebeck} \\ \text{Peltier} \end{Bmatrix} + \bar{\bar{\beta}}_a \begin{Bmatrix} \text{Ettinghausen} \\ \text{Nernst} \end{Bmatrix} \quad \text{for} \quad \begin{Bmatrix} \bar{q}_e \\ \bar{R}_{ie} \end{Bmatrix}.$$

If ray tracing is not required (negligible ray crossing) the light energy flux is

$$\bar{S}_L = \bar{s}_i I_i + \bar{s}_r I_r$$

where the subscripts refer to rays incident and reflected (at the critical surface). One then has[2]

$$\nabla \cdot \bar{s}_{i,r} I_{i,r} = -k_{br} I_{i,r} \tag{8}$$

$$\bar{s}_{i,r} \cdot \nabla \bar{s}_{i,r} = \left[\nabla - \bar{s}_{i,r}(\bar{s}_{i,r} \cdot \nabla)\right] \ln(1-n_e/n_c)^{1/2} \tag{9}$$

where k_{br} is the absorption coefficiente for inverse bremsstrahlung[3]

$$k_{br} = \frac{n_e/n_c}{c\tau_e(1-n_e/n_c)^{1/2}}.$$

IV. DIMENSIONLESS PARAMETERS

System (2)-(9), together with the auxiliary equations for $\bar{q}_e$, $\bar{R}_{ie}$, Q_{ei}, and k_{br}, and the expressions for τ_e and $\bar{S}_L$, is a set of ten equations for the ten variables

$$n_e,\ \bar{v}_i,\ T_e,\ T_i,\ \bar{u},\ e\bar{B}/c,\ \bar{s}_{i,r},\ I_{i,r}.$$

The system involves a number of dimensional parameters and a dimensionless one (Z_i).

Writing $c\tau_e = m_e c \times \tau_e/m_e$ in k_{br} and defining $\bar{K}(z)$ by setting

$$\frac{\tau_e}{m_e} \equiv \frac{\bar{K}(Z_i)}{\gamma_o(Z_i)} \frac{T_e^{3/2}}{n_c}$$

we count eight parameters

$$W_m,\ \tau_L,\ R,\ n_c,\ \bar{m},\ k_L^2 m_e,\ \bar{K},\ \text{and}\ m_e c;$$

$\gamma_o \bar{\bar{I}}$ is the limit form of $\bar{\bar{\gamma}}$ in $\bar{q}_e$ for $\omega_{ce}\tau_e \to 0$. Note that $\bar{K}$ is then the coefficient in Spitzer's thermal conductivity

$$K(\text{Spitzer}) \equiv \bar{K}\, T_e^{5/2};$$

we neglect its weak dependence on n_e and T_e due to the Coulomb logarithm.

Five dimensionless combinations of the above parameters can be obtained. However, if a dimensional analysis of Eqs. (2)-(9) is carried out only four combination show up. A fifth one, $n_c R^3$, the number of electrons in a macroscopic volume, involves microscopic information for which our equations have no use.

Thus, finally, dimensionless results from the present formulation will depend on the dimensionless numbers

$$\sigma_1 \equiv \left(\frac{W_m}{R^2 \bar{m} n_c}\right)^{1/3} \frac{\tau_L}{R}, \qquad \sigma_2 \equiv \frac{\bar{K}\,\bar{m}^{5/2} R^3}{n_c \tau_L^4},$$

$$\sigma_3 \equiv \frac{\bar{m} R}{m_e c \tau_L}, \qquad \sigma_4 \equiv \frac{m_e}{\bar{m}} (k_L R)^2,$$

and Z_i.

V. ONE-DIMENSIONAL SOLUTIONS

For atomic number Z not too high, atoms in the corona are fully stripped ($Z_i = Z$) and the dependence of the flow on Z_i shows no particular features. The main effect is that as Z_i increases, ion pressure and entropy per unit volume become negligible against the corresponding electron values. There is a slight simplification: T_i remains in Eq. (4) only, and may be ignored

when determining all other variables.

Consider now target and irradiation that are both spherically symmetric. Current and magnetic field then vanish identically. As a result σ_4 drops off the analysis, leaving σ_1-σ_3 as remaining parameters.

For σ_1 small the corona is a thin layer ($L \sim c_s^* \tau_L \ll R$) that may be considered planar (one-dimensional, straight flows). Introducing convenient, reference values of velocity and intensity

$$U \equiv (n_c \tau_L / \bar{m}^{5/2} \bar{K})^{1/3}, \quad I_o \equiv W_m / 4\pi R^2$$

we then use parameters $\bar{I}_o$ and $\bar{U}$ instead of σ_2 and σ_3:

$$\bar{I}_o \equiv \frac{I_o}{\rho_c U^3} = \frac{\sigma_1^3 \sigma_2}{4\pi} = \frac{W_m \bar{K} \bar{m}^{3/2}}{4\pi R^2 n_c^2 \tau_L}$$

$$\bar{U} \equiv \frac{\bar{m} U}{m_e c} = \frac{\sigma_3}{\sigma_2^{1/3}} = \frac{n_c^{1/3} \tau_L^{1/3} \bar{m}^{-1/6}}{m_e c \bar{K}^{1/3}}.$$

One easily verifies that $L_c / c_s^* \tau_L \sim \bar{I}_o$.

For $\bar{I}_o$ small we have $L_c \ll L$: conduction is restricted to a thin sublayer, having both overdense and underdense regions and lying next to the target. This sublayer may be considered quasisteady. If $W(t) \propto t^{3/2}$ the larger region outside the layer has a self-similar behaviour; as a consequence the entire problem is reduced to the analysis of systems of ordinary differential equations. For $\bar{U}/\bar{I}_o^{2/3}$ small, inverse bremsstrahlung is negligible and surface absorption at n_c must be considered (Sec. VII). If then $W(t) \propto t$, the entire corona has a self-similar behaviour, leading again to ordinary differential equations.

For σ_1 large ($c_s^* \tau_L >> R$), quasisteady conditions are attained during most of the pulse, and the characteristic length of the corona is R itself. We are led once more to ordinary differential equations. Introducing a velocity

$$V \equiv (n_c R/\bar{m}^{5/2}\bar{K})^{1/4}$$

we then use parameters $\bar{W}$ and $\bar{V}$ instead of σ_2 and σ_3:

$$\bar{W} \equiv \frac{I_o}{\rho_c V^3} = \frac{\sigma_1^3 \sigma_2^{3/4}}{4\pi} = \frac{W_m \bar{K}^{3/4} \bar{m}^{7/8}}{4\pi R^{11/4} n_c^{7/4}},$$

$$\bar{V} \equiv \frac{\bar{m} V}{m_e c} = \frac{\sigma_3}{\sigma_2^{1/4}} = \frac{\bar{m}^{3/8} R^{1/4} n_c^{1/4}}{m_e c \bar{K}^{1/4}}.$$

One easily verifies that $L_c/R \sim \bar{W}^{4/3}$. For $\bar{W}^{4/3}$ small we have $L_c << L$: conduction is restricted to a thin layer having both overdense and underdense regions and lying next to the target. For $\bar{V}/\bar{W}$ small, inverse bremsstrahlung becomes negligible.

Consider next a foil target. For σ_1 large, the flow will be quasisteady and divergent, but only in a crude sense may it be taken as (hemispherically) symmetric; $\bar{B}$ and $\bar{u}$ effects will be essential to the analysis. For σ_1 small, however, we again have a thin corona ($L \sim c_s^* \tau_L << R$), which may be considered planar if, as usual, transverse variations across the laser spot have its radius R as characteristic length. One may then repeat the previous discussion on $\bar{I}_o$ and $\bar{U}$, just omitting the factor 1/4 in I_o and $\bar{I}_o$.

In all above cases, universal laws for quantities such as peak electron and ion temperatures, mass ablation rate, ablation pressure, and fractional absorption can be obtained. The laws

are analytical in a sense usual in fluid mechanics: they represent dimensionless functions of a few dimensionless parameters, result from ordinary differential equations as nonlinear boundary value problems, and usually involve eigenvalues determination by requiring the crossing of some singular points.

There is clearly a richness of behaviour depending on coronal length relative to pellet or spot radius, conduction-to-coronal length ratio, fractional inverse bremsstrahlung absorption, and even ion-to-electron energy storage ratio. That richness is necessarily reflected in target implosion.

An example is the implosion of a thin foil. The hydrodynamic efficiency η_H for its acceleration is a function of the ratio of ablated mass ΔM at the end of the pulse to the initial mass M_o. The function $\eta_H(\Delta M/M_o)$ was calculated for different coronal regimes.[4] The efficiency was found to depend substantially on the particular regime considered (Fig. 2 of Ref. 4).

Quite detailed results on coronal flows in different regimes have been obtained for both planar[5] ($\sigma_1 \to 0$) and spherical[6] ($\sigma_1 \to \infty$) conditions.

VI. WEAKLY TWO-DIMENSIONAL FLOWS

When target or irradiation conditions are not perfectly symmetric or uniform, coronal flows become two-dimensional and the parameter σ_4, characterizing current and magnetic effects, enters the picture. The analysis of such flows may be quite complex.

Particularly simple are problems that may be considered as only weakly two-dimensional. The main examples are the analy-

sis of a) the stability of the 1-D flows of Sec. V, and b) the smoothing of impressed, weak, nonuniformities in irradiation or surface finish: i.e. perturbations of the Sec. V flows. The ratio of perturbation wavelength to coronal length is an additional parameter characterizing these problems.

Since both $\bar{B}$ and $\bar{u}$ are then small quantities, one finds with all generality that

$$\bar{R}_{ie} \simeq -n_e\left(\frac{m_e}{\tau_e}\alpha_o\bar{u} + \frac{\beta_o''}{\delta_o}\frac{\tau_e e\bar{B}}{m_e c}\wedge\nabla T_e + \beta_o\nabla T_e\right),$$

$$\bar{q}_e \simeq -n_e T_e\left(\frac{\tau_e}{m_e}\left(\gamma_o\nabla T_e + \frac{\gamma_o''}{\delta_o}\frac{\tau_e e\bar{B}}{m_e c}\wedge\nabla T_e\right) - \beta_o\bar{u}\right).$$

Then, Faraday's law becomes

$$\frac{\partial}{\partial t}\left(\frac{e\bar{B}}{c}\right) + \nabla\wedge\left[\frac{e\bar{B}}{c}\left(\bar{v}_i - \frac{\beta_o''}{\delta_o}\frac{\tau_e}{m_e}\nabla T_e\right) - \frac{m_e}{\tau_e}\alpha_o\bar{u}\right] = \nabla T_e\wedge\nabla\ln n_e \quad (10)$$

and the first three terms on the right-hand side of Eq. (5) become

$$-n_e T_e\bar{u}\cdot\nabla\ln\frac{T_e^{3/2}}{n_e} - \nabla\cdot\bar{q}_e - \bar{u}\cdot\bar{R}_{ie} \rightarrow -n_e T_e\bar{u}\cdot\nabla\ln\frac{T_e^{3/2}}{n_e} +$$

$$+\nabla\cdot(\bar{K}T_e^{5/2}\nabla T_e) + \nabla\cdot\left[\bar{K}T_e^{5/2}\frac{\gamma_o''}{\gamma_o\delta_o}\frac{\tau_e e\bar{B}}{m_e c}\wedge\nabla T_e\right]. \quad (11)$$

Note that only Ohm and Nermst terms enter (10), while the $\bar{u}$-convection of electron entropy, and Righi-Leduc conduction, enter (11). The thermoelectric effects (β_o-terms) and the term $\bar{J}\wedge\bar{B}/c$ in Eq. (3) drop out. On the contrary, the refraction equations (8), (9) are an essential part of weakly 2-D flows. The Braginskii coefficients (α_o, β_o'', etc.) only depend on Z_i.

Problems of type b) (thermal and refractive smoothing) have been recently analyzed in a series of papers.[7]

Full 2-D coronal flows can be simplified in special limits Consider first σ_1 large. For $\sigma_4 \to 0$, Faraday's law generates a current through Ohm's term, the heating in (5) is due to $\bar{u}$ convection of entropy, and Ampere's law gives $\bar{B}$, which is small ($\omega_{ce}\tau_e << 1$). For $\sigma_4 \to \infty$, the $\partial\bar{B}/\partial t$ and $\bar{v}_i \wedge \bar{B}$ terms and the Nermst effect enter Faraday's law, yielding $\bar{B}$ (now we have $\omega_{ce}\tau_e \sim 1$), Ampere's law gives a small $\bar{u}$, and Righi-Leduc heating occurs. In both the small and large σ_4 limits, the force $\bar{J} \wedge \bar{B}/c$ is negligible. For σ_1 small the same results apply, if $\sigma_1^2\sigma_4$ is small and large respectively.

VII. CORRECTIONS TO THE MODEL

i) Thermal radiation

For atomic number Z not too large, and thus ions fully stripped, the transport of thermal radiation has a simple description if polarization and refraction are neglected: only bremsstrahlung processes and Thomson scattering are involved. Letting $I_\nu(\bar{\Omega})$ be the specific intensity for frequency ν and directional unit vector $\bar{\Omega}$, we have[8]

$$\bar{\Omega}\cdot\nabla I_\nu(\bar{\Omega}) = \kappa'_{a\nu}\left[I_{p\nu} - I_\nu(\bar{\Omega})\right] + \\ + \kappa_{s\nu}\int d\bar{\Omega}' \frac{3}{4\pi}\left[1+(\bar{\Omega}\cdot\bar{\Omega}')^2\right]\left[I_\nu(\bar{\Omega})-I_\nu(\bar{\Omega}')\right], \qquad (10)$$

where the time derivative was neglected ($c\tau_L >> R$) and

$$I_{p\nu} = 2h\nu^3/c^2(e^{h\nu/T_e}-1),$$

$$\kappa'_{a\nu} = \frac{\pi\sigma}{3^{1/2}\ln\Lambda}\left(\frac{\hbar\omega}{T_e}\right)^2 \frac{n_e/n_c}{c\tau_e}\,\frac{1-e^{-h\nu/T_e}}{(h\nu/T_e)^3},$$

$$\kappa_{s\nu} = \frac{(2\pi)^{1/2}}{Z_i \ln \Lambda} \left(\frac{T_e}{m_e c^2}\right)^{3/2} \frac{1}{c\tau_e}.$$

For an optically thin corona ($L \ll \kappa'^{-1}_{a\nu}, \kappa^{-1}_{s\nu}$), Eq. (10) becomes

$$\bar{\Omega}\cdot\nabla I_\nu(\bar{\Omega}) = \kappa'_{a\nu} I_{p\nu}.$$

The thermal radiation flux, $\bar{S}_{th} \equiv \int d\nu\, d\bar{\Omega}\, I_\nu(\bar{\Omega})\,\bar{\Omega}$, is then given by

$$\nabla\cdot\bar{S}_{th} = \frac{4\alpha}{3^{1/2} \ln\Lambda} \frac{n_e T_e^2}{m_e c^2 \tau_e}$$

where $\alpha \equiv e^2/\hbar c = 137^{-1}$ is the constant of fine structure, and a Gaunt factor $g = 1$ was used. A term $-\nabla\cdot\bar{S}_{th}$, representing plasma-radiation energy exchange, should be added to the left-hand side of Eq. (5). With the dimensionless analysis of Secs. IV-VI, the above exchange term is of order $\alpha\bar{V}/\bar{W}^{2/3}$ for σ_1 large; since $\bar{W}$ is large for usual conditions, rarely need thermal radiation be included in the analysis. Similarly, for σ_1 small we have $-\nabla\cdot\bar{S}_{th} \sim \alpha\sigma_1^{1/4}\,\bar{U}/\bar{I}_o^{5/12}$. One easily verifies that the corona is indeed optically thin; for σ_1 large, for instance, we have

$$R\kappa'_{a\nu} \sim \frac{\bar{V}^5}{\sigma_4 \bar{W}^{7/3}} \left(\frac{m_e}{\alpha\bar{m}}\right)^2,$$

$$R\kappa_{s\nu} \sim \frac{\bar{V}^4}{Z_i} \left(\frac{m_e}{\bar{m}}\right)^{3/2}.$$

ii) Ionization energy

This effect was also ignored in the model of Sec. III. If $j^2\epsilon_j$ is the energy required to strip an atom off its j^{th} electron, the total ionization energy is $\Sigma\epsilon_j j^2$, $j = 1,2,\ldots,Z_i$; here

$$\epsilon_j = I_H \times (\text{a factor of order unity})$$

$$I_H \equiv \frac{m_e e^4}{2\hbar^2} = \frac{1}{2}\alpha^2 m_e c^2 \simeq 13.6\ \text{eV}.$$

For $Z_i >> 1$, when the effect is largest, the total plasma energy per electron is $\frac{1}{2}\bar{m}v^2 + \frac{3}{2}T_e + \frac{1}{3}\bar{\varepsilon}Z_i^2$, $\bar{\varepsilon}$ being some average value. To just get an estimate, we set $\bar{m}v^2 = T_e = T_e^*$, $I_o = n_c(T_e^*/\bar{m})^{1/2} \times$ $\times(2T_e^* + \frac{1}{3}\bar{\varepsilon}Z_i^2)$ and $\bar{\varepsilon} = 10$ eV (midway between 4 and 25 eV). Then we have $T_e^* \propto 1 + Z_i^2\bar{\varepsilon}/9T_e^*$, the last term being the ionization correction, assumed weak. In dimensionless form, this term reads

$$\frac{Z_i^2\bar{\varepsilon}}{9T_e^*} \simeq \frac{\alpha^2\bar{m}}{16m_e}\frac{Z_i^2}{\bar{V}^2\bar{W}^{2/3}} \simeq \left(\frac{Z_i}{9\bar{V}\bar{W}^{1/3}}\right)^2.$$

Typically Z ($\simeq Z_i$) about 10-15 is the largest atomic number for which the ionization energy may be reasonably neglected.

iii) Ionization state

For Z large enough, the ion charge number Z_i lags behind it. This fact introduces complex atomic physics into the analysis. First, some appropriate value for a mean Z_i must be determined as part of the problem; the ion populations for different ionization states may in fact be needed. Secondly, line emission and absorption, frequently quite large, will need be accounted for in the radiation transport; the plasma-radiation exchange must be considered in the plasma energy balance. Finally the ionization energy will also be substantial.

Both high target atomic-number and special target design, result in copious thermal (x-rays) radiation in the corona of holraum targets. On the whole, atomic physics overwhelms fluid mechanics in the holraum approach to laser fusion. By restricting our study to the direct-drive approach, we explicitly exclude

targets with high atomic number.

iv) Non-classical heat flux

At a large ionization state, the mean free paths for ion-electron scattering, λ_{ei}, and electron-electron relaxation $\lambda_{ee} \sim$ $\sim Z_i \lambda_{ei}$ are widely disparate. From Eq. (1), $L_c \sim \lambda_{ei}(\bar{m}/m_e)^{1/2}$, the ratio

$$\frac{\lambda_{ee}}{L_c} \sim Z_i (m_e/\bar{m})^{1/2}$$

need not be small. One then expects that the hypothesis of a local near-Maxwellian electron population may break down, invalidating the classical calculation of transport coefficients. Actually, i) the electrons contributing mostly to the heat-flux have energy ε somewhat above T_e, and ii) their motion between electron-electron collisions is a random walk; the condition for a break-down of local thermal equilibrium for electrons is then that $Z_i^{1/2}(\varepsilon/T_e)^2$ gets near $(\bar{m}/m_e)^{1/2}$. The crude expression $\bar{q} = -f\, n_e T_e (T_e/m_e)^{1/2} \nabla T_e/|\nabla T_e|$, normally used under such conditions, involves an "ad hoc", overall, flux limit factor f, that must change with the regime of the coronal flow. A non-local kinetic formalism should depend on the dimensionles number $Z_i^{1/2}(\varepsilon/T_e)^2 \times$ $\times (m_e/\bar{m})^{1/2}$.

v) Plasma-light interaction

The fast (ω^{-1}) time-scale interaction between laser beam and plasma electrons basically yields the dielectric function, $1-n_e/n_c$, for light propagation, and the absorption coefficient k_{br}. There are however additional interaction phenomena, not included in our model.

First, for Z_i large, the ratio $\lambda_{ce}/\lambda_{ei}$ is of order Z_i, as earlier noticed. This affects the classical result for k_{br} when $Z_i I_o/cn_c T_e^*$ reaches about unity.[10]

Secondly, (linear) resonance absorption occurs at the critical density for oblique incidence and p-polarization. For weakly two-dimensional flow, the absorption will depend on the value of $(\lambda \nabla \ln n_e)^{2/3}(1-\tau_i \cdot \nabla n_e/|\nabla n_e|)$ at n_c, and may be of order unity.[11]

Finally, (nonlinear) parametric effects may affect the fate of light propagating inwards, up to the critical surface. Such inconvenient effects may be avoided by the use of broad laser bandwidth.

vi) Target thickness

If the target is a foil, or a spherical shell, so thick that the inward moving perturbation has not reached its backface by the end of the pulse, then an overall momentum balance shows that

$$\text{inward velocities} \sim c_s^* \times (\rho_c/\rho_{target})^{1/2} \ll c_s^*.$$

This inequality was the basis for the neglect of the receding motion of the ablation surface, an essential point in our model for a coronal analysis. The target thickness ΔR is large enough if

$$\Delta R > \tau_L c_s^* (\rho_c/\rho_{target})^{1/2} \quad \text{or} \quad \rho_c/\rho_{target} < (\Delta R/c_s^* \tau_L)^2. \quad (11)$$

If, however, the opposite is true, then we have

$$\text{inward velocities} \sim c_s^* \times \frac{c_s^* \tau_L}{\Delta R} \times \frac{\rho_c}{\rho_{target}},$$

so that the receding motion may be neglected if

$$\tau_L c_s^*(\rho_c/\rho_{target}) << \Delta R < \tau_L c_s^*(\rho_c/\rho_{target})^{1/2}.$$

The first inequality, weaker than (11), basically means that the ablated mass fraction be small. For a spherical shell of radius R, the pulse will be on, at shell collapse, if

$$c_s^* \tau_L > (R\Delta R)^{1/2}(\rho_{target}/\rho_c)^{1/2}$$

or

$$\Delta R < \tau_L c_s^*(\rho_c/\rho_{target}) \times c_s^* \tau_L / R.$$

REFERENCES

1. S.I. Braginskii, in: Transport Processes in a Plasma, Reviews of Plasma Physics, Vol. 1, ed. M.A. Leontovich (Consultants Bureau, New York, 1965).

2. L.D. Landau and E.M. Lifshitz, Electrodynamics of Continuous Media, (Pergamon, Oxford, 1960).

3. T.W. Johnston and J. Dawson, Phys. Fluids 16 (1973), 722.

4. J.R. Sanmartín, J.L. Montañés, J. Sanz, and R. Ramis, Plasma Phys. 27 (1985), 983.

5. J.R. Sanmartín and A. Barrero, Phys. Fluids 21 (1978), 1957, 1967; A. Barrero and J.R. Sanmartín, Plasma Phys. 22 (1980), 617; J.R. Sanmartín, J.L. Montañés and A. Barrero, Physics Fluids 26 (1983), 2754; R. Ramis and J.R. Sanmartín, Nucl. Fusion 23 (1983), 739; J.A. Nicolás, Plasma Phys. and Contr. Fus. 28 (1984), 1441.

6. J.L. Montañés and J.R. Sanmartín, Phys. Fluids 23 (1980), 650; J. Sanz, A. Liñán, M. Rodríguez and J.R. Sanmartín, Phys. Fluids 24 (1981), 2098; J. Sanz and J.R. Sanmartín, Phys. Fluids 26 (1983), 3370; J.R. Sanmartín, R. Ramis, J.L. Montañés, and J. Sanz, Phys. Fluids 28 (1985), 2282; J.A. Nicolás and J.R. Sanmartín, Plasma Phys. 27 (1985), 279.

7. J.R. Sanmartín, J. Sanz and J.A. Nicolás, Phys. Lett A 124 (1987), 81; J. Sanz, J.A. Nicolás, J.R. Sanmartín and J. Hilario, Phys. Fluids, I and II (to be published); J. Sanz, Plasma Phys. and Contr. Fus. (to be published); J. Sanz, F. Ibáñez, J.A. Nicolás and S.G. Tagare (in press.).

8. G.C. Pomraning, The Equations of Radiation Hydrodynamics, (Pergamon, Oxford, 1973).

9. J.R. Albritton, A. Williams, I.B. Bernstein, and K.P. Swartz, Phys. Rev. Lett 57 (1986), 1887; J.F. Luciani, P. Mora and R. Pellat, Phys. Fluids 28 (1985), 835.

10. A.B. Langdon, Phys. Rev. Lett. 44 (1980), 575.

11. J.P. Friedberg, R.W. Mitchell, R.L. Morse, and L.I. Rudsinski, Phys. Rev. Lett. 28 (1972), 795.

SELF-SIMILAR EXPANSIONS IN ION BEAM FUSION

A. Barrero and A. Fernández
Department of Thermo and Fluid Mechanical Engineering.
University of Sevilla, 41012 Sevilla, Spain.

The self-similar expansion generated by an intense light ion beam pulse of energy per nucleon $E_b=E_o(t/\tau)^p$ and current intensity $I_b=I_o(t/\tau)^{2p-1}$ $(0<t<\tau)$ impinging on a planar target is considered. The structure of the expansion flow is analyzed and profiles of beam density and velocity and density, velocity and temperature of the plasma are found from the analysis. Quantities of interest in inertial confinement fusion such as the ablation pressure and the mass ablated rate as functions of time for several values of the law time exponent p are obtained. The acceleration efficiency of thin foils, defined as the fraction of absorbed energy that goes to foil kinetic energy as function of p has been also calculated.

. remitted to Nuclear Physics A
Controlled Fusion

1. INTRODUCTION

In a recent paper (Fernández and Barrero 1986) called I hereafter, the authors found that the one-dimensional motion generated by an intense ion beam pulse impinging on an initially cold half-space of electron density n_o becomes self-similar when the beam parameters (energy per nucleon E_b and current intensity per unit area I_b), depend on time as $E_b = E_o(t/\tau)^{2/3}$, $(0<t<\tau)$ and $I_b = I_o(t/\tau)^{1/3}$. They showed that the plasma motion depends on a dimensionless number

$$\alpha = \frac{9\pi^3 e^{11} Z_b^5 m_b^3 (\ln\Lambda)^3 n_o^2 \tau^3 I_o}{4 m_i m_e^3 E_o^5} \quad , \qquad (1)$$

which contains the basic beam and plasma parameters, and found two asymptotic limits for large and small values of the parameter α; m, Z, e and $\ln\Lambda$ are mass, charge number, electron charge and Coulomb logarithm respectively and subscripts e, i and b refer to electrons, ions and beam. For large α values which are usually found in light ion beam fusion, with the exception of extremely short pulses, two different regions may be distinguished in the plasma motion: an isentropic compression region separated by a shock from the undisturbed plasma, followed by a much wider expansion flow where energy absorption occurs. A well defined ablation surface exits in between (see Figure 1a). The analysis yields quantities such as the ablation pressure and the mass ablated rate which are of interest in inertial confinement fusion. As α decreases down to values of order of

unity (E_o and I_o being larger and smaller respectively than in the preceding case) the beam velocity is so large that the boundary with the undisturbed plasma runs ahead of the shock. The characteristic lenghts of the compression and expansion regions becomes of comparable extent (see Fig. 1b). The plasma ahead of the shock is heated but not compressed and the compression behind the shock is not isentropic. As α goes on decreasing, the E_o and I_o values being those of heavy ion beam fusion, the shock intensity weakens and becomes a rarefaction wave (the plasma is heated but not compressed) that runs for behind the undisturbed plasma boundary since its velocity is much smaller than the beam velocity. The espansion flow region becomes very thin as compared with the heating region (see Fig. 1c).

In this paper we have considered the effect of the time law on the hydrodynamics of the ion beam plasma interaction. To this end, we consider a planar target impinged by an ion beam whose parameters depend on time as

$$E_b = E_o(t/\tau)^p \quad , \quad I_b = I_o(t/\tau)^{2p-1} \quad , \qquad (2)$$

and assume that the values of E_o, I_o and τ satisfy the condition $\alpha >> 1$ (ablation regime). The expansion flows produced in this cases, neglecting heat conductiɒn and radiation becomes self-similar since the restriction imposed by solid density is relaxated (density becomes infinity at the ablation surface as we shall see later). We have carried out an analysis of these self-similar expansion flows for different

values of the exponent p and the results obtained, which are entirely independent of the compression region, yield both the ablation pressure P_a and the mass ablated rate $\dot{m}$ as a function of the beam design parameter E_o and I_o, τ and p.

We present the mathematical problem and introduce self similar variables and equations in Section 2. The resulting equations are analyzed in Section 3. In Section 4 we calculated the accleration efficiency of thin foils and finally, the results obtained are discussed in Section 5.

2. STATEMENT OF THE PROBLEM.

The equations describing the expansion flow of a fully ionized plasma produced by impinging a solid target with an ion beam pulse are:

$$\frac{\partial n_b}{\partial t} + \frac{\partial (n_b v_b)}{\partial x} = 0 \qquad (3)$$

$$m_b n_b \left(\frac{\partial v_b}{\partial t} + v_b \frac{\partial v_b}{\partial x}\right) = - R \qquad (4)$$

$$\frac{Dn}{Dt} + n\frac{\partial v}{\partial x} = 0 \quad , \quad \left(\frac{D}{Dt} = \frac{\partial}{\partial t} + v\frac{\partial}{\partial x}\right) \qquad (5)$$

$$\frac{m_i n}{Z_i} \frac{Dv}{Dt} = - \frac{Z_i + 1}{Z_i} \frac{\partial}{\partial x}(nkT) + R \qquad (6)$$

$$\frac{n}{Z_i}\frac{D}{Dt}\left[\frac{3}{2}(Z_i+1)kT + \frac{m_i v^2}{2}\right] = -\frac{Z_i+1}{Z_i}\frac{\partial}{\partial x}(nkvT) + R(v_b - v) \quad ; \quad (7)$$

where n, v, T are density, velocity and temperature respectiely, m, Z and k are mass, charge number and Boltzman's constant, and subcripts i and b refer to ions and beam. We have assumed planar geometry, and a quasi-neutral, collision dominated plasma. The beam, which is considered both cold and neutralized, transfer to the free electrons a momentum per unit volume and time R given by

$$R = 4\pi e^4 Z_b^2 \ln\Lambda \frac{n n_b}{m_e v_b^2} \Phi\left[\frac{v_b}{(2kT/m_e)^{1/2}}\right] \quad , \quad (8)$$

$$\Phi(y) = 2\pi^{-1/2}\left[\int_0^y exp(-t^2)dt - y exp(-y^2)\right] \quad , \quad (9)$$

MIYAMOTO (1980), JACKSON (1975); e, m_e and $\ln\Lambda$ are electron mass and charge and Coulomb logarithm respectively (the weak dependence of $\ln\Lambda$ on n, v_b and T will be neglected in our analysis). Notice that we do not include the effect of the inellastic collisions on the stopping power, so that we should only consider low Z_i targets, NARDI et al. (1977), MELHORN (1981), OLSEN (1985).

The beam pulse, starting at t=0, is incident from $x = -\infty$ on the solid half-space x>0; assuming that the beam parameters depend on time as

$$I_b(t) = eZ_b n_b(-\infty,t)v_b(-\infty,t) = I_o(t/\tau)^{2p-1} \quad , \quad (10)$$

and

$$E_b(t) = m_b v_b^2(-\infty,t)/2 = E_o(t/\tau)^p \quad , \quad (0<t<\tau) \quad , \qquad (11)$$

we may introduce self-similar variables

$$u_b(\xi) = v_b(x,t)/[(2E_o/m_b)^{1/2}(t/\tau)^{p/2}] \quad , \qquad (12a)$$

$$v_b(\xi) = (eZ_b/I_o)(2E_o/m_b)^{1/2} n_b(x,t)(t/\tau)^{1-3p/2} \quad , \qquad (12b)$$

$$v(\xi) = n(x,t)(t/\tau)^{1-3p/2} n_r^{-1} \quad , \qquad (12c)$$

$$u(\xi) = v(x,t)/[(Z_i kT_r/m_i)^{1/2}(t/\tau)^{p/2}] \quad , \qquad (12d)$$

$$\theta(\xi) = T(x,t)/[T_r(t/\tau)^p] \quad , \qquad (12e)$$

$$\xi = x/[(Z_i kT_r/m_i)^{1/2}\tau(t/\tau)^{p/2+1}] \quad , \qquad (12f)$$

to transform Equations (3)-(9) into the system

$$v_b u_b = 1 \quad , \qquad (13)$$

$$\frac{du_b}{d\xi} = -\frac{v}{u_b^3}\,\Phi(\beta u_b/\theta^{1/2}) \quad , \qquad (14)$$

$$(3\frac{p}{2}-1)v - (\frac{p}{2}+1)\xi\frac{dv}{d\xi} + \frac{d(vu)}{d\xi} = 0 \quad , \qquad (15)$$

$$v[\frac{p}{2}u - (\frac{p}{2}+1)\xi\frac{du}{d\xi} + u\frac{du}{d\xi}] = -\frac{Z_i+1}{Z_i}\frac{d(v\theta)}{d\xi} \quad , \qquad (16)$$

$$v\left\{p(\frac{u^2}{2}+\frac{3}{2}\frac{Z_i+1}{Z_i}\theta) + [u-(\frac{p}{2}+1)\xi]\frac{d}{d\xi}(\frac{u^2}{2}+\frac{3}{2}\frac{Z_i+1}{Z_i}\theta)\right\} = -\frac{Z_i+1}{Z_i}\frac{d(vu\theta)}{d\xi} + \frac{vv_b}{u_b}\Phi \quad , \qquad (17)$$

where

$$\beta = (m_e E_o/m_b kT_r)^{1/2} \quad , \qquad (18)$$

and to simplify the equations, we chose a convenient reference temperature and density

$$T_r = \frac{2\pi e^3 Z_b (\ln\Lambda)\tau I_o m_b}{m_e k E_o} \quad , \tag{19}$$

and

$$n_r = \left(\frac{m_e^3 m_i E_o^5}{2\pi^3 e^{11} Z_b^5 (\ln\Lambda)^3 \tau^3 m_b^3 Z_i I_o}\right)^{1/2} \quad , \tag{20}$$

and neglected terms of order of $[m_b Z_i kT_r/(2m_i E_o)]^{1/2}$ which are assumed small (the case of interest in ion beam fusion). Notice that equations (13) and (14) show the quasi-steadiness of the beam motion.

For $n_r << n_o$ (n_o being solid density) there exists a well defined ablation surface separating the rarefied expansion flow, where the absorption energy occurs, from the high density compression zone on the right. It is worth to notice that inequality $n_r << n_o$ corresponds to condition $\alpha >> 1$.

For a proton beam pulse (2Mev, $10^7 Acm^{-2}$, 40 ns) impinging on D-T pellets ($n_o = 5\times10^{22} cm^{-3}$), one has $n_r = 3.5\times10^{21}$ cm^{-3}, so that condition $n_r << n_o$ (or $\alpha >> 1$) may be well accomplished for light ion beam fusion. On the other hand, the ablation regime will not usually develop for heavy ion beam fusion (except for very long pulses) since the values of the energy per nucleon E_o and current intensity I_o are larger and smaller respectively than the corresponding ones for light ion beam fusion. The regime $\alpha << 1$ (heating regime) for the case p=2/3 was analyzed in paper I; a qualitative view of the plasma behaviour when parameter α goes from large to

small values was also given there.

The implosion velocity of the ablation surface is slow when compared with velocities in the expansion flow, so that to analyze the expansion in the ablation regime, the ablation surface may be set at $\xi=0$, where to match with the cold high density compression region the density goes to infinity, both temperature and velocity vanish, and the pressure takes a finite value; then for values of the beam and plasma parameter such as $n_r << n_o$ we may write as boundary conditions

$$u = \theta = 0 \quad , \quad v\theta = \gamma \quad , \quad \text{at } \xi = 0 \tag{21}$$

where γ is an unknown constant defined in terms of the ablation pressure as:

$$\gamma = \frac{Z_i P_a (t/\tau)^{1-5\frac{p}{2}}}{(Z_i+1) n_r k T_r} \quad . \tag{22}$$

In addition, at the plasma vacuum interface $x_v(t)$ (which must satisfied the condition $dx_v/dt=v(x_v,t)$) we have zero density and undisturbed values of the beam parameters:

$$v = 0 \quad , \quad v_b = u_b = 1 \quad \text{at } \xi \to 2u/(p+2) \quad ; \tag{23}$$

notice that system (15)-(17) must be solved subject to six boundary conditions since γ is unknown.

3. GENERAL SOLUTION OF THE EQUATIONS

It is ease to verify that the solutions of system (13)-(17) satisfying conditions (21) behave in the neighbourhood

of $\xi = 0$ as

$$\theta = A(-\xi)^{1/3} \quad , \qquad (24)$$

$$v = (\gamma/A)(-\xi)^{-1/3} \quad , \qquad (25)$$

$$u = -B(-\xi)^{1/3} \quad , \qquad (26)$$

$$u_b = C(-\xi)^{1/6} \quad , \qquad (27)$$

where

$$C = \left[\frac{6\gamma}{A}\,\Phi(\beta C/A^{1/2})\right]^{1/4} \quad , \qquad (28)$$

$$B = Z_i C^2/[5\gamma(Z_i+1)] \quad , \qquad (29)$$

and A is an arbitrary constant. On the other hand equations (17) and (16) show that the temperature in the plasma vacuum boundary ($u=(p+2)\xi/2, v=0$) is given by the expression

$$\theta_v = \frac{1}{(2p+1)}\,\frac{Z_i}{(Z_i+1)}\,\Phi(\beta/\theta_v^{1/2}) \quad . \qquad (30)$$

For the numerical integration of system (13)-(17) we start from the origin with arbitrary values of A and γ and sweep through them until we find the solution that allows for satisfying conditions (23) and (30) ($u_b=1$, $\theta=\theta_v$) at the plasma vacuum boundary. Figure 2 shows profiles of θ, u, v, v_b and u_b as a function of the dimensionless distance ξ for a proton beam impinging on D-T (E_o = 2Mev, $I_o = 10^7$ Acm^{-2}, τ =40 nsec, p = 4/3). For this case we have $n_r = 3.5\times10^{21}$ cm^{-3}, $T_r = 1.39\times10^7$ºK, β = 0.95 and numerically find A = 0.278 and γ = 0.24.

Once the expansion is determined one may calculate the ablation pressure P_a and the ablated mass rate per unit area $\dot{m}$ as a function of the parameters of the problem:

$$P_a = [(Z_i+1)n_r kT_r/Z_i]\gamma(p)(t/\tau)^{5\frac{p}{2}-1} = \bar{P}_a\gamma(p)(t/\tau)^{5\frac{p}{2}-1} \quad , (31)$$

$$\dot{m} = (m_i kT_r/Z_i)^{\frac{1}{2}} n_r \frac{\gamma B(p)}{A(p)}(t/\tau)^{2p-1} = \bar{\dot{m}}\frac{\gamma B(p)}{Z_i A(p)}(t/\tau)^{2p-1} \quad , (32)$$

in terms of the beam and plasma parameters $\bar{P}_a$ and $\bar{\dot{m}}$ become

$$\bar{P}_a = 5.9\times10^2 \frac{Z_i+1}{Z_i}\left[\frac{A_i E_o^3 I_o}{A_b Z_b^3 Z_i \tau}\right]^{\frac{1}{2}} \text{ Mbars} \quad , \quad (33)$$

$$\bar{\dot{m}} = 1.75\times10^6 \frac{1}{Z_i}\frac{E_o^2 A_i}{A_b Z_b^2 \tau} \quad \text{g cm}^{-2}\text{s}^{-1} \quad , \quad (34)$$

where E_o, I_o, and τ are in Mev, Acm^{-2} and nanoseconds respectively. Figure 3 and 4 shows the ablation pressure and the ablated mass rate as a function of time for several values of p.

4. ACCELERATION EFFICIENCY OF THIN FOILS

The obtained results may now applied to determine the acceleration efficiecy ϵ of thin foils impinged by an intense ion beam. This efficiency is defined as the fraction of absorbed ion beam energy that goes to target kinetic energy

$$\epsilon = MU^2/\left[2\int_0^\tau E_b(t)I_b(t)(eZ_b)^{-1}dt\right] \quad , \quad (35)$$

The unablated mass foil per unit area M and its velocity U, assumed uniform throught it, are given by the equations

$$\frac{dM}{dt} = - \dot{m} \quad , \tag{36}$$

$$M\frac{dU}{dt} = - P_a \quad . \tag{37}$$

From (36) and (37) taking into account (31) and (32) we arrive at

$$\epsilon = \frac{3}{4} \frac{\bar{P}_a^2 \gamma(p) A(p) e Z_b}{\bar{\dot{m}} B(p) E_o I_o} F(\Delta) \quad , \tag{38}$$

$$F(\Delta) = \frac{1-\Delta}{\Delta^{3/2}}\left[2\tan^{-1}\Delta^{1/4} + \ln\frac{1+\Delta^{1/4}}{1-\Delta^{1/4}} - 4\Delta^{1/4}\right]^2 \simeq 0.65\Delta \quad , \tag{39}$$

where

$$\Delta = 1 - M/M_o = \bar{\dot{m}}\gamma B\tau/(2pAM_oZ_i) \quad , \tag{40}$$

M_o being the initial mass per unit area. Finally we arrive at

$$\epsilon = .84\times10^{-3}\left(\frac{Z_i+1}{Z_i}\right)^2 \frac{A_i E_o^2}{A_b Z_b^2 Z_i M_o} \frac{\gamma^2}{p} \quad , \tag{41}$$

where E_o and M_o are given in Mev and $g\,cm^{-2}$ respectively. Notice that the acceleration efficiency depends on the time law through the values of γ^2/p. Table I give values of γ^2/p as a function of p. For given values of the beam and plasma parameters, our calculation shows that the efficiency for p=1/3 is three times larger than that corresponding for p=2.

5. DISCUSSION OF THE RESULTS

We have considered the self-similar expansion flow of the ablated plasma produced by irradiating a planar target with an intense ion beam pulse of energy per nucleon $E_b = E_o(t/\tau)^p$ and current intensity per unit area $I_b = I_o(t/\tau)^{2p-1}$. The analysis is valid for large values of the parameter

$$\alpha \equiv 1.18\times10^{-53}\ \frac{Z_b^5 A_b^3}{A_i}\ \frac{[n_o(cm^{-3})]^2 I_o(Acm^{-2})[\tau(ns)]^3}{[E_o(Mev)]^5} \quad . \quad (42)$$

and the obtained results for the expansion are completely independent of the target compression. Profiles of density, velocity, temperature and beam density and velocity in the expansion for several values of the exponent p are obtained. Figure 2 shows this profiles for the case p=4/3 and β=0.95. We also found the ablation pressure P_a and the ablated mass rate $\dot{m}$ per unit area. Figures 3 and 4 show the values of P_a and $\dot{m}$ as a function of time for several values of p. The ablation pressure rises with time for p≥2/5 and the final pressure at t=τ grows with p (the final pressure for p=2 is about a 30% larger than the pressure obtained for p=2/5).

The acceleration efficiency ϵ of thin foils impinged by an intense ion beam has been also calculated. Equation (41) gives the efficiency as function of the beam and plasma parameters and the results given in Table I show that the value of the efficiency is multiplied by a factor of 3 when the law time exponent p ranges from 2 to 1/3. Assuming a D-T foil 1 mm thick (M_o = .21 g cm^{-2}), equation (41) yields ϵ=.013 for p=2/5 and ϵ=.005 for p=2.

Notice that from an inertial confinement view point the regimes corresponding to $\alpha\sim(1)$ are more approproate than those corresponding to $\alpha>>1$ since the expansion to compression energy ratio for $\alpha\sim(1)$ is smaller inthe former than in the latter case. The weak dependence of E_o with α ($E_o\sim\alpha^{1/5}$) suggets that the condition $\alpha=1$ may be used to find the optimun value E_o for a given I_o

$$E_o = \left[1.18\times10^{-53}\left\{\frac{Z_b^5 A_b^3 n_o^2 \tau^3 I_o}{A_i}\right\}\right]^{1/5} . \qquad (43)$$

where n_o, τ, and I_o are given in cm^{-3}, ns, and $A\,cm^{-2}$ respectivaly.

Finally it is worth noticing that the influence of radiation transport may be evaluated since the hydrodynamical equation including radiation becomes self-similar for $p=0$ if an optically thin plasma model is assumed. The results show that radiation is indeed negligible.

TABLE I

p	1/3	2/5	1/2	2/3	1	2
γ^2/p	.097	.080	.066	.055	.052	.033

ACKNOWLEDGEMENTS

This research was supported by the Comisión Asesora de Investigación Cientifica y Técnica (Proyect 2862/83).

REFERENCES

FERNANDEZ A. and BARRERO A. (1986) Plasma Physics and Controlled Fusion 27, 989.

JACKSON J.D. (1975) Electrodinamica Clásica, Wiley, 3th Edition.

MELHORN T.A. (1981) J.Appl.Phys. 52, 6522.

MIYAMOTO K. (1980) Plasma Physics for Nuclear Fusion, MIT Press, Cambridge.

NARDI E., Peleg E. and Zinamon A. (1978) Physics Fluids 21, 574.

OLSEN J.N. MELHORN T.A., MAENCHEN J. and Johnson D.J. (1985) J. Appl. Phys. 58, 2958.

LIST OF FIGURES.

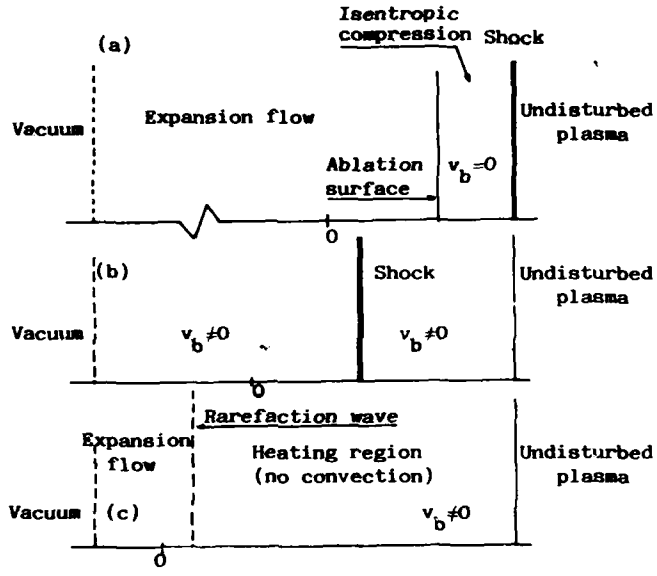
(a)
Isentropic compression
Shock
Vacuum
Expansion flow
Undisturbed plasma
Ablation surface
$v_b=0$
0
(b)
Shock
Undisturbed plasma
Vacuum
$v_b\neq0$
$v_b\neq0$
0
Rarefaction wave
Expansion flow
Heating region (no convection)
Undisturbed plasma
Vacuum
(c)
$v_b\neq0$
0

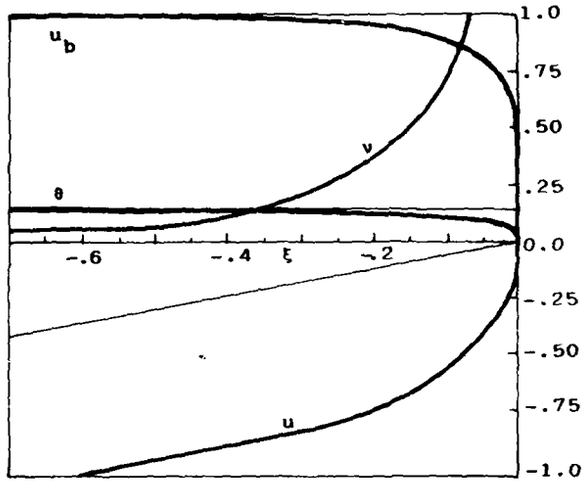
u_b
v
θ
u
-.6
-.4
ξ
-.2
1.0
.75
.50
.25
0.0
-.25
-.50
-.75
-1.0

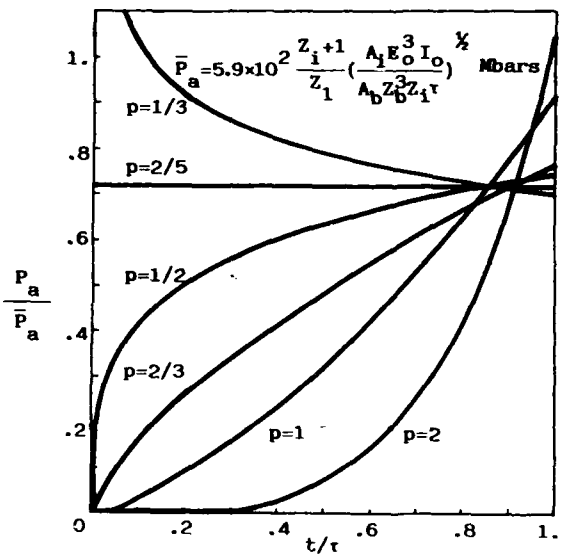
$\bar{P}_a = 5.9\times10^2 \frac{Z_i+1}{Z_1}\left(\frac{A_1 E_o^3 I_o}{A_b Z_b^3 Z_1^2}\right)^{1/2}$ Mbars
p=1/3
p=2/5
p=1/2
p=2/3
p=1
p=2
$\frac{P_a}{\bar{P}_a}$
t/τ
0
.2
.4
.6
.8
1.

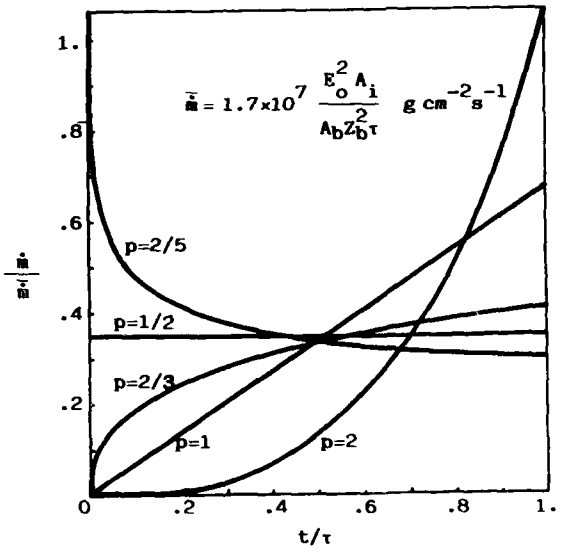
$\bar{\dot{m}} = 1.7 \times 10^7 \frac{E_o^2 A_i}{A_b Z_b^2 \tau}$ g cm^{-2}s^{-1}
$\frac{\dot{m}}{\bar{\dot{m}}}$
1.
.8
.6
.4
.2
0
.2
.4
.6
.8
1.
t/τ
p=2/5
p=1/2
p=2/3
p=1
p=2

Finite ion-relaxation and nonequilibrium radiation effects on laser-driven implosions

T. Yabe and K. A. Tanaka

Institute of Laser Engineering, Osaka University
Yamada-Oka 2-6, Suita, Osaka 565

Abstract

The implosion dynamics of recent experiments with high-aspect-ratio laser-driven targets are re-examined by taking account of finite mean free paths of the ion. The mean free path is found to be comparable to the fuel size and this can cause a significant departure from a fluid-like description. One of such effects stemming from the finite mean free path of the ion, real viscosity, seriously changes the results ; the compression ratio becomes 5 times smaller with this real viscosity. In addition to this, inclusion of non-LTE(local thermodynamic equilibrium) atomic process is shown to critically determine the implosion dynamics.

During implosion experiments in past several years theorists met a serious difficulty in interpreting the neutron production from ordinary (not thin) D-T filled GMBs (glass microballoon) ; the theoretical prediction was many orders of magnitude larger than the experimental results on neutron yield. One of the reasonable explanations on this discrepancy was clearly presented by a French group[1] ; the experimental neutron yield can be well replicated by the one-dimensional hydrocode if only the neutron yield from the first shock reflection is counted and that from the following adiabatic compression is disregarded. This conclusion has been confirmed[2] from the comparison between the experiments performed at ILE and the simulation with HIMICO[3].

Once the origin of the difficulty has been found, it is natural to consider that the experimental result should become closer to the theoretical prediction if the neutron production at the first shock reflection could be much higher than that from subsequent adiabatic compression ; in other word, shock collapse and adiabatic compression simultaneously occur without delay. This idea is very close to the collapse of the multiple shock waves analyzed by Kidder[4] and Nuckolls et al[5].

Along the above guide lines, the author designed a target for the GEKKO XII neodimium glass laser sys-

tem and achieved 10^{12} neutrons[2]. The experiments performed at LLE[6](Laboratory for Laser Energetics, University of Rochester) may also be along the same line. However, there still remain some uncertainty in the results with hydrodynamic codes HIMICO.

In this letter, we will point out two critical aspects in the implosion physics which may seriously change the results but have not been considered before ; one is a finite ion mean free path λ and the other is the atomic process. In case of the high-neutron-yield experiment given in Ref.2, the ion density and temperature are about 10^{21} to 10^{22} cm^{-3} and 10 keV. In these plasmas the mean free paths are λ =1000 to 100 μ m ; this is comparable to the final target radius 50 to 100μ m. Since the structure of the shock wave is determined by this mean free path, the shock wave may not be clearly formed with such a long mean free path. However, when we use the artificial viscosity[7] in the code, a fictitious shock wave can be formed. In order to observe this effect , we performed a similar calculation as in Ref.2(EXP-B) by adopting a real viscosity Q as[8]

$$Q = -n_i T_i \tau \nabla .v \ , \qquad (1)$$

where n_i and T_i are the density and temperature of ions and v is the ion velocity. τ is the ion-ion thermalization time and is 1 to 0.1 nsec for the densities and temperature given above. Although the for-

mula (1) for the viscosity is not the exact one, we adopt it for numerical simplicity. This Q is added to the ion pressure both in momentum and energy equations. As in the case of electron thermal conduction, a well known flux limit

$$Q_{limit}=n_i m_i v_{Ti} v \qquad (2)$$

should be imposed to maintain the validity of the formula (1) for $\lambda \sim \nabla^{-1}$, where m_i is the ion mass and v_{Ti} the ion thermal velocity..

The implosion dynamics with the artificial viscosity (AV) and the viscosity given by Eqs.(1) and (2) (RV) are depicted in Fig.1 ; the flux limit f_c for thermal electrons is 0.03[2,9]. The mean free path of AV corresponds to the size of only a few meshes so that the shock wave is formed within a few meshes[10][Fig.1(a)], whereas the calculation with RV [Fig.1(b)] does not show any well-defined shock structure. The various quantities obtained with these models are compared in Table 1. The neutron yield does not differ so much in RV and AV with non-LTE model, whereas the minimum diameter with RV is larger than that with AV. This is due to the "ion preheating" of the fuel before final compression by dissipating the kinetic energy through viscosity. In the previous study[2], we used a large fraction (20% of the incident energy) of "warm" electrons (treated by multi-group model with two times larger temperature

than thermal electrons; this simulates the higher energy tail of thermal electrons), thus increasing artificially the fuel "electron" preheating, otherwise the compression ratio becomes higher as in the case of AV with non-LTE in Table 1. In all calculations used here, however, we used only 5% of suprathermal electrons consistent with the experimental value. Although the compression ratio with RV model is improved, the neutron yield is still 10 times larger than the experimental one. This reason will be discussed later on.

In reality, however, physics could be more complicated. In Eqs.(1) and (2), we used the ion temperature to estimate the ion mean free path. Near the collapse center, extremely high-speed($\sim$ 10^8 cm/sec) ions collide with each other and hence the mean free path of these ions should be estimated by the drift velocity not by the slower thermal velocity. The time evolution of the mean free path and collision time are shown in Fig.2, and the mean free path estimated with the drift velocity is about 30 times longer than the thermal one. If this is true, the ion temperature given in Table 1 becomes meaningless ; two counter ion beams can give an "effective" temperature but most of the physical processes based on the thermal ions in the Maxwell distribution become invalid.

When the ion-ion thermalization time τ (0.06-0.1

nsec)is comparable to the neutron production time (~ 0.1nsec) as in Fig.2, the fusion reaction should also be re-examined[11]. In such a situation, ions pass through each other without relaxing to thermal ions and escape towards the pusher. In one sence, this phenomenon is similar to that pointed out by Petschek and Henderson[12] ; ions responsible for the fusion reaction escape from the reaction region. Interestingly this argument may also explain the discrepancy of the neutron yield in between the experimental and simulation results. In the previous case[2], the neutron production stopped when the reflected shock wave reached the pusher because of pusher-fuel mixing[13,14]. Following our argument, almost collisionless ions pass through each other at the center and then reach the pusher being absorbed in the pusher material and thus the neutron production stops. In both cases, the fuel mixes with the pusher, but difference is whether the mixing comes from the hydrodynamic instability[13,14] or collisonless nature[12]. If the fusion cross section[15] is estimated by the relative velocity $v_b=2\times 10^8$ cm/sec and the reaction time is determined from R_f/v_b = 25 psec (R_f is the final fuel radius), neutron yield becomes (1/4) $\sigma v_b n_i^2(4\pi/3)R_f^4/v_b \sim 8.6\times 10^{11}$, which is very close to the experimetal one. On the contrary, if we use the Maxwell-averaged cross section at 10(7.4) keV ,

the peak fuel density 0.32(1.39) g/cm^3, and the final radius 56(34.4) μ m as in the case of RV(AV) in Table 1, then $(1/4)\langle\sigma v\rangle n_i^2(4\pi/3)R_f^4/v_{Ti} \sim 1.1(1.6)\times 10^{13}$; these are very close to the results in Table 1.

Here arise many future problems. One is how to describe the finite ion relaxation in the hydrocode. For example, non-local treatment of ion viscosity is needed, or we may directly solve the collisionless ions by a particle code. As is well known, even in such a collisionless plasma a shock wave may be formed[16] ; two-stream instability may give rise to anomalous dissipation but the Mach number can not be so large. Furthermore, the interaction between fuel plasmas and pusher in such a long mean free path case becomes similar to the ion-beam driven fusion ; the ion beam causes the mass ablation of the pusher leading to fuel-pusher mixing. From the experimental point of view, if the ion velocity distribution is not the Maxwellian (but rather beam-like), the data deconvolution from neutron signals should be re-examined. These will be future subjects.

We should point out another important effect which needs a further investigation ; that is the non-LTE radiation physics. As shown in Table 1, the neutron production in LTE calculation is significantly smaller than others'. The reason for this is apparent in Fig.3, where the spatial profiles at 0.5 ns (This

time is measured from the laser peak) are compared between LTE and non-LTE. In non-LTE because of the larger mass ablation of GMB, the less remained shell is accelerated by 1.5 times faster than in LTE. In LTE the GMB is completely ionized at lower density and hence the opacity there drops. In this case, the radiation escapes preferentially towards the lower density side[17]. Actually the radiation loss (towards the vacuum) in LTE is 1.5 times larger. In contrast, in non-LTE hydrogen-like ions still exist even at a relatively lower density ; these ions provide an opacity slightly larger than the case of LTE model and hence the radiation flux towards the high density side is about 2 times larger, leading to higher mass ablation rate[18]. It should be noted that this does not mean the plasma is optically thick.

The reason why the neutron production with LTE model is significantly smaller than others is due to the time delay of the peaks of density and temperature; temperature peak given in Table 1 is attained 0.1-0.2 nsec before the density peak and the temperature at the density peak is about 2 keV, at this temperature fusion cross section is order of magnitude smaller than that at 7 keV. In non-LTE(AV), peak temperature 7 keV occurs almost in phase with density peak.

In summary, the implosion dynamics of recent ex-

periments with high-aspect-ratio targets is re-examined by taking account of the finite ion mean free path. The ion mean free path could become comparable to the target size in the experiment[2] and hence this non-thermal effect of the ions may explain why the calculated compression ratio was quite larger than the experimental one[2,6]. The instability and two-dimensional effects might also be one of the origin of this discrepancy[19] but all the calculations which used the artificial viscosity should be re-examined even in two dimensional calculation[8,14,19]. It is still to be investigated whether the hydrodynamic instability can still occur in such a collsionless plasma.

The atomic physics is also shown to be sensitive to the implosion dynamics. The average ion model[3] used here should be re-examined further since the small fraction of H-like and He-like ions are responsible for the opacity and the use of the more advanced model[20,21] will be an interesting future subject.

The authors would like to thank Prof. K.Abe at the University of Tokyo and Prof.K.Niu at the Tokyo Institute of Technology for invaluable comments.

References

1. C.Bayer *et al.*, Nucl.Fusion 24,573(1984).

2. C.Yamanaka *et al.*, Phys.Rev.Lett.56,1575(1986); EXP-B used 3.0-atm-DT-filled GMB of 911 μm diam, 1.46 μm thickness, irradiated by 8045 J per 750 psec at 0.53 μm.

3. T.Yabe and C.Yamanaka, Comm.Plasma Phys.Contr. Fusion 9,169(1985) and references therein.

4. R.Kidder, Nucl.Fusion 16,3(1976).

5. J.Nuckolls *et al.*, Nature 239,139(1972).

6. M.C.Richardson *et al.*, Phys.Rev.Lett. 56,2048(1986).

7. J.Von Neumann and R.D.Richtmyer, J.Appl.Phys.21, 232(1950).

8. S.I.Braginskii, in *Reviews of Plasma Physics*,ed.by M.A.Leontovich (Consultants Bureau, New York, 1965) Vol.1, p.205.

9. The free-streaming value is estimated on the upstream side of the flux. By this choice of f_c, the absorption rate agrees with the experimental result (see also Ref.2).

10. The difficulty with AV has already been pointed out ; D.Colombant, S.I.Anisimov, private communications ; K.Niu, AIP Conf.Proc. 152(1986)454.

11. J.M.Dawson,H.P.Furth, and F.H.Tenney, Phys.Rev. Lett. 26,1156(1971).

12.A.G.Petschek and D.B.Henderson, Nucl.Fusion 19, 1678(1979).

13. Yu.F.Afanas'ev *et al.*, Pis'ma Zh. Eksp. Teor. Fiz. 23,617(1976)[JETP Lett.23,566(1976)].

14.J.R.Freeman,M.J.Clauser, and S.L.Thompson, Nucl. Fusion 17,223(1977).

15.W.R.Arnold *et al.*,Phys.Rev. 93,483(1954).

16.D.A.Tidman and N.A.Krall, *Shock Waves in Collisionless Plasmas* (Wiley-Interscience, New York, 1971).

17.T.Yabe,Jpn.J.Appl.Phys. 23,L57(1984).

18.T.Yabe *et al.*, Jpn.J.Appl.Phys.22,L88(1983).

19.T.Yabe *et al.*,in *Laser Interaction and Related Plasma Phenomena*, ed. by H.Hora and G.H.Miley (Plenum, 1984) Vol.6, p.863 ; in similar calculations, some cases with larger deformation can give higher neutron yield. This phenomenon is as if the remnants of a disintegrated shell impinge against the fuel gas thus producing shock waves by impact. If this impact velocity is high enough, shock waves produced by each remnant interact with each other making the fuel temperature higher.

20.D.Duston and J.Davis, Phys.Rev. A21,1664(1980).

21.M.Itoh,T.Yabe,and S.Kiyokawa, Phys.Rev. A35,233 (1987).

Table 1

	T_i [keV]	Ny [$\times 10^{12}$]	minimum fuel diameter [μ m] (density g/cm^3)
EXP-B[a]	6.6-8.6	1.25	100-140 (0.29)[a]
non-LTE (RV)	10.9	16.5	112.0 (0.32)[b]
non-LTE (AV)	7.4	11.9	68.8 (1.39)[b]
LTE (AV)	4.6	2.2	50.0 (3.5)[b]

Figure Captions

Fig.1 : Fluid trajectories calculated with (a) artificial viscosity and (b) real viscosity with non-LTE model. In (a), the first shock wave arrives at 0.55 nsec and is reflected back to the pusher. In (b), however, this reflected shock and other subsequent shock waves do not show up.

Fig.2 : Time evolutions of the mean free path (λ) and the collision time (τ) ; λ (T) and τ (T) are estimated only with the ion temperature at the mid point of fuel, λ (V) is estimated with the implosion velocity at the center (the error bar is due to the density changed). The dashed line denotes the radius of the pusher-fuel interface. This result is given with RV, non-LTE model.

Fig.3 : Spatial profiles of the ion density and electron temperature in LTE and non-LTE at t=0.5 nsec. ρ r is measured from the inner boundary of the GMB.

Table 1 : Comparison among the experimental results and various models. [a]·fuel density (g/cm^3) estimated with the experimental result[2] on Ar line. [b]·fuel density estimated by the mass conservation.

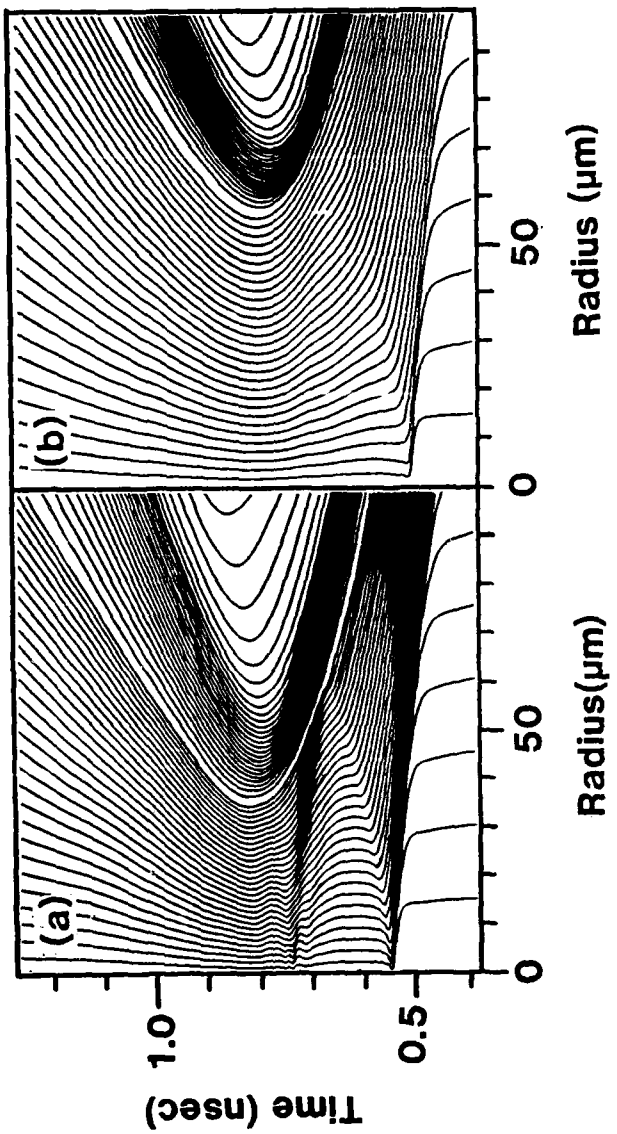

Fig.1

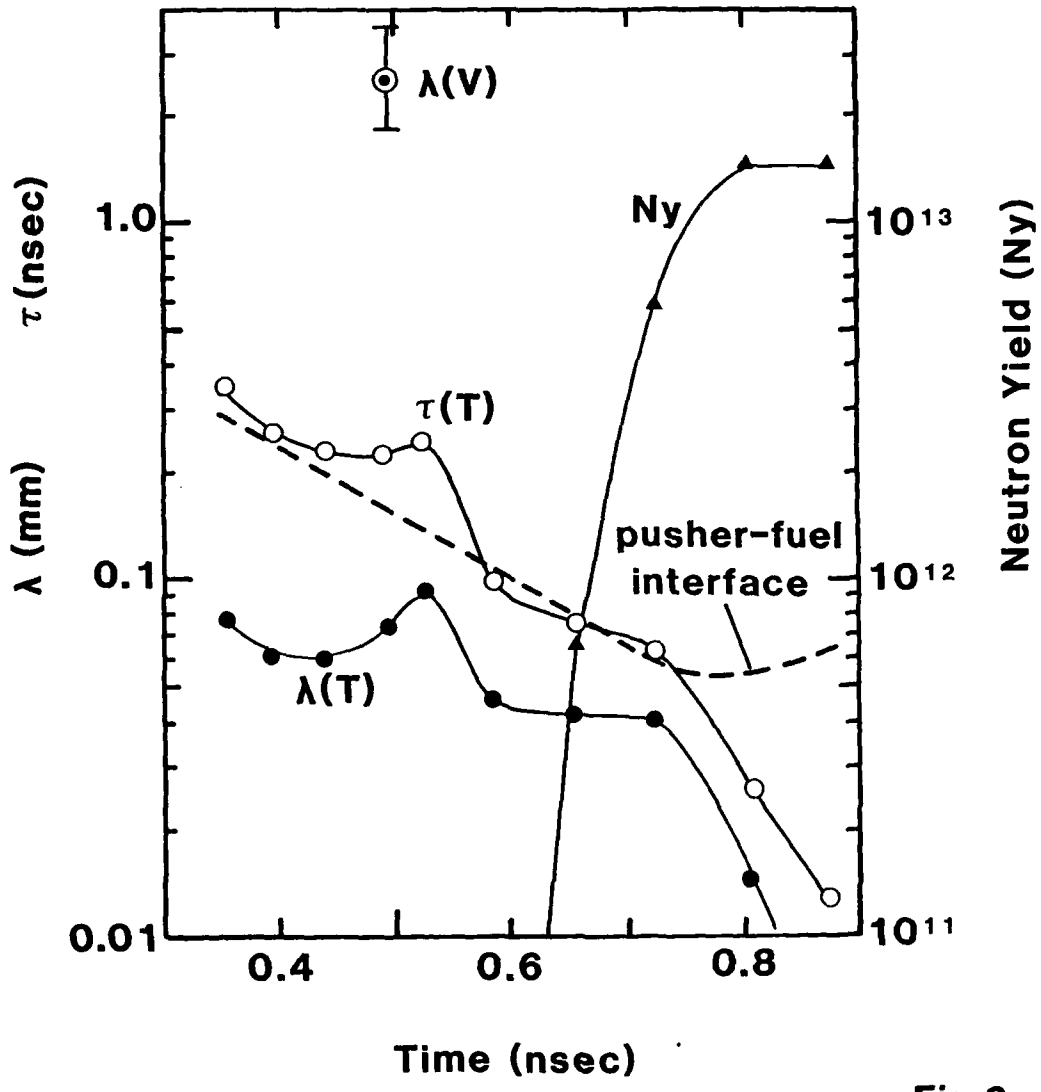
λ(V)
τ (nsec)
λ (mm)
1.0
0.1
0.01
τ(T)
λ(T)
Ny
pusher-fuel
interface
10¹³
10¹²
10¹¹
Neutron Yield (Ny)
0.4
0.6
0.8
Time (nsec)

Fig.2

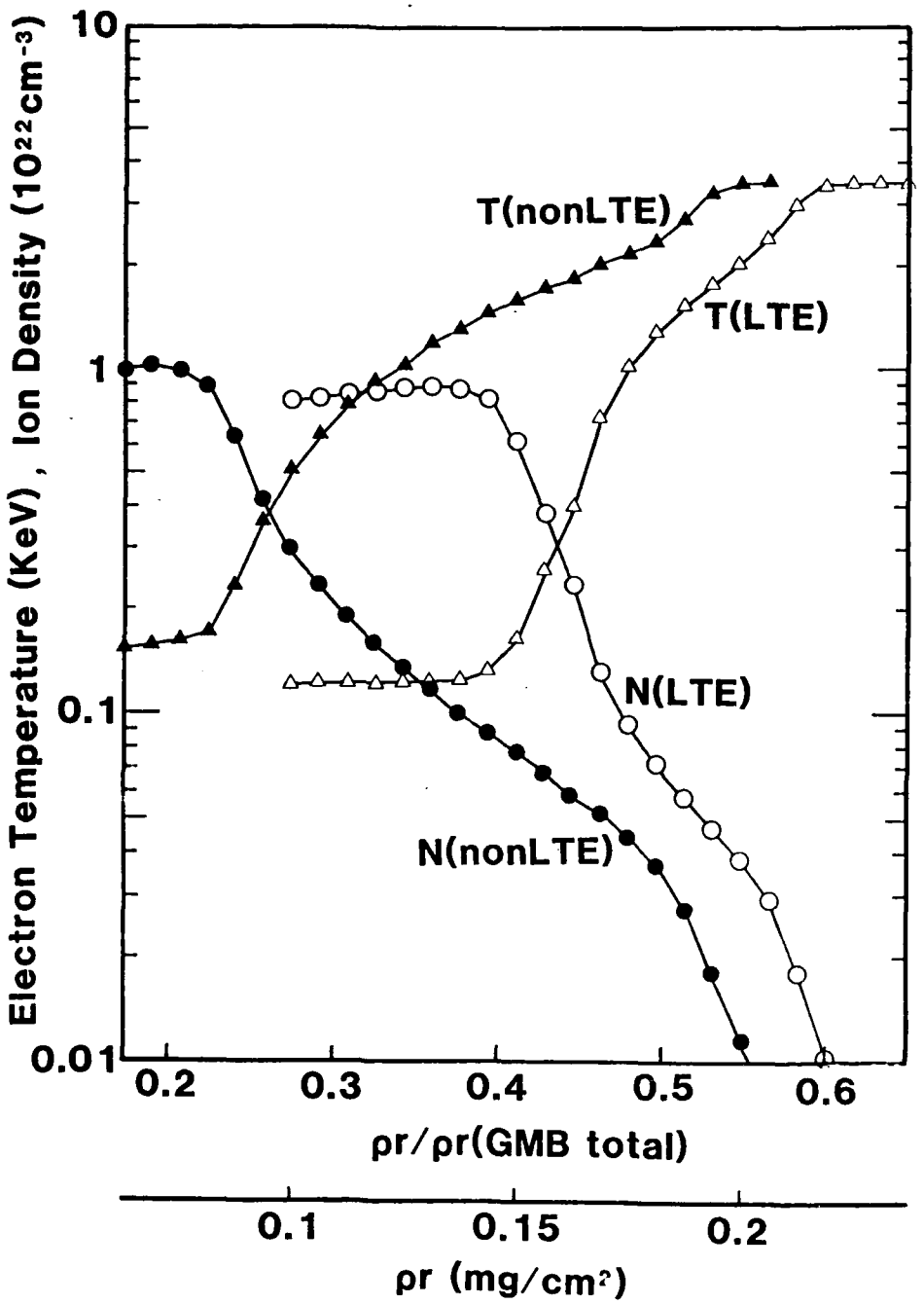
Electron Temperature (KeV), Ion Density (10^{22}cm^{-3})
10
1
0.1
0.01
T(nonLTE)
T(LTE)
N(LTE)
N(nonLTE)
0.2
0.3
0.4
0.5
0.6
ρr/ρr(GMB total)
0.1
0.15
0.2
ρr (mg/cm^2)

Fig.3

GENERATION OF HIGH BRIGHTNESS ION BEAM FROM INSULATED ANODE PED

Yoshinobu Matsukawa

Research Institute for Atomic Energy, Osaka City University,

Sugimoto 3-3-138, Sumiyoshi-ku, Osaka 558, Japan

Generation and focusing of a high density ion beam with high brightness from a organic center part of anode of a PED was reported previously[1)~4)]. Mass, charge and energy distribution of this beam were analyzed. Three kind of anode were tried. Many highly ionized medium mass ions (up to C^{4+}, O^{6+}) accelarated to several times of voltage difference between anode and cathode were observed. In the case of all insulator anode the current carried by the medium mass ions is about half of that carried by protons.

For power concentration by ion beam, it is necessary to increase the brightness. In order to obtain a diode with high brightness, some atempts to decrease the divergence angle have been made for MID but an alternate approach is to increase the current density for PED.

It was reported previously that the high density ion beam with high brightness is generated around the apex of the anode of a conical PED[1)] and it was also reported that the ion beam from a concave insulator spherical apex of anode (its radius is 2cm) was focused on its center of curvature in the vicinity of the source[4)]. In that experiment three kinds of anode for other part of anode excepting the concave insulator apex were tried. Anode A is made from insulator only (Fig. 1-A). Anode B consists of floating metal and insulator (Fig. 1-B). Anode C has insulator part of 6 cm diameter around the concave apex in addition to the

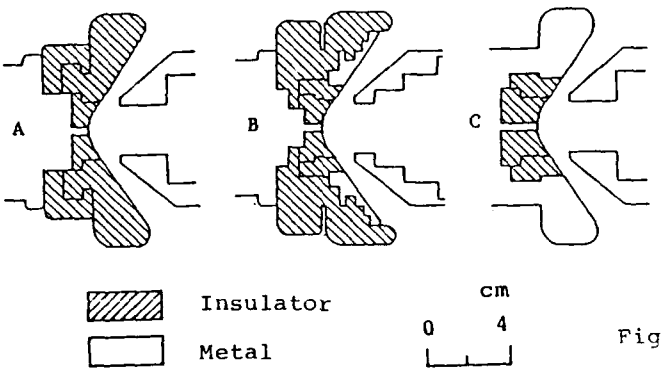

Fig. 1

major metal part (Fig. 1-C).

The zenith angle distribution of the ion beam current density to the center of curvature of the concave spherical apex was measured by a biased ion collector embeded in the cathode basement as shown in Fig. 2.

In the case of anode C the total ion current is 2.6kA and the current density on the anode surface at the center is 1.05 kA/cm^2 [4]. In the case of anode A the total ion current is 8 kA and the current density at the center is 4.3 kA/cm^2 [4]. These values are about three times as large as those in the case of anode C. From the damage of a plate fixed at the center of curvature it was known that the ion beam from the concave spherical apex of the anode is focused within the region of 5mm in diameter.

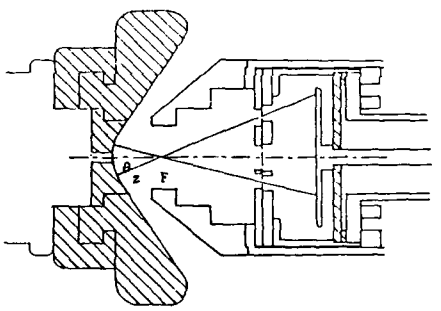

Fig. 2

Thus in the most powerful case the ion current density and the power density at the target attain to about 40 kA/cm^2 and 0.8~1.0x10^{10}W/cm^2 respectively[4].

The measurement of the charge and the mass and the energy distribution of the emitted ions was studied by a Thomson parabola analyzer. Fig.

3 shows the arrangement of the diode and the detectors. Fig. 4-a,b,c and d show the trace of tracks of ions on CR-39 plate. It can be observed that many multi-charged ions of medium mass (carbon or oxygen) are emitted.

In the case of anode A as shown Fig.4-a and 4-b the medium mass ions

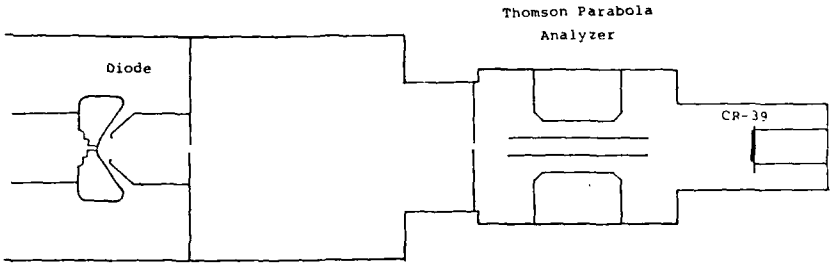

Fig. 3

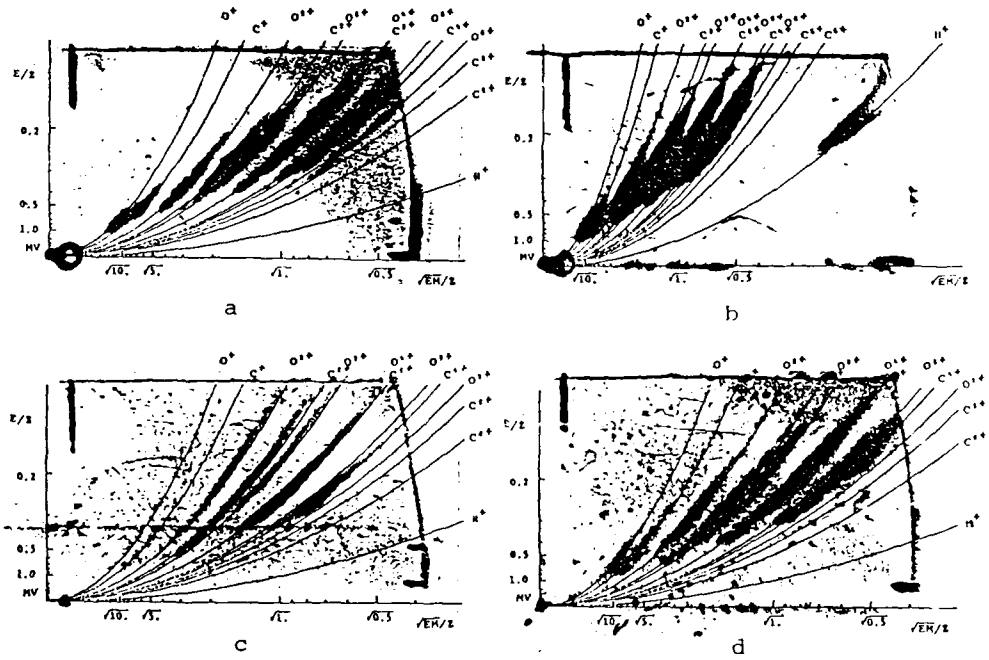

Fig. 4

up to O^{6+} ions are detected and the component with high intensity concentrates within rather narrow region near a velocity line of energy and momentum coordinate of Thomson parabola screen (CR-39), but this velocity is different from that of the proton beam. On the other hand in the case of anode C, the velocity distribution of the medium mass ions is broad and intensiy is more uniform and O^{6+} ions are not detected but ions with lower charge than C^{4+} or O^{5+} are detected (Fig. 4-c). In the case of anode B the energy distribution of medium mass ions is similar that in the case of anode A (Fig. 4-d).

From these distribution it can be known that even lower charged medium mass ions (C^{+},C^{2+},O^{+} or O^{2+}) are accelerated into the energy above about 500keV up to about 1MeV, these values are higher than the energy accelerated by the voltage difference between anode and cathode directly (see V_D on Fig. 5).

The temporal variation of the ion beam current was measured by a biased ion collector at the vicinity of the diode (Fig. 2) and at the distance of 50cm from the diode (Fig. 3).

In the case of anode A and the measurement at 50cm, two separated signal of the ion beam was detected correspond to the proton beam and the medium mass ion beam as shown in Fig. 6-a. The peak value of the former is about twice of that of the latter. If the ion beam was generated at the peak of the diode current, the velocity of the proton beam and that of the medium mass ion beam known from the time of flight are nearly equal to the each velocity of two groups known from the pattern of tracks on the CR-39 plate. In the case of anode C the signal of ion beam is not separated clearly compared with in the case of anode A (Fig. 6-b).

Following interpretation for these results is considered. Many highest charged ions (C^{4+} or O^{6+}) are produced and accelerated by the

anode A

a

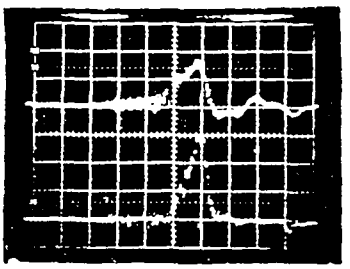

upper: V_D 195 kV/div
lower: I_i 210 A/cm^2/div
sweep: 100 nsec/div

anode C

b

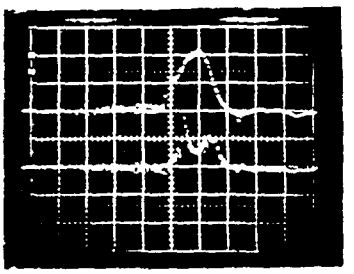

upper: V_D 195 kV/div
lower: I_i 84.8 A/cm^2/div
sweep: 100 nsec/div

Fig. 5

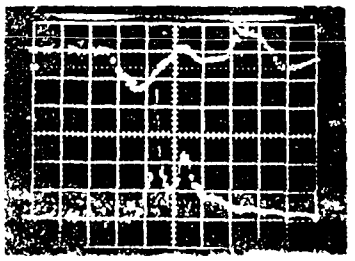

upper: I_D
lower: I_i
sweep: 100 nsec/div

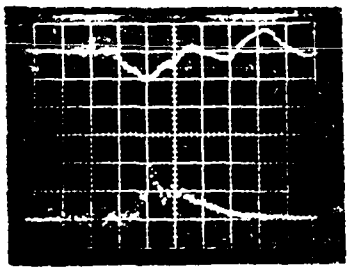

upper: I_D
lower: I_i
sweep: 100 nsec/div

Fig. 6

static potential between the anode and the cathode (150~300kV) and after then charge of some ions reduce to lower charge by recombination with electrons or charge exchange interaction with neutral atoms or lower charged ions. Ions with charge lower than the highest charge are also neutralized by the same interaction and might become even the fast neutral atoms which cannot be detected.

If this interpretation is reasonable, the total kinetic power density of the particles of the medium mass ions $J_F E_p = (\Sigma n_i) v_h Z_h e V_{AK}$ extracted from the diode and focused on the target is greater than the

value estimated from the current density and the voltage difference $J_i V_{AK} = (\sum n_i Z_i e) v_h V_{AK}$, because the effective charge of the medium mass particle is less than Z_h, where $J_F, E_p, n_i, v_h, Z_h e$ are flux flow density, particle energy, number density of ions in the ith state of charge, velocity and charge of the highest charged ions and $J_i, Z_i e$ are current density and charge of ion in the ith state of charge respectively.

References

1) Y. Matsukawa and Y. Nakagawa : Jpn. J. Appl. Phys. 21 (1982) L675

2) Y. Matsukawa and Y. Nakagawa : Proc. 5th Int. Conf. High-Power Particle Beams, San Francisco (1983) 155

3) Y. Matsukawa, K. Imasaki and S. Sawada : Proc. 6th Int. Conf. High-Power Particle Beams, Kobe (1986) 81

4) Y. Matsukawa : Laser and Particle Beams 5 (1987) 473

THE APPLICATION OF RUTHERFORD BACKSCATTERING FOR ANALYZING MULTILAYERED STRUCTURE CHANGE INDUCED BY PULSED ION BEAM BOMBARDMENT

N.SASAKI, N.TAKAGI* and S.YANO

Department of Nuclear Engineering
Kobe University of Mercantile Marine
5-1-1 Fukaeminamimachi Higashinadaku Kobe
658 Japan

Abstract

Using the proton backscattering technique, plane-shaped samples consisting of a double layered film Pb/parylene(polyparaxylene) chemically deposited on a silicon plate were analyzed after bombarded by pulsed proton beams of about 400keV with different current densities upto 1kA/cm^2. We obtained very clear backscattering spectra indicating changes of the layer-structure caused by LIB bombardment. Almost all Pb-layer was ablated, and the boundary between parylene and silicon became diffusive. This method is proved to be very useful for analysis of LIB bombarded samples.

1. Introduction

Intense pulsed ion beams can be used to produce an instantaneous strong heat load near the surface of the target material. Effects of ion beam bombardment depend on the power deposition rate and the energy of the ion beam. For high energy density beams with the deposition energy of over 10^7J/g in several tens of ns, we predict strong implosion of the target material relating to the ICF research. Pulsed ion beams of intermediate intensity of kA/cm^2 with the deposition energy of $\sim 10^4$J/g are considered to be useful to study material behavior at instantaneous strong pressure and temperature rises.

* Present Address: Tokyo Institute of Technology
Ōokayama, Tokyo

We have started to study bombardment effects of pulsed proton beams of kA/cm^2 onto multilayered solid surfaces using our LIB device. Around this beam intensity, the surface materials may not completely be lost, but the remainder of the materials will be expected to change the layer structure. In the present experiment, we are investigating the effectiveness of the beam current density on the following properties: (1) loss of any surface layer, (2) changes in their boundary layers, and (3) if any, a tamper effect of surface coating with a heavy material.

2. Analytical method and experimental procedures

2.1 Target structure and sample preparations

To make clear bombarding effects we used double layered targets: the outer layer is lead and the inner one is parylene(polyparaxylene $\left[C_8H_7Cl\right]_n$). Since parylene has low thermal conductivity, heat deposited by a strong pulsed proton beam has enough time to diffuse through this material. Therefore, the layer will melt or vaporize at rather small current density. Moreover, an instantaneous strong pressure and temperature increase in the parylene layer will allow atoms or molecules of parylene to diffuse into the silicon or Pb surface at their boundaries. Rutherford backscattering is thought to be useful to analyze these structural changes of the multilayers.

We have used Si-plates with 3mm thick and 15mm square, as a substrate material, because Si is of high purity material with low atomic weight and can be polished to a very flat surface. After polishing with 3μm alumina powder, we asked Tomoe Company to coat parylene on Si. Since parylene-coating is believed to make a homogeneous film with no pinholes and have strong coherence on material surfaces, we have chosen parylene as the material for the main layer of beam energy deposition. After coating parylene

in 7μm thick on Si, we covered the parylene surface with Pb by rf-sputtering in argon discharges. Coating thickness of Pb were adjusted to three different values, 1.9, 1.1 and 0.8μm. Lead is supposed to work like a tamper in ICF target structure.

2.2 Outline of the RBS analytical method

We preferred proton RBS to He-RBS, because the layers were relatively thick. Using the formula for stopping power in Table-1 derived by J.F.Ziegler[1], we have calculated thicknesses of multilayers from proton RBS spectra. The constants A_1, A_2···· specified to the elements in the material are given in reference 1. This calculation was applied to analyze the spectra obtained for samples with and without proton bombardment.

To calculate the film thickness, we used the following equation,

$$E_{out} = K\left(E_{in} - \int_0^x \frac{dE}{dx}dx\right) - \int_0^{x/|\cos\theta|} \frac{dE}{dx}dx, \quad (1)$$

where E_{in} is an incident proton energy, E_{out} is the energy of the emitted backscattered proton, dE/dx is the stopping power, and K is the proton kinematic factor for target atoms depending only on the target mass and the scattering angle θ. By determining E_{out} value from the RBS spectrum, the value of x which satisfies the above relation is numerically calculated with our computer program.

Figure 1 shows a schematic proton RBS spectrum for the Pb/parylene/Si samples. In this figure the peak for Cl is clearly shown, which is included in parylene, but this peak is covered with the spectral tail of Pb and is difficult to be identified when the large amount of Pb exists.

2.3 Energy deposition and temperature calculations

We calculated the particel energy versus time on the target with time of flight corrections to the measured

diode voltage. A wave form of the diode voltage which is equal to the proton energy at the diode exit is simplified as shown in Fig.2.

The temperature rise and the deposited heat can be derived from the heat conduction equation,

$$c\rho\frac{\partial T}{\partial t} = \frac{\partial}{\partial x}\left(\kappa\frac{\partial T}{\partial x}\right) + \frac{j_i(t)}{e}\frac{dE}{dx}\ , \qquad (2)$$

where $j_i(t)$ is the beam current density.

With a rough evaluation of heat conduction, however, we estimated the time in which a half of the deposited energy is transferred from the region of energy deposition to the outer region, and this time is in the order of 10^{-5}s or longer in parylene, assuming the thermal conductivity of parylene is 0.3W/m°K and the depth of energy deposition region is equal to the ion beam range. This is 10^3 times larger than tha beam pulse duration. Therefore, we neglected thermal conduction in the calculation of energy deposition. Power deposition is calculated from stopping power which is a function of particle energy and particle current density.

We used the waveform of current density on the target surface by correcting the waveform measured with an MIC, as shown in Fig.3. Power deposition in the parylene layer was derived by subtracting the deposited power in the Pb-layer from the total input power into the sample.

Figure 4 shows these results for three samples with different thicknesses of Pb-layer. The upper curves are total power, and the lower curves are those in parylene. The difference corresponds to the power in Pb. The deposited energies in each layer also shown as functions of time in the same figures. Target temperature variations were calculated and the saturation values together with vaporization points are also indicated in Fig.4. It is evident that each Pb and parylene layer of the sample is heated above their vaporization temperature. Even if the current

density is below 1kA/cm^2, the sample temperature will still reach their vaporization temperature. It is to be noted that the deposited energy in parylene increases as the thickness of Pb decreases.

3. Experiment

A pulsed power device, ERIDATRON-II , was used to produce pulsed proton beams of about 400keV, 1kA/cm^2 with 100ns pulse duration at the maximum performance. The diode is a self-pinch type with a polyethylene disc anode of 8mm in thickness and 80mm in diameter. Figure 5 shows the experimental arrangement of the bombarding system. Diode voltages were measured with a $CuSO_4$ voltage divider, current densities were measured with an MIC, and also a shadow box was used to observe the beam directions. This measurement showed that each part of the beam propagated in parallel at the target position.

The samples were placed 50mm apert from the anode of the diode, and at this target position twelve samples as shown in Fig.6 were simultaneously bombarded by a one-shot ion beam. The radial current density variation of the ion beam made the irradiation condition in two grades, about 1kA/cm^2 and 0.1-0.2kA/cm^2.

For RBS analysis a tandem peiletron accelerator (NEC 5SDH) in our laboratory was utilized. Figure 7 shows the experimental geometry for the RBS analysis. The main parameters in the RBS analysis are shown in Table-2.

4 Experimental results and discussion

The features of the typical RBS spectrum for Pb/parylene /Si samples are already shown in Fig.1. The energy at the half height at the leading edge gives the atom mass, and the depth of the atom position is given if the atomic mass

is known. A fwhm gives thickness of the atom distribution along the depth. A peak height corresponds to the maximum concentration of this species.

The present experimental results are arranged as follows. Concentration of atoms in layers, and the shape of distribution or thicknesses of the remained layers are considered to be functions of LIB current density. Since we used approximately same voltage shapes for each proton pulse, range distribution of the protons is same for each pulse. Therefore, the deposited power density is proportional to the current density.

For simplicity, we abbreviate sample structures as follows; for example, 1.9-Pb(1.0) means the Pb-thickness on parylene is 1.9μm and this film is irradiated with a 1.0kA/cm^2 proton beam. Similarly, 0-Pb(0) means that parylene without Pb-coatings is unirradiated.

First, we compare the spectra for unirradiated samples. As seen in Figs.8 and 9, the Cl-edge and C-edge in the 0-Pb(0) spectrum have higher energies than those in the 1.9-Pb(0) spectrum. The energy loss of the RBS proton beam in the Pb layer decreases these edge energies. Similar results are also given by comparing the spectrum for 0-Pb(0) with those for 1.1-Pb(0) and 0.8-Pb(0). Leading edges of signals from Si, however, are not definitely determined, probably due to the increased energy struggling. The above comparisons result in that there is no inconsistency among these spectra.

Second, comparing the spectrum for 0-Pb(0) with that for 1.9-Pb(1) which is shown in Fig.10, we recognize that the 1.9-Pb(1) spectrum agrees quite well with the spectrum of 0-Pb(0). This fact means that all Pb layer in the 1.9-Pb sample was ablated by LIB bombardment and the structure of irradiated sample became identical to that of 0-Pb(0). In 1.9-Pb(0.15) spectrum a small quantity of Pb remains, but energy edges of other atoms have nearly as same value

with almost equal slope as that for 1.9-Pb(1). Thus above 0.15kA/cm^2 level, almost all 1.9-Pb layer is ablated.

Third, comparing the 1.1-Pb(1) spectrum in Fig.11 to 0-Pb(0) spectrum, we find steepness of the Cl leading edge for 1.1-Pb(1) is remarkable less than that for 0-Pb(0). The 1.1-Pb(1) sample has a spectrum very close to those of 0-Pb(1) in Fig.12 and 0-Pb(0.15) in Fig.13. Also, 0-Pb(1) and 0-Pb(0.15) have slight slopes of Cl-leading edges, and total Cl quantity seems to be decreased.

Finally, in 1.1-Pb(1) a special feature is seen at low energy side C-edge, that is, the back tail of C-peak. In this spectrum the C back tail decreases very gradually compared to that of 0-Pb(0) spectrum. Also there is a clear difference in carbon tail gradient between 0-Pb(0) and 0-Pb(1), 0-Pb(0.15). Since these samples have no Pb layer on the surface, the energy struggling is only caused by parylene and it is small. The above fact suggests that in the 1.1-Pb(1) sample large part of the beam energy was deposited to the parylene part, and it is likely that the vaporization of parylene caused mixing of a small quantity of carbon explosively into silicon substrate. This situation is quite similar to that for 0-Pb-irradiated spectrum.

The experimental results are summarized as follows. The spectrum of 1.9-Pb(1) agrees well with that of 0-Pb(0). At 0.15kA/cm^2 level, a very small quantity of Pb layer remains in 1.9-Pb samples. For 1.1-Pb(1) Cl and C atoms in parylene mixed into Si substrate. The situation is similar in the 0-Pb(1) and 0-Pb(0.15) samples.

5 Conclusion

RBS analysis is shown to be applicable to analyze the surface change for special multilayered samples caused by LIB bombardment with intermediate intensity.

In this experiment, nearly all Pb layer and a fraction of

parylene layer were lost by 0.15～1kA/cm^2, 400keV proton bombardment. The boundary between parylene and silicon became diffusive. At this stage of study, we are not able to say whether tamper effect from Pb-coating existed or did not exist. Further study is neccessary.

Acknowledgment

We are indebted to Dr. T.Nakajima and Dr. A.Kitamura for giving useful guidances in the experiment.

Reference

1) H.H.Andersen and J.F.Ziegler: Hydrogen Stopping Powers and Ranges in All Elements (Pergamon Press 1977)

Table 1 Stopping Power 1)

Proton Energy 1～10 keV

$$\text{STOPPING} = A_1 \cdot E^{1/2} \quad \text{eV}/(10^{15}\ \text{atoms/cm}^2)$$

Proton Energy 10～999 keV

$$(\text{STOPPING})^{-1} = (S_{LOW})^{-1} + (S_{HIGH})^{-1} \quad \text{eV}/(10^{15}\ \text{atoms/cm}^2)$$

$$S_{LOW} = A_2 \cdot E^{.45}$$

$$S_{HIGH} = (A_3/E) \ln \left\{ 1 + (A_4/E) + (A_5 \cdot E) \right\}$$

Proton Energy 1000～100,000 keV

$$\text{STOPPING} = (A_6/\beta^2) \left[\ln\left(\frac{A_7\beta^2}{1-\beta^2}\right) - \beta^2 - \sum_{i=0}^{4} A_{i+8} (\ln E)^i \right] \quad \text{eV}/(10^{15}\ \text{atoms/cm}^2)$$

where,

$$E = \frac{\text{HYDROGEN ENERGY}}{\text{HYDROGEN MASS}} \quad [\text{keV/amu}]$$

Table 2. Conditions in RBS analysis

ITEM	CONDITION
Ion Species	H^+
Particle Energy	2.8 MeV
Total Charge Irradiated	1 μC
Time of Irradiation	about 300 sec
Incident Angle	0 deg.
Scattering Angle	150 deg.

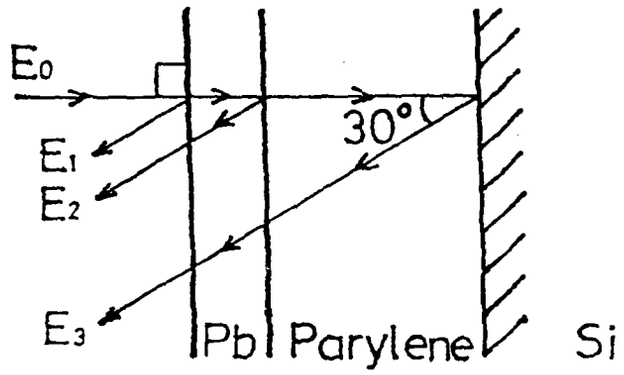

Fg.1a Schematic of sample structure.

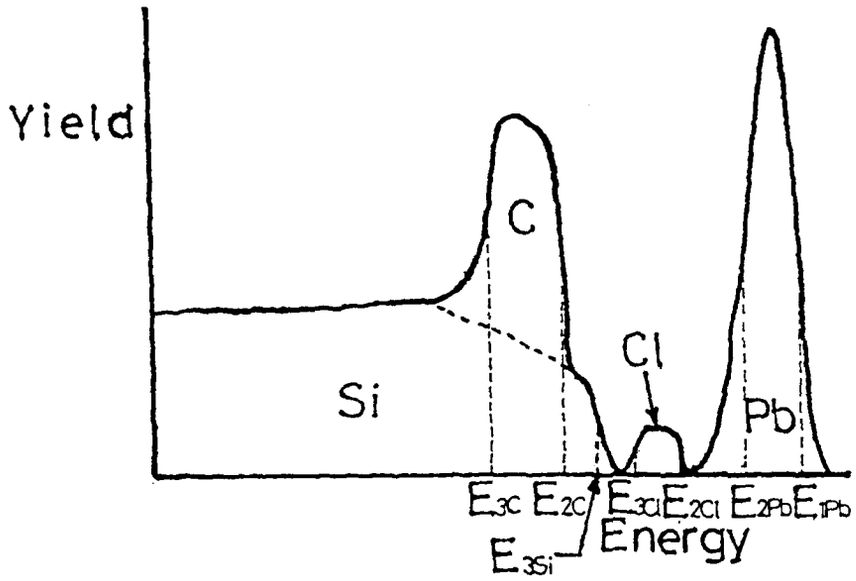

Fig.1b RBS energy spectrum predicted from the layers shown in (b).

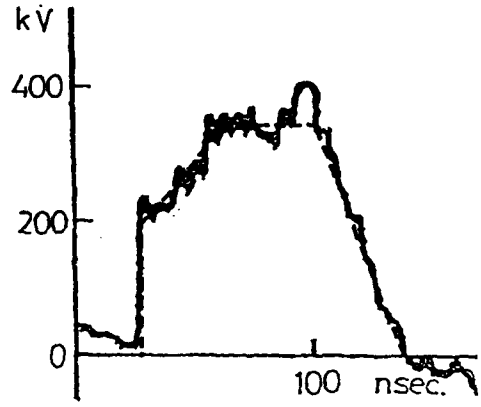

Fig.2 A diode voltage and the simplified waveform (broken line)

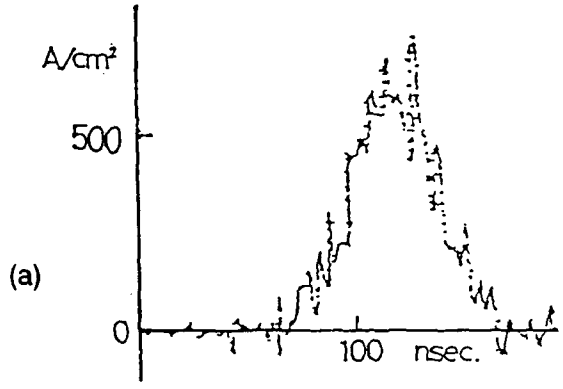

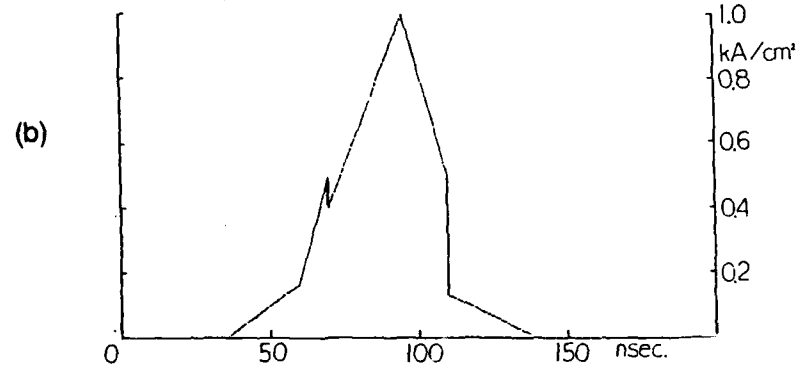

Fig.3 Current density waveform (a)measured with MIC and
(b) corrected waveform for power deposition calculation

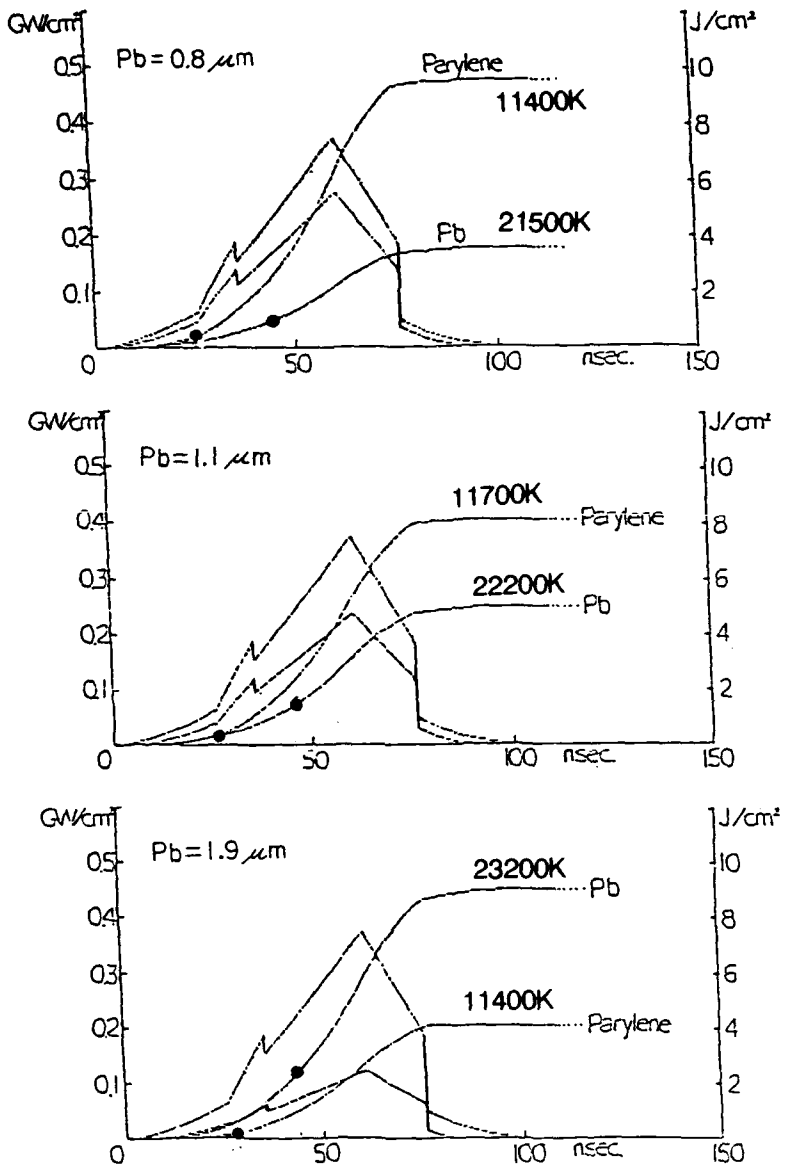

Fig.4 Power and energy deposition calculated for three different samples. Black circles show the vaporization points for each material. Maximum temperature estimated from a simple calculation are also shown.

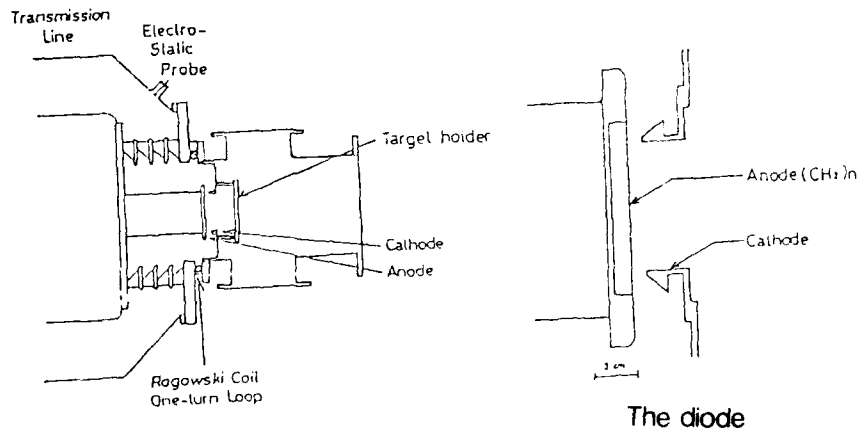

Fig.5 A schenatic of the pulsed beam bombardment system

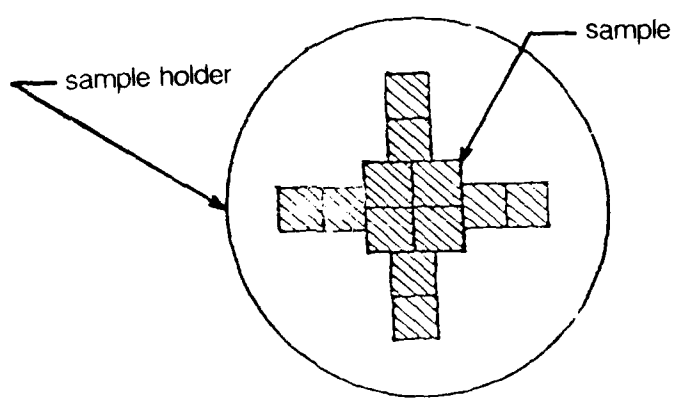

Fig.6 Sample arrangement for pulsed ion beam bombardment

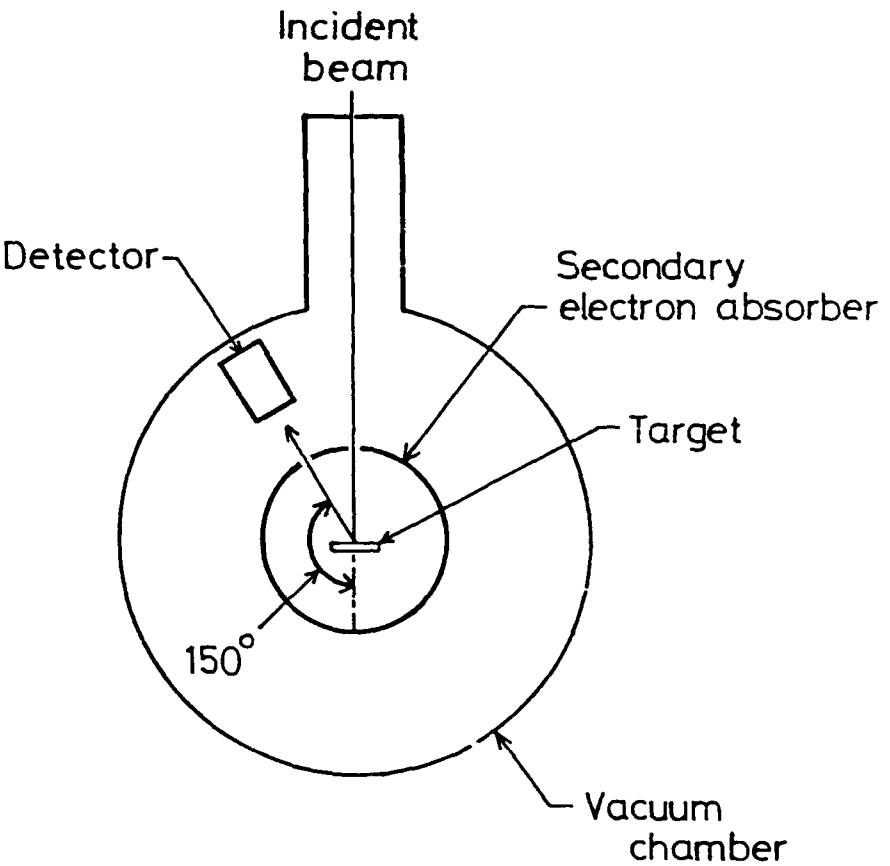

Fig.7 Schematic layout of RBS experiment

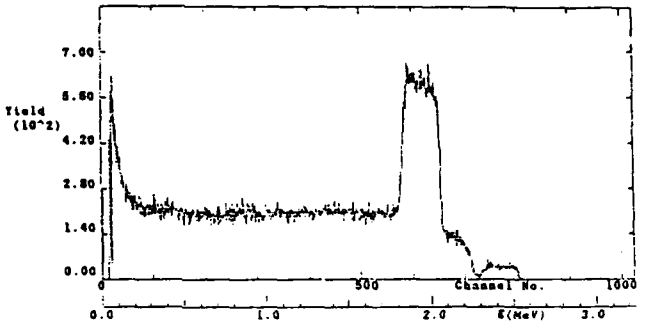

Fig.8 RBS spectrum of 2.8MeV protons from 0-Pb(0) sample

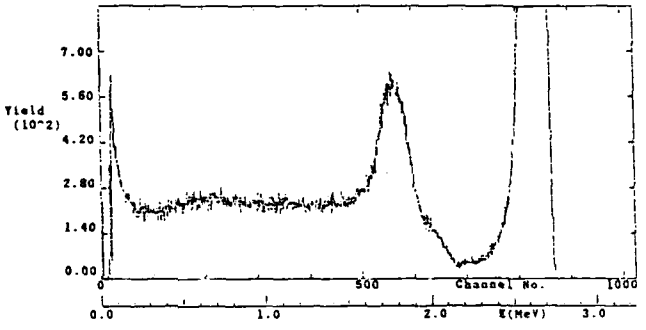

Fig.9 RBS spectrum of 2.8MeV protons from 1.9-Pb(0) sample

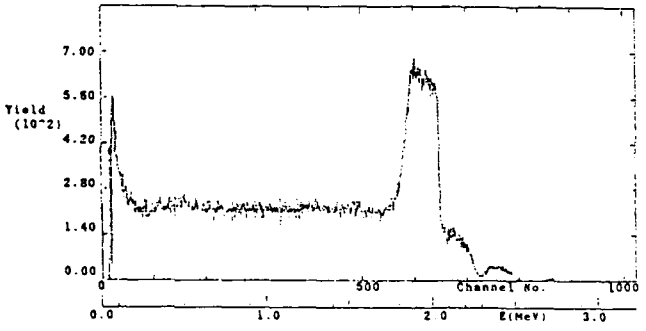

Fig.10 RBS spectrum of 2.8MeV protons from 1.9-Pb(1) sample

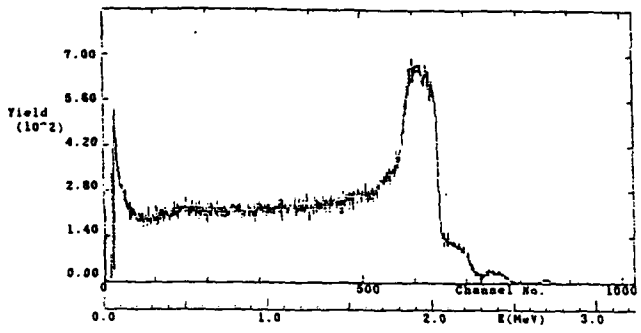

Fig.11 RBS spectrum of 2.8MeV protons from 1.1-Pb(1) sample

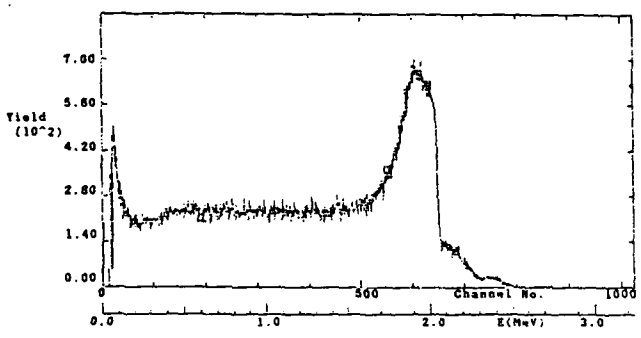

Fig.12 RBS spectrum of 2.8MeV protons from 0-Pb(1) sample

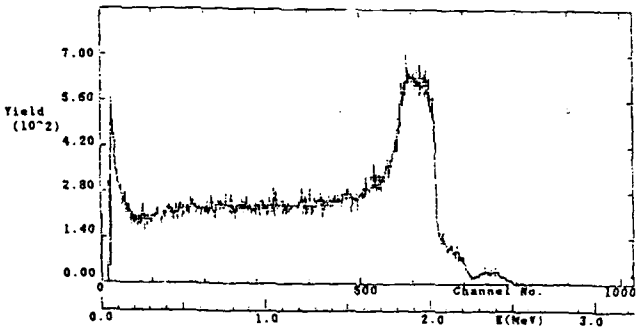

Fig.13 RBS spectrum of 2.8MeV protons from 0-Pb(0.15) sample

Two-Dimensional Focusing of Self-Magnetically Insulated "Plasma Focus Diode"

Katsumi Masugata, Hironobu Isobe, Keigo Aga,
Masami Matsumoto, Shigeo Kawata, and Kiyoshi Yatsui

Laboratory of Beam Technology, The Technological University of Nagaoka, Nagaoka, Niigata 940-21, Japan

Abstract

A new and simple type of self-magnetically insulated vacuum ion diode named "Plasma Focus Diode" has been successfully developed with a large solid angle of irradiation and low divergence angle. The diode has a pair of coaxial cylindrical electrodes similar to Mather type plasma focus device. Ion-current density of 1.9 kA/cm^2 has been obtained at the anode surface under the experimental conditions of diode voltage ~ 1.4 MV, diode current ~ 180 kA, and pulse width ~ 75 nsec. The ion beam generated has been two-dimensionally focused (line focused) with the focusing radius of ~ 0.18 mm, giving the maximum ion current density and beam power density at the axis to be ~ 130 kA/cm^2 and ~ 0.19 TW/cm^2, respectively. The motion of electrons in the gap has been numerically simulated by use of newly developed particle-in-cell computer simulation code, and good agreement has been obtained between the simulation and the experiment.

I. Introduction

In an inertial confinement fusion (ICF) research by an intense pulsed light ion beam (LIB), the most important problem to be solved is to concentrate the LIB with power density more than 10^{14} W/cm^2 on a small target of diameter 5~10 mm. To obtain such a high power density, it is very important for us to achieve large solid angle of irradiation and low divergence angle of the LIB.[1] From these points of views, we have successfully developed a new and simple type of self-magnetically insulated "Plasma Focus Diode" (PFD), [2-5] which satisfies these requirements.

Figure 1 shows the basic principle of the PFD schematically. It consists of two concentric cylindrical electrodes; anode (outer cylinder) and cathode (inner cylinder). Its shape is basically very similar to a Mather type of "Plasma Focus" device, and therefore we have named it the PFD. When pulse power is applied to the diode, electrons produced at the cathode initialy irradiate the anode. The diode current itself produces self-magnetic field (B_θ) in the azimuthal direction. When the diode current exceeds a certain critical value,[2-6] the flow of electrons is self-insulated by B_θ.

The anode plasma is produced by the initial irradiation of electrons and/or the surface flashover caused by a strong electric field. Since the cathode consists of perforated board or mesh structure, ions accelerated in the anode-cathode gap pass through the cathode, and is concentrated onto the axis of the diode.

Features of the PFD can be summarised as follows:

1) The configuration is very simple.
2) The axial symmetric configuration assures axial symmetry of any field and quantity.
3) Since the initial irradiation of electrons onto the anode promotes the formation of anode source plasma, the enhancement of the ion-current density is expected.[7]
4) It is possible to irradiate a spherical target with large solid angle.
5) Electrons do not pinch on the active area of the ion source, which makes us practical a multiple-shots operation without changing the flashboard.

In this paper, the experimental and theoretical studies of the PFD will be presented. Particularly, properties and characteristics of the PFD will be described in detail such as the measurement of electrical characteristics, divergence angle, focusability in two-dimensional (line focus) geometry, ion energy spectrum, the result of the computer simulation by use of a 2.5-dimensional particle-in-cell code, and so on.

II. Experimental Setup

The experiment has been carried out in the pulse-power

generator, "ETIGO-II",[8,9] in the Technological University of Nagaoka. The output parameters of the machine designed are as follows; voltage = 3 MV, current = 0.46 MA, impedance = 6.5 ohm, pulse duration = 50 ns. Diagnostics on diode voltage (V_d) and diode current (I_d) were done at the water-vacuum interface. The inductively-calibrated voltage (V_d^*) was calculated from V_d and I_d measured with taking the inductance of magnetically-insulated vacuum transmission line (MITL, L ~ 240 nH) into account.

Figure 2 shows the crossectional view of the PFD. It is located at the end of the MITL. The cathode, that is connected to the outer conductor of the MITL, is a cylinder (brass) with the outer radius of r_k = 10.5 mm (thickness = 1 mm). It is uniformly perforated by holes (1 mm diameter each) to extract ions, the transparency of which is ~ 40 %. The anode, which is also made of brass, is a cylinder with the inner diameter of r_k = 17.5 mm, and has the length of 40 mm in the z direction. On the inner surface of the anode, we have prepared grooves (depth = 1 mm, width = 1 mm) filled by an epoxy, which has an interval of 2 mm.

III. Experimental Results

III-a) Typical Waveforms

Figure 3 shows typical waveforms of diode voltage (V_d^*) inductively calibrated, diode current (I_d), input power to the PFD ($P_d = I_d V_d^*$), and impedance ($Z = V_d^*/I_d$). Prior to the main pulse of V_d^* and I_d, as seen from Fig. 2, there exists a prepulse, which has the magnitude less than ~ 10 % of their peak values and the pulse width of ~ 150 ns. Furthermore, the maximum value of V_d^* and I_d are seen to be ~ 1.4 MV and ~ 180 kA, respectively. The impedance (Z) during the main pulse is seen to be 6 ~ 8 ohm. The maximum power is seen to be ~ 0.24 TW, and the pulse width ~ 75 nsec (FWHM, Full Width at Half Maximum).

III-b) Ion-Current Density

Figure 4 shows waveforms of ion-current density (J_i) measured by three-channel, biased-ion collector (BIC) located inside the cathode. The BIC has three apertures (diameter = 0.5 mm) at r = 10 mm at three different

positions in the z direction, z = 7 mm, 20 mm, and 33 mm from the root of the diode, hence being possible to get three data of J_i simultaneously. The vertical axis has two scales; one is the ion-current density (J_i) actually measured, and the another is that on the surface of the anode (J_a) estimated. Here, we have calculated J_a by assuming two-dimensionally, geometric focusing of the beam,

$$J_a = (r/r_a)\, J_i . \tag{1}$$

As seen from Fig. 4, the peak values of J_a at the above three positions increase with increasing axial positions, and can be written by

$$\begin{aligned} J_a &\sim 1.4 \text{ kA/cm}^2 \text{ at } z = 7 \text{ mm}, \\ J_a &\sim 1.7 \text{ kA/cm}^2 \text{ at } z = 20 \text{ mm}, \\ J_a &\sim 1.9 \text{ kA/cm}^2 \text{ at } z = 33 \text{ mm}. \end{aligned} \tag{2}$$

The enhancement of J_a near the top of the diode could be due to the facts that the thickness of the electron sheath increases there and that correspondingly the effective diode gap tends to be decreased. This can be clearly demonstrated from a computer simulation as shown in a later section. By use of the value of J_a ($\sim$ 1.67 kA/cm^2) averaged at the above three positions and the surface area (44 cm^2) of the anode, we have calculated the net ion current (I_i) to be

$$I_i \sim 73.5 \text{ kA}. \tag{3}$$

Using eq. 3 and the peak value of I_d ($\sim$ 180 kA) in Fig. 2, we roughly estimate the efficiency of the diode as

$$\eta = I_i/I_d \sim 41\ \%.$$

III-c) Divergence Angle of the Beam

By use of a shadow box where a heat-sensitive paper is utilized as a detector of the ions, we have also measured local divergence angle (ϕ) and deviation angle (δ) from the ideal trajectories. Figure 5 plots ϕ and δ in the z-direction. As seen from Fig. 5, we see that ϕ and δ

increase with increasing z. The averaged values of these angles can be written by

$$\begin{aligned} \phi_z &= 1.1^\circ, \\ \phi_\theta &= 1.4^\circ, \\ \delta_z &= 0.4^\circ, \\ \delta_\theta &= 0.5^\circ. \end{aligned} \tag{4}$$

From the above, we may calculate the total divergence angles to be

$$\begin{aligned} (\phi_\theta^2 + \delta_\theta^2)^{0.5} &\sim 1.5^\circ, \\ (\phi_z^2 + \delta_z^2)^{0.5} &\sim 1.2^\circ. \end{aligned} \tag{5}$$

If we compare ϕ and δ obtained above with those in other diodes ($\phi \sim 2^\circ$ and $\delta \sim 6^\circ$ in single-current-feed magnetically-insualted diode,[7] $\phi \sim 1.2^\circ$ and $\delta \sim 0.9^\circ$ in dual-current-feed magnetically-insulated diode,[10] $\phi \sim 2.6^\circ$ and $\delta \sim 6.5^\circ$ in planar-type self-magnetically-insulated diode[11]), we find that the deviation angle of the PFD is significantly smaller than any other diodes studied. Such the reduction of ϕ seems to be due to the fact that the actual cathode has been utilized in this experiment, and that correspondingly the electric field can be made very uniform.

III-d) Focusability of the PFD

Using Rutherford-scattering pinhole camera technique,[12,13] we have measured the focusing radius of the beam extracted from the PFD. Figure 6 schematically illustrates the basic principle of the experiment. The ion beam extracted inside the cathode is led through a slit with the width of ~ 6 mm. The ions are then Rutherford scattered by a lead plate (0.5 mm thick, being thicker than the range of protons) that is declined at 45° with respect to the axis. The scattered ions are pinhole imaged on a CR-39 recording film that is covered by a 2-μm mylar film (filter) to eliminate carbons. The CR-39 film for this experiment detects protons in the energy range of 0.4 ~ 3.5 MeV. Since the beam first converges toward the axis and later diverges, we expect to

obtain a pattern like a "sandglass". From the spatial width of the constricted part of such the "sandglass " pattern, it is possible for us to determine the focusing radius. The space resolution of the system has been found to be ~ 0.15 mm, since the diameter of the pinhole is 0.2 mm and the magnification of the pinhole is 2.

Figure 7 (A) shows photographs of the pinhole image obtained. Figure 7 (B) shows distributions of the number density of tracks on the CR-39 film (normalized by their peak values), which has been obtained near the constricted region of each images shown in Fig. 7 (A). From Fig. 7 (B), we have estimated the focusing radius (r^*) of the beam (FWHM of these distributions) or the corresponding total divergence angles,

$$\begin{aligned} r^* &= 0.18 \text{ mm } (0.60^\circ) \text{ at } z = 7 \text{ mm}, \\ r^* &= 0.23 \text{ mm } (0.74^\circ) \text{ at } z = 20 \text{ mm}, \\ r^* &= 0.25 \text{ mm } (0.82^\circ) \text{ at } z = 33 \text{ mm}. \end{aligned} \tag{6}$$

As found from the above, we have achieved very tight focusing of the beam to be $r^* = 0.18$ mm near the root of the PFD. Furthermore, the focusing radius tends to increase toward the top of the diode where the ion current density is high. The total divergence angles obtained by this technique are smaller than those determined by the heat-sensitive paper (cf. eq. (5)). Such a disagreement comes from the facts that the focusing radius obtained by the pinhole-camera techneque gives the divergence only due to the high-energy protons, but that the local divergence angle measured by the heat-sensitive paper includes all the information associated with lower-energy proton beam as well as heavier ions than protons.

III-e) Estimate of Beam-Power Density

Assuming that all the ions produced on the anode are focused two-dimensionally (line focusing) onto the coaxial cylinder with the radius r^*, we here estimate the power density of the beam on the focusing point.

From these assumptions, we write the power density (P) at the focal point to be

$$P = (r_a/r^*)\ J_a\ V_d^*. \qquad (7)$$

Table I summarizes the power density (P) thus extimated for three axial positions. From Table I, the power density is seen to be approximately same at the three positions, which seems to be due to the fact that the focusing radius linearly increases as the ion current density increases toward the top of the diode. These characteristics qualitatively agree with the data obtained by the dual-current-feed magnetically insulated diode.

In spite of the two-dimensional focusing, however, the beam power density on the focal point thus estimated is much larger than those obtained by any other diodes with three-dimensional focusing, spherically-shaped electrodes.

III-f) Measurement of Ion Energy

Energy spectrum of the ion beam has been measured by use of a Rutherford-scattering Thomson-parabola spectrometer.[7] Figure 8 shows the cross-sectional view of the spectrometer. The ion beam focused onto the axis is irradiated onto a "thin" foil scatterer that is composed of 0.25-μm lead and 2-μm mylar. The scatterer declines at 45° with respect to the axis. Since the scatterer is "thick" for heavier ions such as carbons but "thin" for protons, only protons are able to pass it. The ions scattered are collimated by use of two pinholes, and later injected into a deflector, where the electric- and magnetic-fields are applied. The ions deflected are irradiated onto the track recording film (CR-39).

Counting the number density of the tracks for each energy, we have evaluated the energy spectra of protons. These spectra has been corrected to those incident onto the scatterer by taking the energy loss and scattering cross-section of protons in the scatterer into account.

Figure 9 typically shows the spectrum of protons. From Fig. 9, we find that the peak energy of protons is ~ 1.4 MeV in a reasonable agreement with the peak voltage (V_d^*). Furthermore, high-energy protons dominates the beam, where ~ 80 % of protons have the energy more than 1 MeV. Such a result does not agree with that obtained in another diodes,

where the beam is dominated by low-energy protons. Such a discrepancy may be due to the fact that the measurement in this experiment has been carried out on the axis of the diode where the beam is tightly focused. From these experimental results, we conclude that the focusability of high-energy protons is much better than that of the low-energy protons.

IV. Numerical Simulations

Using a newly developed computer simulation code named by PCS-KfK, furthermore, we have also carried out the numerical simulation of electrons in the anode-cathode gap.

The PCS-KfK is a 2.5-dimensional particle-in-cell (PIC) code, which has been developed by the cooperation with Kernforschungszentrum Karlsruhe (KfK), West Germany.[14] The code consists of the following three regions; the region where particles are produced, the relativistic particle pusher region, and the electric- and magnetic-field solver region.

In the first region where particles are produced, new particles are created by use of Gauss low which is adopted to a half space mesh beside the electrode. The velocity of each particles is determined by using a Maxwell distribution function and random numbers. In the second region for the particle pusher, the relativistic equation of motion is solved by Buneman scheme. In the electric- and magnetic fields region, Poisson's equation and the static Ampere low are solved to obtain the fields.

To check the reliability of the code, Child-Langmuir electron current-density (space-charge-limited electron-current-density) in the diode gap has been computed and compared with that obtained analytically. At V (applied voltage) = 1 V, the current density obtained by the simulation has been found to be 9.36×10^{-6} A/cm^2, while that by analytical evaluation 9.30×10^{-6} A/cm^2. At V = 1 MV, furthermore, we have obtained 7910 A/cm^2 from the simulation and 8050 A/cm^2 from the analytical estimate. From these results, the numerical errors of this code has been found to be less than 2 %.

Figure 10 shows the typical example of the simulation

for the typical parameters of the experiment. In this simulation, only electrons are produced and moved in the gap. Figure 10 a) and b) shows the distribution of electrons and equi flux-density lines of self magnetic field (B_θ) in the anode-cathode gap, respectively. Such the distribution has been obtained after 1200 steps of the calculation, which corresponds to the time ~ 0.5 nsec after the application of the diode voltage. From Fig. 10 a), we clearly find that electrons are perfectly insulated in the effective area of the gap. The electrons in the gap tend to drift toward the top of the electrode. The electron sheath becomes much thicker in the downstream of the electron drift. As the result, the direction of the electric field in the gap declines a little bit, and trajectories of the ions are bended toward the z-direction. Such the effect has also been observed in the experiment; the deflection angle of the ion trajectories in the z-direction observed experimentally becomes larger than that predicted theoretically by taking only the self magnetic field into account.

From Fig. 10 b), we see that the magnetic field near the cathode is weakened by the electron current drifting in the z-direction. The magnetic field significantly decreases near the top of the diode due to the radial current of electrons passing through the gap.

The total electron current passing through the gap has been calculated to be I_e ~ 43 kA. This value, however, is much less than that obtaind experimentally, I_0 ~ I_d - I_i ~ 110 kA. Such the disagreement may be due to the facts that ions in the gap has been ignored in the simulation, and that furtheremore the gap closure by the expansion of anode- and cathode-plasma has not been taken into account.

More exact simulations including these effects will be carried out in the near future.

V. Concluding Remarks

Self-magnetically insulated "Plasma-Focus Diode" has been successfully developed. The diode has been operated with good reproducebility and stability typically at diode voltatge ~ 1.4 MV and diode current ~ 180 kA in the "ETIGO II", an intense pulse power generator at Nagaoka. The ion-

current density on the anode surface has been obtained to be ~ 1.9 kA/cm^2, yielding total ion current and diode efficiency to be ~ 73.5 kA and 41 %, respectively. The current density has been found to increase spatically toward the top of the diode. Very good focusing has been obtained with the focusing radius ~ 0.18 mm. The ion-current-density, the divergence angle, and the focusing radius increase toward the dowstream of the E x B electron drift. Power density of the beam at the focal point has been estimated to be 0.18 TW/cm^2. In spite of two-dimensional focusing, it has given the highest power density compared with any other diodes under the same experimental conditions. The energy spectra at the axis of the diode has also been measured by Rutherford-scattering Thomson-parabola technique, indicating that the beam is found to be dominated by high-energy protons.

The motion of electrons has been simulated by a particle-in-cell computer simulation code. The thickness of the electron sheath tends to increases toward the downstream of the electron drift, hence decreasing the effective gap length. Such the result predicted from the simulation qualitatively agrees with the experimental observation.

At present, the experimental studies has been carried out in more detail to obtain much high power densiy in higher voltage region. Furhtermore, we are also carring out the three-dimensional focusing experiment by use of spherically shaped electrodes, which will be reported elsewhere.

References

1) J. P. VanDevender, J. A. Swegle, D. J. Johnson, K. W. Bieg, E. J. T. Burns, J. W. Poukey, P. A. Miller, J. N. Olsen and G. Yonas: Laser and Particle Beams 3, 93 (1985).

2) K. Masugata, T. Yoshikawa, A. Takahashi, K. Aga, Y. Araki, M. Ito and K. Yatsui: Proc. 6th Int'l Conf. on High-Power Particle Beams, Kobe, 1986, ed. by C. Yamanaka (Inst. Laser Eng., Osaka Univ.), 152 (1986).

3) K. Masugata, K. Aga, A. Takahashi and K. Yatsui: Proc. of 2nd Int't Top. Symp. on ICF Res. by High-Power Particle Beams, Nagaoka, 1986, ed. by K. Yatsui (Lab. Beam Tech., Tech. Univ. of Nagaoka), 81 (1986).
4) K. Yatsui, Y. Shimotori, Y. Araki, K. Masugata, S. Kawata and M. Murayama: Proc. 11th Int'l Conf. on Plasma Phys. and Controlled Nucl. Fusion Res., Kyoto, IAEA-CN-47/B-Ⅲ-9 (1986).
5) K. Yatsui, K. Masugata and S. Kawata; Proc. 8th Int'l Workshop on Laser Interaction and Related Plasma Phenomena, Monterey, USA (1987).
6) M. S. Di Capua: IEEE Transactions on Plasma Science PS-11, 205 (1983).
7) K. Yatsui, A. Tokuchi, H. Tanaka, H. Ishizuka, A. Kawai, E. Sai, K. Masugata, M. Ito and M. Matsui: Laser and Particle Beams 3, 119 (1985).
8) K. Yatsui, Y. Araki, K. Masugata, M. Murayama, M. Ito, E. Sai, M. Ikeda, Y. Shimotori, A. Takahashi and T. Tanabe: in Ref. 2, 329 (1986).
9) A. Tokuchi, N. Nakamura, T. Kunimatsu, N. Ninomiya, M. Den, Y. Araki, K. Masugata and K. Yatsui: in Ref. 3, 430 (1986).
10) E. Sai, Y. Shimotori, K. Aga, K. Masugata, M. Ito, and K. Yatsui: Proc. Collab. Res. Mtg. on Development and Applications of High-Power Particle Beams, Nagoya, 1984, ed K. Yatsui, IPPJ-742 (Inst. Plasma Phys., Nagoya Univ.) 69 (1985).
11) T. Yoshikawa, K. Masugata, M. Ito, M. Matsui, and K. Yatsui: J. Appl. Phys. 56, 3137 (1984).
12) D. J. Johnson, P. L. Dreike, S. A. Slutz, R. J. Leeper, E. J. T. Burns, J. R. Freeman, T. A. Mehlhorn and J. P. Quintenz: J. Appl. Phys. 54, 2230 (1985).
13) Y. Shimotori, K. Masugata, E. Sai, T. Matsuzawa, K. Aga and K. Yatsui: in Ref. 2, 97 (1986).
14) S. Kawata, E. Halter, E. Gabowitsch, M. Sararu and T. Westerman: Kernforschungszentrum Karlsruhe (KfK) Primarbericht, 14.04.01P44A, (1986).

Table I Beam power density (P) estiamted for three axial positions.

z (mm)	r (mm)	J (kA/cm²)	P (TW/cm²)
7	0.18	1.4	0.18
20	0.23	1.7	0.17
33	0.25	1.9	0.18

Figure Captions

Fig. 1 Basic principle of the PFD.

Fig. 2 The PFD installed in "ETIGO-II".

Fig. 3 Typical waveforms of (a) diode voltage and diode current, and (b) input power and impedance.

Fig. 4 Waveforms of ion-current dehsity at three positions.

Fig. 5 Distributions of (a) local divergence angle (ϕ) and (b) deviation angle (δ) from the ideal trajectories in the z-direction.

Fig. 6 Outline of the measurement of focusing radius by Rutherford-scattering pinhole camera.

Fig. 7 (A) Photographs of the pinhole image by the method of Fig. 6, and (B) the corresponding distribution of number density of the tracks.

Fig. 8 Cross-sectional view of Rutherford-scattering Thomson-parabola spectrometer.

Fig. 9 Energy spectrum of protons obtained by the method of Fig. 8.

Fig. 10 (a) Electron map and (b) equi-magnetic-flux density (B_θ) lines in the PFD obtained by the simulation. Parameters of this simulation is as follows; applied voltage = 1.4 MV, radius of anode = 17.5 mm, radius of cathode = 10.5 mm, anode-cathode gap = 7.0 mm, length of anode = 40 mm (from z = 0 to z = 40 mm), length of cathode = 50 mm (from z = 0 to z = 50 mm), electron emissive region = 40 mm (from z = 0 to z = 40 mm).

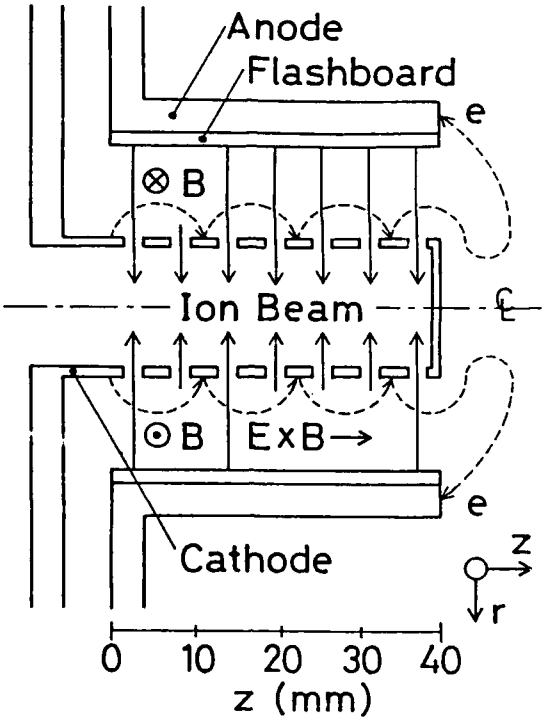
Anode
Flashboard
e
⊗B
Ion Beam
℄
⊙B
ExB→
e
Cathode
z
r
0
10
20
30
40
z (mm)

FIG. 1

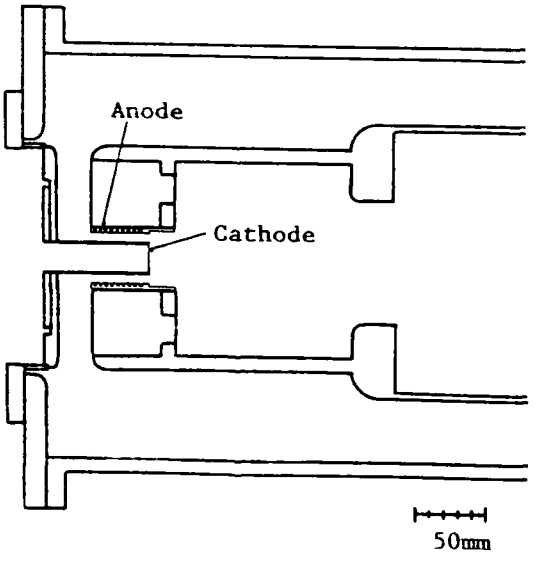
Anode
Cathode
50mm

FIG. 2

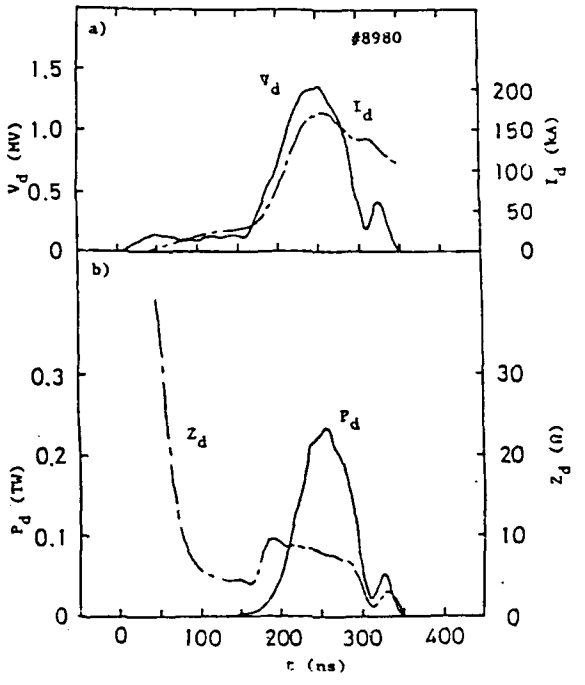
a)
#8980
V_d
I_d
V_d (MV)
I_d (kA)
b)
Z_d
P_d
P_d (TW)
Z_d (Ω)
t (ns)

FIG. 3

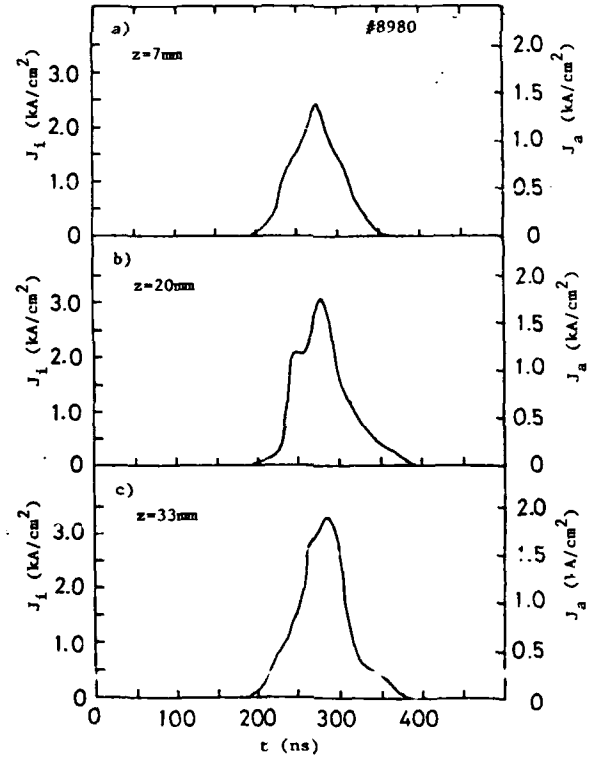
a)
#8980
z=7mm
b)
z=20mm
c)
z=33mm
J_i (kA/cm^2)
J_a (kA/cm^2)
t (ns)

FIG. 4

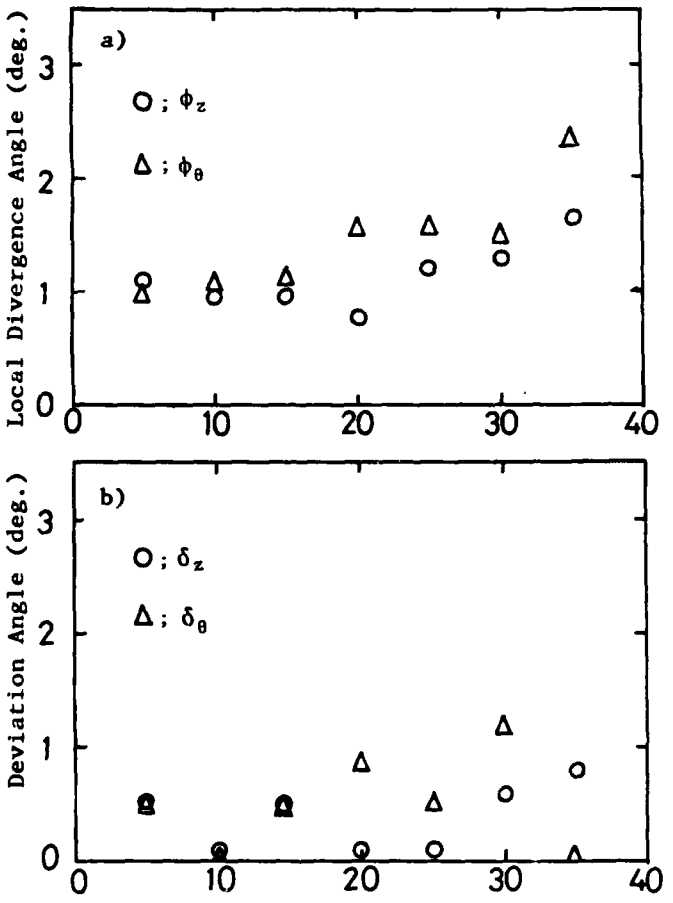
a)
○ ; ϕ_z
△ ; ϕ_θ
Local Divergence Angle (deg.)
0
1
2
3
0
10
20
30
40
b)
○ ; δ_z
△ ; δ_θ
Deviation Angle (deg.)
0
1
2
3
0
10
20
30
40

FIG. 5

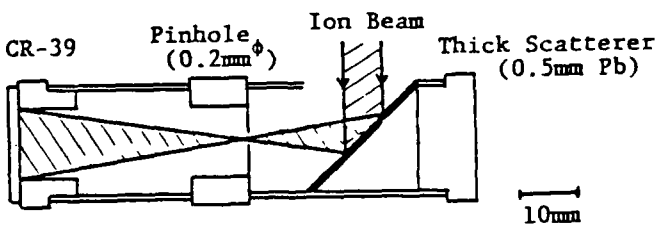
CR-39
Pinhole
(0.2mmϕ)
Ion Beam
Thick Scatterer
(0.5mm Pb)
10mm

FIG. 6

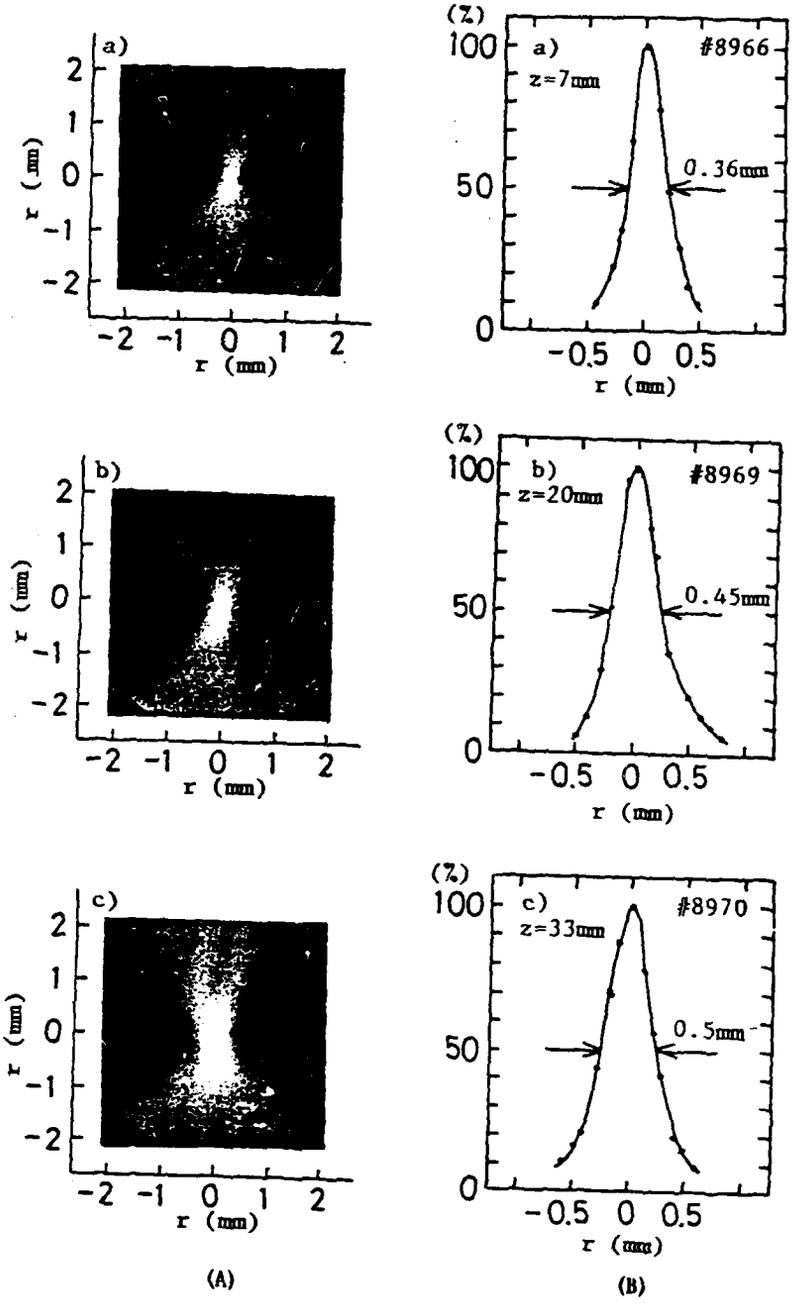
a)
b)
c)
r (mm)
2
1
0
-1
-2
-2 -1 0 1 2
(%)
100
50
0
a) #8966
z=7mm
0.36mm
b) #8969
z=20mm
0.45mm
c) #8970
z=33mm
0.5mm
-0.5 0 0.5
(A)
(B)

FIG. 7

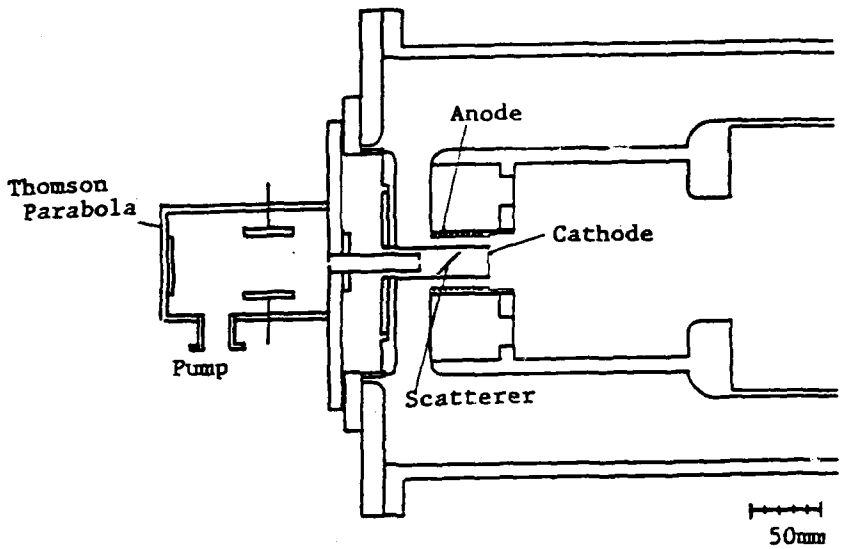
Thomson
Parabola
Anode
Cathode
Pump
Scatterer
50mm

FIG. 8

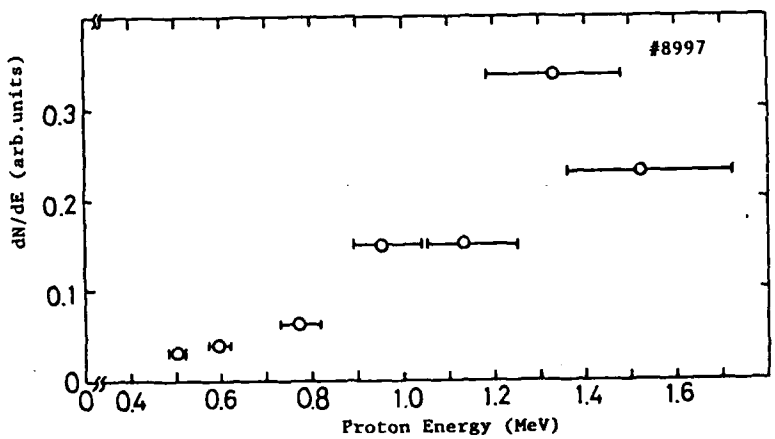
#8997
dN/dE (arb.units)
0.3
0.2
0.1
0
0
0.4
0.6
0.8
1.0
1.2
1.4
1.6
Proton Energy (MeV)

FIG. 9

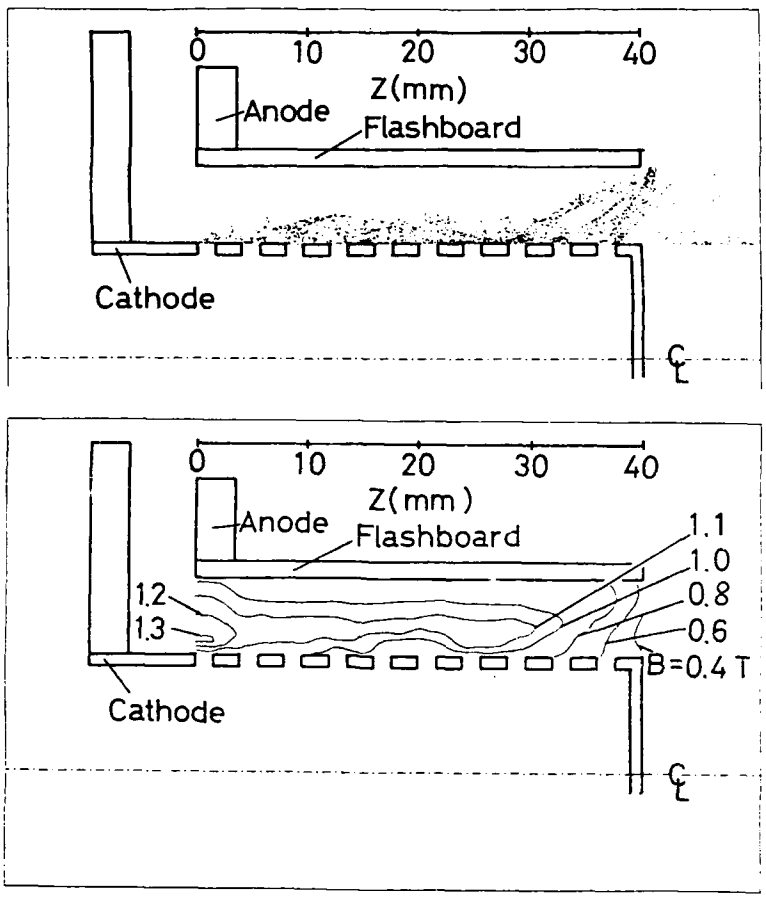
0
10
20
30
40
Z(mm)
Anode
Flashboard
Cathode
0
10
20
30
40
Z(mm)
Anode
Flashboard
1.1
1.0
0.8
0.6
1.2
1.3
B=0.4 T
Cathode

FIG. 10

Research on Anode Plasma Behavior of Flashover Pulsed Ion Sources.

H.YONEDA, H.Tomita, K.HORIOKA, and K.KASUYA

Department of Energy Sciences, The Graduate School at Nagatsuta,
Tokyo Institute of Technology, 4259 Nagatsuta, Midori-ku
Yokohama 227, Japan

Abstract

We measured physical parameters of anode plasma in a magnetically insulated pulsed ion diode with various diagnostic tools. The result denotes that a large amount of neutral gas particle is emitted in diode operation, and it has an important role on the determination of anode plasma characteristics and the diode performance.

1. Introduction

Intense pulsed ion sources with pulsed power technology are simple and low cost drivers for Inertial Confinement Fusion (ICF) research. A MJ-order ICF driver can be constructed, if the ion beam can well focus on the target. However, to achieve this, there are still some unsolved problems in diode; rapid anode plasma turn-on, impedance control, purity improvement, etc.. The exact mechanisms of the initiation, expansion, or ionization-processes is still not understood. As the most of these problem are related to anode plasmas, we observed anode plasma in magnetically insulated diode, to get the key solutions for these problems. First, we estimated electron number density profiles in the anode plasma from Stark broadening of hydrogen line, the electron temperature from line intensity ratio. Second, we developed a new simple diagnostics method for time resolved ion energy measurements, and measured the ion energy with spatial and temporal resolution. And last, we achieved laser aided diagnostic of anode plasma. A pulsed nitrogen laser was used and several shadowgraphs were taken during and after the diode pulse.

2. Experimental Apparatus

The block diagram of the experimental apparatus is shown in **Fig.1**. The diode was an annular magnetically insulated diode, which was driven by a 5ohm-60ns Blumlein line. Liquid nitrogen was fed to the anode for cooling down of the ion sources through a vacuum transfer tube, which had a shape of spiral coil for inductive electrical isolation[1]. In the case of liquid or gas state ion sources, they were supplied by the gas from the reservoir and frozen on the anode metal surface with about 1mm thickness, while conventional hydrocarbon sources were put into the anode grooves. The anode voltage was measured under the inductive correction of the line voltage. The metal transfer tube was also utilized for the inductive voltage monitor. The diode current was measured by a Rogowski coil. The light from the anode plasma was focused on the spatial resolution slit. It was guided to a 50 cm monochromator in a shield room through a 7m optical fiber to avoid electromagnetic noises and was detected by a PM tube. The extracted ion beam current was measured by a biased ion corrector and the energy profile of the ion beam was measured by a time resolved Thomson parabola analyzer.

To diagnose the plasma dynamics in the A-K gap, a nitrogen laser was used. It had typical parameters shown below;

Laser energy: 1mJ, Pulse width: 6ns FWHM,
Wavelength: 337.1nm, Divergence: 3mrad.

The shadow photographs were taken at various time after the main pulse to observe dynamics of neutral gas particle in the diode gap.

3. Experimental Results

3.1 Anode plasma turn-on

We measured the anode plasma light emission spectroscopically, and estimated the temporal history of electron number density from the Stark line broadening[2]. **Figure 2** is one of the results about these measurements. The ion source used was H_2O ice, and two different anode temperatures were chosen (90K and 160K). At the higher temperature, higher density of anode plasma was achieved at early time. This difference was explained as

follows; The quantity of neutral gas emission had much influences on the anode plasma initiation, and this became larger at the higher temperature material. Next, to ascertain this explanation, we measured the Hα line intensity with different materials (CH_3OH and H_2O) at the same temperature. Although in general, the line intensity is related to both of number density and temperature, it showed number density qualitatively in our experimental condition. This result is shown in **Fig.3** and the line intensity was much higher, as expected, in the case of CH_3OH, which was expected to emit more gas quantity than H_2O.

3.2 Anode Plasma Expansion

The anode plasma expansion decreases the effective diode acceleration gap and causes the diode impedance collapse in a high efficiency diode. This is one of the serious problems. We measured the profile of electron number density in A-K gap and the result is shown in **Fig.4**. At diode time t=30ns, the measured anode plasma thickness was about 2mm. This value was larger than the one expected from the thermal motion of the anode plasma (~1eV) without transverse magnetic field. To get a key to understand these phenomena, we measured the profiles of some parameters in anode plasma. **Figure** 5 is the spatial profiles of Hα and Hβ line intensity at an interval of 20ns. Each excitation energy is 12.09eV for Hα and 12.75eV for Hβ from the graound state, which means the ratio of Hβ/Hα denotes anode plasma temperature qualitatively. From **Fig.5**, we can see that Hα and Hβ had the same expansion velocity, but these intensity profiles in the anode plasma had a little bit difference. Particularly, at t=80ns, the Hβ intensity profile had a peak at z=1mm, while Hα line intensity decreased monotonically with the distance from anode. This means not only electron density but also the electron temperature had a spatial profile and the temperature had a peak at slightly far from the metal anode.

Next, we investigated the influence of atomic mass on the expansion velocity. However, we were afraid that if the different materials were used as the ion sources, the different diode operation would be realized; for example, the different turn-on time as shown in Sec. 3.1. We chose isotopes of H_2O and D_2O for the ion sources. They have analogous chemical character, while atomic mass of D are twice larger than that of H, and measured Hα

and Dα line intensity profiles. The Dα line has a peak at slightly different wavelength from that of Hα line (∿ 1.7A), and we, therefore, could monitor the purity of anode plasma spectroscopically. The spectral line profiles of D_2O and H_2O ion sources are shown in **Fig.6**, and we confirmed that our measured line was exactly the Dα line in the case of D_2O. **Figure 7** shows the spatial profile of Dα line intensity in A-K gap. From these results and **Fig.5**, we can conclude that D and H atom expanded at the same velocity (of about 3cm/μs). Moreover, we measured the spectral profile of ion source of half-and-half mixed D_2O and H_2O. These results are shown in **Fig.8**. The peak intensity ratio of Dα and Hα didn't vary at various place and time. These results also assured that D and H atom expanded at the same velocity.

From above-mentioned results, the velocity of anode plasma exparsion is not explained by the thermal one, and there may be other mechanisms, for example, the fast neutral particles.

3-3. Ion Energy measurements

The measurement of the ion species and the energy spectrum is important to obtain the data for ion species composition, anode plasma temperature, A-K gap acceleration voltage, and so on. Particularly, the time resolved measurements give much information about the anode plasma characteristic. So, we tried to make the ion energy measurements with time integrated method and also developed a simple time resolved ion energy analyzer.

Figure 9 shows that the N^{++}/N^{+} ratio depended on the ion energy per charge in the case of nitrogen ion sources[3]. We also show anode plasma temperature calculated from this data with the Saha equilibrium model. Because the diode voltage falls down with time in general, this result means that anode plasma temperature increases with diode time. We can conclude from this results and results in Sec.3-2 that ion beam emitting surface runs to the cathode direction with time.

Although many kinds of time resolved ion energy analyzer are proposed, the time-ramped electric deflection method is seemed to be better than others to get quantitative data with continuous energy and time resolution. Dreike et.al. proposed this method[4] with Krytron tubes for switching oscillators. On the contrary, we propose a simpler method[5] without a high voltage generator and a switching tube. **Figure 10** shows a schematic drawing of our

apparatus. The line voltage monitor signal (1.5kV 80ns FWHM) is split into three 50ohm cables and added series in a 50ohm cable which is terminated by an anti-ringing capacitor (Cri) and a monitor resistor. The final voltage waveform at deflection plate can be controlled by each cable length, the number of cables, and capacitance of the terminate capacitor. **Fig.10** also shows the monitored deflection voltage, diode voltage waveform, and temporal history of ion energy measured at 21cm from the anode. We also measured spatial and temporal irregularity of the anode plasma with this analyzer. **Figure 11** shows three traces recorded on the CR-39 of triple pinhole analyzer, each trace is corresponded to different radius position of the anode surface. This results show ion emitting points moved toward outer radius with time, and is consistent with the streak photograph of the visible light from the anode plasma (**Fig.11**).

3-4. Laser aided diagnostic of anode plasma

From the experimental results mentioned above, we can conclude that neutral gas emission makes an important role for flashover plasma source. Under the assumption of LTE model, ionization ratio of hydrogen can be calculated from electron number density and temperature measured spectroscopically. It was very low in the anode plasma. It meant that there was a large amount of neutral gas particle and it is easy to predict that a lot of neutral particle enter the diode gap. If it is true, many incomprehensible matter in the diode gap can be explained; for example, high expansion velocity of anode plasma, rapid impedance collapse, spread of ion energy and so on. So we tried to measure the dynamics of neutral particle with laser aided method.

Figure 12 shows the results of the nitrogen laser shadowgraphs of the anode-cathode gap. The six series of photographs are taken after the diode main pulse with time interval of about 100ns. From this results, we can see large amount of neutral particles expand into the gap, particularly from the anode side. This results also encourage us to measure the neutral particle directly.

4. Conclusion

We conclude here as follows; The neutral gas emission is one of key factors of the anode plasma initiation. The large quantity of the neutral gas results in the rapid formation and the dense anode plasma. The anode plasma thickness was measured spectroscopically and it was about ∿ mm. There were density and temperature profiles in this. The anode plasma expansion velocity was 3cm/μs and this value was not changed with atomic mass changed from H to D. The temperature of the plasma at emitting surface increased and it moved to the cathode direction with time. A new diagnostics method was proposed and time resolved ion energy spectrum was measured. We observed that ion emitting point moved toward outer radius on the anode surface. A large amount of neutral gas particle was emitted from the anode surface after the diode pulse and it may be able to explain some unsolved phenomenon in the diode gap.

References

1) T.Takahashi, K.Horioka, H.Yoneda, and K.Kasuya; Appl. Phys. Lett., 46, 249 (1985)

2) R.Pal and D.Hammer; Phys. Rev. Lett., 50, 732 (1983)

3) K.Kasuya, K.Horioka, H.Yoneda, K.Mitobe; Proc. 11th Int. Conf. Plasma Phys. and Controlled Nuclear Fusion Research at Kyoto IAEA-CN47/B-III-7 (1987)

4) P.L.Dreike, E.J.T.Burns, S.A.Slutz, J.T.Crow, D.J.Johnson, P.R.Johnson, R.J.Leeper, P.A.Miller, L.P.Mix, D.B.Seidel, and D.F.Weger; J. Appl. Phys. , 60, 878 (1986)

5) H.Yoneda, K.Horioka, Y.Kim, and K.Kasuya; Rev. Sci. Inst., (published in March, 1988)

Figure caption

Fig.1 Schematic diagram of experimental apparatus.
Fig.2 Temporal histories of electron number density
with ion source temperature as a parameter.
Fig.3 Hα line intensity with various materials.
Fig.4 Spatial profiles of electron number density.
Fig.5 Spatial profiles of Hα and Hβ line intensity.
Fig.6 Spectral profiles of light from D_2O and H_2O ion source.
Fig.7 Spatial profiles of Dα line intensity.
Fig.8 Spectral line shapes of mixed D_2O and H_2O.
Fig.9 Ion species ratio N^{++}/N^{+} and ion temperature vs ion energy.
Fig.10 Time resolved Thomson parabola analyzer.
a) Driving electric field circuit.
b) Diode voltage, driving voltage, and measured ion energy.
Fig.11 Results of triple pinhole analyzer a),
and Streak photograph of the visible light from anode b).
Fig.12 Nitrogen laser shadowgraphs of the diode gap taken
with time interval of about 100ns.

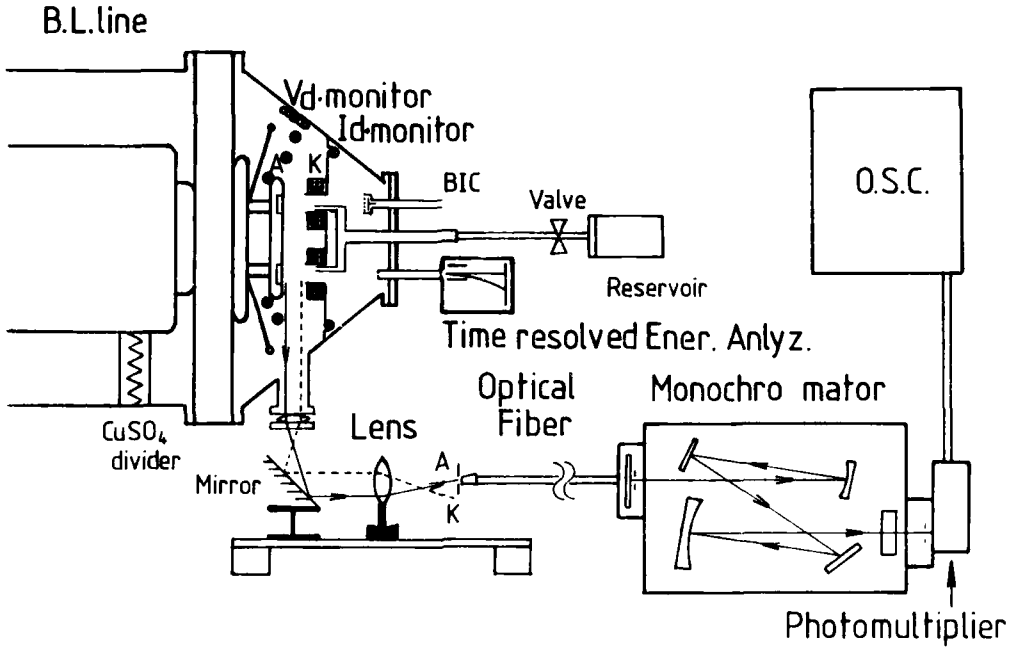

Fig-1

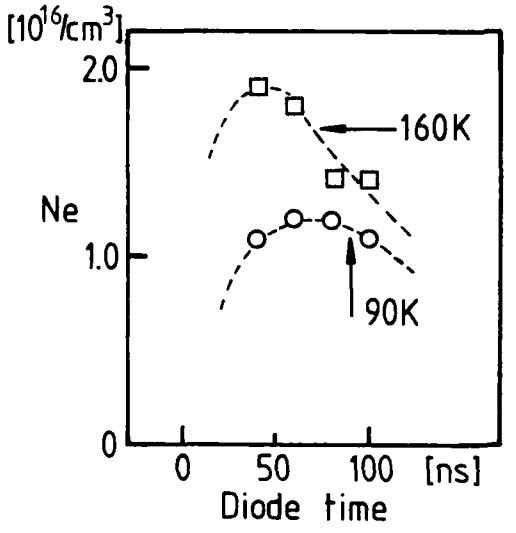

Fig-2

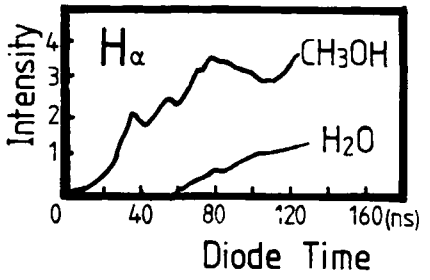

Fig-3

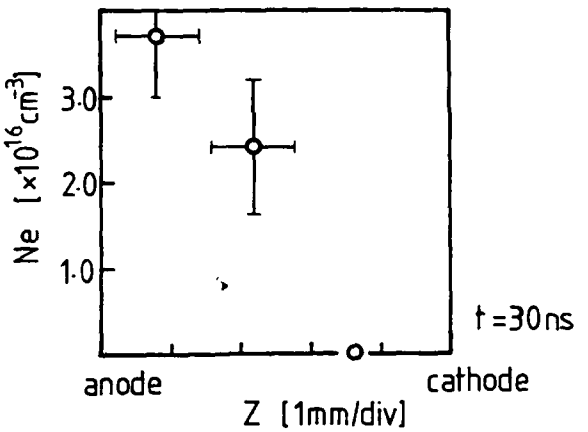

Fig-4

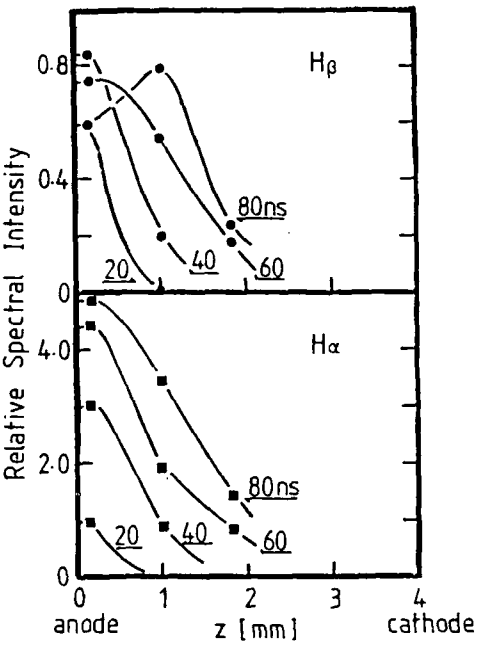

Fig-5

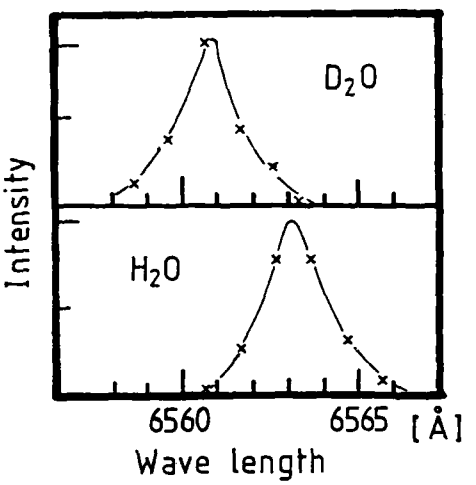

Fig-6

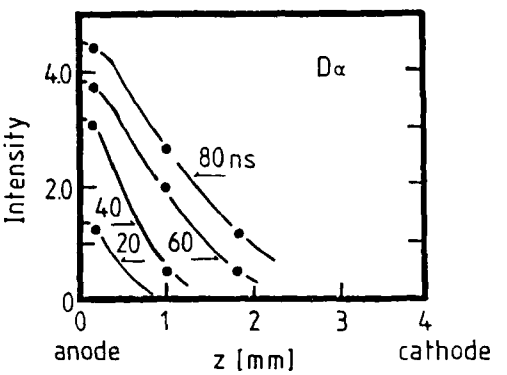

Fig-7

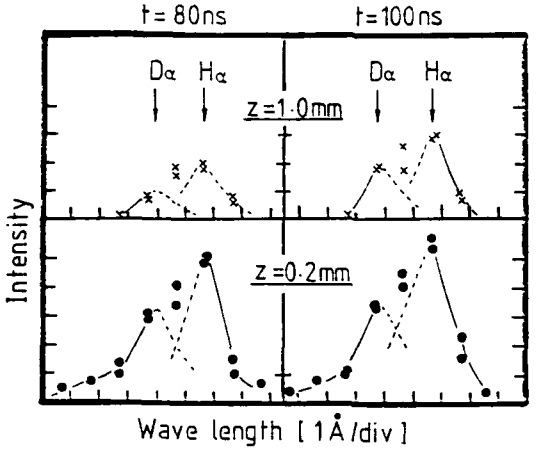

Fig-8

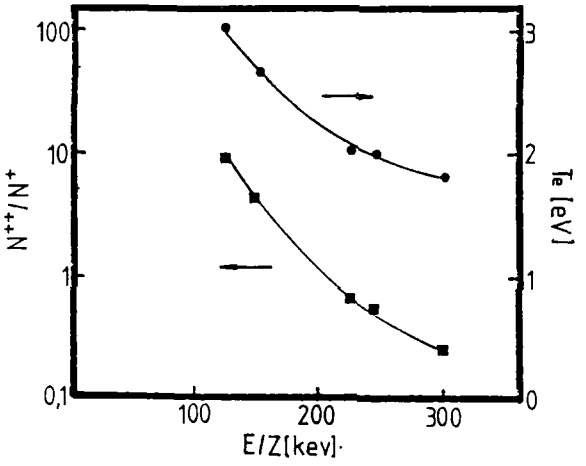

Fig-9

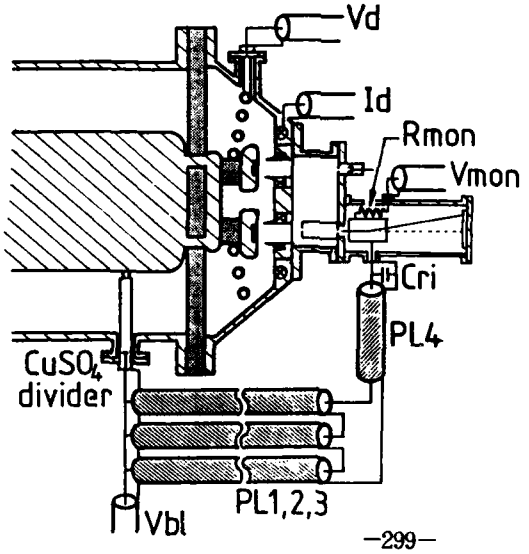

Fig-10-a)

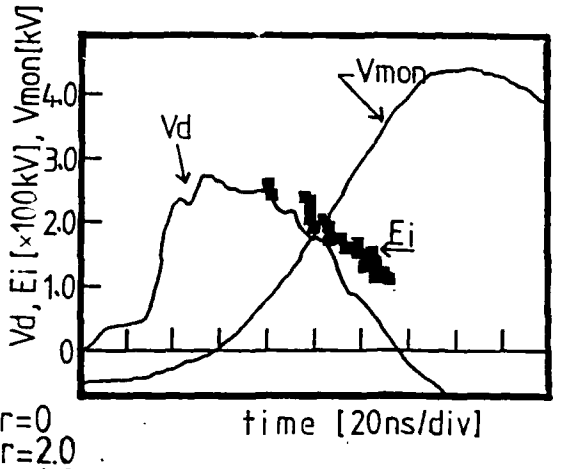

Fig-10-b)

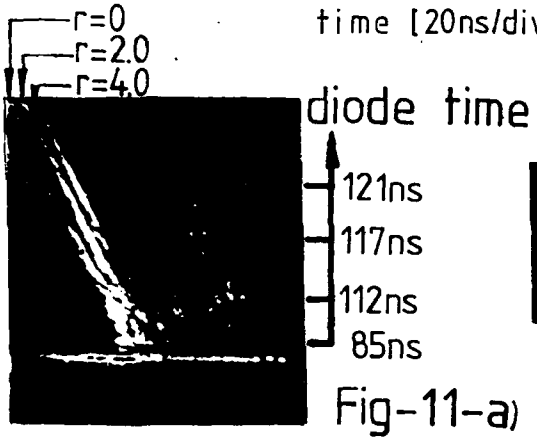

Fig-11-a)

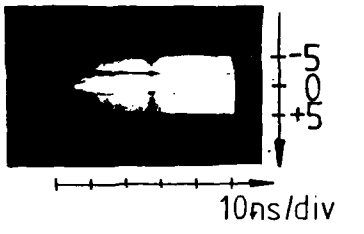

Fig-11-b)

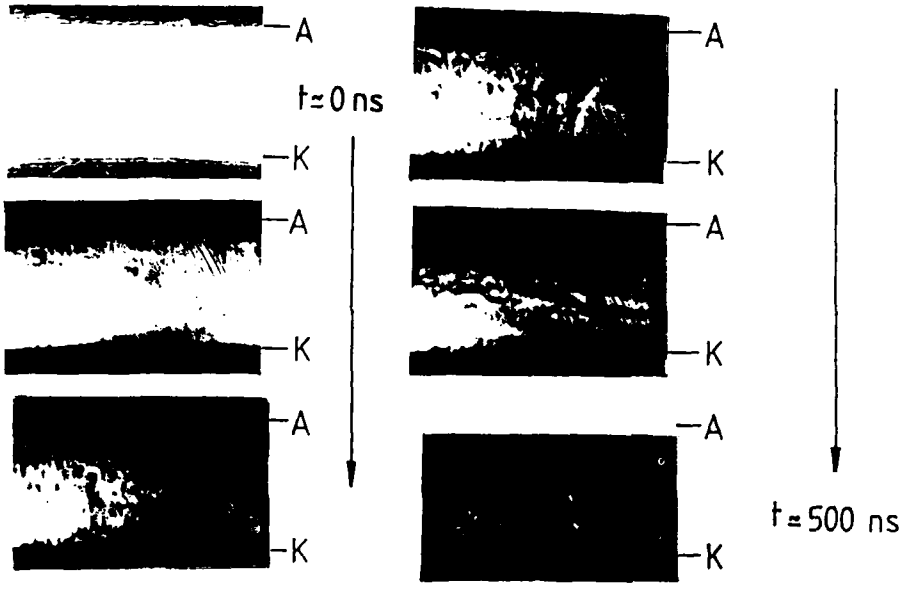

Fig-12

Time-Resolved Spectroscopic Measurement of Anode Plasma in Magnetically-Insulated Diode

Yasunori KAWANO, Norihide YUMINO, Yuhzo ARAKI,
Katsumi MASUGATA, and Kiyoshi YATSUI
Laboratory of Beam Technology, The Technological University of Nagaoka, Nagaoka, Niigata 940-21, Japan

A new diagnostic technique has been developed for the time-resolved spectroscopic measurement of anode plasma in a single-current-feed magnetically-insulated ion diode. From the measurement of Stark broadening of H_α line of hydrogen, we have estimated the electron density to be $4 \sim 5 \times 10^{16}$ cm^{-3} using the pulse-power generator, "ETIGO-Ⅰ", typically operated with diode voltage = 550 and 600 kV, diode current = 36 and 53 kA, and pulse width $\sim$ 90 ns (FWHM of diode current). Assuming local thermodynamic equilibrium, we have estimated the electron temperature to be $1.9 \sim 2.4$ eV from the measurement of light intensity ratio of successive ionization stages of carbon. The expansion velocity of the anode plasma has been found to be $4 \sim 4.5$ $cm/\mu s$.

Ⅰ. Introduction

The development of an intense pulsed light-ion beam (LIB) with very high power density is one of the important key issues for the effective achievement of the LIB-driven inertial confinement fusion. As well known, the characteristics of the LIB strongly depend on the conditions of the anode plasma (density, temperature, ion species, etc.). From such a point of view, the detailed understanding of the characteristics of the anode plasma is very important to make clear the properties of the LIB.

To diagnose the anode plasma of the LIB in detail, a spectroscopic measurement is very effective.[1~4] For this purpose, highly time-resolved diagnostic is required since the

pulse width of the LIB is normally on the order of several tens of nanosecond. Several authors have utilized the spectroscopic system in the combination with optical fibers and photomultipliers.[2~4] Such the system, however, has not given us the spectra continuously both in time and wavelength.

To use a streak camera as a detector of the spectrometer was tried at Sandia National Laboratories,[1] which made possible to obtain data continuously both in time and wavelength. A direct processing by computers, however, could not be made since the data was recorded by photographs in the above system. To acquire data continuously both in time and wavelength, we have successfully developed a spectroscopic diagnostic system in the combination of a spectrometer with a streak camera. This system can be possible for various data processing where streak images are taken by a SIT camera (highly sensitive TV camera) and then led to a frame memory of microcomputer via A/D converter. By this technique, we have succeeded in highly time-resolved and continuous measurement of the spectra as well as the real time processing. In this paper, we would like to present some preliminary data of this measurement of the anode plasma in a single-current-feed magnetically-insulated diode (MID).

Ⅱ. Experimental Setup

Figure 1 shows the outline of the experimental setup. The experiment has been carried out in the pulse-power generator, "ETIGO-Ⅰ", at the Tech. Univ. of Nagaoka.[5] The output parameter of the generator is as follows; voltage = 1.2 MV, current = 240 kA, power = 0.3 TW, pulse width = 50 ns, energy = 14.4 kJ. The ion diode used is a planar type of MID, where the anode-cathode gap is 12 mm wide. On the surface of the anode (aluminum), a polyethylene sheet (160 mm × 160 mm; 1.5 mm thick) has been attached as the flashboard. As the cathode, we have utilized the perforated brass (5 mm thick), which has the transparency of 11 % with 25 holes (12 mm' each).

The window from which the light signal is extracted is made of pyrex glass (55 mm × 75 mm; 5 mm thick). The light signal from the anode plasma is led to the diagnostic system that is installed at approximately 7 m apart in the optical length.

Figure 2 shows the time-resolved system developed here. The light signal is introduced into Czerny-Turner spectrometer (focal length; 25 cm, grating; 1800 grooves/mm), and later led to a streak camera (temporal disperser).[6] The wavelength covered by the streak camera ranges from 4000 ~ 8500 Å. If the central wavelength is chosen at ~ 6500 Å, the range of the wavelength measured by one shot is 67 Å/frame. The streak images are taken by a SIT camera and A/D converted, which is recorded into a frame memory (8 bit, 256 channel × 256 channel) as digital data. These data of images memoried are analysed by a temporal analyser, which gives a profile of spectra both in time and wavelength.

The sweep rate of the streak camera is 667 ns/256 channels, hence yielding ~ 2.6 ns/channel. The time resolution in this system is ~ 20 ns, which is mainly determined by a slit width of the streak camera. The resolution of the wavelength is measured to be ~ 1 Å at this sweep rate, which is determined by a slit width of the injection to the spectrometer. The dynamic range (the ratio of the maximum value of the input divided by the background level) is as large as more than 100.[6]

Ⅲ. Experimental Results and Discussions

Figure 3 presents typical waveforms of (a) the diode voltage inductively corrected (V_d), (b) the diode current (I_d), and (c) the ion-current density (J_i) measured by a biased-ion collector at 27 mm downstream from the anode. At t ~ 150 ns where the diode voltage attains the peak, we see

$V_d \sim 600$ kV, $I_d \sim 36$ kA, $J_i \sim 55$ A/cm² at $B/B_c \sim 2.5$,
$V_d \sim 550$ kV, $I_d \sim 53$ kA, $J_i \sim 70$ A/cm² at $B/B_c \sim 1.5$.

Here, the critical magnetic flux density (B_c) is given by[7]

$$B_c = \{2eV/mc^2 + (eV/mc^2)^2\}^{1/2} mc/ed, \quad (1)$$

where m, e and c is the electron mass, the electron charge, and the speed of light, respectively.

Figure 4 shows the streak photographs, where the time axis corresponds to that shown in Fig. 3. Figure 4 (a) shows that of H_α line (6562.8 Å) of hydrogen together with those of CⅡ (6578.0 and 6582.9 Å). Figure 4 (b) and 4 (c) show the streak photographs of CⅡ (4267.2 Å) and CⅢ (4647.4 Å), from which we can estimate the electron temperature. Table Ⅰ presents the transition parameters of the line spectra.[8,9] In Fig. 4 (c), we see the presence of CⅢ (4650.2 Å) in addition to the CⅢ (4647.4 Å). Although there should be present two lines of CⅡ (4267.0 Å and 4267.3 Å), it is too close to separate these two lines in Fig. 4 (b), and we here treat them to be 4267.2 Å. From Fig. 4, the light intensities of these lines observed attain the peak at t = 100 ~ 150 ns, damp at t ~ 200 ns, and again begin to be enhanced at t ~ 250 ns.

Figure 5 shows the time variation of the light intensity of the line spectra obtained by this system, where we have integrated the light intensity within 4 ~ 10 Å. The sensitivity of the system is same between Figs. 5 (a) and (d), and identical among Figs. 5 (b), (c), (e) and (f). From Fig. 5, we see the light signal starts at t ~ 40 ns. This suggests that the anode plasma is produced before it, which approximately corresponds to the build up of the diode current. Furthermore, all the light signal has the first peak at t = 100 ~ 150 ns, tends to be weakened at t ~ 200 ns, and again the second peak at t = 300 ~ 500 ns. Such a behavior seems to correlate with that of the electron density. Although, in Fig. 5, we see clearly the presence of the first peak of the light signal for z = 1.5 mm (nearby the anode surface), furthermore, we do not observe the first peak of the light signal

at z = 5 mm, almost the center of the anode-cathode gap.

From the time difference at different positions of the light signal, we estimate the expansion velocity of the anode plasma at the gap to be

$$(4 \sim 4.5) \pm 1.5 \text{ cm}/\mu\text{s}.$$

Figure 6 shows the time variation of the H_α spectrum that has been shown in Fig. 4 (a). We see the broadening of (2~5) Å (FWHM) in the profile of Fig. 6. Since the resolution of the wavelength of this system is less than ~ 1 Å, such a broadening is considered to be principally due to Stark effect.[10] Figure 7 shows the theoretical relation between the electron density and the half width of the broadening of the H_α line for T = 20000 K. Here, the relation utilized in this estimate is written by[11]

$$n_e = C(n_e, T_e)\Delta\lambda_s^{3/2}, \tag{2}$$

where $\Delta\lambda_s$ is the half width of the Stark broadening and the coefficient $C(n_e, T_e)$ has been given in Table (14-1) of Ref.11.

Figure 8 shows the electron density thus obtained. Here, we have assumed the electron temperature to be T_e = 20000 K. The resolution of the density measurement resulted from the wavelength resolution of this system is estimated to be less than ~ 1×10^{16} cm^{-3}. At the first peak at t ~ 100 ns, we find the electron density (n_e) to be

$$n_e \sim 4 \times 10^{16} \text{ cm}^{-3} \text{ at } B/B_c \sim 2.5,$$
$$n_e \sim 5 \times 10^{16} \text{ cm}^{-3} \text{ at } B/B_c \sim 1.5.$$

Hence, we find the electron density increases at a small B-field. Comparing this estimate with Fig. 3, we find that both the diode current and the ion-current density increase at a small B-field, and that correspondingly the electron density

is enhanced. Furthermore, the ion-current density has the similar behavior as the electron density.

If a local thermodynamic equilibrium is assumed to be satisfied in a plasma, the light intensity ratio (I'/I) of the spectra of the ions with the successive ionization stages of the same element is given by[11]

$$I'/I = (f'g'\lambda'^{3}/fg\lambda^{3})(4\pi^{3/2}a_0^{3}n_e)^{-1}(kT_e/E_H)^{3/2} \times \exp\{-(E'+E_\infty-E-dE_\infty)/kT_e\}, \quad (3)$$

where E_H denotes the ionization energy of hydrogen, a_0 the Bohr radius ($h^2/4\pi me^2$ = 0.53 Å), E the energy of the upper level of the transition, E_∞ the ionization energy from the lower to the higher stage, and dE_∞ the reduction of the ionization energy for the lower charged ions. The prime represents the quantity corresponding to the higher ionization stage, and f, g, and λ indicates the emission oscillator strength, the multiplicity of the upper level of (2J+1), and the transition wavelength, respectively.

Using eq. (3) for lines of singly ionized (C Ⅱ, 4267.2 Å) and doubly ionized ions (C Ⅲ, 4647 Å) of carbon,[12] we have estimated the electron temperature. The light intensity of C Ⅱ and C Ⅲ lines has been obtained from Fig. 5. The transition parameters of each lines have been calculated from Table I. Figure 9 shows the electron temperature thus estimated. From Fig. 9, we see that the electron temperature does not change so much in time, and that no significant change against B field. From Fig. 9, the electron temperature in this experiment can be sumarized as

$$T_e = 1.9 \sim 2.4 \text{ eV}.$$

Ⅳ. Summary

By use of the time-resolvable spectroscopic technique, we have measured the anode plasma of the single-current-feed MID that is fired in the Nagaoka "ETIGO-Ⅰ" pulse-power generator. Typically, we have operated the diode at V_d = 550 and 600 kV and I_d = 53 and 36 kA at B/B_c ~ 1.5 and 2.5, respectively. We have observed H_α, C Ⅱ and C Ⅲ lines, and obtained data of spectroscopic profiles continuously both in time and wavelength. From these experimental studies, we have obtained the following conclusions.

(1) From the Stark broadening of H_α line of hydrogen, we have found the electron density to be $4 \sim 5 \times 10^{16}$ cm^{-3}. The density behaves similarly as the diode current. The ion current density also strongly depends on the electron density of the anode plasma.

(2) From the intensity ratio of C Ⅱ and C Ⅲ lines, we have calculated the electron temperature to be 1.9 ~ 2.4 eV under the assumption of a local thermodynamic equilibrium. The temperature does not depend on the diode current.

(3) From the time difference of the spectra at different positions, we have estimated the expansion velocity of the anode plasma to be $4 \sim 4.5$ $cm/\mu s$.

Acknowledgements

This work was partly supported by the Grant-in-Aid from the Ministry of Education, Science and Culture of Japan. The authors would like to express their sincere thanks to Mr. Y. Shimotori of Laboratory of Beam Technology for his useful advice and fruitful discussions.

References

1) E. J. T. Burns: Paticle Beam Fusion Progress Report of Sandia National Lab., Jan. 1979 to June 1979, SAND 79-1944, p. 55 (1979).

2) D. J. Johnson, E. J. T. Burns, J. P. Quintenz, K. W. Bieg, A. V. Farnsworth, Jr., L. P. Mix and M. A. Palmer: J. Appl. Phys. 52, 168 (1981).

3) Y. Maron, M. D. Coleman, D. A. Hammer and H. S. Peng: Phys. Rev. Letters 57. 699 (1986).

4) H. Yoneda, K. Horioka, K. Kasuya, K. Mitobe, K. Ohbayashi, Y. Hashitate, H. Murase, Y. Kim, T. Saito, T. Urata, H. Sumitani: The Institute of Electrical Engineers of Japan (in Japanese), EP-87-17 (1987).

5) K. Yatsui, A. Tokuchi, H. Tanaka, H. Ishizuka, A. Kawai, E. Sai, K. Masugata, M. Ito, and M. Matsui: Laser and Particle Beams 3, 119 (1985).

6) Temporal disperser (C1155-01) catalogue, Hamamatsu Photonics K.K., Hamamatsu, Shizuoka (1982).

7) R. V. Lovelace and E. Ott: Phys. Fluids 17, 1263 (1974).

8) W. L. Wiese, M. W. Smith and B. M. Glenon: "Atomic Transition Probabilities", Vol. 1 (NBS, United States of Commerce, 1966).

9) A.B. Striganov and N. S. Sventitskii: "Tables of Spectral Lines of Neutral and Ionized Atoms", (IFI/Plenum, 1968).

10) Generally, the line spectra tend to broaden due to Doppler effect or Zeeman effect in addition to Stark effect. These two effects do not depend on the electron density. At $T_e \sim 2$ eV and $B \sim 7$ kG, for example, we estimate the broadening for this case to be ~ 0.7 Å and ~ 0.1 Å for the Doppler and Zeeman effects, respectively.

11) H. R. Griem: "Plasma Spectroscopy", (McGraw Hill, N. Y., 1964). Equations (2) and (3) in this text are cited from p. 305 and p. 272, respectively.

12) N. B. McNeils and A. W. Desilva: Plasma Phys. 24, 1261 (1982).

Table I. Transition parameters of the line spectra,[8,9] where the subscript i and k denotes the lower and the upper state of the transition, respectively.

Line (Å)	E_i(eV)	E_k(eV)	g_i	g_k	f_{ik}	Transition Array	E_∞(eV)
H_α (6562.8)	10.21	12.10	8	18	0.641	$2p^2P^\circ$- $3d^2D$	---
C Ⅱ (4267.2)	18.07	20.98	10	14	0.94	$3d^2D$ - $4f^2F^\circ$	11.26
C Ⅱ (4267.0)	18.07	20.98	4	6	0.94		
C Ⅱ (4267.3)	18.07	20.98	6	8	0.89		
C Ⅱ (6578.0)	14.47	16.35	2	4	0.62	$3s^2S$ - $3p^2P^\circ$	
C Ⅱ (6582.9)	14.47	16.35	2	2	0.311		
C Ⅲ (4647.4)	29.57	32.24	3	5	0.423	$3s^3S$ - $3p^3P^\circ$	24.38
C Ⅲ (4650.2)	29.57	32.24	3	3	0.253		

Figure captions

Fig. 1 Outline of the experimental arrangement.

Fig. 2 Schematic diagram of the time-resolved spectroscopic system.

Fig. 3 Typical waveforms of (a) diode voltage, (b) diode current and (c) ion-current density with the B-field as a parameter ($B/B_c \sim 1.5$ and 2.5). Here, the BIC has an aperture 1-mm in diameter and is biased to - 400 V.

Fig. 4 Typical streak photographs observed at z = 1.5 mm and $B/B_c \sim 2.5$: (a) H_α of hydrogen (6562.8 Å, 2p-3d), (b) singly ionized carbon (C II, 4267.2 Å, 3d-4f) and (c) doubly ionized carbon (C III, 4647.4 Å, 3s-3p).

Fig. 5 Temporal variation of light intensity for H_α line of hydrogen ((a) and (d)), C II ((b) and (e)) and C III ((c) and (f)) lines of carbon. The data of (a), (b) and (c) are taken at $B/B_c \sim 2.5$, while those of (d), (e) and (f) at $B/B_c \sim 1.5$. The solid and dotted lines indicate the data observed at z = 1.5 mm and = 5 mm downstream from the anode surface.

Fig. 6 Three-dimensional plot of the H_α line of hydrogen shown in Fig. 4 (a).

Fig. 7 Calculated Stark broadening of H_α line of hydrogen.[11]

Fig. 8 Time variation of electron density of anode plasma with the B-field as a parameter.

Fig. 9 Time variation of electron temperature of anode plasma, with the B-field as a parameter, where we have used eq. (3) and the electron density of Fig. 8.

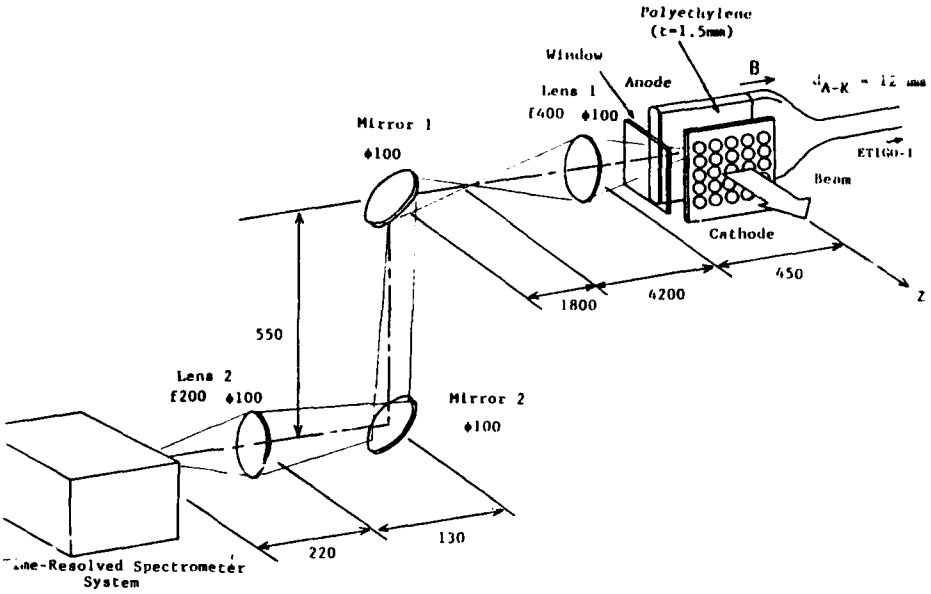
Polyethylene
(t=1.5mm)
Window
Anode
B
Lens 1
f400 ϕ100
Mirror 1
ϕ100
Beam
Cathode
1800
4200
450
z
550
Lens 2
f200 ϕ100
Mirror 2
ϕ100
220
130
Time-Resolved Spectrometer
System

FIG. 1

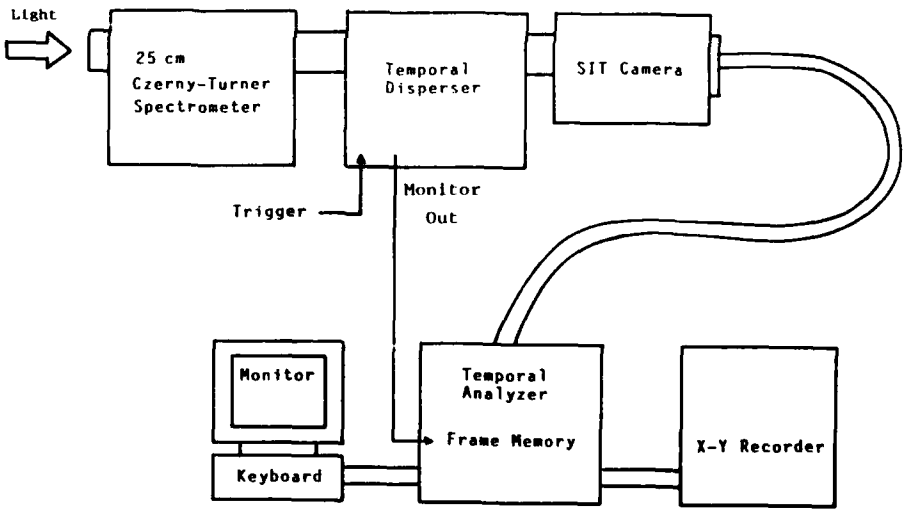
Light
25 cm
Czerny-Turner
Spectrometer
Temporal
Disperser
SIT Camera
Trigger
Monitor
Out
Monitor
Keyboard
Temporal
Analyzer
Frame Memory
X-Y Recorder

FIG. 2

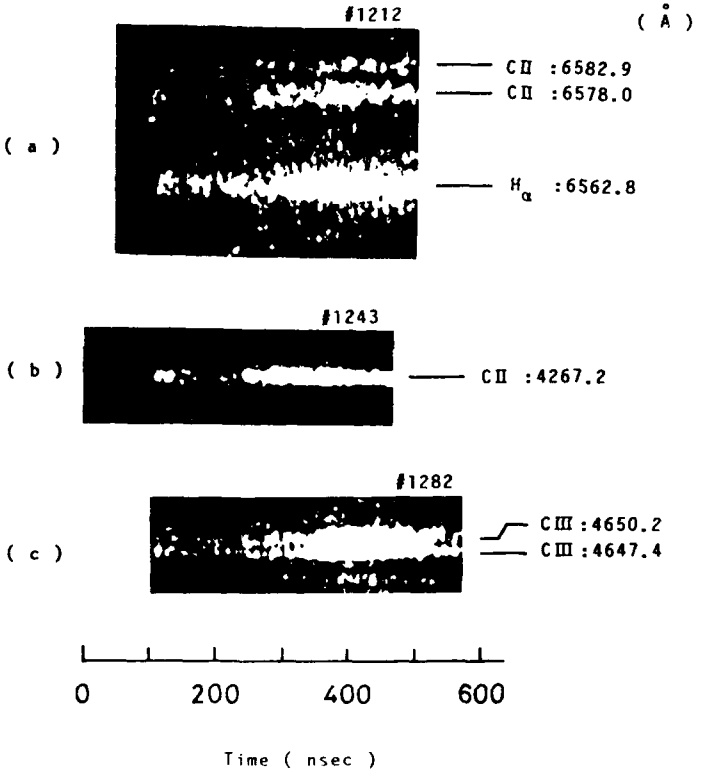
#1212
(Å)
(a)
CII :6582.9
CII :6578.0
H_α :6562.8
#1243
(b)
CII :4267.2
#1282
(c)
CIII :4650.2
CIII :4647.4
0
200
400
600
Time (nsec)

FIG. 4

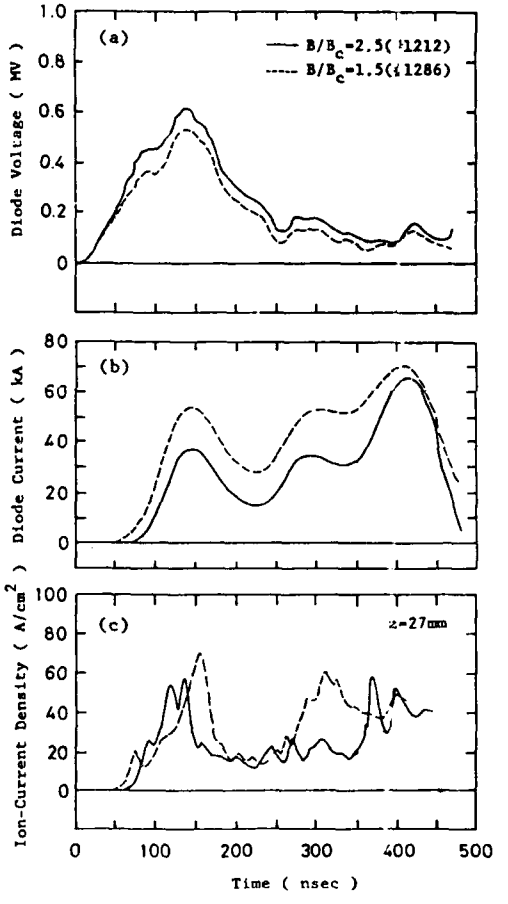
(a)
B/B_c=2.5(#1212)
B/B_c=1.5(#1286)
Diode Voltage (MV)
1.0
0.8
0.6
0.4
0.2
0
(b)
Diode Current (kA)
80
60
40
20
0
(c)
z=27mm
Ion-Current Density (A/cm^2)
100
80
60
40
20
0
0
100
200
300
400
500
Time (nsec)

FIG. 3

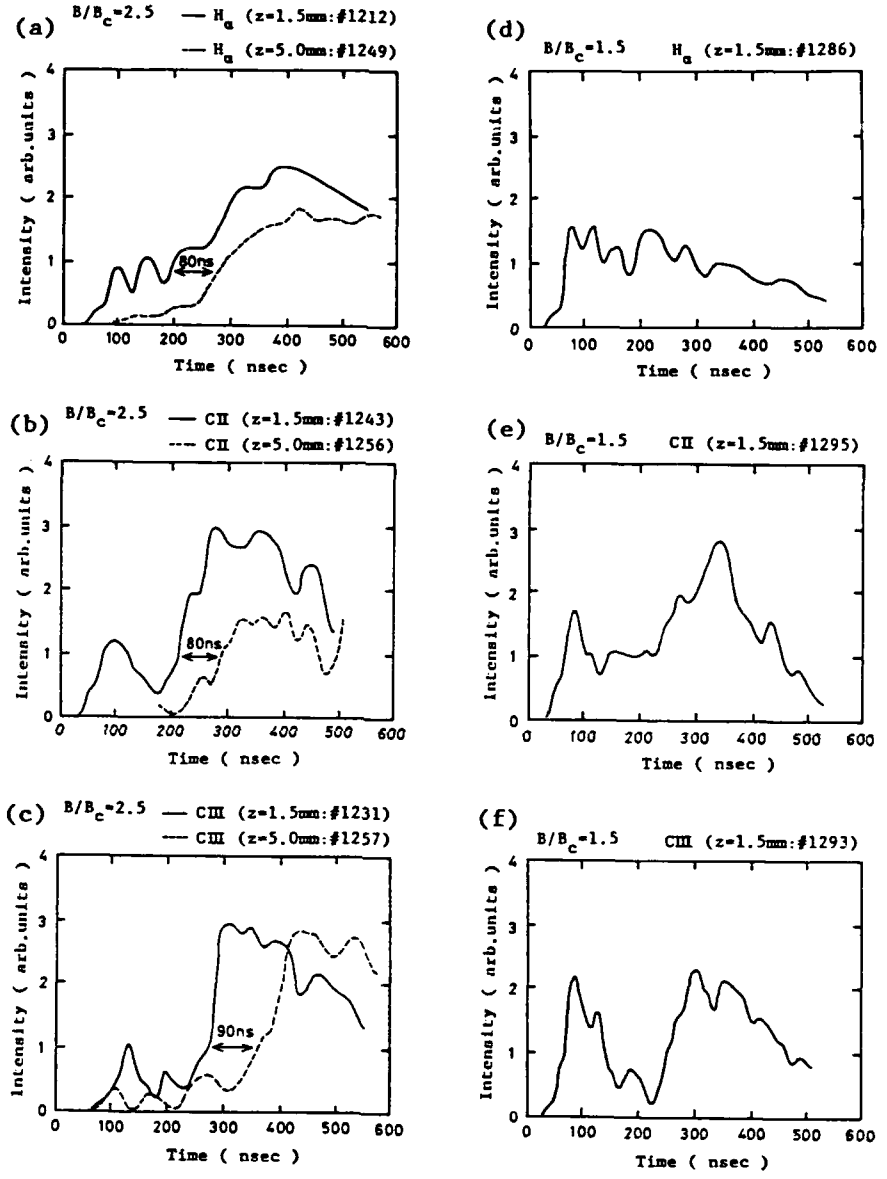
(a)
B/Bc=2.5
— Hα (z=1.5mm:#1212)
— Hα (z=5.0mm:#1249)
80ns
(b)
B/Bc=2.5
— CII (z=1.5mm:#1243)
--- CII (z=5.0mm:#1256)
80ns
(c)
B/Bc=2.5
— CIII (z=1.5mm:#1231)
— CIII (z=5.0mm:#1257)
90ns
(d)
B/Bc=1.5
Hα (z=1.5mm:#1286)
(e)
B/Bc=1.5
CII (z=1.5mm:#1295)
(f)
B/Bc=1.5
CIII (z=1.5mm:#1293)
Intensity (arb.units)
Time (nsec)

FIG. 5

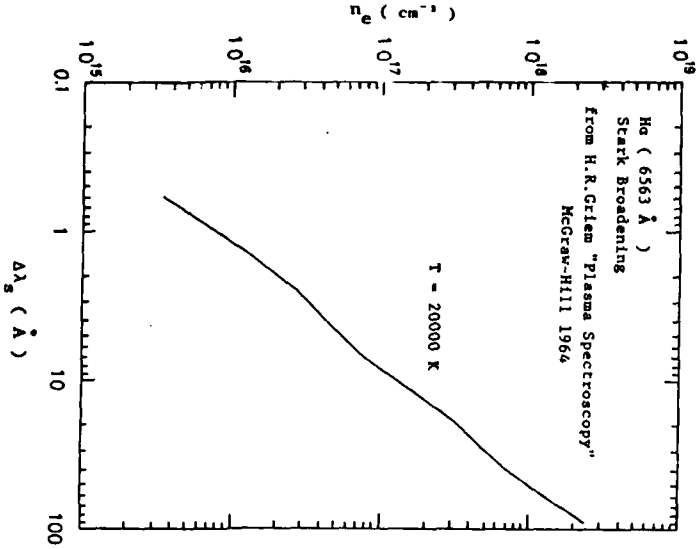
n_e (cm^{-3})
10^{15}
10^{16}
10^{17}
10^{18}
10^{19}
Hα (6563 Å)
Stark Broadening
from H.R.Griem "Plasma Spectroscopy"
McGraw-Hill 1964
T = 20000 K
0.1
1
10
100
$\Delta\lambda_s$ (Å)

FIG. 7

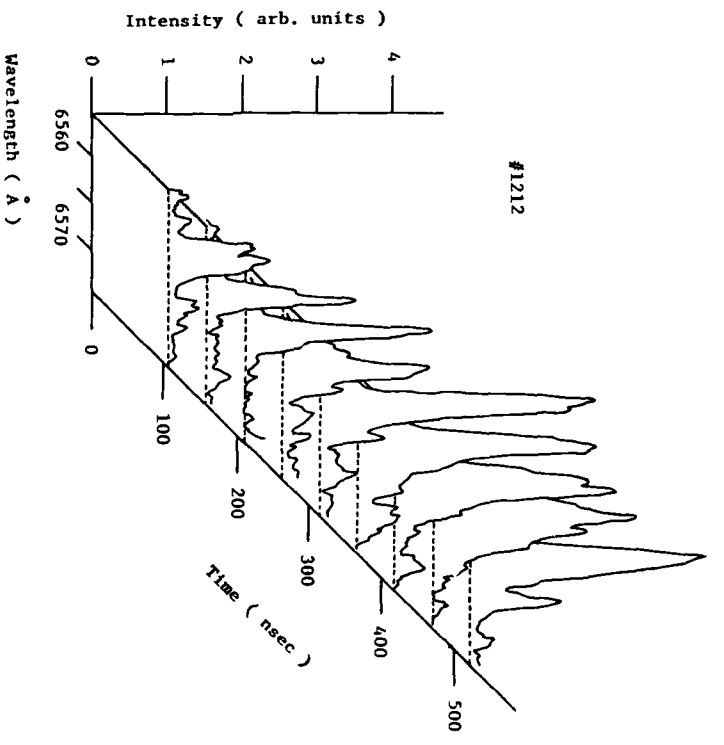
Intensity (arb. units)
0
1
2
3
4
Wavelength (Å)
6560
6570
0
100
200
300
400
500
Time (nsec)
#1212

FIG. 6

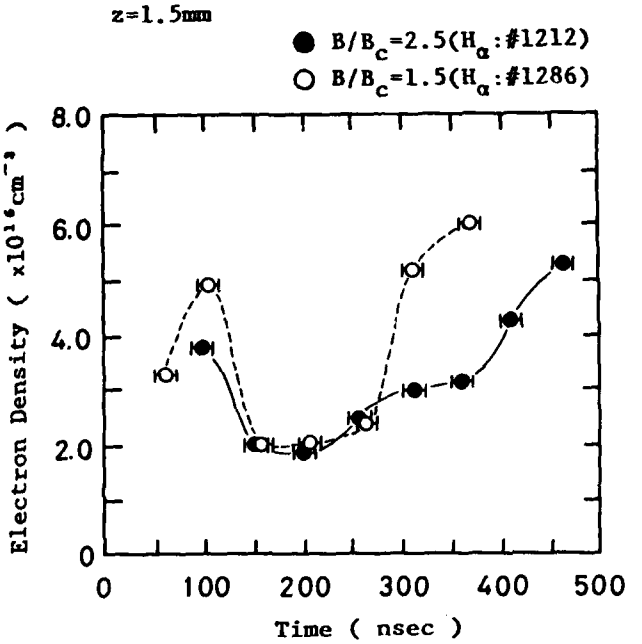
z=1.5mm
B/B$_c$=2.5(H$_\alpha$:#1212)
B/B$_c$=1.5(H$_\alpha$:#1286)
Electron Density (x10^{16}cm^{-3})
8.0
6.0
4.0
2.0
0
0
100
200
300
400
500
Time (nsec)

FIG.8

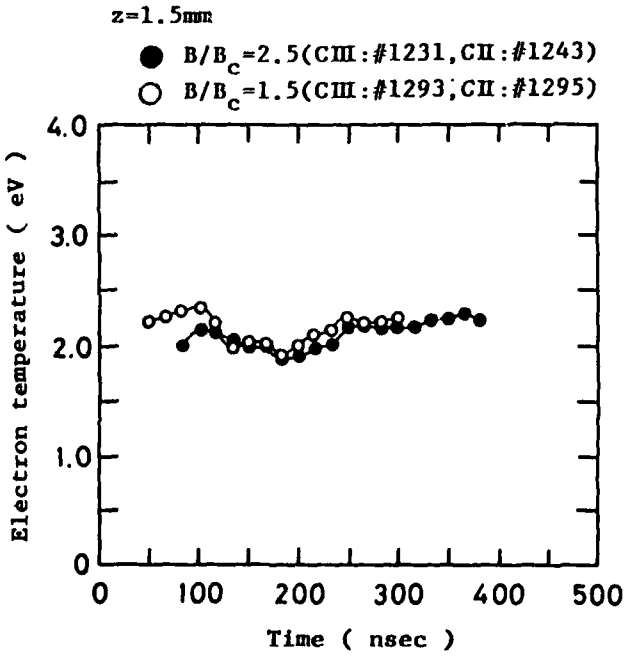
z=1.5mm
B/B$_c$=2.5(CIII:#1231,CII:#1243)
B/B$_c$=1.5(CIII:#1293,CII:#1295)
Electron temperature (eV)
4.0
3.0
2.0
1.0
0
0
100
200
300
400
500
Time (nsec)

FIG. 9

Study on the Flashover Ion Diode with Cryogenic Anode

K.Horioka, H.Yoneda and K.Kasuya

Tokyo Institute of Technology, Department of Energy Sciences,
The Graduate School at Nagatsuta, Midori-ku Yokohama,
Kanagawa 227,Japan

Abstract

Our recent experimental issues to clarify the behavior of acceleration gap of flashover type magnetically insulated diodes are shown. The main issues are to investigate the cause of impurity of the extracted beam and to examine the effect of neutral particle on the impedance characteristics of the diode. A magnetically insulated diode which has a cooled anode is used for the experiments.

1. Introduction

As well known, the pulsed ion diode is an energy rich and poor focus driver from the point view of its application to inertial confinement fusion (ICF). However, it is also true that only this type of ion source can be operated at MJ output energy level within tolerable construction cost. If we can get well controlled tightly focused beam, light ion beam (LIB) will become most hopeful ICF energy driver.[1)]

Therefore most important issue for the LIB-ICF is to get the sufficient power on the several millimeter fuel target. The temporally and spacially focusable power depends on the purity of the extracted beam, the brightness and the impedance characteristics of the diode. This is why we strongly concentrate our effort on the investigation of diode acceleration gap behavior especially on the electrodes plasmas.

Although there are many types of LIB diodes, magnetically insulated flashover-type ion diode is most simple, reliable and matured one. At present, this type of diode is the only reliable beam source which can operate at TW power level with moderate repetition capability.

2. Flashover Ion Source

The surface-flshover ion source has also some drawbacks; they are impurity of the extracted beam, nonuniformity of the anode plasma and the impedance falling of the acceleration gap.

The cause of beam impurity may be the contamination of anode surface or may be the ion filtering mechanism at the surface of anode plasma. Generally, the impedance of this type of diode is falling with time, which is undesirable from the point of view of the coupling efficiency and the target irradiation. At high output power level, the most important cause of impedance falling is supposed to be the electron accumulation in the gap which results in the decrease of effective A-K gap.[2] However the neutral particle injection into the gap or the turn-on delay of anode plasma should also play some roles on the impedance characteristics.

Then our recent experimental issues are to examine the cause of beam impurity, the formation process of the anode plasma and the effect of neutral gas injection into the gap on the impedance characteristics including its effect on the anode plasma expansion.[3]

The final goal of us is to make the appropriate density, temperature of anode plasma and to upgrade the purity of the extracted beam with controlable manner.

For the above mentioned purpose, we will use the cryogenic diode[4], because it can use various anode materials or their mixture under a wide range of operating condition. Figure 1 shows the schematic diagram of the diode. Frozen or condensed dielectric materials on the cryogenic anode are used as ion sources. It has the capability of ion species selection and repetitive operation. All of these characteristics are very much useful for the investigation of the issues mentioned above.

3. Diagnostics

For the above mentioned purpose, besides the conventional measuring tools such as biased ion collector, Rogowski coil and the resistive or inductive voltage monitor, we are preparing various diagnostics. They are the spectroscopy, interferometry and the particle measurements including the neutron detection.

We can estimate the density and temperature of anode plasma with the spectroscopic method, macroscopic behavior of the electrode plasma with interferometry, species and the energy spectrum of extracted beam with a time-resolved Thomson parabola analyzer,[5] and neutral particle with resonance interferometry, laser induced fluorescence and a neutral particle detector which can detect fast neutral particles.[6]

A schematic diagram of the experimental setup for the spectroscopic measurements is shown in Fig.2. The light emission from the electrode plasma is guided through an optical fiber of 7m in length to avoid electromagnetic noise. The light is detected by a photomultiplier behind a 50cm monochromator. Typical line profiles from D_2O or H_2O ion source are shown in Fig.3-(a). The plasma electron density is estimated from the Stark broadening of them and the temperature from line ratios. When we use a D_2O-H_2O mixture as the ion source, the observed spectrum changed as shown in Fig.3-(b). With this kind of measurements, we can get the information about the purity of the beam and the expansion velocity of anode plasma.

A schematic of the interferometric measurements is shown in Fig.4. At first we used a nitrogen laser as a light source of interferometry of the diode gap. Typical results taken by this method is also shown in Fig.4. Unfortunately, the wavelength of the laser is too short for the measurements. Conventional interferometric method requires about $10^{17}cm^{-2}$ particles to obtain measurable fringe shift. Furthermore, in general, it gives only electron number density. In our configuration the sensitivity limit of the plasma electron density is about $10^{18}cm^{-3}$. Then we made a dye laser excited by a nitrogen laser to measure the particle number density with higher resolution. The main difficulty of the neutral particle measurements is also the low density of them. If we can use resonance effect, the sensitivity of the density measurements increases upto hundreds times compared with the conventional nonresonance method.[7] The enhanced refraction n is given as a function of,

$$n - 1 = (r_0 f/4\pi)(\lambda^3 N_0/(\lambda - \lambda_r))$$

where λ is the wavelength, f is the absorption oscillator strength, r_0 is the classical electron radius, and N_0 is the atomic density. As shown, with this technique, we can get the density or macroscopic motion of specific atom or ion by tuning the laser to appropriate resonance line. As a preliminary experiments, we measured refractivity dispersion near the neutral hydrogen Hα line by the hook method. The experimental setup and a typical result are shown in Fig.5. At the resonance region, the fringe were distorted as shown in the figure. From this kind of experiment, we can directly estimate the number density of excited hydrogen atom. We can also estimate the total number of hydrogen atom under an appropriate plasma model.

A typical trace of Thomson parabola energy analyzer is shown in Fig.6. The trace was measured by a CR-39 track detector and was computer processed. When we make use of time modulation on the deflecting electric field of the analyzer, we can get much more information about the diode gap.[8] We can determine the energy spectrum of the extracted beam with time resolution.

We can also utilize the neutron measurements because we can use D_2O ice or D_2O doped material as the ion source. Typical signals of the neutron measurements are shown in Fig.7. In this experiment, a barrel shaped magnetically insulated diode was used and a D_2O ice was used as the ion source to hit the central D_2O ice target. In the figure, the first peak is the brems-X-ray signal from the diode region and the second peak corresponds to the D-D neutron signal. When we use a polyethylene shield , the neutron signal was disappeared as shown in Fig.7.

4. Experimental Issues

Our experimental issues are as follows,

1. How many surface layers are evaporated with diode operation?
2. Neutral particle effect on impedance falling
3. Temperature dependence of anode plasma formation
4. Is there filtering mechanism at the anode surface?

The first issue of our experiments is "How many surface layers are evaporated with diode operation?"

A preliminary experiment was performed for this issue. Figure 8 shows the total number of the neutral particle emission from the diode region during its operation. In this experiment, a Br-diode powered by a 5Ω-60nsec pulse forming line was used. The charge voltage and the field configuration of the cathode coil were changed as parameters. The total number of the particles is estimated by the pressure rise of the vacuum chamber.[9] As shown with this figure, it was observed that nearly 10^5 times of neutral particles compared with ions extracted from the diode gap was emitted with the diode operation, and the particle emission increased almost linearly with the extracted charge from the diode gap. This value corresponds to about 1000 layers of the dielectric materials if we assume the emission is limited from the anode dielectric surface. The experimental set-up planned in our laboratory is shown in Fig.9. A D_2O coated H_2O ice, whose coating thickness will be changed as a parameter, will be used as the ion source. In order to make clear the beam composition extracted from the source, the beam will be measured by the time resolved Thomson parabola analyzer, neutron detector and the anode plasma by the spectroscopic method.

The second issue is "neutral particle effect on the impedance falling." The formation of the surface-flashover plasma occurs with large neutral gas emission. The ionization of neutral atoms injected into the gap during flashover may cause the expansion of plasma front or the impedance falling. As shown in Sec.3, the quantity of them will be measured by the resonance optical method with temporal resolution. Figure 10 also shows the planned experiment for the above issue. A highly underexpanded supersonic neutral gas is puffed continuously into the gap. The another region of the vacuum chamber will be maintained at high vacuum condition because the surface of the cryogenic anode acts as the cryo-pump, which is the perfect sink against the gas injection, if the anode temperature is sufficiently low. An example of this kind of experiment is shown in Fig.11. Too much neutral particle density may result in

an electron avalanche that leads breakdown and A-K shorting. However, as can be seen in this figure, when we puffed the N_2 gas against the cryogenic anode which is cooled down to 20K, the extracted ion current increased two-to-three times compared with the normal operation. At present, it is not known why this increase was observed, and this reason is now under investigation.

The third issue is the investigation of the temperature dependence of the anode plasma formation processes The temperature dependence of the extracted ion current is shown in Fig.12[10]. In this experiment, a magnetically insulated Br diode was used. The temperature dependence may be explained by the surface flashover mechanism along the dielectric surface. Electrons emitted from a triple junction point bombard the sample surface to cause vaporization of the material there by triggering the surface flashover. As shown in our previous report, the turn-on time of anode plasma also has a temperature dependence[11]. The temperature dependence could be explained by the ease of vaporization at the higher temperature of dielectric materials. However, much more effort is needed to clarify this effect because there must be many factors which influence the anode plasma formation process.

The time-resolved mass-energy spectroscopy will be used as a main diagnostics for the forth issue. The composition of the extracted beam from various mixture ratio of H_2O-D_2O ice will be measured with diode insulation field as a parameter.

5. Summary

Our recent experimental issues to clarify the diode gap behavior of flashover type magnetically insulated ion diode were shown. Various diagnostic tools including resonant interferometry for the measurement of neutral particle density are developing for that purpose. In order to obtain the information about the issues several experiments were proposed and preliminary experimental results were shown.

References

(1) J.Maenchen et. al., ; BEAMS'86, Proc. 6th Int. Conf. on High-Power Particle Beams, Ed. by C.Yamanaca, 85 (1986)

(2) P.A.Miller and C.W.Mendel, Jr.; J. Appl. Phys., **61** (2) 529 (1987)

(3) R.Pal and D.Hammer; Phys. Rev. Lett., **50** (10) 732-735 (1983)

(4) K.Kasuya, K.Horioka, T.Takahashi, H.Yoneda and H. Kuwabara: IEEE Trans. Plasma Sci., **PS-13**, 5, 327 (1985)

(5) H.Yoneda, Y.Kim, K.Horioka and K.Kasuya ; Rev. Sci. Inst., (To be Published in March 1988)

(6) J.B.Greenly and Y.Nakagawa ; Cornell Univ. Laboratory of Plasma Studies Report **286** (1980)

(7) M.Gazaix, H.J.Doucet, B.Etlicher, J.P.Furtlehner, H.Lamain and C.Rouille; J. Appl. Phys., **56** (11) 3209 (1984)

(8) H.Yoneda, H.Tomita, K.Horioka and K.Kasuya ; In this Proceedings

(9) K.Horioka, H.Yoneda, K.Ohbayashi, K.Mitobe and K.Kasuya; Proc. 12th Int. Sympo. Discharges & Electrical Insulation in Vacuum, 162 (1986)

(10) K.Horioka, T.Takahashi, K.Kasuya, J.Mizui and T.Tazima; Jap. J. Appl. Phys., **23** (6) L374-L376 (1984)

(11) H.Yoneda, K.Horioka, K.Ohbayashi and K.Kasuya; Appl. Phys. Lett., **48** (18) 1196 (1986)

Figure Captions

Fig.1 Schematic Diagram of the Cryogenic Diode

Fig.2 Schematic of the Experimental Setup for Spectroscopic Measurements

Fig.3 Typical Spectral Profiles of Light Emitted from H2O or D2O Ion Source (a) and from H2O-D2O Mixture (b)

Fig.4 Schematic Diagram of Mach-Zender Interferometric Measurements

Fig.5 Schematic of the Resonance Interferometry and its Typical Result

Fig.6 Example of Computer Processed Thomson Parabola Trace

Fig.7 Example of D-D Neutron Signal Produced by using Cryogenic Diode

Fig.8 Total Number of Neutral Particle Emission as a Function of the Extracted Charge from Diode Gap

Fig.9 Planned Experimental Setup for the First Issue

Fig.10 Experimental Arrangement for the Second Issue

Fig.11 Examples of the Ion Current Trace with (a) and without (b) N2 Gas Injection into Diode Gap

Fig.12 Temperature Dependence of the Ion Current Extracted from Br-Magnetically Insulated Diode

CRYOGENIC DIODE

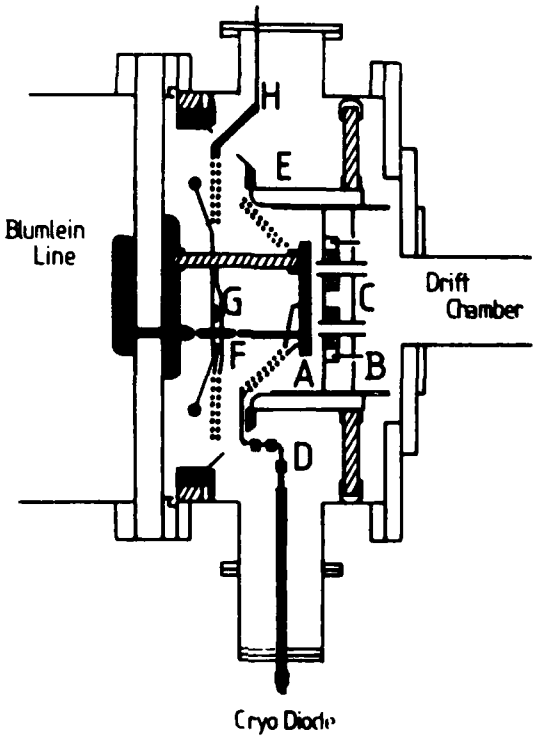

Fig.1

A; ANODE
B; GAS INJECTION NOZZLE
C; CATHODE
D; TRANSFER TUBE
E; RADIATION SHIELD
F; PREPULSE SWITCH
G; SHIELD PANEL
H; LIQ.N_2 FEED

SPECTROSCOPY

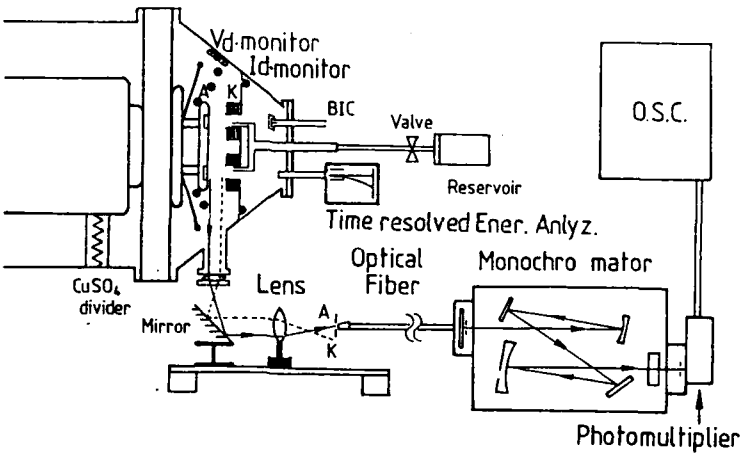

Fig.2

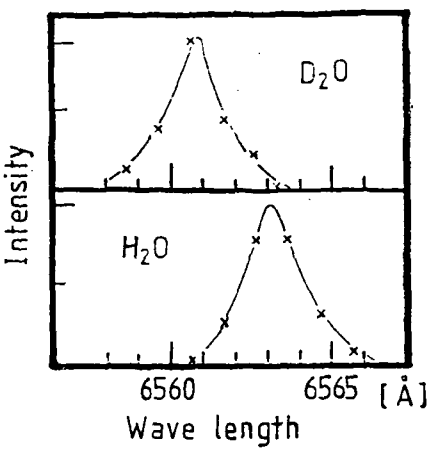

(a)

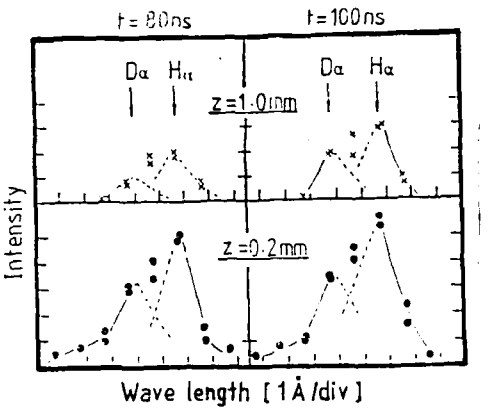

(b)

Fig.3

INTERFEROMETRY

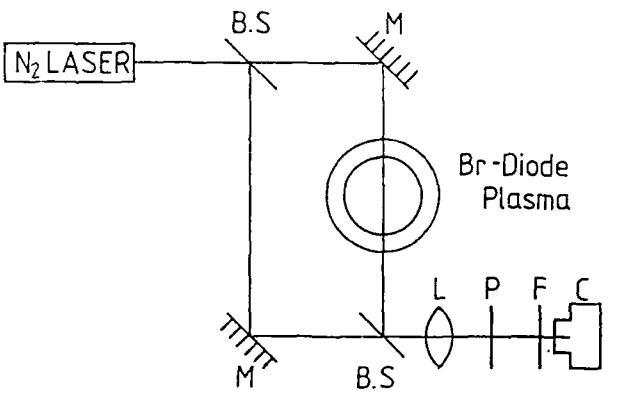

Fig.4

Interferogram of Diode Gap

Shadowgraph of Diode Gap

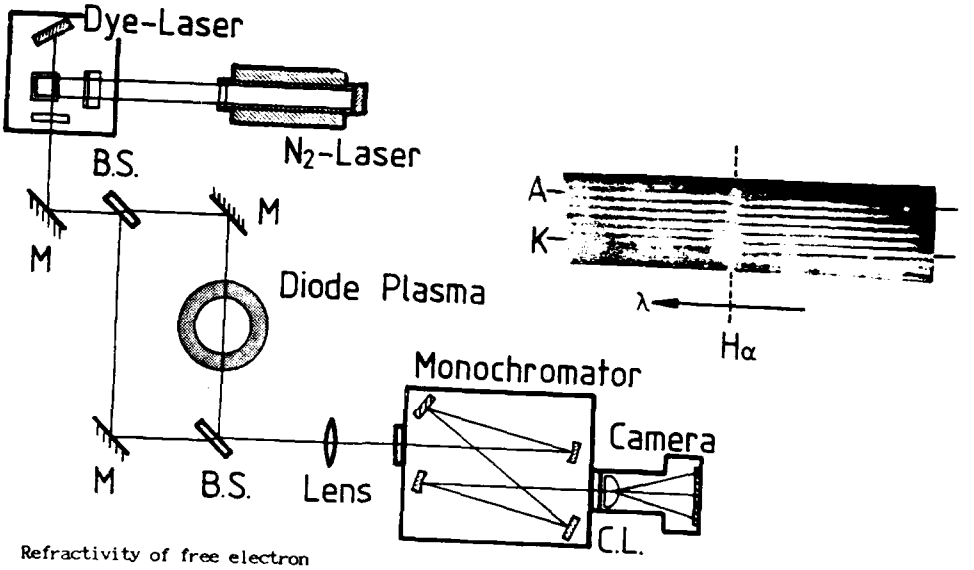

Refractivity of free electron

$\eta_e - 1 = -4.49\times10^{-28}\lambda^2 Ne$

$\delta = L(\eta-1)/\lambda = 0.044$

at $\lambda = 500$nm, $Ne = 10^{16}$cm^{-3}.

λ in nm,

Ne in cm^{-3}

resonant effect

$\eta_r - 1 = \frac{r_0 f}{4\pi}\frac{\lambda^3}{\lambda-\lambda r} N_0$

$\delta = 8.38\times10^{-16}\, N_0/(\lambda-\lambda r)$

Hα line, $\lambda = 656.2$nm, f=0.435.

Fig.5

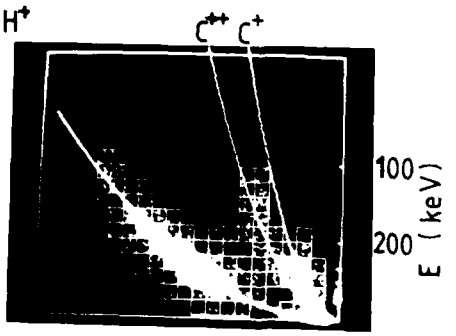

Fig.6

Fig.7
D-D NEUTRON SIGNAL

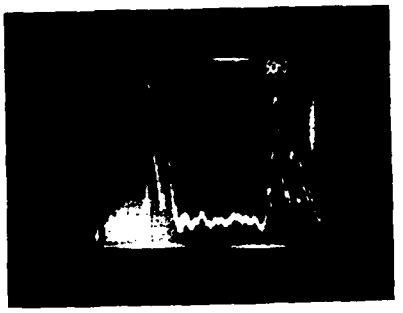

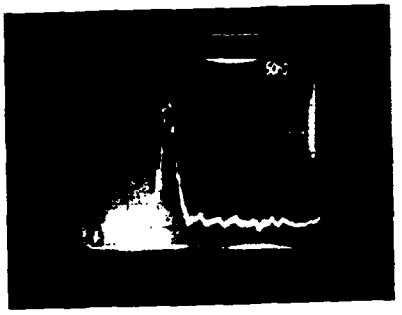

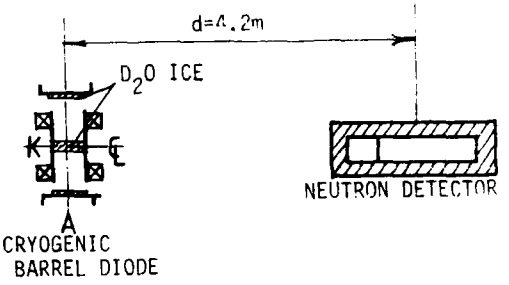

with Shield

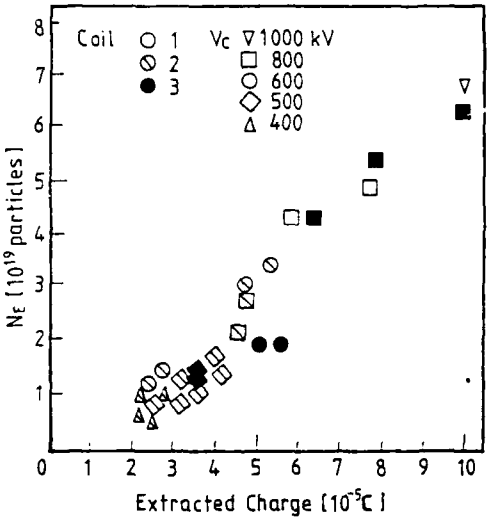

Fig.8

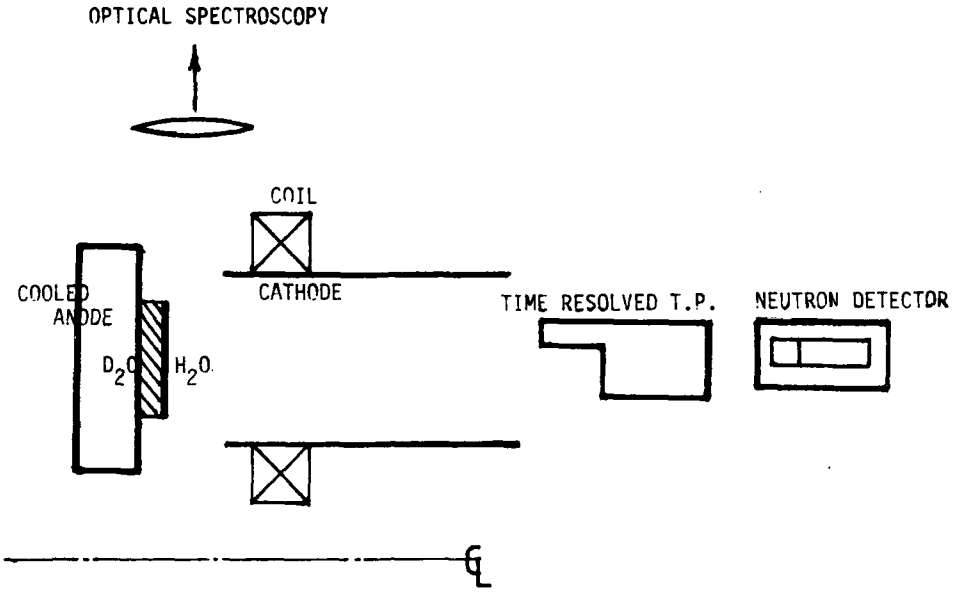
OPTICAL SPECTROSCOPY
COIL
CATHODE
COOLED ANODE
D_2O
H_2O
TIME RESOLVED T.P.
NEUTRON DETECTOR

Fig.9

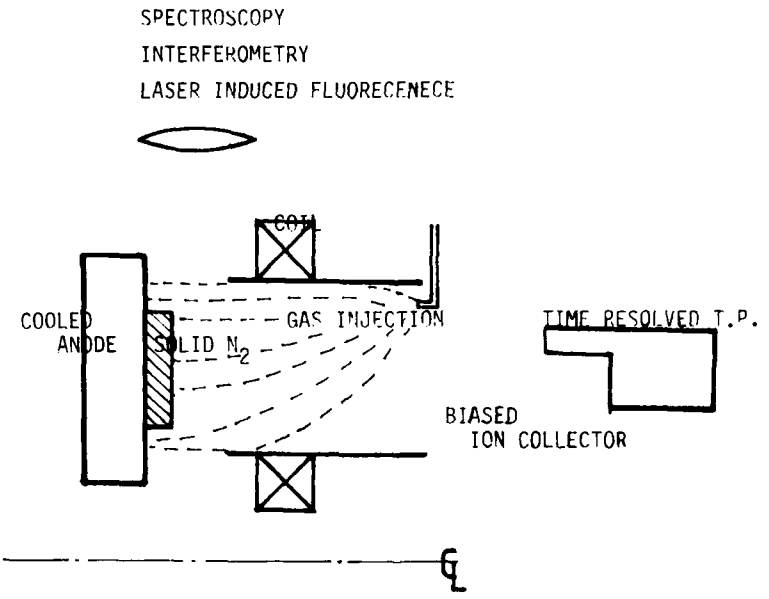
SPECTROSCOPY
INTERFEROMETRY
LASER INDUCED FLUORECENECE
COIL
COOLED ANODE
GAS INJECTION
SOLID N_2
TIME RESOLVED T.P.
BIASED ION COLLECTOR

Fig.10

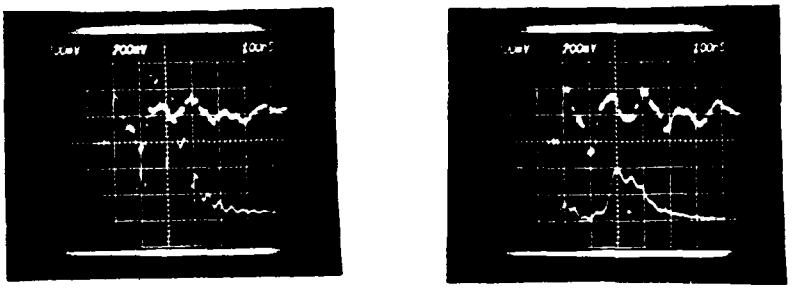

(a)

Diode Operation with Gas Injection

(b)

Normal Operation

(t; 100ns/d, I_i ; 129A/d, V_p ; 240kV/d)

Fig.11

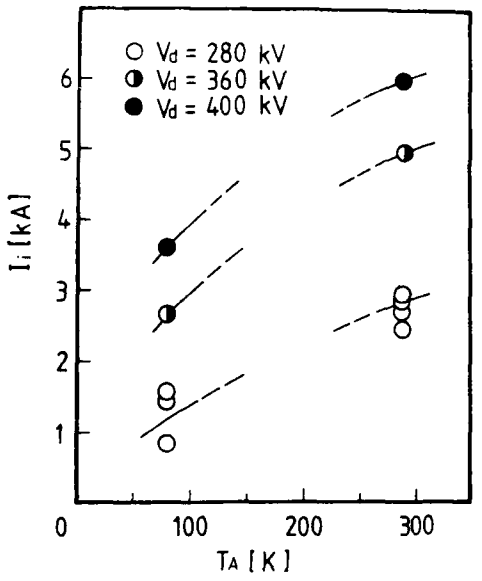

Fig.12

High Pressure Operation of Beam Diodes for Generating Relativistic Electron Beams

Hidenori Matsuzawa and Tetsuya Akitsu
Faculty of Engineering, Yamanashi University, Kofu 400

Abstract

A beam diode was operated successfully at a pressure as high as 10^{-1}∿ 10^{-2} Torr of gases (He, H_2, Ne, N_2, CO_2, and SF_6). Each gas had its optimum pressure p_m at which electron beam currents were higher in peak values than those for conventional in-vacuum operation by a factor of 1.5 or more. A relationship $p_m \times \sigma_H^{1.18}$ = const. was obtained where σ_H is the total ionization cross sections in gases at some hundred keV. A model was proposed for such operations, and those high pressure operations are preferable to the conventional if one needs higher currents.

Introduction

Most beam diodes for generating relativistic electron beams (REB's) have been operated at a pressure of 10^{-4} Torr or less. In our previous paper,[1] on the contrary, a beam diode was operated successfully at a pressure of as high as 0.2-Torr-N_2. In this report, we tried to accumulate experimental data for understanding such an operation.

The beam diode was operated both in the foilless and in the conventional type. Six different kinds of gases were introduced into the beam diode. Electron beam currents were observed as a function of the pressure of the gases introduced. Each gas had its optimum pressure for generating the maximum electron beam currents, which were always higher in peak values than those for

the in-vacuum operation. The optimum pressures were found to be inversely proportional to the total ionization cross sections in gases. From the experimental results we propose a model for the high pressure operation and suggest that the high pressure operation is preferable to the conventional in-vacuum operation.

Experimental results

An REB generator used was reported in an earlier paper.[2] Figure 1 shows the cross sectional view of the diode. The pressure of the diode was varied by controlling the flow rate of gases, and a Faraday cup was kept in an evacuated atmosphere of 10^{-4} Torr. A carbon cathode faced an anode of 30-μm-thick titanium foil. The REB generator was coaxial Marx-type, consisted of t n stages with output voltage pulses of 450 kV, 82 J/pulse, and a pulse width of less than 40 ns. Temporal waveforms of electron currents were observed with a storage oscilloscope of 500 MHz bandwidth (Tektronix 7934).

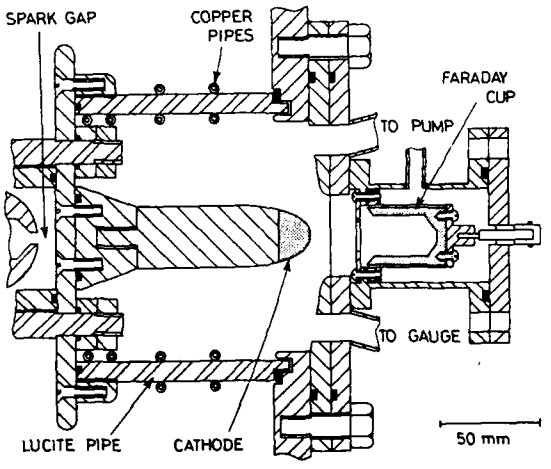

Fig. 1. Cross sectional view of beam diode.

Experimental results

Figure 2 shows the waveforms of electron currents for N_2 and SF_6. Peak values of the electron currents increase with gas pressures, and decrease above 0.065 Torr for N_2 gas and 0.015 Torr for SF_6. Hereafter we call the pressure at which maximum currents are generated the optimum pressure p_m. Figure 2 shows furthermore that pulse widths decrease above the optimum pressures. This is probably because the high voltage pulses applied on the beam diode are shorted by formation of dense plasma between the anode and the cathode. Waveforms similar to Fig. 2 were observed for such gases

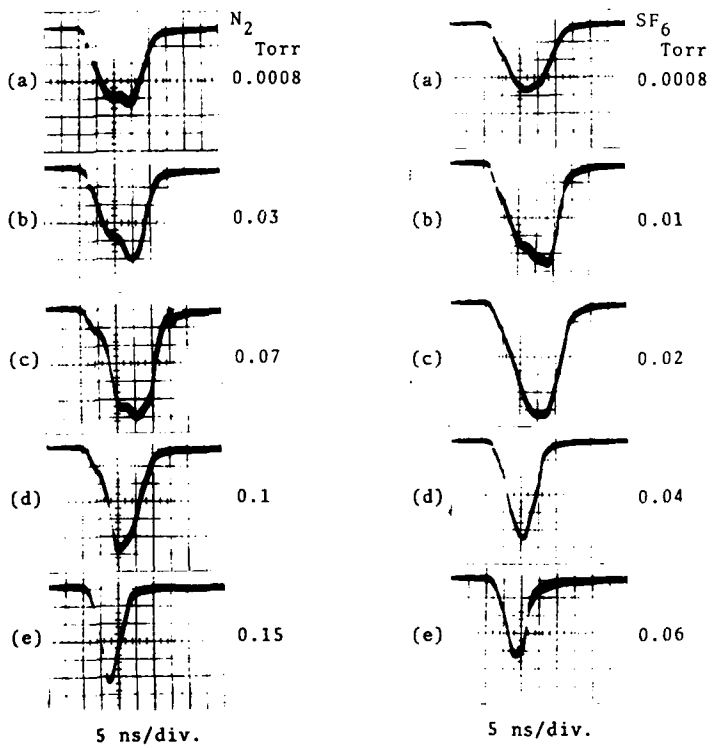

Fig. 2. Waveforms of electron currents for N_2 (a) and SF_6 (b). Vertical :74 A/div.;Horizontal:5 ns/div.

as He, H_2, Ne, and CO_2.

Figures 3(a)-(f) show the data of those gas species. The open circles indicate the peak values of the electron currents, and the solid circles indicate the pulse widths. Each point represents

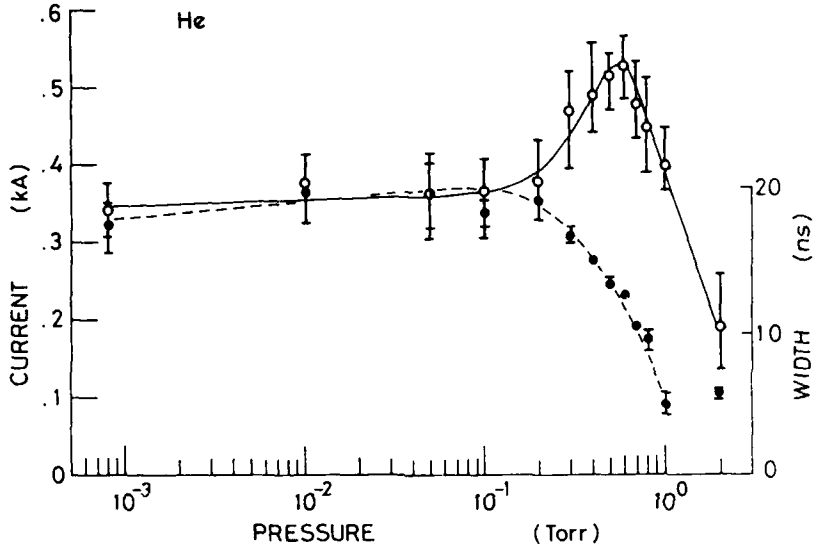

Fig. 3(a)

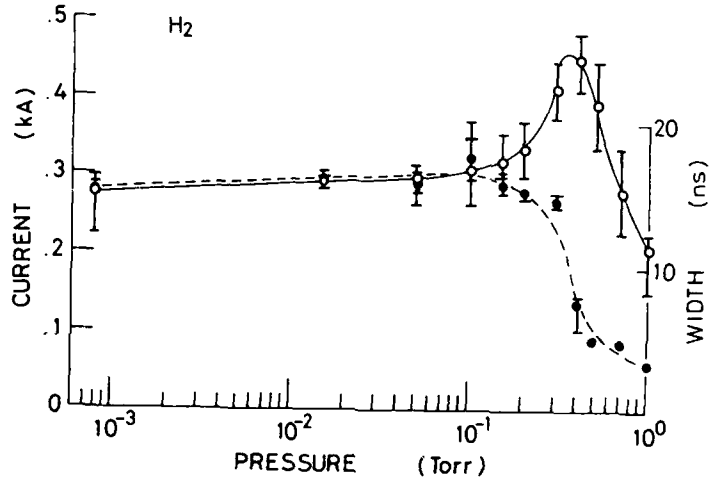

Fig. 3(b)

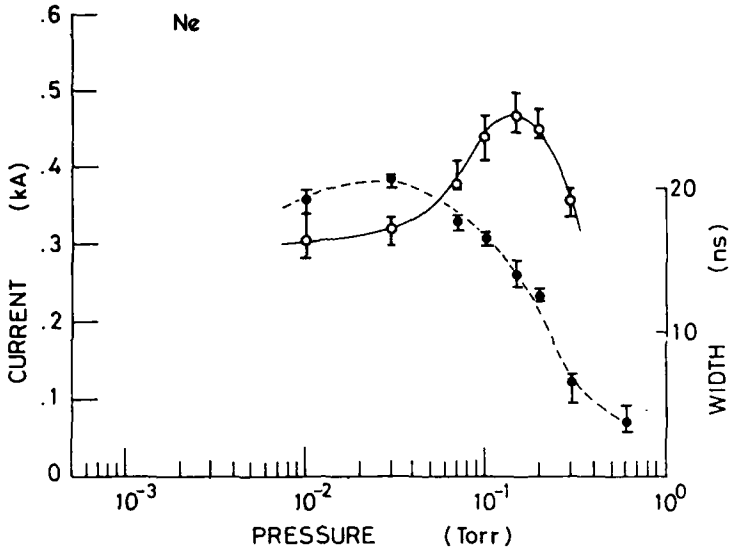
Ne
.6
.5
.4
.3
.2
.1
0
CURRENT (kA)
20
10
WIDTH (ns)
10^{-3}
10^{-2}
10^{-1}
10^{0}
PRESSURE (Torr)

Fig. 3(c)

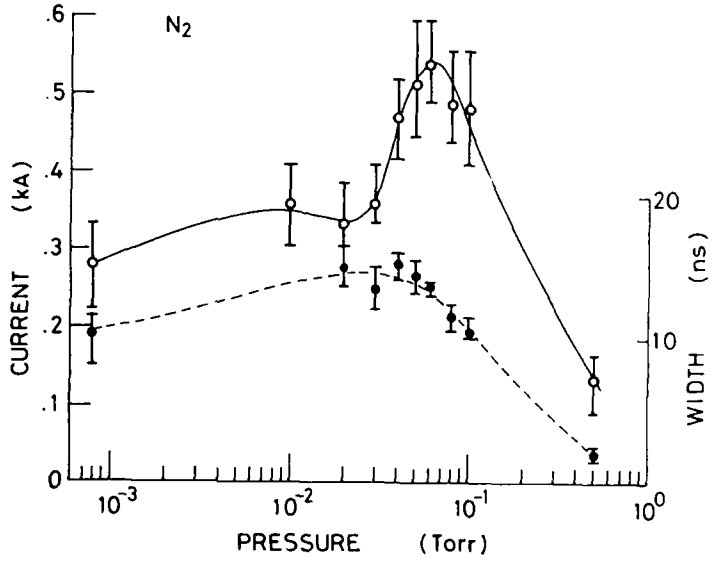
N_2
.6
.5
.4
.3
.2
.1
0
CURRENT (kA)
20
10
WIDTH (ns)
10^{-3}
10^{-2}
10^{-1}
10^{0}
PRESSURE (Torr)

Fig. 3(d)

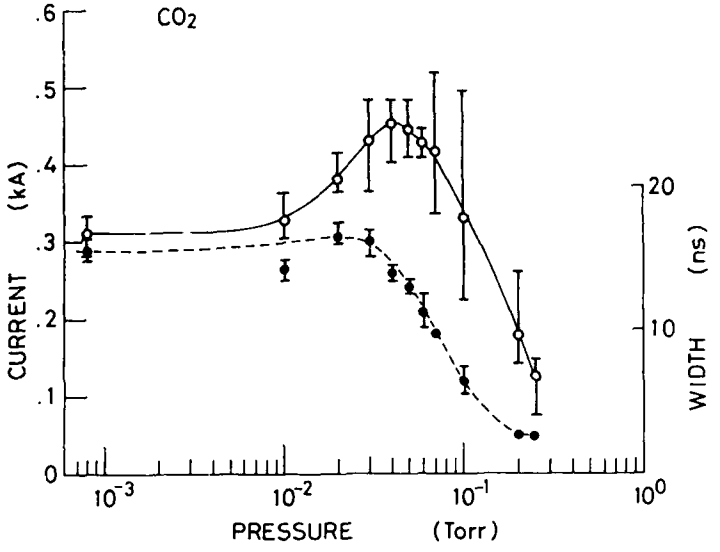

Fig. 3(e)

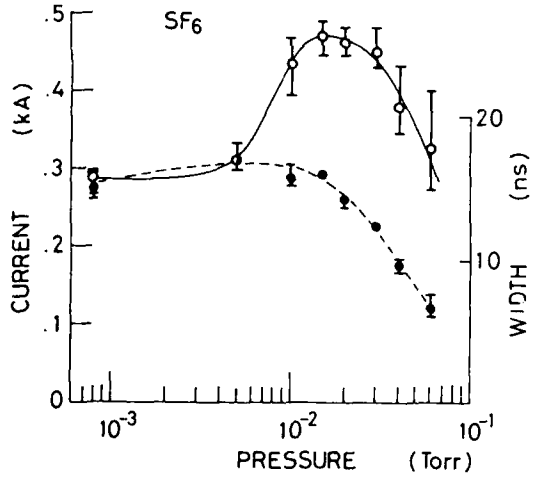

Fig. 3(f)

Fig. 3. Pressure dependence of electron currents (open circles) and of pulse widths (solid circles) for (a)He, (b)H_2, (c)Ne, (d)N_2, (e)CO_2, and (f)SF_6.

the average of about twenty shots. The error bars indicate the highest and the lowest value obtained at the respective time.

Next, kinetic energies of the electron currents for N_2 are roughly estimated from an unfolding method based on the experiments on the fractional transmission. A stack of aluminum foil was mounted on the top of the aperture of the Faraday cup, and transmitted electron currents were observed as a function of the thickness of aluminum foil. From the agreement between the experimental and the numerical results,[3] kinetic energies of the electron currents were estimated to be 270 keV. The kinetic energy thus obtained was nearly equal to that for the in-vacuum operation.

For discussions the data of total ionization cross sections[4-9] are summarized in Fig. 4 for the gases employed. From Fig. 4, the relative values of cross sections at some hundred keV are

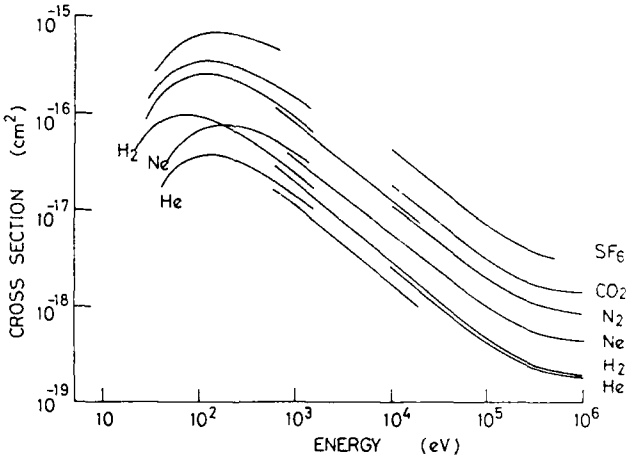

Fig. 4. Ionization cross sections as a function of kinetic energy of electrons.[4-9]

kept unchanged. The curves for H_2 and Ne cross each other at about 200 eV.

The optimum pressures p_m which were read from Fig. 3 are plotted in Fig. 5 as a function of the relative total ionization cross sections, σ_H, against those of H_2 at 480 keV. The approximated line in Fig. 5 has a slope of -1.18. Therefore, p_m satisfies the relationship $p_m \times \sigma_H^{1.18} = \text{const.}$

The optimum pressures were also plotted against the relative total ionization cross sections at 100, 150, 200, and 300 eV, because the relative total ionization cross sections change drastically at some hundred eV for H_2 and Ne. The points for H_2 and Ne, however, deviated much from an approximated straight line for either case of those low energies. The reasons for choosing the kinetic energy of 480 keV are that the ionization cross

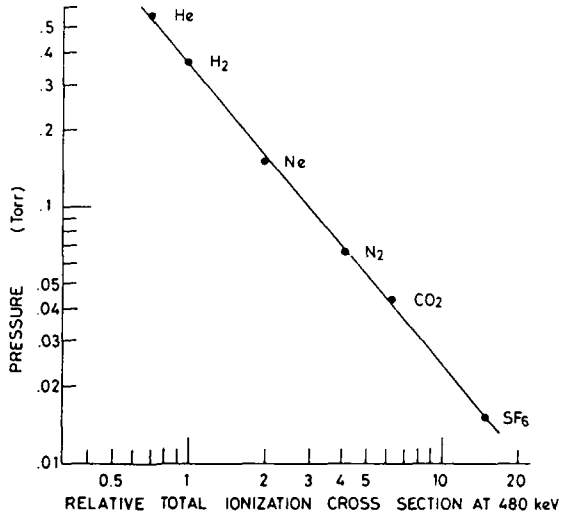

Fig. 5. Optimum pressures p_m at which maximum currents are obtained vs. the relative total ionization cross sections at 480 keV.

sections for SF_6 were discussed previously concerning the self-focusing of REB's[7] at the kinetic energy and that the cross sections at 480 keV are almost equal to those at 270 keV.

For a comparison, we mention here experimental results for a foilless diode: The anode of titanium foil was removed, and net currents were detected with an axially movable Faraday cup[10] which was mounted 20 mm apart from the cathode, inside the periodic permanent magnets (PPM).[1] The optimum pressures for these conditions are summarized in Fig. 6, following the relationship $p_m \times \sigma_L^{0.75} = \text{const.}$ where σ_L is the relative total ionization cross section at a low energy of 150 eV. This value of the kinetic energy was deduced from the facts that for either value of the total ionization cross sections at 100 and 200 eV the points for H_2 and Ne deviated from an approximated line connecting the points for other gases.

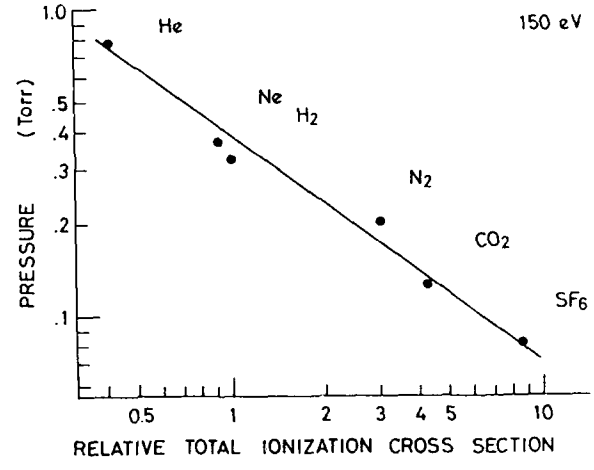

Fig. 6. Optimum pressures p_m for foilless diode operation as a function of relative total ionization cross sections at 150 eV. Approximated line has slope of -0.75.

Discussions and summary

Many reports have been published on the propagation of REB's through low pressure gases [11-15] and on collective ion acceleration. [16,17] Miller et al [13] derived experimentally a relationship $P_{60\%} \times \sigma_i$ = const. where $P_{60\%}$ is the pressure at which 60 % of the injected REB's was collected by a Faraday cup after travelling a tube filled with low pressure gases and σ_i is the total ionization cross sections at the kinetic energies of injected primary electrons. The number density of ions produced via collision processes is proportional to $p \times \sigma_i$ where p is the gas pressure. Therefore, Miller et al's relationship is understood to be a condition that a given number of ions must be produced to charge-neutralize [17] the injected REB's and to realize the highest transport of REB's.

Figure 6 suggests that electron multiplication is governed mainly by electrons of the kinetic energy of one hundred and some ten eV. From Figs. 4, 5, and 6 and Miller et al's results, [13] we can picture the processes of electron multiplication observed in this paper as follows: A certain amount of primary electrons is produced when a high voltage pulse is applied to the diode as in the conventional in-vacuum operated diode. The primary electrons accept kinetic energies of some hundred eV quickly while travelling a very short distance from the cathode. These electrons of such energies produce many secondary electrons via ionization collisions with gas molecules as shown in Fig. 4. Both the primary and the secondary electrons are then accelerated toward the anode, and collide with gas molecules less frequently as the electrons are accelerated more. While these electrons are accelerated, they are charge-neutralized by positive ions and are less influenced by space-charge force. There exists, therefore, an optimum gas

pressure at which the electron currents are charge-neutralized. As a result of these processes, we can collect the maximum electron currents at optimum pressures p_m.

The deviation of the slope from unity in Fig. 5 is probably due to the process that electrons collide with neutral gases while being accelerated in contrast to the process in Miller et al's experiments[13] where electrons were injected into gases after being accelerated. The accuracy of indication of a vacuum gauge (Pirani type) used also may have affected the slope in Fig. 5.

Diodes of high pressure operation have some drawbacks: One of them is that the diodes can not produce long pulses in duration time of electron currents due to shorting of the diodes. Another of them is that the electron beams have in principle energy spectra degraded as compared with those for in-vacuum operated diodes. When higher electron currents are required in spite of these drawbacks, however, diodes should be operated at pressures of the order of $10^{-1} \sim 10^{-2}$ Torr.

Acknowledgments

The authors would like to thank M. Fujiwara, Y. Ohtsuka, D. Takano, K. Tashiro, A. Furumizu, J. Ueno, and H. Yamazaki for their help in carrying out the experiments, O. Ohmori for his skillful assistance in experiments, and Y. Matsuno of the machine shop for his technical assistance.

References

1. H. Matsuzawa, T. Akitsu, Y. Suzuki, and S. Fuki, J. Appl. Phys. 61, 45 (1987).
2. H. Matsuzawa and T. Akitsu, Rev. Sci. Instrum. 56, 2287 (1985).
3. K. Kanayama and S. Okayama, J. Phys. D 5, 43 (1972).
4. D. Rapp and P. Englander-Golden, J. Chem. Phys. 43, 1464 (1965).
5. F. F. Rieke and W. Prepejchal, Phys. Rev. A6, 1507 (1972).
6. H. Hotta, R. Tanaka, H. Sunaga, and H. Arai, Radiat. Res. 63, 24 (1975).
7. H. Hotta, R. Tanaka, and H. Arai, Radiat. Res. 63, 32 (1975).
8. F. J. de Heer and R. H. J. Jansen, J. Phys. B10, 3471 (1977).
9. F. J. de Heer, R. H. Jansen, and W. van der Kaay, J. Phys. B12, 979 (1979).
10. H. Matsuzawa and T. Akitsu, Rev. Sci. Instrum. 58, 140 (1987).
11. W. T. Link, IEEE Trans. Nucl. Sci. NS-14, 777 (1967).
12. S. E. Graybill, IEEE Trans. Nucl. Sci. NS-18, 438 (1971).
13. P. A. Miller, J. B. Gerardo, and J. W. Poukey, J. Appl. Phys. 43, 3001 (1972).
14. J. R. Smith, R. F. Schneider, M. J. Rhee, H. S. Uhm, and W. Mankung, J. Appli Phys. 60, 4119 (1986) and references cited therein.
15. M. A. Greespan and R. E. Juhala, J. Appl. Phys. 57, 67 (1985) and references cited therein.
16. W. W. Destler, P. G. O'Shea, and Z. Segalov, J. Appl. Phys. 61, 2458 (1987).
17. R. B. Miller, *An Introduction to the Physics of Intense Charged Particle Beams* (Plenum, New York, 1982).